# Comportement à la corrosion, passivité et mécanismes de transport des ions sur les alliages contenant du Cr

Luntao Wang

## ▶ To cite this version:

HAL Id: tel-03549703

https://pastel.hal.science/tel-03549703

Submitted on 31 Jan 2022

# THÈSE DE DOCTORAT

## DE L'UNIVERSITÉ PSL

Préparée à Chimie ParisTech

# Corrosion behaviour, passivity and ion transport mechanisms on Cr-containing alloys

Soutenue par
**Luntao WANG**
Le 2 octobre 2020

Ecole doctorale n° 388
**Chimie physique et chimie analytique de Paris centre**

Spécialité
**Chimie Physique**

Composition du jury :

| | |
|---|---|
| M. Bernard NORMAND<br>Professeur, INSA Lyon | *Rapporteur*<br>*(Président du jury)* |
| M. Didier LEONARD<br>Professeur, Université Claude Bernard Lyon 1 | *Rapporteur* |
| Mme. Anne-Sophie MAMEDE<br>Maître de Conférences, Université Lille | *Examinateur* |
| Mme. Clara DESGRANGES<br>Ingénieur, Safran-Tech | *Examinateur* |
| M. Philippe MARCUS<br>Directeur de Recherche, Chimie ParisTech | *Directeur de thèse* |

# Acknowledgements

# Table of contents

# General introduction

Chromium pure metal left standing in air is passivated, by forming a thin, protective, surface layer of oxide. This chromium oxide layer is very dense and inhibits the diffusion of oxygen into the underlying metal. However, pure chromium is brittle and is rarely used as a structural material. The much more important aspect is the use of chromium in Cr-containing alloys (including high entropy alloys and stainless steels) which, if sufficiently rich in chromium (at least 13%), are spontaneously passivated and forming a protective surface oxide film, usually called the passive film, in the environment.

Generally, the properties of the passive films and thus the corrosion resistance of alloys are governed by their composition and structure. Several surface analytical techniques, including X-ray Photoelectron Spectroscopy (XPS) and Time-of-Flight Secondary Ion Mass Spectrometry (ToF-SIMS) can be applied to measure the surface structure and composition. XPS can identify the surface chemical species and quantify their concentrations, while ToF-SIMS can probe the variations of the elemental composition with depth and the eventual stratification of the surface oxide. These methods are often used in combination with electrochemical analysis, which is widely used to study the reactivity and especially the corrosion resistance of alloys. One objective of this work was to understand the reactivity of CoCrFeMnNi high entropy alloy using fine surface characterization techniques combined with electrochemical measurements.

As mentioned above, the surface oxide film is known to play a key role in the corrosion resistance of metals and alloys. Thus, the understanding of their nature, structure, composition and growth kinetics is important and requires a detailed knowledge of the ion-transport mechanisms. There is a lack of data on the ion transport process in the oxide film formed on Cr-containing alloy surfaces. Another objective of this work was to determine the ion transport mechanisms on Cr-containing alloys (304L and 316L stainless steels).

This manuscript contains six chapters.

Chapter I is a bibliographic study of the state of the art. This chapter starts with a general introduction to Cr-containing alloys, including stainless steels and high entropy alloys. Then

the electrochemical aspects of the passivity of Cr-containing alloys as well as the composition and structure of passive films are summarized. Then, the ion transport mechanisms on Cr-containing alloys are introduced. The last part concludes and contextualizes the objective of this work.

Chapter II presents the different techniques applied in this work. Surface spectroscopic techniques include XPS and ToF-SIMS. They were used to characterize the composition and structure of the oxide films. In addition, two-step oxidation experiments were carried out with *in situ* ToF-SIMS. Electrochemical techniques, including potentiodynamic and potentiostatic polarisation, were used to characterize the electrochemical aspects of passivity of the surface oxides.

Chapter III reports on the corrosion behavior of an equiatomic CoCrFeMnNi high entropy alloy with emphasis on the characterization of the surface oxide layers by XPS and ToF-SIMS combined with electrochemical measurements. An XPS methodology based on analysis of the 3p core level spectra was developed to determine the composition and thickness of oxide films. The modifications of surface oxide film after exposure to acidic aqueous solution at the open circuit potential were determined. The passivity of the HEA at different passive potentials has been studied.

Chapter IV investigates the thermal stability of pre-formed passive films on 316L stainless steel up to 300°C in ultra-high vacuum (UHV). 316L stainless steel was electrochemically passivated in $H_2SO_4$ and then annealed in UHV by increasing step by step the temperature, from room temperature up to 300°C. The stability of the passive oxide film has been monitored *in situ* during heating, and modifications of the composition and structure of the oxide films have been analyzed by ToF-SIMS.

Chapter V and Chapter VI investigate the ion transport process in pre-formed oxide films (native oxide and passive film) on 304L and 316L SS. The native film was formed in air, while the passive film was electrochemically formed in $H_2SO_4$. Following the investigation of the thermal stability of the oxide films at 300°C, the ion transport processes in oxide films on stainless steels were investigated by a re-oxidation step performed at 300°C in isotopic oxygen gas ($^{18}O_2$) at low pressure.

The four chapters presenting the results of this work, Chapters III, IV, V and VI, are in the form of articles published in scientific journals.

The main conclusions of this thesis are given in the final section together with the perspectives opened by the present study.

A summary of this work in French language is presented in Annex.

# Chapter I

# State of the art and objectives of the thesis

**I-1. Introduction to Cr-containing alloys**

**I-1.1. Introduction to stainless steel**

Stainless steels are iron-based alloys that contain a minimum of approximately 12 wt% chromium, less than 1.2 wt% carbon, and other alloy components [1-3]. Stainless steels are well known for their corrosion resistance, which is an intrinsic quality achieved thanks to the reaction of chromium with oxygen or water that creates a very thin and self-protecting layer on the surface. Stainless steels' corrosion resistance and their physical properties can be further improved by the addition of other components [2, 4], such as nickel [5-8], molybdenum [7, 9-11], niobium [12-16], manganese [6, 17, 18], nitrogen [19-24], copper [25-29], silicon [30-34] and vanadium [35-38]. Fig.I-1 provides a useful summary of some of the compositional and property linkages in the stainless-steel family. From this moment stainless steels were classified in three different types: ferritic, martensitic and austenitic stainless steels [2].
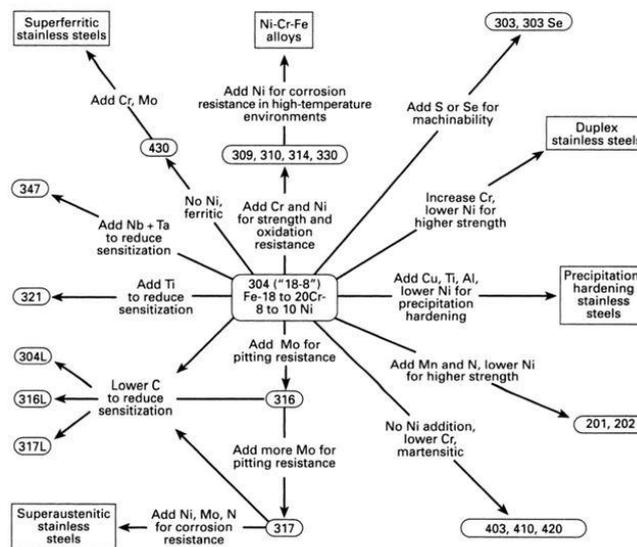
**Fig.I-1** Compositional and property linkages in the stainless steel family of alloys [38]

There are many different stainless steels, and the main types are grouped according to their metallurgical structure as follows.

*a. Martensitic Stainless Steels*

They are Fe-Cr-C alloys with or without addition of other alloying elements. Chromium content is 12-18 wt.% and carbon is 0.1-1.2 wt.%. These alloys are austenitic at 1050°C, but transform to martensite on cooling [39]. Steels with a higher chromium content require a higher carbon content to ensure the formation of martensite during heat treatment. However, the carbon will react with chromium in steel to form carbide, which affects the corrosion resistance of stainless steel [40]. These stainless steels are characterized by very high strength and low toughness. Typical applications include turbine blades, springs, aircraft fittings, surgical instruments, knives, cutlery, razor blades and other wear-resisting parts. Typical examples of martensitic stainless steel and their compositions are shown in Table I-1.

| AISI grades | C | Cr | Mo | Others |
|---|---|---|---|---|
| 410 | 0.12 | 12.5 | — | — |
| 420 | 0.20 | 13.0 | — | — |
| 430F | 0.14 | 16.5 | 0.40 | S: 0.25 |
| 440C | 1.10 | 17.0 | 0.60 | — |
| 431 | 0.17 | 16.0 | — | Ni: 2.00 |
| 630 (17/4PH) | ≤ 0.07 | 16.0 | — | Ni: 4.00 Cu: 4.00 Nb: 5xC to 0.45 |

**Table I-1** Chemical composition of martensitic stainless steel grades

*b. Ferritic stainless steels*

The ferritic stainless steels are Fe-Cr alloys with 15-30 wt. % Cr, low C, no Ni and often Mo, Al, Nb or Ti [41]. In general, ferritic stainless steels are cheaper than the austenitic and duplex stainless steels, and usually possess good stress corrosion cracking resistance and deep drawability [42]. However, their applications are restricted by poorer resistance to localized corrosive attack, their inferior stretch formability, poor weldability, their tendency to brittle fracture, and the need to constrain their carbon and nitrogen contents to very low levels. Modern melting and refining techniques like Vacuum-Oxygen-Decarburisation and Argon-Oxygen-Decarburisation have achieved considerable reduction in C and N contents in these alloys. The steels with low precipitates have improved formability, weldability and toughness

[1]. Typical applications include lower-cost kitchenware, solar heaters, slate hooks and coins [42]. Some typical ferritic steels and their compositions are shown in Table I-2.

| AISI grade | Cr | Other elements |
|---|---|---|
| 405 | 12.0 - 14.0 | — |
| 409L | 10.5 - 12.5 | 6(C+N)<Ti<0.65 |
| 410L | 10.5 - 12.5 | 0.3<Ni<1.0 |
| 430 | 16.0 - 18.0 | — |
| 439 | 16.0 - 18.0 | 0.15+4(C+N)<Ti<0.8 |
| 430Ti | 16.0 -18.0 | Ti: 0.6 |
| 441 | 17.5 - 18.5 | 0.1<Ti<0.60.3+3C<Nb<1.0 |
| 434 | 16.0 - 18.0 | 0.9<Mo<1.4 |
| 436 | 16.0 - 18.0 | 0.9<Mo<1.40.3<Ti<0.6 |
| 444 | 17.0 - 20.0 | 1.8<Mo<2.50.15+4(C+N)<Ti+Nb<0.8 |
| 447 | 28 - 30.0 | 3.5<Mo<4.50.15+4(C+N)<Ti<0.8 |

**Table I-2** Chemical composition of important ferritic stainless steel grades

*c. Austenitic stainless steels*

These stainless steels contain 18-25 wt.% Cr and 8-20 wt.% Ni and low C. Austenitic stainless steels possess austenite as their primary crystalline structure (face cubic centered) [1]. This austenite crystalline structure is achieved by sufficient additions of the austenite stabilizing elements such as nickel, manganese and nitrogen [43-47]. The austenitic group contains more grades, that are used in greater quantities, than any other category of stainless steel. Austenitic stainless steels exhibit superior corrosion resistance to both ferritic and martensitic stainless steels [48]. Corrosion performance may be varied to suit a wide range of service environments by careful alloy adjustment e.g. by varying the carbon or molybdenum content [49-51]. Typical applications include tanks, storage vessels and pipes for corrosive liquids, mining, chemical, cryogenic, food and beverage, and pharmaceutical equipment, cutlery, architecture, sinks and so on [52].

| AISI grade | C | Cr | Mo | Ni |
|---|---|---|---|---|
| 301 | 0.10 | 17.5 | — | 8 |
| 304 | < 0.07 | 18.5 | — | 9 |
| 304L | < 0.03 | 18.5 | — | 9 |

| | | | | |
|---|---|---|---|---|
| 303 | < 0.10 | 18 | — | 9 |
| 321 | < 0.08 | 18 | — | 10.5 |
| 316 | < 0.07 | 17.5 | 2.2 | 11.5 |
| 316L | < 0.03 | 17.5 | 2.25 | 11.5 |
| 316Ti | < 0.08 | 17.5 | 2.25 | 12 |

**Table I-3** Chemical composition of austenitic stainless steel grades

*d. Duplex stainless steels*

The metallurgical structure of duplex stainless steels consists of two phases, austenite (face-centered cubic lattice) and ferrite (body centered cubic lattice) in roughly equal proportions. They are designed to provide a better corrosion resistance, particularly to chloride stress corrosion and chloride pitting corrosion, and have a higher strength than standard austenitic stainless steels such as typical 304 or 316 SS [53-55]. The balance between ferrite and austenite is achieved by adjusting the amounts of Cr (18-26 wt.%), Ni (5-6 wt.%), Mo (1.5-4 wt.%) and nitrogen [1]. Duplex stainless steels are subdivided into lean, standard, super, or hyper duplex based on the quantity of alloying elements [55]. Duplex stainless steels contain more chromium and less nickel than 300-series (e.g. 316, 304 stainless steel) and typically include nitrogen as an additional austenite stabilizer and molybdenum for corrosion resistance [55, 56]. 2205 (22% chromium, 5% nickel, and 3% molybdenum) is a common standard duplex stainless steel, and 2507 (25% Cr, 7% Ni plus 4% Mo) is a common super-duplex steel. Typical applications include oil and gas equipment: flowlines, manifolds, risers, pumps, valves; pulp and paper industry: digesters, pressure vessels, liquor tanks; chemical engineering: pressure vessels, heat exchangers, condensers, distillation columns, agitators, marine chemical tankers and so on [57].

### I-1.2. Introduction to CoCrFeMnNi high entropy alloys

In 2004, Cantor et al. [58] firstly manufactured the equiatomic CoCrFeMnNi high entropy alloy (HEA) by melt spinning, and the five transition metal elements used to manufacture that HEA were found to exhibit a high degree of intersolubility to form a single FCC solid solution. In the same period, Yeh et al. [59] reported several HEAs produced by arc melting, including a huge number of elements such as Cu, Ti, Cr, Ni, Co, Cr, V, Fe and Al.
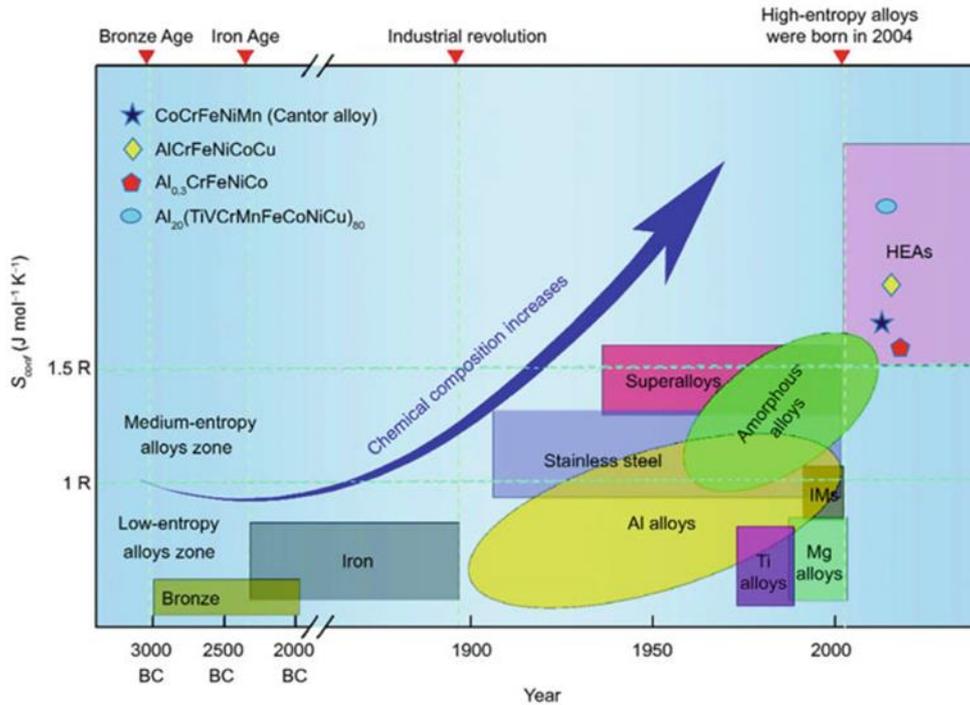
**Fig.I-2** The history of materials development [60]

HEAs with single-phase solid-solution structure with more than five principal elements has been a research focus for several years. With the in-depth understanding of HEAs, the limitations (single-phase and equimolar) have been gradually broken. Now, the second generation of HEAs has become an important part, named non-equimolar multiphase solid solution alloys or complex concentrated alloys (CCAs) [60], as shown in Fig.I-3 and Table I-4. The research scope of HEAs expands from the central region to the surroundings, which means the development from the equimolar single-phase solid-solution alloys to the non-equimolar multi-phase solid-solution alloys, which affects the definition of HEAs and the research scope. In other words, the evolution of HEAs conception facilitates the material design and development, meanwhile extends this idea to meet the specific needs, rather than rigidly adheres to the classical high-entropy definition [60]. The HEAs often have excellent comprehensive mechanical, physical, and chemical properties (including high hardness values, high yielding strengths, large ductility, excellent fatigue resistance, and good fracture toughness) [61-64], and show potential applications in heat and wear resistant coatings, mold linings, magnetic materials, hard alloys, and high-temperature alloys [65-68].

| Classification | Component | Feature | Composition | Atoms arrangement | Typical alloys |
|---|---|---|---|---|---|
| The traditional alloys | 1–2 principal elements | Tougher than the elementary substance | | A B | Fe-Ni, Fe-C, Cu-Al, Al-Mg |
| The 1$^{st}$ generation HEAs | At least 5 principal elements | Single phase, equimolar | | A B C D E | CoCrFeNiMn, AlCoCrFeNi |
| The 2$^{nd}$ generation HEAs | At least 4 principal elements | Dual or complex phases, non-equimolar | | A B C D | NbMoTaW, Al$_{0.3}$CoCrFeNi, Fe$_{50}$Mn$_{30}$Cr$_{10}$Co$_{10}$ |

**Table I-4** Characteristics for the two generations of HEAs [60]
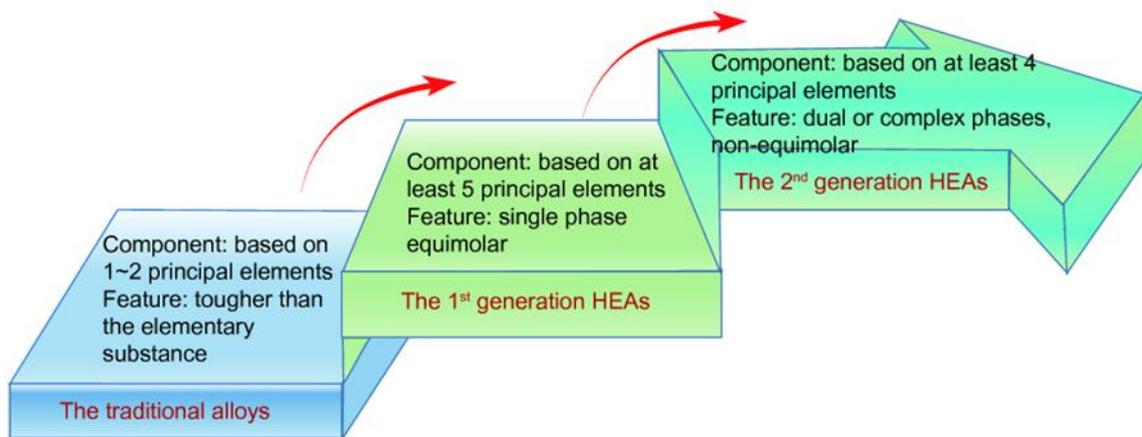


**Fig.I-3** The evolution of alloys [60]

Being different from the conventional alloys, compositions in HEAs are complex due to the equimolar concentration of each component. Yeh [69] summarized mainly four core effects for HEAs, that is: (1) Thermodynamics: high-entropy effects; (2) Kinetics: sluggish diffusion; (3) Structures: severe lattice distortion; and (4) Properties: cocktail effects.

*a. High entropy effects*

The most important characteristic of HEAs is the high-entropy effect. Gibbs free energy is showed in the following equation: $\Delta G = \Delta H - T\Delta S$ (H is the enthalpy, T is temperature, and S is the entropy). For conventional alloys, solid solution phases (including terminal and intermediate solid solution) have a higher configurational entropy than intermetallic compounds [70]. Because intermetallic compounds are ordered, and have continuous chemical compositions and specific lattice structures, the configurational entropy is approximately zero. High entropy can reduce the Gibbs free energy and promote the formation of solid solution phase, especially at high temperature [71]. Under the high mixing entropy, the number of generated phases is much smaller than the maximum value determined

according to the Gibbs phase law, which improves the compatibility between the components, then it is easier to form stable and single phases [72, 73]. Besides, high entropy can reduce the electronegativity difference and avoid phase separation, formation of some terminal solid solution or intermetallic compound in the alloys that may occur [74].
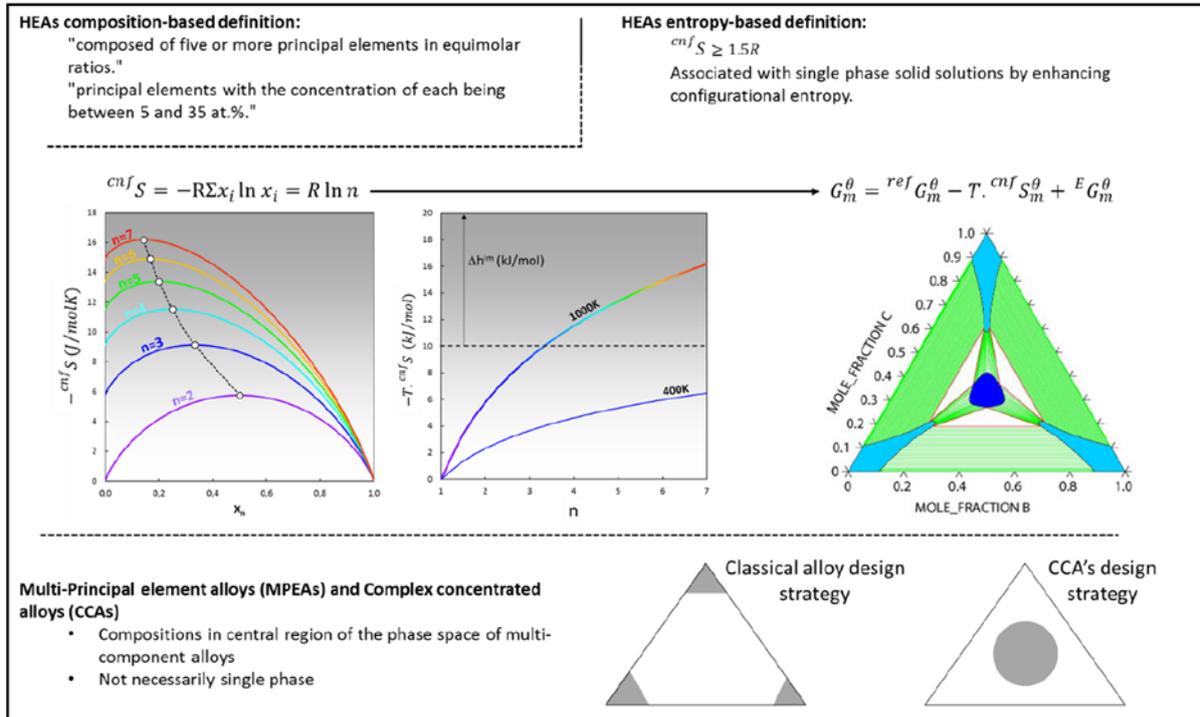


**Fig.I-4** A schematic displaying the effect of configurational entropy on the stabilization of single-phase solid solution around the equiatomic composition, where xi is the molar fraction of component i, n the number of components in equiatomic proportion, G the Gibbs free energy of a phase t (ref, cnf and E stand for reference, configurational and excess, respectively) [75]

*b. Sluggish diffusion effect*

The sluggish diffusion effect means that the self-diffusion coefficient of elements is much lower in HEAs than in other traditional alloys [76-79]. Yeh et al [80] have compared the diffusion coefficients for the elements in pure metals, stainless steels, and HEAs, and found that the order of diffusion rates in the three types of alloy systems is HEAs < stainless steels < pure metals. This is due to the interaction between different atoms and the lattice distortion, which seriously affects the effective diffusion rate of the atoms. This effect allows better high-temperature strength, structural stability and creep resistance of HEAs. However, Miracle [81] gives an opposite opinion on the sluggish diffusion effect. Although the sluggish diffusion

effect was one of the core effects for HEAs, this effect is still under debate, and its accuracy is still not validated now.

*c. Lattice distortion*

The lattice of HEAs comprises a number of elements, each of which has a different atomic size [82]. These dimensional differences inevitably lead to lattice distortion. Larger atoms push away adjacent atoms, while smaller ones have voids around them [83]. The strain generated by the lattice distortion can increase the total free energy of the HEAs, which also affects the properties [84]. For example, lattice distortion impedes dislocation movement and leads to pronounced significant solid solution strengthening effects. The lattice distortion can be too high due to excessive atomic size, so that the crystal configuration cannot be maintained, resulting in lattice collapse, formation of an amorphous phase structure [84-86]. The lattice distortion could also lead to increased scattering of propagating electrons and phonons, which translates to lower electrical and thermal conductivity [87].

*d. Cocktail effects*

The various elements of HEAs have different characteristics, and the interaction between different elements makes the HEAs exhibit a composite effect, that is known as the "cocktail" effect, first proposed by Indian scholar Ranganatha [88]. Alloying trace elements (including metalloid elements such as C, B, Si, etc.) can change the microstructure and properties of the alloys [89-91], and therefore many types of elements that can be selected [92]. The HEAs composed of elements with different properties have different microstructures and properties. The interaction and influence of the alloy components on the atomic scale will ultimately be reflected in the macroscopic comprehensive properties of the alloy, and even produce additional effects (high hardness [93], high strength [94], superconducting [95]).

**I-2. Passivity of Cr-containing alloys steel**

Passivity of metals and alloys is a central issue in corrosion science and engineering since the formation of ultra-thin, continuous, adherent and insoluble surface oxide films is the best of all means for protection of metallic materials against corrosion, and a key for their use in our environment [96, 97]. The global cost of corrosion in 2013 is around US$2.5 trillion, equivalent to roughly 3.4 percent of the global Gross Domestic Product (GDP) [98]. Passivity of metals and alloys is a phenomenon of great technical importance as it prevents many construction materials from rapid deterioration [99, 100]. For the majority of metals, passivity

is based on the spontaneous formation of a thin oxide layer (the passive film), in a specific environment. This film can slow down corrosion (dissolution) reactions by many orders of magnitude [101, 102]. The oxide passive films have thicknesses most commonly limited to a few nanometers; and form a well continuous, adherent and insoluble surface oxide barrier between corrosive environment and the substrate [96, 97, 103]. Today's studies on passivity continue to be directed toward gaining a better understanding of the chemical and physical properties of passive films.

### I-2.1. Passivation mechanism

*a. Early History of Passivity*

Observations on passivity date back to over 200 years. Uhlig [104] has traced the first use of the word "passivity" to C. Schönbein in 1836 [105], although earlier observation on passivity had been made by M. Lomonosov in Russia in 1738 [106], C. Wenzel in Germany in 1782 [107], J. Keir in England in 1790 [108], and subsequently by Schönbein [105] and Michael Faraday [109]. These early investigators established that the dissolution of iron in certain acid solutions stopped after first undergoing vigorous active dissolution [110].

In the case of passivity, for example, it has been already shown in 1911 that alloying chromium to iron leads to a radically improved corrosion resistance of the alloy [111]. This was immediately applied in the manufacturing of cutlery. However, it took another 50 years for researchers to understand that passivity is based on the spontaneous formation of a highly protective oxide film, the passive film, on the metal surface, as it reacts with the environment. These films, which in many cases are no thicker than only a few nanometers, act as a reactivity barrier between the metal surface and the aggressive environment.

It has been established that the quality of the film in terms of the ion- and electron-transport properties, or in terms of its structure and chemistry, determines the dissolution rate of passive metals in a specific environment [96, 100, 103, 112-114]. This is, of course, of enormous technological significance, since dissolution rate often determines the lifetime of structural materials [115, 116]. Areas such as construction materials, electronics, and transportation are affected and thus any measure that enhances the passive state may also have a considerable economic impact.

*b. Electrochemical Basis for Passivity*

The electrochemical basis for passivity is found in the anodic polarization curve illustrated in Fig.I-5. The shape of this curve is typical of various metals (e.g., iron) which undergo an active-passive transition in acid solutions (such as sulfuric acid).
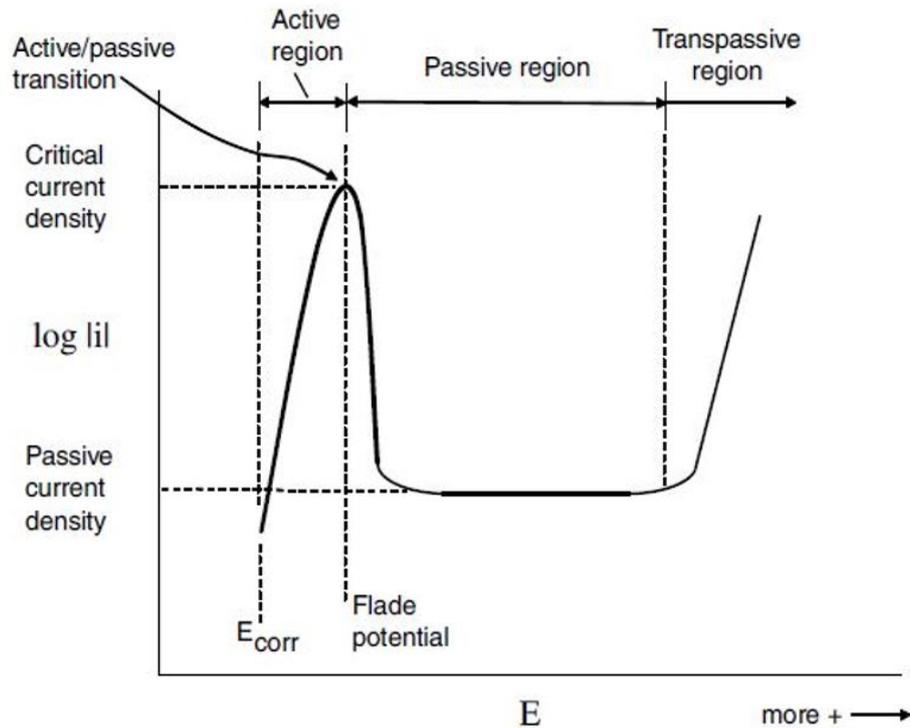


**Fig.I-5** Schematic anodic polarization curve for metals [117]

Beginning with the open-circuit corrosion potential (Ecorr) and moving in the anodic direction, first pass through a region of active corrosion in which the open-circuit corrosion rate can be determined as usual by the Tafel extrapolation method. But at a certain potential, further increases in potential cause a decrease in the anodic current density, as a consequence of the formation of a protective passive film being formed on the metal surface. Thus, the metal is undergoing an active/passive transition. The current is observed to drop rapidly as the passive oxide is formed and as the metal enters the passive region of the anodic polarization curve. The current density in the passive region is called the passive current density. With further increases in anodic potential, the current restarts to increase. This current increase in transpassive region is the consequence of the passive film breakdown due to the dissolution of metallic ions and the oxygen evolution reaction. The region beyond the passive region in which the current density again increases with increasing potential is called the transpassive region.

## I-2.2. The passive film and corrosion behavior of Cr-containing alloys

Chromium pure metal left standing in air is passivated, by forming a thin, protective, surface layer of oxide. This chromium oxide layer is very dense and inhibits the diffusion of oxygen into the underlying metal [110, 118]. In contrast, iron forms a porous oxide through which oxygen can migrate, causing continued rusting with the presence of water in the surface or in humid environments [106, 119]. However, pure chromium is brittle and is rarely used as a structural material [120, 121]. The much more important aspect is the use of chromium in Fe-Cr based alloys which, if sufficiently rich in chromium (at least 13%), are spontaneously passive in the environments [99, 122, 123].

Generally, the properties of the passive film and thus the corrosion resistance of metals and alloys are governed by their composition and structure [96, 100, 103]. Several surface analytical techniques, including X-ray Photoelectron Spectroscopy (XPS), Time-of-Flight Secondary Ion Mass Spectrometry (ToF-SIMS) and Auger Electron Spectroscopy (AES) can be applied to measure the surface structure and composition. XPS can identify the surface chemical species and quantify their concentrations, while ToF-SIMS can probe the variations of the elemental composition with depth and the eventual stratification of the surface oxide. These methods are often used in combination with electrochemical analysis, which is widely used to study the reactivity and especially the corrosion resistance of alloys [53, 124-128].

In the following, we present the composition and structure of passive films prepared electrochemically on Fe-Cr based alloys, in order to illustrate the influence of addition elements, including Ni, Mn, Co and Mo, on corrosion behavior of the alloys. The composition and structure of oxide film formed on high temperature will be discussed in part I-3.1(e).

*a. Fe-Cr alloys*

The passivation stability is strongly enlarged by alloying Cr into Fe. The remarkable changes in the corrosion behavior of Fe-Cr alloys at a critical Cr concentration were systematically studied by Monnartz in 1911 [111]. Since these early studies, the existence and origin of critical threshold values for the Cr concentration in Fe-Cr alloys has often been discussed [122, 129, 130]. In a study of the corrosion behavior of Fe-Cr alloys in 1 M $H_2SO_4$ (pH=0) it was found that alloys containing more than 13 at% Cr show Cr-like behavior and alloys with a Cr concentration below 10% behave similarly to Fe regarding their activation behavior [122]. Fig.I-6 shows the polarization curves of Fe-Cr alloys in 0.5M sulfuric acid. The Fe-Cr

alloys with a higher chromium content have lower passivation potentials and passive currents. This confirms that the increasing addition of Cr improves the passivity of the Fe-Cr alloy [131]. On the other hand, measurements of the critical current density of Fe-Cr (Cr: 0-16%) alloys in neutral sulfate solutions show a linear dependence on the Cr concentration [132].
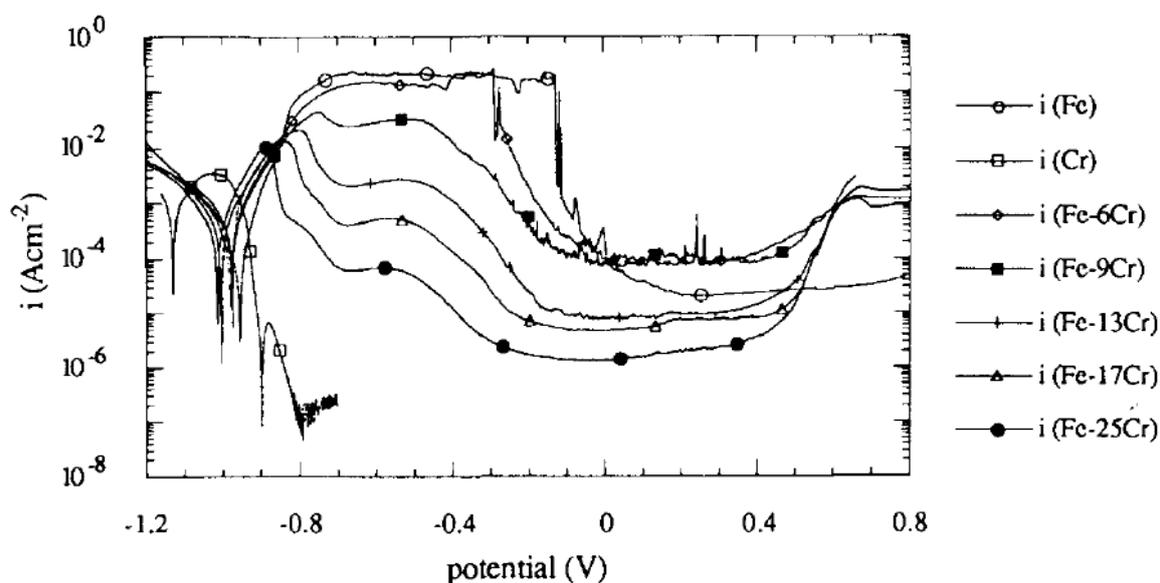


**Fig.I-6** The polarization curves of iron, chromium, Fe-x%Cr (x=6, 9, 13, 17, 25) in 0.5M $H_2SO_4$ [131]

Principally, the chemical composition and the thickness of electrochemically formed passive films depend on the passivation potential, time, electrolyte composition, and the temperature, i.e., on all passivation parameters [99, 100, 102, 103, 110, 133].

In acid solution, anodic polarization of a Fe-Cr alloy in the passive potential region leads to selective dissolution of iron, leaving chromium enriched in the passive film to fractions around 50-70% [123, 127, 134]. This behavior is governed by the difference in diffusion rates of iron and chromium in the passive film [119, 135, 136]. For an alkaline solution, the solubility is lower for Fe and higher for Cr; this affects the level of chromium enrichment in the film and would result in a higher fraction of iron in the passive film [137-139].

As for Fe-Cr alloys, the passive oxide film, formed in sulfuric acid, is generally thought to be duplex, with an inner region mixing Cr(III) and Fe(III) oxides and enriched in chromium, and an outer region of Fe(III) or Cr(III) oxides/hydroxides [133, 136, 138-148].

In acidic solution, the passive film thickness is estimated to few nanometers [123, 136, 140-142, 146]. However, in alkaline solution, the thicker passive film is formed on the sample surface, since dissolution is less pronounced compared to the film in acidic solution [140, 147, 148].

*b. Effect of Ni*

The role of nickel in the alloys is more important with respect to mechanical properties such as ductility and toughness than with respect to corrosion.

The thickness of the passive film is in the range of few nanometers, with no significant influence of the addition of Ni in the alloy [149, 150]. The composition of the passive film formed on Fe-Cr-Ni alloys, except Ni-based alloy, is also similar to that on Fe-Cr alloys [99, 118, 143, 149-151]. For Ni-based alloys, the outer layer is describing as a Fe rich layer, while the inner layer is mainly composed of chromium oxide (with a small amount of nickel and iron oxides) that could transform into spinel oxide (of the form $Ni_xFe-xCr_2O_4$) with oxidation time [152-155]. According to the standard Gibbs free energy of formation ($\Delta G298.15k°$) for oxides ($Cr_2O_3$: -1058 kJ/mol; $Fe_2O_3$: -714 kJ/mol; $NiO$: -211 kJ/mol) [156], nickel is less reactive towards oxygen than iron and chromium. Thus, no or little Ni oxide could be observed in the passive film. However, Ni is found enriched in the modified alloy region underneath the passive film compared to the concentration in the bulk alloy [99, 133, 143, 149, 150].

*c. Effect of Mo*

Molybdenum is an alloying element with a strong beneficial influence on the suppression of active dissolution and increased resistance to localized corrosion of Fe-Cr alloys [134, 157, 158]. The positive influences of Mo on pitting corrosion behavior have been observed in various types of stainless steels, including Fe-Cr based ferritic stainless steels [11, 159-163] and Fe-Cr-Ni based austenitic stainless steels [127, 134, 159, 162-166]. The beneficial role of molybdenum on corrosion resistance has long been discussed and several effects have been proposed. They can be sorted into two main classes depending on whether Mo is proposed to mitigate passive film breakdown [99, 118, 137, 164, 167-170], or to promote passive film repair [99, 137, 160, 171, 172]. However, which effect prevails remains subject to debate. Several effects may combine to improve passivity and pitting corrosion resistance.

Including molybdenum in the Fe-Cr alloys has little influence on the thickness and composition of the passive film [103, 127, 134, 173]. The main components of the passive film are still Cr(III) and Fe(III) oxides [127, 134, 166]. The main valence state of molybdenum in the passive film are presented mainly as Mo(VI), which is independent of the pH of the solution [99, 137, 160, 168, 172, 174]. The Mo(IV) can be found for passivation in acidic solution [51, 173].

The structure of the passive film formed on Fe-Cr-Mo alloys remains duplex, with a Cr oxide rich inner layer and a mix of Fe/Cr/Mo (hydr)oxides outer layer [99, 102, 127, 134, 137, 150, 166, 174-176]. In the latest research, a duplex model proposed by Maurice et al. [127] for the passive film formed on 316L (Fe-19Cr-13Ni-2.7Mo) surface is presented in Fig.I-7. According to their work, the inner layer essentially consists of Cr(III) oxide and the outer layer of Fe(III) and Cr(III) (hydr)oxide. Mo(IV-VI) oxide would be in the outer layer of the passive film.
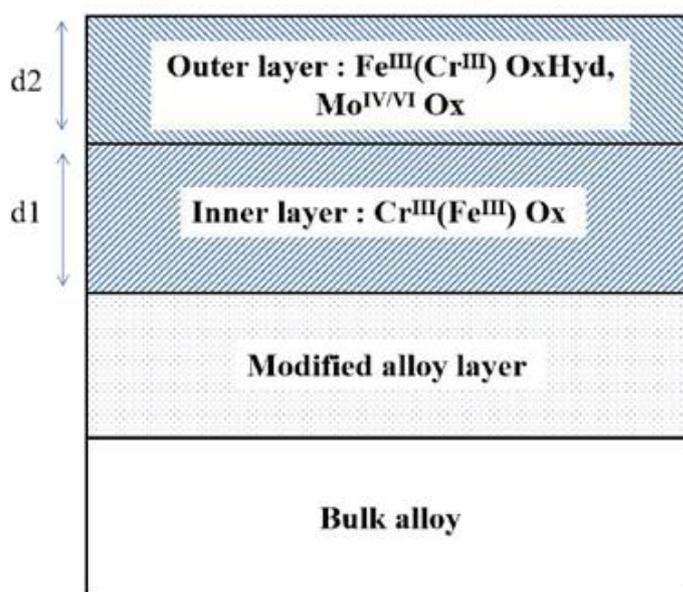


**Fig.I-7** Model of duplex structure proposed for the passive film on 316L stainless steel surface [127]

*d. Effect of Mn*

Mn is an important alloying element, because it is an economical austenite former, and it is effective in increasing the nitrogen solubility in Fe-based alloys [51, 173, 177-185]. However, alloying Mn is known to be harmful to the corrosion resistance of various types of stainless steels [186-192]. Wu et al. [190, 191] reported that high Mn alloying element in high nitrogen

stainless steels caused degradation of the resistance to uniform, intergranular, and pitting corrosions. Furthermore, Park et al. [188] observed that Mn as alloying element, decreases the pitting corrosion resistance and delay the re-passivation kinetics of Fe-18Cr based alloys containing 0, 6, and 12 wt% Mn. Pardo et al. [51] investigated AISI 304 and AISI 316L alloys with various amounts of Mn, and they conclude that even a small amount of Mn ($< 2$ wt%) was harmful to the pitting corrosion resistance.

Most researchers have explained that the reason of the reduced resistance to corrosion of various stainless steels containing Mn was the formation of Mn-related non-metallic inclusions such as Mn sulphides (MnS) and Mn oxides (mostly MnO) [51, 173, 185, 188-196]. They reported that the Mn-rich non-metallic inclusions react as nucleation sites for localized corrosion, and the alloying Mn increases the number and size of the inclusions; therefore, the alloying Mn in stainless steels results in degradation of the resistance to corrosion [51, 173, 185, 186, 189-200]. The selective dissolution of Mn-rich inclusions forming micro-crevices between the inclusion and matrix [51, 192, 199, 200] and/or poor passivity at the inclusions [198], are considered as possible mechanisms for pit nucleation localized at the Mn-rich inclusions.

*e. The corrosion behaviour of HEAs*

The Cr concentration in Cr-containing HEAs is typically higher than 12%, and it is therefore reasonable that Cr-containing HEAs should have good corrosion resistance (like Fe–Cr–Ni [127, 149, 150] and Ni–Cr alloys [201, 202]) with formation of a continuous, adherent and insoluble surface chromium oxide [100]. The Co1.5CrFeNi1.5Ti0.5Mo0.1 alloy has a very high general corrosion and pitting resistance, with Epit values of these alloys being $>0.5$ V/SHE, in 1M NaCl for temperatures ranging from 20 to 80 °C [203]. However, alloying some other elements (such as Al, Cu) tends to lower the corrosion resistance of Cr-containing HEAs. The Epit of the $Cu_{0.5}NiAlCoCrFeSi$ alloy in 1M NaCl is well below 0 V/SHE [204]. Similarly, for $Al_xCrFe_{1.5}MnNi_{0.5}$, the Epit values drop below 0 VSHE when the Al molar ratio is $>0.3$ [205]. The AlCoCrFeNi system was also observed to have relatively poor corrosion resistance in 3.5 wt.% NaCl [206], and this is due to an interdendritic microstructure, with a Cr-depleted (and Al-rich) dendritic region. The addition of Cu to the alloy gives the same problem as with Al addition. Hsu et al. [207] investigated the corrosion behavior of the $FeCoNiCrCu_x$ alloy in a 3.5 wt % NaCl solution, and the results showed that, after 30day immersion test, the major types of corrosion were localized corrosion and pitting. The

localized corrosion in FeCoNiCrCu$_{0.5}$ and FeCoNiCrCu was found along the interdendrites, which was caused by the Cu segregation. Due to the weaker binding force with other elements such as Fe, Co, Ni, and Cr, Cu tends to segregate as clusters, forming Cu-rich interdendrites and grain boundaries during the period of solidification [208]. Therefore, the Cu-rich, Cr-depleted interdendrites act as the anode coupled with the cathodic Cu-depleted, Cr-rich dendrites, forming the galvanic corrosion at the interdendrites. A highly corrosion resistant HEA with elemental composition of 38Ni-21Cr-20Fe-13Ru-6Mo-2W at% was proposed based upon a computational design approach exploiting many of the attributes desired in alloys resistant to Cl- and reducing acids [209]. Pitting was found to be significantly inhibited because of the extremely strong passivity, even in solutions with lower pH and higher chloride concentration than found in a typical local pit environment [210]. The presence of Mo and W in the oxide film is believed to be a main factor conferring its extremely high corrosion resistance. Ru enrichment in the film appears to be a secondary factor with stability of RuO$_2$ [211]. Through the atomic emission spectra electrochemistry measurement, Cr and Ru enrichment was observed in the passive film [212].

Alloying Cr as a principal element in HEAs does not mean that Cr-containing HEAs are highly corrosion resistance. As demonstrated above, alloying Ni, Mo, Ru, W elements will have positive effect on the corrosion resistance of the Cr-containing alloys. While alloying Al, Cu, Mn elements will lower the corrosion resistance of the alloy. The impact of other alloying elements on the corrosion characteristics and passivity of the alloy still needs to be studied [213, 214]. The surface films (native and passive films) formed upon typical HEAs need to be extensively characterized to estimate their chemical compositions and to ratify their correlation with corrosion behaviour of the alloys.

**I-3. Ion transport mechanisms on Cr-containing alloys**

As discussed previously, the surface oxide film plays a key role in the corrosion resistance of metals and alloys. Thus, the understanding of their nature, structure, composition and growth kinetics, is important and requires a detailed knowledge of the oxidation mechanism and ion-transport mechanisms.

### I-3.1. Oxidation kinetics

*a. Wagner theory of oxidation*

The most recognized description of oxidation rates at elevated temperatures considering transport processes through a growing scale was postulated by Carl Wagner in 1933 [215]. A complete and precise analysis of the Wagner model has been done by Seyeux et al. [112]. Later, the Point Defects Model (PDM) [113, 216] and Marcus-Seyeux-Leistner (MSL) model [112, 217] are originated and developed based on this Wagner theory.

In Wagner model, the thermodynamic equilibrium is assumed to be established at the metal–scale and scale–gas interfaces, it follows that activity gradients of both metal and non-metal (oxygen, sulphur, etc.) are established across the scale. Consequently, metal ions and oxide ions will tend to migrate across the scale in opposite directions. Because the ions are charged, this migration will cause an electric field to be set up across the scale resulting in consequent transport of electrons across the scale from metal to atmosphere. The relative migration rates of cations, anions, and electrons are, therefore, balanced and no net charge transfer occurs across the oxide layer as a result of ion migration.
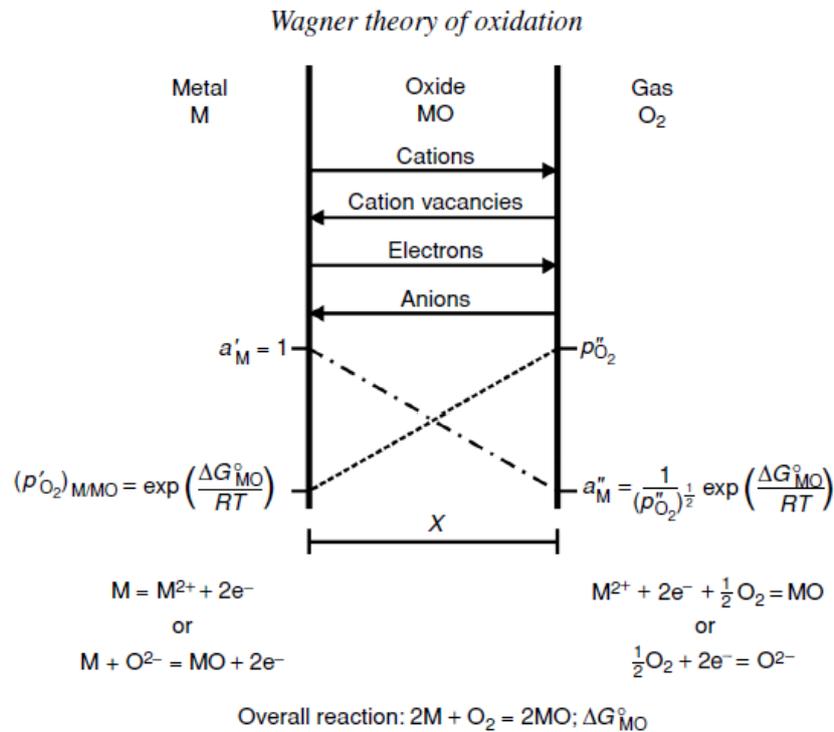


**Fig.I-8** Diagram of scale formation according to Wagner's model [218]

Although such conditions are rarely found, Wagner's theory of oxidation is still widely used to characterize diffusion-driven oxidation processes on metals and alloys. While for

electrochemical growth of oxide films, the PDM or MSL models are usually used.

The mathematics of oxidation kinetics involves diffusion and mass transfer migration. According to Fick's first law of diffusion, the flux is related to the rate of oxide growth (dx/dt) is given by

$$J = -D\frac{dC}{dt}$$ (equation I-1)

$$J = -C\frac{dx}{dt}$$ (equation I-2)

From which the rate of thickness growth is

$$\frac{dx}{dt} = \frac{D}{C_x}\frac{\Delta C}{x}$$ (equation I-3)

Where D is diffusivity (diffusion coefficient) ($cm^2$/s), $C_x$ is concentration of the diffusing species (ions/$cm^3$) and x is thickness of the oxide scale (cm).

The eq.I-3 describes the parabolic law for the oxide growth at high temperature.

Integrating eq.I-3 yields what is known as the parabolic equation for the oxide thickness

$$x = \sqrt{k_p t}$$ (equation I-4)

$$k_p = \frac{2D\Delta C}{C_x} \approx 2D$$ (equation I-5)

Where $k_p$ is known as the parabolic rate constant ($cm^2$/s).

*b. Volatilization*

The oxidation of pure Cr is, in principle, a simple process since a single oxide, $Cr_2O_3$, is observed to form. However, under certain exposure conditions, several complications arise, which are important both for the oxidation of pure Cr and for many important engineering alloys which rely on a protective $Cr_2O_3$ layer for oxidation protection [219-221]. The two most important features are scale thinning by $CrO_3$ evaporation [219, 222], and scale buckling [223, 224] as a result of compressive stress development.

The thinning of the $Cr_2O_3$ is the result of its volatilization in $CrO_3$ by the reaction shown in the following equation,

$$Cr_2O_3\ (s) + \frac{3}{2}O_2(g) = 2CrO_3\ (g) \qquad\qquad\text{(equation I-6)}$$

This chromium evaporation has been reported at 700°C, and becomes significant at high temperatures above about 1000°C and high oxygen partial pressures ($P_{O2}$=1atm) [225-229]. Recently, Poulain et al. [222] have proved that the chromium evaporation phenomenon could also occur at lower temperature (300°C) under very low oxygen pressures.
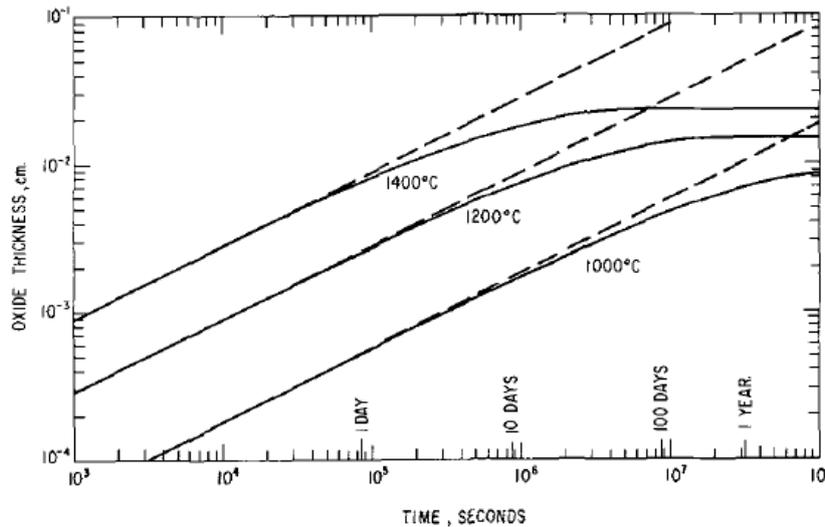


**Fig.I-9** Scale thickness versus time for the oxidation of Cr. (The dashed lines correspond to oxide growth following parabolic kinetics for the case of negligible evaporation) [230]

Fig.I-9 indicates a greater limiting thickness at higher oxidation temperature. The dashed lines show the expected growth assuming only parabolic kinetics. For short times, e.g., t< $10^5$ sec, the growth rate appears to be nearly parabolic. By $10^8$ sec, however, significant departures from parabolic behavior, which is assigned to the Cr oxide evaporation, are seen at all three temperatures.

The model of the volatilization on the oxidation kinetics has been first built by Tedmon [219]. The instantaneous change in scale thickness is the sum of two contributions: thickening due to diffusion and thinning due to volatilization. A constant of volatilization $k_v$, which slows down the apparent kinetics of oxide growth, is added in the Wagner's parabolic equations in the following way:

$$\frac{dx}{dt} = \frac{k_p}{x} - k_v \qquad\qquad\text{(equation I-7)}$$

which gives after integration:

$$t = \frac{k_p}{k_v^2}[-\frac{k_v}{k_p}x - \ln\left(1 - \frac{k_v}{k_p}x\right)] \qquad\qquad \text{(equation I-8)}$$

The kinetics of oxidation (eq.I-8) seems to follow a logarithmic-type law, however, according to previous research [152, 222], the oxide growth kinetics can be explained by the competition between parabolic growth and oxide layer volatilization. From Fig.I-9, two parts can be observed on each curve. In the first part, the straight line represents the rapid growth of the oxide layer. Then, the plateau that is reached for longer times, means that the growth of the oxide layer is slow down, and a quasi-stationary film thickness is observed (growth rate = volatilization rate).

*c. The point defects model*

The Point Defects Model (PDM) was developed by Macdonald et al. in 1981 [113, 216]. This model originates from the ideas of Wagner for the electrochemical growth of oxide films on metal surfaces. It describes the electrochemical formation of the oxide layers by a mechanism involving migration *via* defects in the oxide network.

The PDM model was the first one to consider the potential drops at the interfaces and describe anodic oxide film growth on metals in aqueous solution. The interfacial potential drops at both interfaces ($\varphi_{m/f}$ and $\varphi_{f/s}$) and in the film ($\varphi_f$) are taken into account and the potential drops at the interfaces are assumed to be functions of the pH of the medium and the applied potential $V_{app}$ across the system. With regard to the transport of charged species through the film, this model uses the generalized Fick expression which makes it possible to obtain a logarithmic growth law (x = A + Blnt) where A is a function of pH, the applied potential $V_{app}$ and the electric field in the film.

Although this model is the first macroscopic model to take into account the evolution of potentials at the interfaces to describe the growth of oxide films on metals, major simplifying hypotheses were used, which limit its use.

1. In its original version, this model assumes that a constant drop in potential at the oxide / medium interface ($\varphi_{f/s}$) is maintained during the growth of the oxide film. This hypothesis necessarily implies that the reaction $O_{oxide} + 2H^+ \rightarrow H_2O$, at the oxide/electrolyte interface, is faster than the kinetically rate-limiting step (transport of the anionic vacancies through the film) and that an equilibrium is maintained at this interface during oxide growth. This assumption would be valid for stationary conditions (i.e. when the oxide growth rate is equal

to the dissolution rate) when the interfacial potential drops $\varphi_{m/f}$ and $\varphi_{f/s}$ are imposed by the structure of the metal/oxide interface and the Nernst equilibrium, respectively. However, these potential drops at the interfaces must necessarily evolve during the growth of the oxide film (i.e. non-stationary conditions).

2. In the stationary state, the potential drop ($\varphi_{f/s}$) at the oxide/electrolyte interface is assumed to be a function of the applied potential. At the equilibrium state, the potential drop ($\varphi_{f/s}$) must be given by the Nernst equilibrium only and therefore cannot be a function of the applied potential.

3. The electric field is constant in the film. This assertion, true when stationary, cannot be applied during the growth of the oxide film (non-stationary conditions).

4. The growth of the oxide film by migration of cations via the interstitial or vacancy positions is not considered.

5. The composition of the metallic substrate is not taken into account, so that this approach is limited for alloys.

*d. Marcus-Seyeux-Leistner model*

The Marcus-Seyeux-Leistner (MSL) model was published in 2013 [112, 217]. This recent model is based on the PDM model, that is to say that the growth of the oxide is the result of the migration of species *via* point defects in the oxide layer. However, one of the major advances of this model is that it takes into account non-stationary conditions during film growth (unlike the PDM model described above) and that it also includes all of the reactions (migration of cations via interstitial and vacancy positions, and dissolution of the oxide) to describe the growth of the oxide layer.

As indicated previously, the major advantage of the MSL model is that it takes into account the potentials at the interfaces and in the oxide and their evolution during the growth of the oxide film. It was seen previously (see Fig.I-10) that the potential drop in the metal /oxide/electrolyte system is divided into three potential drops ($\varphi_{m/f}$, $\varphi_f$ and $\varphi_{f/s}$). During the growth of the oxide film, the potential drops ($\varphi_{m/f}$, $\varphi_f$ and $\varphi_{f/s}$) vary until the oxide film reaches a stationary thickness. Thus, in non-stationary conditions, the potential drops are functions of the thickness of the oxide film (x). Any modification of the chemistry of the electrolyte, of the temperature will therefore lead to a variation of the potential, the potentials

drops are modified and the thickness of the oxide film will evolve up to a new stationary thickness ($x_g$).
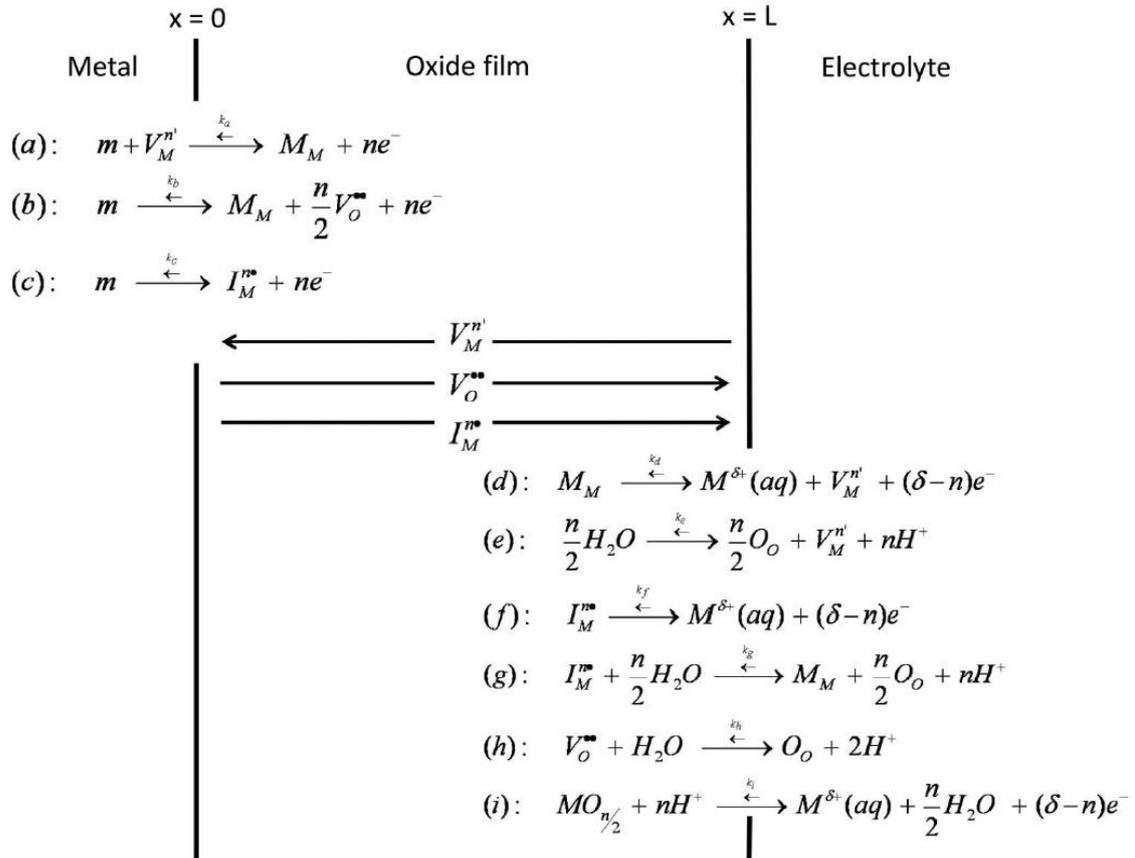


**Fig.I-10** Scheme describing the reaction and transport processes involved in the system metal/oxide/electrolyte during the growth of the oxide layer. Oxygen vacancies, metallic vacancies and metallic interstitials are implied. The dissolution of the oxide film is also taken into account. The Kröger-Vink notation is used to describe the defects. (a) cation injection into cation vacancy position of the oxide at the metal/oxide interface, (b) oxygen vacancies formation in the oxide at the metal/oxide interface, (c) cation injection in interstitial position of the oxide at the metal/oxide interface, (d) cation dissolution via cation vacancies at the oxide/electrolyte interface, (e) formation of cation vacancies in the oxide at the oxide/electrolyte interface, (f) cation dissolution via interstitial position at the oxide/electrolyte interface, (g) growth of the oxide via interstitial positions at the oxide/electrolyte interface, (h) injection of oxygen in anionic vacancy position at the oxide/electrolyte interface, and (i) dissolution of the oxide at the oxide/electrolyte interface. [112]

To determine the variations in potential drops at the interfaces and in the film, the authors make the following assumptions:

1. The potential drop at the metal/oxide interface ($\varphi_{m/f}$) is constant during the oxide growth (i.e. the structure of the inner layer and the composition of the alloy below the oxide are

assumed to remain unchanged during the growth)

2. At the steady state, $\varphi_{f/s}$ is determined by the Nernst equation.

3. The potential drop in the film $\varphi_f$ is assumed to be linear.

Thus, the potential drops are expressed as follows:

$$\varphi_{m/f}(x) = \varphi^0_{m/f}(x) = constant$$

$$\varphi_{f/s}(x) = \varphi^0_{f/s}(x) + \Delta\varphi_{f/s}(x) = \varphi^0_{f/s}(x) + \alpha\Delta V f(x) \qquad \text{(equation I-9)}$$

$$\varphi_f(x) = \varphi^0_f(x) + \Delta\varphi_f(x) = \varphi^0_f(x) + \Delta V(1 - \alpha f(x))$$

where $\alpha$ is a constant for a given system reflecting the fraction of the potential $\Delta V$ applied to the metal/oxide interface.
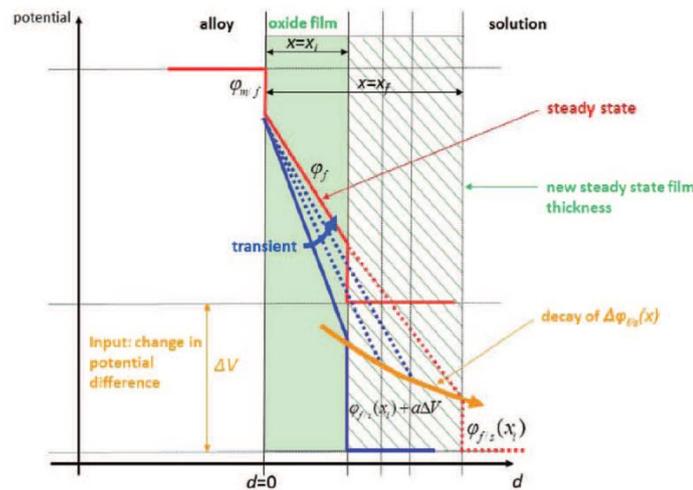


**Fig.I-11** Diagram of the evolution of the potential drop controlled by the ion transport mechanisms, the thickness of the film, and the external reactions [217]

Fig.I-11 describes the evolution of the potential drops at the two interfaces and in the film following the Marcus-Seyeux-Leistner model.

Oxide film growth law:

In this model, growth is considered to be controlled by the transport of charged species through the oxide film. Consequently, the growth kinetics are given by the flow of charged species (interstitials or vacancies) passing through the film. However, in the presence of a

potential and concentration gradient, the flux is given by Fick's law:

$$J_i = D_i^* \frac{\partial C_i}{\partial D} + D_i^* \frac{C_i}{RT} q_i \mathcal{F} \frac{\partial \varphi}{\partial d}$$   (equation I-10)

where $J_i$ is the flux of species i per unit area per unit time, $D_i^*$ and $C_i$ are the diffusion coefficient and the concentration of charged species i in the oxide, respectively, and d is a position in the oxide of thickness x.

Consequently, by combining Equation X and Equation Y and assuming a uniform electric field in the film (model hypothesis) it is possible to express the flux of the species diffusing through the oxide:

$$\frac{\partial C_i}{\partial D} \; J_i(x) = q_i \frac{\mathcal{F}\varphi_f(x)}{RTx} D_i^* \frac{C_i|_{m/f} \exp\left[ q_i \frac{\mathcal{F}[\varphi_f^0 + \Delta V(1 - \alpha f(x))]}{RT} \right] - C_i|_{f/s}}{\exp\left[ q_i \frac{\mathcal{F}[\varphi_f^0 + \Delta V(1 - \alpha f(x))]}{RT} \right] - 1}$$   (equation I-11)

where $C_i|_{m/f}$ and $C_i|_{f/s}$ are the concentrations of species I (in units of number of species/m$^3$) at the metal/oxide and oxide/electrolyte interfaces, respectively.

*e. Oxidation of Cr-containing alloys*

The formation of thin oxide layers on Fe-Cr based alloys surface by oxidation at different oxygen pressures and temperatures have been widely studied [220, 221, 224, 231-245].

For high temperature oxidation (above 800°C), the chromium oxide is the main species in the oxide film on the Fe-Cr based alloy surface, trace or no iron oxide could be observed [231, 232, 246, 247]. Habib et al. [224] studied and compared the oxidation behaviour of 304 and 316 stainless steels at 1000°C in air. The results showed that the films are mainly chromium oxide, the weight gain of 304 SS was about 8 times greater than that of 316 SS, showing that 316 SS is more oxidation resistant than 304 SS due to the presence of Mo.

For oxidation at temperatures below 800°C, the oxide layers formed on the Fe-Cr based alloys are normally rich in Fe and Cr oxides [151, 224, 238, 239, 241, 242, 244, 246, 248, 249]. Swart et al. [243] studied the oxide composition of Fe-9Cr-1Mo after oxidation in UHV for 1000L of oxygen below 600°C. At temperatures lower than 400°C, the oxide layer consists mainly of $Fe_2O_3$ in the outer layer and a small amount of $Cr_2O_3$ in the inner layer. Between 400°C and 600°C the oxide layer consists of a mixture of FeO, $Fe_2O_3$ (outer layer) and $Cr_2O_3$ (inner layer). Olefjord [250] has examined the oxide formed on Fe-(6.5-2l at%)Cr alloys

exposed to 0.2 atm oxygen at room temperature using ESCA techniques and suggested that the oxide consists of $(FeCr)_2O_3$ in the outermost layer and $FeCr_2O_4$ in the inner layer.

Besides studies of the composition and structure of the oxide film formed on Fe-Cr based alloy surfaces at different temperatures, some studies focused on the initial oxidation process of Fe-Cr based alloys. Lince et al. [251] investigated the initial oxidation on Fe-Cr based alloys at low temperatures (below 300°C). The results showed that in the first oxidation stages (1 to 20 L), the formation of Cr oxide is favored by the higher thermodynamic stability for oxides containing chromium such as $Cr_2O_3$, compared to that of iron oxides. For exposures between 30 and 100 L, the layer whose growth is controlled by diffusion would become increasingly rich in iron due to the higher mobility of iron in the region of oxides. Note that the iron would diffuse faster towards the surface of the oxide film at this stage.

D. J. Young et al. [239] studied the oxide formation process of Fe-24Cr alloy in oxygen ($10^{-2}$ Pa) at 190-490°C. They concluded that oxidation proceeds in three stages. An initial period of accelerating rate was accompanied by oxide island nucleation and growth. Following island coalescence, and the coalescence rate was controlled by the mass transport through the oxide grain boundaries left by the island impingement process. During the first two stages, the oxide formed was γ- $M_2O_3$ (M=Fe,Cr) The final stage of reaction involved the appearance of α- $M_2O_3$ on the outer oxide surface and a substantial slow down of the oxidation rate due to the low diffusivity in this phase.

Recently, Ma et al. [151] used *in situ* XPS measurements to investigate the oxide growth mechanisms on 304 SS in the very initial stages of oxidation at 150°C and 250°C. In the very first stage of oxidation (0.5L), Cr oxide formation is preferential over Fe oxide formation. Then, the competitive oxidation of iron is gradually promoted in the oxide growth leading to the decrease of Cr enrichment in the oxide.

## I-3.2. Ion transport

To understand the oxidation of alloys, ion transport in the oxide scale is a key issue. Usage of isotope tracers of metal elements or oxygen to elucidate transport mechanisms in the oxide scales is a classical experimental approach extensively applied for various materials in a wide range of temperatures [126, 152, 227, 229, 252-263].

### I-3.2.1. Study of ion transport in pure Cr oxide

Waiters [264], Hoshino [265], Taylor [266], and Graham [254] investigated the diffusion of Cr in chromium oxide on chromium single crystals at different temperatures and oxygen pressures. The effect of the fast grain boundary diffusion is excluded in these experiments. Thus, the chromium diffusion coefficients, mainly lattice diffusion, are some orders of magnitude lower than that calculated in the polycrystals of chromium [257, 258]. These studies also showed that the diffusion coefficient of chromium depends on oxygen pressure which will change the defect structure of chromium oxide [256, 267].

The defects formed in chromium oxide during oxidation of pure chromium are function of the oxygen pressure leading to the formation of either p- or n-type semiconductors [222, 247, 268]. High oxygen pressure will result in a p-type semiconductor, e.g. electron holes and chromium vacancies act as the predominant defects. At intermediate oxygen pressure, $Cr_2O_3$ behaves as an intrinsic semiconductor with electrons and electron holes as the major defects. Low oxygen pressure leads to the formation of an n-type semiconductor with oxygen vacancies and chromium interstitials as the dominant defects.

To understand the transport properties of chromia, not only the transport of chromium and oxygen in the $Cr_2O_3$ layer are of interest but also the diffusivity of other alloying elements, including Fe, Mn and Ni, in the chromium oxide are of interest. Lobnig [255] compared the diffusivity of Fe, Mn and Ni in the chromium oxide, and concluded that the lattice diffusivity of Mn is about two orders of magnitude greater than that of Fe and Ni in $Cr_2O_3$. Sabioni [263] determined the diffusivity of Fe in chromium oxide using the iron isotopic tracers.

### I-3.2.2. Study of ion transport in Fe-Cr based alloys

As demonstrated previously, the composition of oxide film formed on Fe-Cr based alloys is Cr and Fe oxide. Thus, the transport of both anions and cations in the film should be different from the transport behaviour in pure chromium oxide.

Sabioni and Huntz [262, 263, 269-273] conducted a series of experiments to determine the diffusivity of ions in the oxide film formed on Fe-Cr based alloys. They studied the oxygen and chromium ions diffusion in oxide layers grown on AISI 304 austenitic stainless steel (18 wt.%Cr) and on AISI 439 ferritic stainless steel (17 wt.%Cr), between 750 and 900 °C, in air. Although these works give values of ion diffusivity in the oxide film, they do not elucidate the ion transport processes during the oxide growth, because these data were obtained by

depositing isotopic tracers ([54]Cr and [57]Fe) on the oxidized surface of the alloy followed by the diffusion annealing. After the diffusion annealing, the depth diffusion profiles of the tracers [54]Cr or [57]Fe were established by secondary ion mass spectrometry (SIMS), as showed in the Fig.I-12. By fitting the depth profiles of isotopic tracer (Fig.I-12(c)), the diffusivity of Cr or Fe in the oxide was calculated.
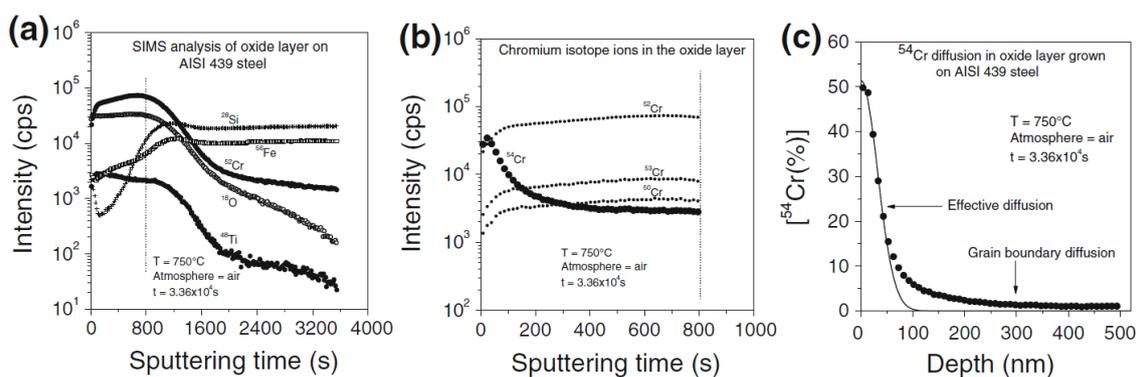


**Fig.I-12** SIMS depth profiles of the oxide layer grown on the AISI 439 stainless steel after [54]Cr diffusion at 750°C [272]

### I-3.2.3. Isotopic tracers exchange experiments in [18]O containing atmosphere

To study the O diffusivity, [18]O isotopic tracer are always involved in a two-step oxidation technique in which the specimen is first oxidized in natural oxygen (^{16}O) and subsequently oxidized in [18]O atmosphere at elevated temperatures [126, 152, 222, 274, 275]. After the formation of an initial oxide layer during the first stage, the composition of isotopes in the oxidizing environment is changed. To sustain scale growth, oxygen and/or metal has to be transported to the reactions zone. Therefore, distribution of isotopic oxygen in the oxide scale gives direct information on transport mechanisms during oxidation.

Oxidation kinetics of metals or alloys are either controlled by the diffusion of cationic species (outward diffusion of metallic ions through the oxides) [255] or anionic species (inward oxygen diffusion) [254]. Mechanisms including both cationic and anionic diffusion have also been reported [274, 276].

Secondary ion mass spectroscopy (SIMS) is the most commonly used technique to locate the oxygen isotopic tracer in the oxide scales [126, 152, 222]. Anion diffusion will indeed lead to the formation of the new [18]O oxide at the alloy/oxide interface, whereas cationic diffusion will result in a surface formation, i.e. at the oxide/gas interface.

Thian Gnan Ooi [277], using the two-step oxidation method with FIB-SIMS (Focused Ion Beam-Secondary Ion Mass Spectrometry) technique, determined that both anions and cations diffusion are the predominant mechanism governing the transport in the oxide film formed on Ni-based superalloy. Pint [278] revealed inward oxygen diffusion governing the growth of oxide film on α-Al2O3 at 1200°C. The work of Young [275] on the scales grown on NiAl indicated that, rather than an inward growth mechanism, the outward diffusion of A1 was the predominant growth mechanism. Recently, the oxidation mechanisms for Alloy 600 in high temperature water [152] and Hastelloy BC-1 at high temperature in oxygen atmosphere [126] have been investigated *in situ* by ToF-SIMS with oxygen isotopic maker, and anion diffusion was found to be the dominant ion transport mechanism for Alloy 600, whereas cation diffusion is the governing oxidation mechanism for Hastelloy BC-1 alloy.

## I-4. Objectives of the thesis

This study aims to understand the corrosion behavior and ion transport mechanisms in surface oxide films on Cr-containing alloys.

Generally, the addition of a minor concentration of alloying elements in the Fe-Cr based alloys, like 316 stainless steel, can provide good corrosion resistance by forming an oxide film on the surface. However, the corrosion behavior of CoCrFeMnNi high entropy alloys with five elements in equal concentration in the bulk, which is not the case in stainless steel, has rarely been studied.

The first objective of this thesis was to understand the reactivity of CoCrFeMnNi high entropy alloys using fine surface characterization techniques combined with electrochemical measurements. The composition and structure of oxide films is a key aspect for understanding the corrosion resistance of high entropy alloys. The results obtained in this part of the work are presented in chapter III.

The second part of this thesis was to determine the ion transport mechanisms on Cr-containing alloys (304L and 316L stainless steels). To study the ion transport process in the oxide film on stainless steels, two-step oxidation was done to the substrate, using a sequence of $^{16}O$ and $^{18}O$ isotopic species. For the second oxidation step, a suitable re-oxidation temperature had to be found, since, at lower temperatures, the ion-transport process would be very slow (or even blocked), and it would take a long time to observe the transport of species in the passive film. At higher temperatures, the composition and structure of the pre-formed

passive film may be changed and the analysis of the modifications of the structure and composition of the oxide film during heat treatment had to be studied.

The second objective of this thesis was, thus, to investigate the thermal stability of passive film on stainless steel. The modifications of the passive film formed on 316L stainless steel surface during stepwise heating in ultrahigh vacuum from room temperature to 300°C has been studied. The results obtained on this part of work are presented in chapter IV.

After the study of the thermal stability of passive film at different temperatures, a suitable re-oxidation temperature can be selected and the oxidation of Cr-containing alloys (304L and 316L stainless steels) at different temperatures and oxygen pressures can be carefully studied.

The third objective of this thesis was thus to study ion transport process in the pre-formed passive film on 304L and 316L stainless steel surfaces at 300°C. The native film was formed after mechanical polishing down to 0.25µm, while the passive film was electrochemically formed in sulfuric acid solution at 0.4V/SCE. Re-oxidation was conducted by exposure of the passive film to isotopic $^{18}O_2$ gas. The results obtained in this part of the work are presented in chapter V and VI.

## References

[1] D. Peckner, I.M. Bernstein, D. Peckner, Handbook of stainless steels, McGraw-Hill New York, 1977.

[2] P. Marshall, Austenitic stainless steels: microstructure and mechanical properties, Springer Science & Business Media, 1984.

[3] H.M. Cobb, The history of stainless steel, ASM International, 2010.

[4] A.H. Grobe, Mechanical properties, (1996).

[5] B.R. Kumar, S. Sharma, P. Munda, R. Minz, Structure and microstructure evolution of a ternary Fe–Cr–Ni alloy akin to super martensitic stainless steel, Materials & Design, 50 (2013) 392-398.

[6] A. Kisko, A. Hamada, J. Talonen, D. Porter, L. Karjalainen, Effects of reversion and recrystallization on microstructure and mechanical properties of Nb-alloyed low-Ni high-Mn austenitic stainless steels, Materials Science and Engineering: A, 657 (2016) 359-370.

[7] I. Calliari, M. Zanesco, M. Dabala, K. Brunelli, E. Ramous, Investigation of microstructure and properties of a Ni–Mo martensitic stainless steel, Materials & Design, 29 (2008) 246-250.

[8] H. Nakagawa, T. Miyazaki, H. Yokota, Effects of aging temperature on the microstructure and mechanical properties of 1.8Cu-7.3Ni-15.9Cr-1.2Mo-low C, N martensitic precipitation hardening stainless steel, Journal of Materials Science, 35 (2000) 2245-2253.

[9] H.-Y. Ha, T.-H. Lee, J.-H. Bae, D. Chun, Molybdenum effects on pitting corrosion resistance of FeCrMnMoNC austenitic stainless steels, Metals, 8 (2018) 653.

[10] J.L. Lv, T.X. Lang, C. Wang, Surface enriched molybdenum enhancing the corrosion resistance of 316L stainless steel, Materials Letters, 171 (2016) 38-41.

[11] W. Tobler, S. Virtanen, Effect of Mo species on metastable pitting of Fe-18Cr alloys—A current transient analysis, Corrosion Science, 48 (2006) 1585-1607.

[12] A.F. Padilha, I.F. Machado, R.L. Plaut, Microstructures and mechanical properties of Fe–15%Cr–15%Ni austenitic stainless steels containing different levels of niobium additions submitted to various processing stages, Journal of Materials Processing Technology, 170 (2005) 89-96.

[13] M. Aksoy, V. Kuzucu, M. Korkut, M. Yildirim, The effect of niobium and homogenization on the wear resistance and some mechanical properties of ferritic stainless steel containing 17–18wt.% chromium, Journal of Materials Processing Technology, 91 (1999) 172-177.

[14] M. Tendo, Y. Tadokoro, K. Suetsugu, T. Nakazawa, Effects of nitrogen, niobium and molybdenum on strengthening of austenitic stainless steel produced by thermo-mechanical control process, ISIJ international, 41 (2001) 262-267.

[15] E. El-Kashif, K. Asakura, T. Koseki, K. Shibata, Effects of boron, niobium and titanium on grain growth in ultra high purity 18% Cr ferritic stainless steel, ISIJ international, 44 (2004) 1568-1575.

[16] V. Kuzucu, M. Aksoy, M. Korkut, M. Yildirim, The effect of niobium on the microstructure of ferritic stainless steel, Materials Science and Engineering: A, 230 (1997) 75-80.

[17] M. Fujikura, K. Takada, K. Ishida, Effect of manganese and nitrogen on the mechanical properties of Fe-18%Cr-10%Ni Stainless Steels, Transactions of the Iron and Steel Institute of Japan, 15 (1975) 464-469.

[18] W. Zhang, L.Z. Jiang, J.C. Hu, H.M. Song, Study of mechanical and corrosion properties of a Fe–21.4Cr–6Mn–1.5Ni–0.2N–0.6Mo duplex stainless steel, Materials Science and Engineering: A, 497 (2008) 501-504.

[19] V. Muthupandi, P.B. Srinivasan, V. Shankar, S. Seshadri, S. Sundaresan, Effect of nickel and nitrogen addition on the microstructure and mechanical properties of power beam processed duplex stainless steel (UNS 31803) weld metals, Materials Letters, 59 (2005) 2305-2309.

[20] J.W. Simmons, Mechanical properties of isothermally aged high-nitrogen stainless steel, Metallurgical and Materials Transactions A, 26 (1995) 2579-2595.

[21] J. Simmons, Overview: high-nitrogen alloying of stainless steels, Materials Science and Engineering: A, 207 (1996) 159-169.

[22] H.B. Li, Z.H. Jiang, Z.R. Zhang, Y. Yang, Effect of grain size on mechanical properties of nickel-free high nitrogen austenitic stainless steel, Journal of Iron and Steel Research International, 16 (2009) 58-61.

[23] D.W. Kim, Influence of nitrogen-induced grain refinement on mechanical properties of nitrogen alloyed type 316LN stainless steel, Journal of nuclear materials, 420 (2012) 473-478.

[24] H. Li, Z. Jiang, H. Feng, S. Zhang, L. Li, P. Han, R. Misra, J. Li, Microstructure, mechanical and corrosion properties of friction stir welded high nitrogen nickel-free austenitic stainless steel, Materials & Design, 84 (2015) 291-299.

[25] T. Xi, M.B. Shahzad, D. Xu, Z. Sun, J. Zhao, C. Yang, M. Qi, K. Yang, Effect of copper addition on mechanical properties, corrosion resistance and antibacterial property of 316L stainless steel, Materials Science and Engineering: C, 71 (2017) 1079-1085.

[26] B.M. Gonzalez, C.S.B. Castro, V.T.L. Buono, J.M.C. Vilela, M.S. Andrade, J.M.D.d. Moraes, M.J. Mantel, The influence of copper addition on the formability of AISI 304 stainless steel, Materials Science and Engineering: A, 343 (2003) 51-56.

[27] S.H. Jeon, S.T. Kim, IS. Lee, J.H. Park, K.T. Kim, J.S. Kim, Y.S. Park, Effects of copper addition on the formation of inclusions and the resistance to pitting corrosion of high performance duplex stainless steels, Corrosion science, 53 (2011) 1408-1416.

[28] M. Gurram, K. Adepu, R.R. Pinninti, M.R. Gankidi, Effect of copper and aluminium addition on mechanical properties and corrosion behaviour of AISI 430 ferritic stainless steel gas tungsten arc welds, Journal of Materials Research and Technology, 2 (2013) 238-249.

[29] D. Uzunsoy, The characterisation of PM 304 stainless steel sintered in the presence of a copper based additive, Materials Letters, 61 (2007) 10-15.

[30] A. Sharon, D. Itzhak, Mechanical properties of sintered austenitic stainless steel—effect of silicon addition, Materials Science and Engineering: A, 157 (1992) 145-149.

[31] M. Youseffi, K. Chong, Enhanced sintering and mechanical properties of 316L stainless steel with silicon additions as sintering aid, Powder Metallurgy, 46 (2003) 30-38.

[32] S. Lal, G. Upadhyaya, Effect of phosphorus and silicon addition on the sintered properties of 316L austenitic stainless steel and its composites containing 4 vol% yttria, Journal of Materials Science, 24 (1989) 3069-3075.

[33] A. Hermas, I. Hassab-Allah, Microstructure, corrosion and mechanical properties of 304 stainless steel containing copper, silicon and nitrogen, Journal of Materials Science, 36 (2001) 3415-3422.

[34] W. Wang, Y.L. Su, Liquid phase sintering of austenitic stainless steel powders with silicon additions, Powder Metallurgy, 29 (1986) 269-275.

[35] A. Reichardt, R.P. Dillon, J.P. Borgonia, A.A. Shapiro, B.W. McEnerney, T. Momose, P. Hosemann, Development and characterization of Ti-6Al-4V to 304L stainless steel gradient components fabricated with laser deposition additive manufacturing, Materials & Design, 104 (2016) 404-413.

[36] J. Cotton, R. Knutsen, C. Lang, The influence of niobium and vanadium on the microstructure and mechanical properties of a high nitrogen stainless steel, Materials Science Forum, (1999) 271-280.

[37] S. Abbasi, A. Shokuhfar, Improvement of mechanical properties of Cr-Ni-Mo-Cu-Ti stainless steel with addition of vanadium, Journal of Iron and Steel Research International, 14 (2007) 74-78.

[38] A.J. Sedriks, Corrosion of stainless steel, 2, (1996).

[39] Y. Murakami, 17 - Martensitic stainless steels, Y. Murakami (Ed.) Metal Fatigue (Second Edition), Academic Press, (2019) 431-451.

[40] A. Kinzel, Chromium Carbide in Stainless Steel, JOM, 4 (1952) 469-488.

[41] J. Demo, Structure, constitution, and general characteristics of wrought ferritic stainless steels, Structure, Constitution, and General Characteristics of Wrought Ferritic Stainless Steels, ASTM International, 1977.

[42] M. Cortie, M. Du Toit, Stainless Steels, Ferritic, 2016.

[43] R.P. Reed, Nitrogen in austenitic stainless steels, JOM, 41 (1989) 16-21.

[44] T. Oshima, Y. Habara, K. Kuroda, Efforts to save nickel in austenitic stainless steels, ISIJ international, 47 (2007) 359-364.

[45] A. Di Schino, J. Kenny, M. Mecozzi, M. Barteri, Development of high nitrogen, low nickel, 18% Cr austenitic stainless steels, Journal of Materials Science, 35 (2000) 4803-4808.

[46] N. Ohkubo, K. Miyakusu, Y. Uematsu, H. Kimura, Effect of alloying elements on the mechanical properties of the stable austenitic stainless steel, ISIJ international, 34 (1994) 764-772.

[47] D. Llewellyn, Work hardening effects in austenitic stainless steels, Materials Science and Technology, 13 (1997) 389-400.

[48] G.S. Was, S. Ukai, Austenitic Stainless Steels, Structural Alloys for Nuclear Energy Applications, Elsevier, (2019) 293-347.

[49] A.F. Padilha, P.R. Rios, Decomposition of austenite in austenitic stainless steels, ISIJ international, 42 (2002) 325-327.

[50] G. Michal, F. Ernst, H. Kahn, Y. Cao, F. Oba, N. Agarwal, A. Heuer, Carbon supersaturation due to paraequilibrium carburization: Stainless steels with greatly improved mechanical properties, Acta Materialia, 54 (2006) 1597-1606.

[51] A. Pardo, M. Merino, A. Coy, F. Viejo, R. Arrabal, E. Matykina, Pitting corrosion behaviour of austenitic stainless steels–combining effects of Mn and Mo additions, Corrosion

Science, 50 (2008) 1796-1806.

[52] G.S. Was, S. Ukai, Chapter 8 - Austenitic Stainless Steels, Structural Alloys for Nuclear Energy Applications, Elsevier, (2019) 293-347.

[53] E. Gardin, S. Zanna, A. Seyeux, A. Allion-Maurer, P. Marcus, Comparative study of the surface oxide films on lean duplex and corresponding single phase stainless steels by XPS and ToF-SIMS, Corrosion Science, 143 (2018) 403-413.

[54] J.O. Nilsson, Super duplex stainless steels, Materials Science and Technology, 8 (1992) 685-700.

[55] I. Alvarez-Armas, S. Degallaix-Moreuil, Duplex stainless steels, John Wiley & Sons, 2013.

[56] A. Kocijan, D.K. Merl, M. Jenko, The corrosion behaviour of austenitic and duplex stainless steels in artificial saliva with the addition of fluoride, Corrosion Science, 53 (2011) 776-783.

[57] J.C.M. Farrar, Group D: Duplex and superduplex stainless steels, The Alloy Tree, Woodhead Publishing, 2004, pp. 53-63.

[58] B. Cantor, I.T.H. Chang, P. Knight, A.J.B. Vincent, Microstructural development in equiatomic multicomponent alloys, Materials Science and Engineering: A, 375-377 (2004) 213-218.

[59] J.W. Yeh, S.K. Chen, S.J. Lin, J.Y. Gan, T.S. Chin, T.T. Shun, C.H. Tsau, S.Y. Chang, Nanostructured high-entropy alloys with multiple principal elements: novel alloy design concepts and outcomes, Advanced Engineering Materials, 6 (2004) 299-303.

[60] W. Zhang, P.K. Liaw, Y. Zhang, Science and technology in high-entropy alloys, Science China Materials, 61 (2018) 2-22.

[61] B. Schuh, F. Mendez-Martin, B. Völker, E.P. George, H. Clemens, R. Pippan, A. Hohenwarter, Mechanical properties, microstructure and thermal stability of a nanocrystalline CoCrFeMnNi high-entropy alloy after severe plastic deformation, Acta Materialia, 96 (2015) 258-268.

[62] S.P. Wang, J. Xu, TiZrNbTaMo high-entropy alloy designed for orthopedic implants: As-cast microstructure and mechanical properties, Materials Science and Engineering: C, 73 (2017) 80-89.

[63] C.C. Tasan, Y. Deng, K.G. Pradeep, M. Yao, H. Springer, D. Raabe, Composition dependence of phase stability, deformation mechanisms, and mechanical properties of the CoCrFeMnNi high-entropy alloy system, JOM, 66 (2014) 1993-2001.

[64] L. Gao, J. Song, Z. Jiao, W. Liao, J. Luan, J.U. Surjadi, J. Li, H. Zhang, D. Sun, C.T. Liu, High-Entropy Alloy (HEA)-Coated Nanolattice Structures and Their Mechanical Properties, Advanced Engineering Materials, 20 (2018) 1700625.

[65] Y. Zhang, High-Entropy Materials, Springer, 2019.

[66] M.-H. Tsai, Physical properties of high entropy alloys, Entropy, 15 (2013) 5338-5345.

[67] B.S. Murty, J.W. Yeh, S. Ranganathan, P. Bhattacharjee, High-entropy alloys, Elsevier, 2019.

[68] M.C. Gao, D.B. Miracle, D. Maurice, X. Yan, Y. Zhang, J.A. Hawk, High-entropy functional materials, Journal of Materials Research, 33 (2018) 3138-3155.

[69] J.W. Yeh, Recent progress in high entropy alloys, Annales de Chimie Science des Materiaux, 31 (2006) 633-648.

[70] J. Beddoes, J.G. Parr, Introduction to stainless steels, 3, (1999).

[71] M.-H. Tsai, J.-W. Yeh, High-entropy alloys: a critical review, Materials Research Letters, 2 (2014) 107-123.

[72] Y. Zhang, Y. Zhou, X. Hui, M. Wang, G. Chen, Minor alloying behavior in bulk metallic glasses and high-entropy alloys, Science in China Series G: Physics, Mechanics and Astronomy, 51 (2008) 427-437.

[73] Y. Zhang, X. Yang, P. Liaw, Alloy design and properties optimization of high-entropy alloys, JOM, 64 (2012) 830-838.

[74] L.M. Martyushev, V.D. Seleznev, Maximum entropy production principle in physics, chemistry and biology, Physics Reports, 426 (2006) 1-45.

[75] S. Gorsse, D.B. Miracle, O.N. Senkov, Mapping the world of complex concentrated alloys, Acta Materialia, 135 (2017) 177-187.

[76] W. Kucza, J. Dąbrowa, G. Cieślak, K. Berent, T. Kulik, M. Danielewski, Studies of "sluggish diffusion" effect in Co-Cr-Fe-Mn-Ni, Co-Cr-Fe-Ni and Co-Fe-Mn-Ni high entropy alloys; determination of tracer diffusivities by combinatorial approach, Journal of Alloys and Compounds, 731 (2018) 920-928.

[77] D. Beke, G. Erdélyi, On the diffusion in high-entropy alloys, Materials Letters, 164 (2016) 111-113.

[78] Q. Li, W. Chen, J. Zhong, L. Zhang, Q. Chen, Z.K. Liu, On sluggish diffusion in fcc Al–Co–Cr–Fe–Ni high-entropy alloys: an experimental and numerical study, Metals, 8 (2018) 16.

[79] K.Y. Tsai, M.H. Tsai, J.W. Yeh, Sluggish diffusion in Co–Cr–Fe–Mn–Ni high-entropy alloys, Acta Materialia, 61 (2013) 4887-4897.

[80] K.H. Cheng, C.H. Lai, S.J. Lin, J.W. Yeh, Recent progress in multi-element alloy and nitride coatings sputtered from high-entropy alloy targets, Annales de chimie (Paris. 1914), (2006) 723-736.

[81] E. Pickering, N. Jones, High-entropy alloys: a critical assessment of their founding principles and future prospects, International Materials Reviews, 61 (2016) 183-202.

[82] H. Song, F. Tian, Q.-M. Hu, L. Vitos, Y. Wang, J. Shen, N. Chen, Local lattice distortion in high-entropy alloys, Physical Review Materials, 1 (2017) 023404.

[83] I. Toda-Caraballo, P. Rivera-Díaz-del-Castillo, A criterion for the formation of high entropy alloys based on lattice distortion, Intermetallics, 71 (2016) 76-87.

[84] Z. Wang, Q. Fang, J. Li, B. Liu, Y. Liu, Effect of lattice distortion on solid solution strengthening of BCC high-entropy alloys, Journal of Materials Science & Technology, 34 (2018) 349-354.

[85] H. Chen, A. Kauffmann, S. Laube, I.-C. Choi, R. Schwaiger, Y. Huang, K. Lichtenberg, F. Müller, B. Gorr, H.-J. Christ, Contribution of lattice distortion to solid solution strengthening in a series of refractory high entropy alloys, Metallurgical and Materials Transactions A, 49 (2018) 772-781.

[86] J. Moon, M.J. Jang, J.W. Bae, D. Yim, J.M. Park, J. Lee, H.S. Kim, Mechanical behavior and solid solution strengthening model for face-centered cubic single crystalline and polycrystalline high-entropy alloys, Intermetallics, 98 (2018) 89-94.

[87] H.P. Chou, Y.S. Chang, S.K. Chen, J.W. Yeh, Microstructure, thermophysical and electrical properties in AlxCoCrFeNi (0≤ x≤ 2) high-entropy alloys, Materials Science and Engineering: B, 163 (2009) 184-189.

[88] S. Ranganathan, Alloyed pleasures: multimetallic cocktails, Current Science, 85 (2003) 1404-1406.

[89] Z. Han, N. Chen, S. Zhao, L. Fan, G. Yang, Y. Shao, K. Yao, Effect of Ti additions on mechanical properties of NbMoTaW and VNbMoTaW refractory high entropy alloys, Intermetallics, 84 (2017) 153-157.

[90] N. Tariq, M. Naeem, B. Hasan, J. Akhter, M. Siddique, Effect of W and Zr on structural, thermal and magnetic properties of AlCoCrCuFeNi high entropy alloy, Journal of Alloys and Compounds, 556 (2013) 79-85.

[91] M.H. Chuang, M.H. Tsai, W.R. Wang, SJ. Lin, J.W. Yeh, Microstructure and wear behavior of AlxCo1. 5CrFeNi1. 5Tiy high-entropy alloys, Acta Materialia, 59 (2011) 6308-6317.

[92] J.W. Yeh, Alloy design strategies and future trends in high-entropy alloys, JOM, 65 (2013) 1759-1771.

[93] Y.F. Kao, T.J. Chen, S.K. Chen, J.W. Yeh, Microstructure and mechanical property of as-cast,-homogenized, and-deformed AlxCoCrFeNi (0≤ x≤ 2) high-entropy alloys, Journal of Alloys and Compounds, 488 (2009) 57-64.

[94] Y. Zhang, Z. Lu, S. Ma, P. Liaw, Z. Tang, Y. Cheng, M. Gao, Guidelines in predicting phase formation of high-entropy alloys, Mrs Communications, 4 (2014) 57-62.

[95] P. Koželj, S. Vrtnik, A. Jelen, S. Jazbec, Z. Jagličić, S. Maiti, M. Feuerbacher, W. Steurer, J. Dolinšek, Discovery of a superconducting high-entropy alloy, Physical review letters, 113 (2014) 107001.

[96] V. Maurice, P. Marcus, Passive films at the nanoscale, Electrochimica Acta, 84 (2012) 129-138.

[97] V. Maurice, P. Marcus, Progress in corrosion science at atomic and nanometric scales, Progress in Materials Science, 95 (2018) 132-171.

[98] G. Koch, J. Varney, N. Thompson, O. Moghissi, M. Gould, J. Payer, International measures of prevention, application, and economics of corrosion technologies study, NACE International, (2016) 216.

[99] I. Olefjord, The passive state of stainless steels, Materials Science and Engineering, 42 (1980) 161-171.

[100] P. Schmuki, From Bacon to barriers: a review on the passivity of metals and alloys, Journal of Solid State Electrochemistry, 6 (2002) 145-164.

[101] D. Hamm, K. Ogle, C.O.A. Olsson, S. Weber, D. Landolt, Passivation of Fe–Cr alloys studied with ICP-AES and EQCM, Corrosion Science, 44 (2002) 1443-1456.

[102] I. Olefjord, L. Wegrelius, Surface analysis of passive state, Corrosion Science, 31 (1990) 89-98.

[103] C.O. Olsson, D. Landolt, Passive films on stainless steels—chemistry, structure and growth, Electrochimica acta, 48 (2003) 1093-1104.

[104] R.P. Frankenthal, J. Kruger, Passivity of metals, (1978).

[105] C.F. Schönbein, Ueber das Verhalten des Zinns und des Eisens gegen die Salpetersäure, Annalen der Physik, 113 (1836) 390-399.

[106] N.D. Tomashov, Theory of corrosion and protection of metals, (1966) 672

[107] L. Gmelin, Gmelins Handbuch der anorganischen chemie, Verlag Chemie gmbh, 1924.

[108] J. Keir, XX. Experiments and observations on the dissolution of metals in acids, and their precipitations; with an account of a new compound acid menstruum, useful in some technical operations of parting metals, Philosophical Transactions of the Royal Society of London, (1790) 359-384.

[109] M. Faraday, Experimental researches in electricity, The Royal Society London, (1851) 592-595.

[110] H.H. Uhlig, Passivity in metals and alloys, Corrosion Science, 19 (1979) 777-791.

[111] P. Monnartz, Iron-chromium alloys with special consideration of resistance to acids, Metallurgie, 8 (1911) 161-176.

[112] A. Seyeux, V. Maurice, P. Marcus, Oxide film growth kinetics on metals and alloys I. Physical model, Journal of The Electrochemical Society, 160 (2013) C189-C196.

[113] D.D. Macdonald, The point defect model for the passive state, Journal of the Electrochemical Society, 139 (1992) 3434.

[114] D.D. Macdonald, The history of the point defect model for the passive state: a brief review of film growth aspects, Electrochimica Acta, 56 (2011) 1761-1772.

[115] G.H. Koch, M.P. Brongers, N.G. Thompson, Y.P. Virmani, J.H. Payer, Corrosion cost and preventive strategies in the United States, Federal Highway Administration, 2002.

[116] B. Hou, X. Li, X. Ma, C. Du, D. Zhang, M. Zheng, W. Xu, D. Lu, F. Ma, The cost of corrosion in China, Npj Materials Degradation, 1 (2017) 1-10.

[117] E. McCafferty, Introduction to corrosion science, Springer Science & Business Media, 2010.

[118] A. Brooks, C. Clayton, K. Doss, Y. Lu, On the role of Cr in the passivity of stainless steel, Journal of the Electrochemical Society, 133 (1986) 2459-2464.

[119] K. Heusler, Growth and dissolution of passivating films, Corrosion Science, 31 (1990) 597-606.

[120] S. Henry, J. Mougin, Y. Wouters, J.-P. Petit, A. Galerie, Characterization of chromia scales grown on pure chromium in different oxidizing atmospheres, Materials at High Temperatures, 17 (2000) 231-234.

[121] J. Di Martino, C. Rapin, P. Berthod, R. Podor, P. Steinmetz, Corrosion of metals and alloys in molten glasses. Part 1: glass electrochemical properties and pure metal (Fe, Co, Ni, Cr) behaviours, Corrosion Science, 46 (2004) 1849-1864.

[122] H. Rocha, G. Lennartz, The activation potential of iron-chromium alloys and its relationship to the sulfur content of these alloys, Archives of Eisenhüttenwese, 26 (1955) 117-123.

[123] K. Asami, K. Hashimoto, S. Shimodaira, An XPS study of the passivity of a series of iron—chromium alloys in sulphuric acid, Corrosion Science, 18 (1978) 151-160.

[124] A. Rossi, B. Elsener, G. Hähner, M. Textor, N. Spencer, XPS, AES and ToF-SIMS investigation of surface films and the role of inclusions on pitting corrosion in austenitic

stainless steels, Surface and Interface Analysis, 29 (2000) 460-467.

[125] E. Gardin, S. Zanna, A. Seyeux, A. Allion-Maurer, P. Marcus, XPS and ToF-SIMS characterization of the surface oxides on lean duplex stainless steel – Global and local approaches, Corrosion Science, 155 (2019) 121-133.

[126] J.D. Henderson, A. Seyeux, S. Zanna, M.C. Biesinger, D.W. Shoesmith, J.J. Noël, P. Marcus, Investigating the transport mechanisms governing the oxidation of Hastelloy BC-1 by in situ ToF-SIMS, Corrosion Science, (2019) 108138.

[127] Z. Wang, F. Di-Franco, A. Seyeux, S. Zanna, V. Maurice, P. Marcus, Passivation-induced physicochemical alterations of the native surface oxide film on 316L austenitic stainless steel, Journal of The Electrochemical Society, 166 (2019) C3376-C3388.

[128] L. Wang, D. Mercier, S. Zanna, A. Seyeux, M. Laurent-Brocq, L. Perrière, I. Guillot, P. Marcus, Study of the surface oxides and corrosion behaviour of an equiatomic CoCrFeMnNi high entropy alloy by XPS and ToF-SIMS, Corrosion Science, (2020) 108507.

[129] K. Sieradzki, R. Newman, A percolation model for passivation in stainless steels, Journal of The Electrochemical Society, 133 (1986) 1979-1980.

[130] M. El-Basiouny, S. Haruyama, The polarization behaviour of FeCr alloys in acidic sulphate solutions in the active region, Corrosion Science, 16 (1976) 529-540.

[131] J.A.L. Dobbelaar, E.C.M. Herman, J.H.W. de Wit, The corrosion behaviour of iron-chromium alloys in 0.5 M sulphuric acid, Corrosion Science, 33 (1992) 765-778.

[132] H.H. Uhlig, G.E. Woodside, Anodic Polarization of Passive and Non-passive Chromium–Iron Alloys, The Journal of Physical Chemistry, 57 (1953) 280-283.

[133] R. Kirchheim, B. Heine, H. Fischmeister, S. Hofmann, H. Knote, U. Stolz, The passivity of iron-chromium alloys, Corrosion Science, 29 (1989) 899-917.

[134] V. Maurice, H. Peng, L.H. Klein, A. Seyeux, S. Zanna, P. Marcus, Effects of molybdenum on the composition and nanoscale morphology of passivated austenitic stainless steel surfaces, Faraday Discussions, 180 (2015) 151-170.

[135] R. Kirchheim, B. Heine, S. Hofmann, H. Hofsäss, Compositional changes of passive films due to different transport rates and preferential dissolution, Corrosion Science, 31 (1990) 573-578.

[136] V. Maurice, W. Yang, P. Marcus, XPS and STM Study of Passive Films Formed on Fe-22Cr (110) Single-Crystal Surfaces, Journal of the Electrochemical Society, 143 (1996) 1182-1200.

[137] I. Olefjord, B.O. Elfstrom, The composition of the surface during passivation of stainless steels, Corrosion, 38 (1982) 46-52.

[138] S. Haupt, H.-H. Strehblow, A combined surface analytical and electrochemical study of the formation of passive layers on FeCr alloys in 0.5 M $H_2SO_4$, Corrosion Science, 37 (1995) 43-54.

[139] H.W. Hoppe, S. Haupt, H.H. Strehblow, Combined surface analytical and electrochemical study of the formation of passive layers on Fe/Cr alloys in 1 M NaOH, Surface and Interface Analysis, 21 (1994) 514-525.

[140] N. Hara, K. Sugimoto, The Study of the Passivation Films on Fe-Cr Alloys by Modulation Spectroscopy, Journal of The Electrochemical Society, 126 (1979) 1328.

[141] P. Marcus, I. Olefjord, Round Robin on combined electrochemical and AES/ESCA

characterization of the passive films on Fe-Cr and Fe-Cr-Mo alloys, Surface and interface analysis, 11 (1988) 569-576.

[142] D. Mitchell, M. Graham, Comparison of Auger and SIMS analysis of a thin passive oxide film on iron—25% chromium, Surface and Interface Analysis, 10 (1987) 259-261.

[143] J. Castle, J. Qiu, The application of ICP-MS and XPS to studies of ion selectivity during passivation of stainless steels, Journal of The Electrochemical Society, 137 (1990) 2031.

[144] C. Courty, H. Mathieu, D. Landolt, Surface oxidation of an electrochemically polarized FeCr alloy studied by SIMS oxygen isotope ratio profiling, Electrochimica Acta, 36 (1991) 1623-1630.

[145] S. Mischler, A. Vogel, H.J. Mathieu, D. Landolt, The chemical composition of the passive film on Fe-24Cr and Fe-24Cr-11Mo studied by AES, XPS and SIMS, Corrosion Science, 32 (1991) 925-944.

[146] V. Maurice, W. Yang, P. Marcus, XPS and STM investigation of the passive film formed on Cr (110) single-crystal surfaces, Journal of The Electrochemical Society, 141 (1994) 3016-3027.

[147] D. Marijan, M. Gojić, Electrochemical study of the chromium electrode behaviour in borate buffer solution, Journal of applied electrochemistry, 32 (2002) 1341-1346.

[148] N. Sato, T. Noda, K. Kudo, Thickness and structure of passive films on iron in acidic and basic solution, Electrochimica Acta, 19 (1974) 471-475.

[149] V. Maurice, W. Yang, P. Marcus, X-Ray photoelectron spectroscopy and scanning tunneling microscopy study of passive films formed on (100) Fe-18Cr-13Ni single-crystal surfaces, Journal of the Electrochemical Society, 145 (1998) 909-920.

[150] E. De Vito, P. Marcus, XPS study of passive films formed on molybdenum-implanted austenitic stainless steels, Surface and Interface Analysis, 19 (1992) 403-408.

[151] L. Ma, F. Wiame, V. Maurice, P. Marcus, New insight on early oxidation stages of austenitic stainless steel from in situ XPS analysis on single-crystalline Fe–18Cr–13Ni, Corrosion Science, 140 (2018) 205-216.

[152] S. Voyshnis, A. Seyeux, S. Zanna, B. Martin-Cabanas, T. Couvant, P. Marcus, Oxide layer growth on nickel-base alloy surfaces in high temperature water and in O2 studied by ToF-SIMS with isotopic tracers, Corrosion Science, 145 (2018) 212-219.

[153] X. Wu, S. Voyshnis, A. Seyeux, Y. Chumlyakov, P. Marcus, ToF-SIMS study of oxide films thermally grown on nickel-base alloys, Corrosion Science, 141 (2018) 175-181.

[154] D. Costa, P. Marcus, Modifications of passive films formed on Ni--Cr--Fe alloys with chromium content in the alloy and effects of adsorbed or segregated sulfur, (1993).

[155] N. McIntyre, R. Davidson, T. Walzak, A. Brennenstuhl, F. Gonzalez, S. Corazza, The corrosion of steam generator surfaces under typical secondary coolant conditions: effects of pH excursions on the alloy surface composition, Corrosion Science, 37 (1995) 1059-1083.

[156] I. Barin, Thermochemical data of pure substances, VCH, (1989).

[157] A. Mishra, D. Shoesmith, P. Manning, Materials selection for use in concentrated hydrochloric acid, Corrosion, 73 (2017) 68-76.

[158] K. Hashimoto, K. Asami, A. Kawashima, H. Habazaki, E. Akiyama, The role of corrosion-resistant alloying elements in passivity, Corrosion Science, 49 (2007) 42-52.

[159] M. Kaneko, H. Isaacs, Effects of molybdenum on the pitting of ferritic-and austenitic-stainless steels in bromide and chloride solutions, Corrosion Science, 44 (2002) 1825-1834.

[160] K. Hashimoto, K. Asami, K. Teramoto, An X-ray photo-electron spectroscopic study on the role of molybdenum in increasing the corrosion resistance of ferritic stainless steels in HC1, Corrosion Science, 19 (1979) 3-14.

[161] D. Landolt, S. Mischler, A. Vogel, H. Mathieu, Chloride ion effects on passive films on FeCr and FeCrMo studied by AES, XPS and SIMS, Corrosion Science, 31 (1990) 431-440.

[162] M. Montemor, A. Simões, M. Ferreira, M.D.C. Belo, The role of Mo in the chemical composition and semiconductive behaviour of oxide films formed on stainless steels, Corrosion Science, 41 (1999) 17-34.

[163] T.J. Mesquita, E. Chauveau, M. Mantel, R.P. Nogueira, A XPS study of the Mo effect on passivation behaviors for highly controlled stainless steels in neutral and alkaline conditions, Applied Surface Science, 270 (2013) 90-97.

[164] K. Sugimoto, Y. Sawada, The role of molybdenum additions to austenitic stainless steels in the inhibition of pitting in acid chloride solutions, Corrosion Science, 17 (1977) 425-445.

[165] C. Loable, I.N. Viçosa, T.J. Mesquita, M. Mantel, R.P. Nogueira, G. Berthomé, E. Chauveau, V. Roche, Synergy between molybdenum and nitrogen on the pitting corrosion and passive film resistance of austenitic stainless steels as a pH-dependent effect, Materials Chemistry and Physics, 186 (2017) 237-245.

[166] Z. Wang, E.-M. Paschalidou, A. Seyeux, S. Zanna, V. Maurice, P. Marcus, Mechanisms of Cr and Mo Enrichments in the Passive Oxide Film on 316L Austenitic Stainless Steel, Frontiers in Materials, 6 (2019) 232.

[167] M.-W. Tan, E. Akiyama, A. Kawashima, K. Asami, K. Hashimoto, The effect of air exposure on the corrosion behavior of amorphous Fe-8Cr-Mo-13P-7C alloys in 1 M HCl, Corrosion Science, 37 (1995) 1289-1301.

[168] C. Clayton, Y. Lu, A bipolar model of the passivity of stainless steel: the role of Mo addition, Journal of the Electrochemical Society, 133 (1986) 2465-2473.

[169] Y. Lu, C. Clayton, A. Brooks, A bipolar model of the passivity of stainless steels—II. The influence of aqueous molybdate, Corrosion Science, 29 (1989) 863-880.

[170] J.E. Castle, J.H. Qiu, A co-ordinated study of the passivation of alloy steels by plasma source mass spectrometry and x-ray photoelectron spectroscopy—1. characterization of the passive film, Corrosion Science, 29 (1989) 591-603.

[171] H. Ogawa, H. Omata, I. Itoh, H. OKADA, Auger electron spectroscopic and electrochemical analysis of the effect of alloying elements on the passivation behavior of stainless steels, Corrosion, 34 (1978) 52-60.

[172] W. Yang, R.-C. Ni, H.-Z. Hua, A. Pourbaix, The behavior of chromium and molybdenum in the propagation process of localized corrosion of steels, Corrosion Science, 24 (1984) 691-707.

[173] A. Pardo, M. Merino, A. Coy, F. Viejo, R. Arrabal, E. Matykina, Effect of Mo and Mn additions on the corrosion behaviour of AISI 304 and 316 stainless steels in $H_2SO_4$, Corrosion Science, 50 (2008) 780-794.

[174] I. Olefjord, B. Brox, U. Jelvestam, Surface composition of stainless steels during anodic dissolution and passivation studied by ESCA, Journal of the Electrochemical Society, 132

(1985) 2854-2861.

[175] J. Lumsden, R. Staehle, Application of auger electron spectroscopy to the determination of the composition of passive films on type 316 SS, Scripta Metallurgica, 6 (1972) 1205-1208.

[176] N. Hakiki, M.D.C. Belo, A. Simoes, M. Ferreira, Semiconducting properties of passive films formed on stainless steels: influence of the alloying elements, Journal of the Electrochemical Society, 145 (1998) 3821.

[177] R.L. Klueh, P.J. Maziasz, E.H. Lee, Manganese as an austenite stabilizer in Fe-Cr-Mn-C steels, Materials Science and Engineering: A, 102 (1988) 115-124.

[178] V. Raghavan, Effect of manganese on the stability of austenite in Fe-Cr-Ni alloys, Metallurgical and Materials Transactions A, 26 (1995) 237-242.

[179] R. Jargelius-Pettersson, Application of the pitting resistance equivalent concept to some highly alloyed austenitic stainless steels, Corrosion, 54 (1998) 162-168.

[180] G. Stein, I. Hucklenbroich, Manufacturing and applications of high nitrogen steels, Materials and Manufacturing Processes, 19 (2004) 7-17.

[181] J. Charles, J.-D. Mithieux, J. Krautschick, N. Suutala, J.A. Simón, B. Van Hecke, T. Pauly, A new European 200 series standard to substitute 304 austenitics, Revue de Métallurgie–International Journal of Metallurgy, 106 (2009) 90-98.

[182] U. Kamachi Mudali, Nitrogen—A boon to the Metals Industry, Materials and Manufacturing Processes, 19 (2004) 1-5.

[183] J.C. Rawers, Alloying effects on the microstructure and phase stability of Fe–Cr–Mn steels, Journal of Materials Science, 43 (2008) 3618-3624.

[184] J. Rawers, J. Bennett, R. Doan, J. Siple, Nitrogen solubility and nitride formation in Fe-Cr-Ni alloys, Acta Metallurgica et Materialia, 40 (1992) 1195-1199.

[185] I.-u.-H. Toor, Evaluation of corrosion performance of two Mn-containing stainless steel alloys, International Journal of Materials Research, 105 (2014) 386-391.

[186] M.P. Ryan, D.E. Williams, R.J. Chater, B.M. Hutton, D.S. McPhail, Why stainless steel corrodes, Nature, 415 (2002) 770-774.

[187] S.J. Zheng, Y.J. Wang, B. Zhang, Y.L. Zhu, C. Liu, P. Hu, X.L. Ma, Identification of MnCr2O4 nano-octahedron in catalysing pitting corrosion of austenitic stainless steels, Acta Materialia, 58 (2010) 5070-5085.

[188] K. Park, H. Kwon, Effects of Mn on the localized corrosion behavior of Fe–18Cr alloys, Electrochimica Acta, 55 (2010) 3421-3427.

[189] I.-u.-H. Toor, Effect of Mn content and solution annealing temperature on the corrosion resistance of stainless steel alloys, Journal of Chemistry, (2014).

[190] X. Wu, S. Xu, J. Huang, E. Han, W. Ke, K. Yang, Z. Jiang, Uniform corrosion and intergranular corrosion behavior of nickel-free and manganese alloyed high nitrogen stainless steels, Materials and Corrosion, 59 (2008) 676-684.

[191] X. Wu, Y. Fu, J. Huang, E. Han, W. Ke, K. Yang, Z. Jiang, Investigation on pitting corrosion of nickel-free and manganese-alloyed high-nitrogen stainless steels, Journal of Materials Engineering and Performance, 18 (2009) 287-298.

[192] K. Chao, H. Liao, J. Shyue, S. Lian, Corrosion behavior of high nitrogen nickel-free Fe-16Cr-Mn-Mo-N stainless steels, Metallurgical and Materials Transactions B, 45 (2014) 381-

391.

[193] J. Park, T. Suter, H. Bohni, Role of manganese sulfide inclusions on pit initiation of super austenitic stainless steels, Corrosion, 59 (2003) 59-67.

[194] P. Schmuki, H. Hildebrand, A. Friedrich, S. Virtanen, The composition of the boundary region of MnS inclusions in stainless steel and its relevance in triggering pitting corrosion, Corrosion Science, 47 (2005) 1239-1250.

[195] H. Krawiec, V. Vignal, O. Heintz, R. Oltra, Influence of the dissolution of MnS inclusions under free corrosion and potentiostatic conditions on the composition of passive films and the electrochemical behaviour of stainless steels, Electrochimica Acta, 51 (2006) 3235-3243.

[196] E. Webb, T. Suter, R.C. Alkire, Microelectrochemical measurements of the dissolution of single MnS inclusions, and the prediction of the critical conditions for pit initiation on stainless steel, Journal of the Electrochemical Society, 148 (2001) B186-B195.

[197] H. Ha, C. Park, H. Kwon, Effects of misch metal on the formation of non-metallic inclusions and the associated resistance to pitting corrosion in 25% Cr duplex stainless steels, Scripta materialia, 55 (2006) 991-994.

[198] N. Parvathavarthini, R.K. Gupta, A.V. Kumar, S. Ramya, U.K. Mudali, Interpretation of electrochemical potentiokinetic reactivation data in the presence of sulphide/oxysulphide inclusions in 316LN stainless steel, Corrosion Science, 53 (2011) 3202-3214.

[199] Y. Wang, P. Hu, X. Ma, Mn ion dissolution from MnS: a density functional theory study, Physical Chemistry Chemical Physics, 15 (2013) 17112-17117.

[200] W. Lv, C. Pan, W. Su, Z. Wang, S. Liu, C. Wang, A study on atmospheric corrosion of 304 stainless steel in a simulated marine atmosphere, Journal of Materials Engineering and Performance, 24 (2015) 2597-2604.

[201] E. Moslehifard, M. Moslehifard, S. Ghasemzadeh, F. Nasirpouri, Corrosion behavior of a Nickel-base dental casting alloy in artificial saliva studied by weight loss and polarization techniques, Frontiers in Dentistry, 16 (2019) 13.

[202] H.H. Huang, Effect of chemical composition on the corrosion behavior of Ni-Cr-Mo dental casting alloys, Journal of Biomedical Materials Research, 60 (2002) 458-465.

[203] Y. Chou, Y. Wang, J. Yeh, H. Shih, Pitting corrosion of the high-entropy alloy $Co_{1.5}CrFeNi_{1.5}Ti_{0.5}Mo_{0.1}$ in chloride-containing sulphate solutions, Corrosion Science, 52 (2010) 3481-3491.

[204] Y. Chen, T. Duval, U. Hung, J. Yeh, H. Shih, Microstructure and electrochemical properties of high entropy alloys—a comparison with type 304 stainless steel, Corrosion Science, 47 (2005) 2257-2279.

[205] C. Lee, C. Chang, Y. Chen, J. Yeh, H. Shih, Effect of the aluminium content of AlxCrFe1. 5MnNi0. 5 high-entropy alloys on the corrosion behaviour in aqueous environments, Corrosion Science, 50 (2008) 2053-2060.

[206] Q. Li, T. Yue, Z. Guo, X. Lin, Microstructure and corrosion properties of AlCoCrFeNi high entropy alloy coatings deposited on AISI 1045 steel by the electrospark process, Metallurgical and Materials Transactions A, 44 (2013) 1767-1778.

[207] Y.J. Hsu, W.C. Chiang, J.K. Wu, Corrosion behavior of FeCoNiCrCux high-entropy alloys in 3.5% sodium chloride solution, Materials Chemistry and Physics, 92 (2005) 112-117.

[208] H. Diao, L.J. Santodonato, Z. Tang, T. Egami, P.K. Liaw, Local Structures of High-Entropy Alloys (HEAs) on Atomic Scales: An Overview, JOM, 67 (2015) 2321-2325.

[209] P. Lu, J.E. Saal, G.B. Olson, T. Li, O.J. Swanson, G.S. Frankel, A.Y. Gerard, K.F. Quiambao, J.R. Scully, Computational materials design of a corrosion resistant high entropy alloy for harsh environments, Scripta Materialia, 153 (2018) 19-22.

[210] T. Li, O.J. Swanson, G.S. Frankel, A.Y. Gerard, P. Lu, J.E. Saal, J.R. Scully, Localized corrosion behavior of a single-phase non-equimolar high entropy alloy, Electrochimica Acta, 306 (2019) 71-84.

[211] K.F. Quiambao, S.J. McDonnell, D.K. Schreiber, A.Y. Gerard, K.M. Freedy, P. Lu, J.E. Saal, G.S. Frankel, J.R. Scully, Passivation of a corrosion resistant high entropy alloy in non-oxidizing sulfate solutions, Acta Materialia, 164 (2019) 362-376.

[212] X. Li, J. Han, P. Lu, J.E. Saal, G.B. Olson, G.S. Frankel, J.R. Scully, K. Ogle, Communication—Dissolution and Passivation of a Ni-Cr-Fe-Ru-Mo-W High Entropy Alloy by Elementally Resolved Electrochemistry, Journal of The Electrochemical Society, 167 (2020) 061505.

[213] Y. Qiu, S. Thomas, M.A. Gibson, H.L. Fraser, N. Birbilis, Corrosion of high entropy alloys, Npj Materials degradation, 1 (2017) 15.

[214] Y. Shi, B. Yang, P. Liaw, Corrosion-resistant high-entropy alloys: A review, Metals, 7 (2017) 43.

[215] C. Wagner, Beitrag zur theorie des anlaufvorgangs, Zeitschrift für physikalische Chemie, 21 (1933) 25-41.

[216] C. Chao, L. Lin, D. Macdonald, A point defect model for anodic passive films: I. Film growth kinetics, Journal of the Electrochemical Society, 128 (1981) 1187.

[217] K. Leistner, C. Toulemonde, B. Diawara, A. Seyeux, P. Marcus, Oxide film growth kinetics on metals and alloys II. Numerical simulation of transient behavior, Journal of The Electrochemical Society, 160 (2013) C197-C205.

[218] D.J. Young, High temperature oxidation and corrosion of metals, Elsevier, 2008.

[219] C. Tedmon, The effect of oxide volatilization on the oxidation kinetics of Cr and Fe-Cr alloys, Journal of the Electrochemical Society, 113 (1966) 766.

[220] F.P. Fehlner, N.F. Mott, Low-temperature oxidation, Oxidation of metals, 2 (1970) 59-99.

[221] G.C. Wood, High-temperature oxidation of alloys, Oxidation of Metals, 2 (1970) 11-57.

[222] C. Poulain, A. Seyeux, S. Voyshnis, P. Marcus, Volatilization and transport mechanisms during Cr oxidation at 300 °C studied in situ by ToF-SIMS, Oxidation of Metals, 88 (2017) 423-433.

[223] T. Jonsson, S. Karlsson, H. Hooshyar, M. Sattari, J. Liske, J.E. Svensson, L.G. Johansson, Oxidation after breakdown of the chromium-rich scale on stainless steels at high temperature: internal oxidation, Oxidation of Metals, 85 (2016) 509-536.

[224] K. Habib, M. Damra, J. Saura, I. Cervera, J. Bellés, Breakdown and evolution of the protective oxide scales of AISI 304 and AISI 316 stainless steels under high-temperature oxidation, International Journal of Corrosion, (2011).

[225] H. Christ, L. Berchtold, H. Sockel, Oxidation of Ni-base alloys in atmospheres with widely varying oxygen partial pressures, Oxidation of metals, 26 (1986) 45-76.

[226] H. Hindam, D. Whittle, Microstructure, adhesion and growth kinetics of protective scales on metals and alloys, Oxidation of Metals, 18 (1982) 245-284.

[227] A. Atkinson, Transport processes during the growth of oxide films at elevated temperature, Reviews of Modern Physics, 57 (1985) 437.

[228] P. Kofstad, High temperature corrosion, Elsevier Applied Science Publishers, Crown House, Linton Road, Barking, Essex IG 11 8 JU, UK, 1988., (1988).

[229] A.C.S. Sabioni, A.M. Huntz, J. Philibert, B. Lesage, C. Monty, Relation between the oxidation growth rate of chromia scales and self-diffusion in Cr2O3, Journal of Materials Science, 27 (1992) 4782-4790.

[230] W.C. Hagel, Factors controlling the high-temperature oxidation of chromium, Journal of The Electrochemical Society, (1962) C78-C78.

[231] T. Gheno, D. Monceau, J. Zhang, D.J. Young, Carburisation of ferritic Fe–Cr alloys by low carbon activity gases, Corrosion Science, 53 (2011) 2767-2777.

[232] M. Hobby, G. Wood, The role of nickel in the high-temperature oxidation of Fe-Cr-Ni alloys in oxygen, Oxidation of Metals, 1 (1969) 23-54.

[233] D. Barnes, J. Calvert, K. Hay, D. Lees, The role of oxygen transport in oxidation of Fe-Cr alloys, Philosophical Magazine, 28 (1973) 1303-1318.

[234] D.G. Lees, J.M. Calvert, The use of 18O as a tracer to study the growth mechanisms of oxide scales, Corrosion Science, 16 (1976) 767-774.

[235] T. Smith, L. Crane, Adsorption of oxygen on steel, Oxidation of Metals, 10 (1976) 135-148.

[236] G. Wallwork, The oxidation of alloys, Reports on Progress in Physics, 39 (1976) 401.

[237] T.J. Driscoll, P.B. Needham, The oxidation of Fe-Cr surface and bulk alloys at 300°C, Oxidation of Metals, 13 (1979) 283-298.

[238] T. Tanabe, S. Imoto, Surface oxidation of type 316 stainless steel, Transactions of the Japan Institute of Metals, 20 (1979) 507-515.

[239] D.J. Young, D.F. Mitchell, Low-temperature oxidation of Fe-24 wt.%Cr, Oxidation of Metals, 13 (1979) 437-456.

[240] G. Allen, P. Tucker, R. Wild, Characterization of iron/oxygen surface reactions by X-ray photoelectron spectroscopy, Philosophical Magazine B, 46 (1982) 411-421.

[241] G. Hultquist, C. Leygraf, The initiation of selective oxidation of a ferritic stainless steel at low temperatures and oxygen pressures, Corrosion Science, 22 (1982) 331-346.

[242] K. Kuroda, P.A. Labun, G. Welsch, T.E. Mitchell, Oxide-formation characteristics in the early stages of oxidation of Fe and Fe-Cr alloys, Oxidation of Metals, 19 (1983) 117-127.

[243] A.P. Greeff, C.W. Louw, H.C. Swart, The oxidation of industrial FeCrMo steel, Corrosion Science, 42 (2000) 1725-1740.

[244] A. Vesel, M. Mozetič, A. Zalar, Oxidation of AISI 304L stainless steel surface with atomic oxygen, Applied Surface Science, 200 (2002) 94-103.

[245] Č. Donik, A. Kocijan, D. Mandrino, I. Paulin, M. Jenko, B. Pihlar, Initial oxidation of duplex stainless steel, Applied Surface Science, 255 (2009) 7056-7061.

[246] G. Betz, G. Wehner, L. Toth, A. Joshi, Composition-vs-depth profiles obtained with Auger electron spectroscopy of air-oxidized stainless-steel surfaces, Journal of Applied

Physics, 45 (1974) 5312-5316.

[247] K. Lillerud, P. Kofstad, On high temperature oxidation of chromium: I. Oxidation of annealed, thermally etched chromium at 800–1100°C, Journal of the electrochemical society, 127 (1980) 2397.

[248] S. Storp, R. Holm, ESCA investigation of the oxide layers on some Cr containing alloys, Surface Science, 68 (1977) 10-19.

[249] S.C. Tjong, J. Eldridge, R.W. Hoffman, EAS studies of the oxides formed on iron-chromium alloys at 400°C, Applications of Surface Science, 14 (1983) 297-306.

[250] I. Olefjord, Esca-studies of the composition profile of low temperature oxide formed on chromium steels—I. Oxydation in dry oxygen, Corrosion Science, 15 (1975) 687-696.

[251] J.R. Lince, S.V. Didziulis, D.K. Shuh, T.D. Durbin, J.A. Yarmoff, Interaction of O2 with the Fe0. 84Cr0. 16 (001) surface studied by photoelectron spectroscopy, Surface science, 277 (1992) 43-63.

[252] S. Basu, J. Halloran, Tracer isotope distribution in growing oxide scales, Oxidation of Metals, 27 (1987) 143-155.

[253] J.A. Bardwell, B. MacDougall, M. Graham, Use of 18O/SIMS and electrochemical techniques to study the reduction and breakdown of passive oxide films on iron, Journal of the Electrochemical Society, 135 (1988) 413-418.

[254] M.J. Graham, J. Eldrige, D. Mitchell, R. Hussey, Anion transport in growing Cr2O3 scales, Materials Science Forum, (1989) 207-242.

[255] R. Lobnig, H. Schmidt, K. Hennesen, H. Grabke, Diffusion of cations in chromia layers grown on iron-base alloys, Oxidation of Metals, 37 (1992) 81-93.

[256] A.M. Huntz, S.C. Tsai, Diffusion in oxide scales: application to Cr2O3 scales, Journal of Materials Science Letters, 13 (1994) 821-825.

[257] S. Tsai, A. Huntz, C. Dolin, C. Monty, Diffusion of 18O in Cr2O3: Bulk and scales and relation with oxidation kinetics, Radiation Effects and Defects in Solids, 137 (1995) 285-290.

[258] S.C. Tsai, A.M. Huntz, C. Dolin, Diffusion of18O in massive Cr2O3 and in Cr2O3 scales at 900°C and its relation to the oxidation kinetics of chromia forming alloys, Oxidation of Metals, 43 (1995) 581-596.

[259] S.C. Tsai, A.M. Huntz, C. Dolin, Growth mechanism of Cr2O3 scales: oxygen and chromium diffusion, oxidation kinetics and effect of yttrium, Materials Science and Engineering: A, 212 (1996) 6-13.

[260] A.M. Huntz, S. Tsai, J. Balmain, K. Messaoudi, B. Lesage, C. Dolin, Atomic transport in Cr2O3 and Al2O3 scales: growth mechanism and effect of yttrium, Materials Science Forum, (1997) 313-324.

[261] A. Pakes, P. Skeldon, G. Thompson, R. Hussey, S. Moisa, G. Sproule, D. Landheer, M. Graham, Composition and growth of anodic and thermal oxides on InP and GaAs, Surface and Interface Analysis, 34 (2002) 481-484.

[262] A.C.S. Sabioni, A.M.J. Daniel, W. Macedo, M. Martins, A.M. Huntz, F. Jomard, A. Persiano, First study of iron self-diffusion in Fe2O3 single crystals by SIMS, Defect and Diffusion Forum, (2005) 277-281.

[263] A.C.S. Sabioni, A.M. Huntz, F. Silva, F. Jomard, Diffusion of iron in Cr2O3: polycrystals and thin films, Materials Science and Engineering: A, 392 (2005) 254-261.

[264] L. Walters, R. Grace, Self diffusion of 51Cr in single crystals of Cr2O3, Journal of Applied Physics, 36 (1965) 2331-2332.

[265] K. Hoshino, N. Peterson, Cation Self-Diffusion in Cr2O3, Journal of the American Ceramic Society, 66 (1983) c202-c203.

[266] A. Atkinson, F. Pummery, C. Monty, G. Simkovich, V. Stubican, Transport in non-stoichiometric compounds, NATO ASI Series, (1985) 285.

[267] A.C.S. Sabioni, B. Lesage, A.M. Huntz, J.C. Pivin, C. Monty, Self-diffusion in Cr2O3 I. Chromium diffusion in single crystals, Philosophical Magazine A, 66 (1992) 333-350.

[268] M. Su, G. Simkovich, Point defect structure of Cr203, Pennsylvania State Univ University Park Applied Research Lab, 1987.

[269] A.M. Huntz, A. Reckmann, C. Haut, C. Sévérac, M. Herbst, F.C.T. Resende, A.C.S. Sabioni, Oxidation of AISI 304 and AISI 439 stainless steels, Materials Science and Engineering: A, 447 (2007) 266-276.

[270] A. Sabioni, A. Huntz, L. Borges, F. Jomard, First study of manganese diffusion in Cr2O3 polycrystals and thin films by SIMS, Philosophical Magazine, 87 (2007) 1921-1937.

[271] A.C.S. Sabioni, R.P.B. Ramos, V. Ji, F. Jomard, W.A.d.A. Macedo, P.L. Gastelois, V.B. Trindade, About the role of chromium and oxygen ion diffusion on the growth mechanism of oxidation films of the AISI 304 austenitic stainless steel, Oxidation of Metals, 78 (2012) 211-220.

[272] A.C.S. Sabioni, E.A. Malheiros, V. Ji, F. Jomard, W.A. de Almeida Macedo, P.L. Gastelois, Ion diffusion study in the oxide layers due to oxidation of AISI 439 ferritic stainless steel, Oxidation of Metals, 81 (2014) 407-419.

[273] A.C.S. Sabioni, J.N.V. Souza, V. Ji, F. Jomard, V.B. Trindade, J.F. Carneiro, Study of ion diffusion in oxidation films grown on a model Fe–15%Cr alloy, Solid State Ionics, 276 (2015) 1-8.

[274] C. Wagner, Theoretical analysis of the diffusion processes determining the oxidation rate of alloys, Journal of the Electrochemical Society, 99 (1952) 369-380.

[275] E. Young, J. De Wit, The use of a 18O tracer and Rutherford backscattering spectrometry to study the oxidation mechanism of NiAl, Solid State Ionics, 16 (1985) 39-46.

[276] S. Brenner, Oxidation of iron-molybdenum and nickel-molybdenum alloys, Journal of The Electrochemical Society, 102 (1955) 7-15.

[277] T.N. Ooi, D.S. Mcphail, R.J. Chater, B.A. Shollock, Isotope exchange studies of oxidation mechanisms in nickel-base superalloys using FIB-SIMS techniques, Surface and Coatings Technology, 201 (2006) 3885-3888.

[278] B. Pint, J.a. Martin, L. Hobbs, 18O/SIMS characterization of the growth mechanism of doped and undoped α-Al2O3, Oxidation of metals, 39 (1993) 167-195.

# Chapter II

# Characterization techniques and experimental conditions

In this chapter, the electrochemical and surface characterization techniques used in this work are presented. In addition to being used to prepared protective passive film on the surfaces of Cr containing alloys, electrochemistry was also used to characterize the passivation properties of these Cr-containing alloys. The XPS and ToF-SIMS surface analytical techniques, used to characterize the composition, structure and kinetics of formation of the surface oxide films, are detailed in this chapter, as well as the sample surface preparation given to the samples before the measurements.

## II-1. Sample composition and surface preparation

304L stainless steel (Fe-18Cr-10Ni), 316L stainless steel (Fe-19Cr-13Ni-2.7Mo) and CoCrFeMnNi equiatomic high entropy alloy were used in this work.

304L SS and 316L SS were purchased commercially and the CoCrFeMnNi HEA was made in the CECM laboratory (Thiais, France).

Pure Fe, Co, Cr, Ni and Mn ingots (purity exceeding 99.9 wt%) were used to prepare the HEA by high frequency electromagnetic induction melting in a water-cooled copper crucible under He atmosphere. Before melting, samples were prepared by mechanical polishing of raw materials. Afterwards, the HEA ingot was shaped into a rod with a diameter of 13 mm and a length of around 8 cm by gravity casting. The cooling rate was estimated to be about 103 $K.s^{-1}$. Finally, the samples were wrapped into a tantalum sheet, and were annealed at 1373 K during 13 h under a He atmosphere to limit oxidation. At the end of the annealing, the samples were air quenched. The objective of this homogenization annealing is to eliminate the dendritic microstructure formed during casting process. To refine the grain size, HEA samples

51

were rolled and then annealed at a temperature of 900°C for 30 min under He atmosphere, followed by air quenching. At the end of the preparation step, the average grain size of the HEA, verified by electron backscatter diffraction (EBSD) is ∼ 30 μm.

Surface preparation was performed by mechanical polishing first with SiC paper of successive 1200 and 2400 grades and then with diamond suspensions of successive 6, 3, 1 and 0.25 μm grades. Cleaning and rinsing were performed after each polishing step in successive ultrasonicated baths of acetone, ethanol and Millipore® water (resistivity > 18 MΩ cm). Filtered compressed air was used for drying.

## II-2. Electrochemical setup

Electrochemical measurements, including potentiodynamic polarization and potentiostatic polarization, have been used in this work. The potentiostat used is an EC Lab SP200 potentiostat from Bio-Logic and a Gamry Reference 600 potentiostat. Potentiodynamic polarization allows to determine characteristic data like: the corrosion potential, the active, passive and transpassive domains, while potentiostatic polarization is used to elaborate well-defined passive films on the sample surface by applying a static potential on sample in sulfuric acid for a certain time.

As showed in Fig.II-1, a typical three-electrodes setup, comprising the working electrode, the counter electrode and the reference electrode, was used. The working electrode is the sample, which is fixed in the sample holder enabling electrical contact with the potentiostat. A viton O-ring with an exposure area of 1.3 cm$^2$ was used to seal the sample in the sample holder. The reference is a saturated calomel electrode (SCE, +0.245 V/NHE), which is connected to the electrolyte via a salt bridge to avoid chloride contamination of the electrolyte. The counter electrode is a Pt/Au wire.
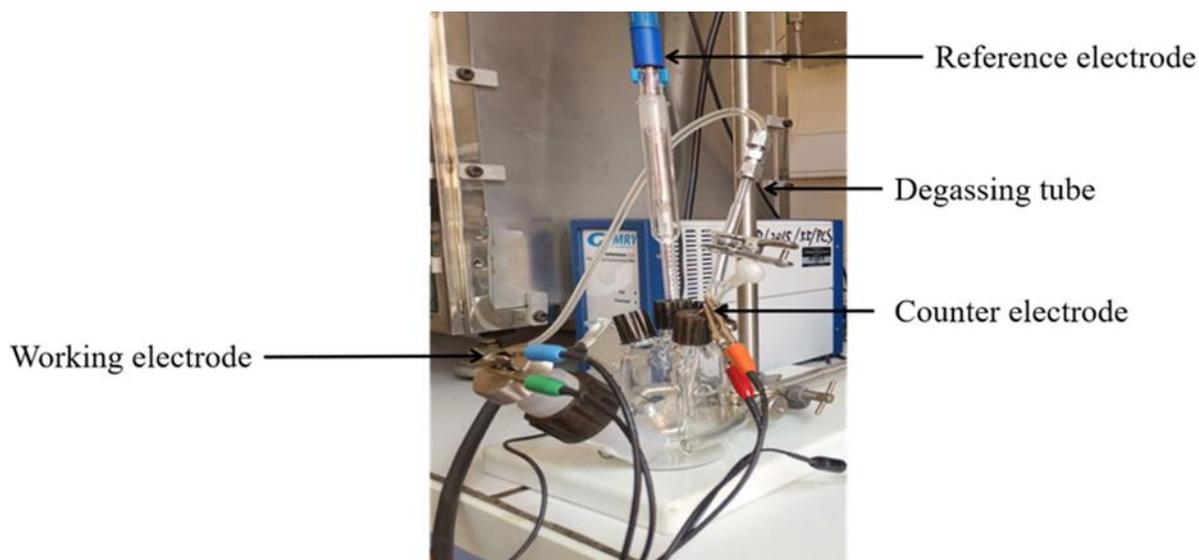
**Fig.II-1** Electrochemical setup with three-electrode system

The electrochemical measurements were carried out at room temperature in 0.05M $H_2SO_4$ (aq) prepared with ultra-pure water (Millipore, resistivity 18.5Mohm.cm) pre-deaerated by Ar bubbling for 30 min.

## II-3. Time-of-Flight Secondary Ion Mass Spectrometry (ToF-SIMS)

Time-of-flight secondary ion mass spectrometry (ToF-SIMS) is a chemical characterization technique allowing elementary, isotopic and molecular analysis of the sample surface. Due to a very large variation in the ionization probabilities as a function of the analysed material, ToF-SIMS spectrometry is generally considered to be a non-quantitative technique. Nevertheless, a pseudo-quantification remains possible from reference materials having a chemical composition close to that of the matrix of the sample to be analysed. Among all the characteristics of the ToF-SIMS spectrometry, the most remarkable ones are: the very high sensitivity, with a detection limit of the order of ppm, the detection of all charged species in a unique measurement (allowing retrospective analysis), and the detection of isotopic species. Depending on the information desired, we choose to work in a mode favouring the mass resolution (spectroscopic mode) or a mode favouring lateral resolution (imaging mode). Like most surface characterization techniques, ToF-SIMS spectrometry requires an Ultra High Vacuum environment (UHV: $10^{-10}$ mbar) in order to protect the surface from environmental contamination and limit, as much as possible, possible interactions and recombination

between the ions emitted from the surface and the environment, causing a significant decrease in the intensity and the modification of the nature of the secondary ions emitted.
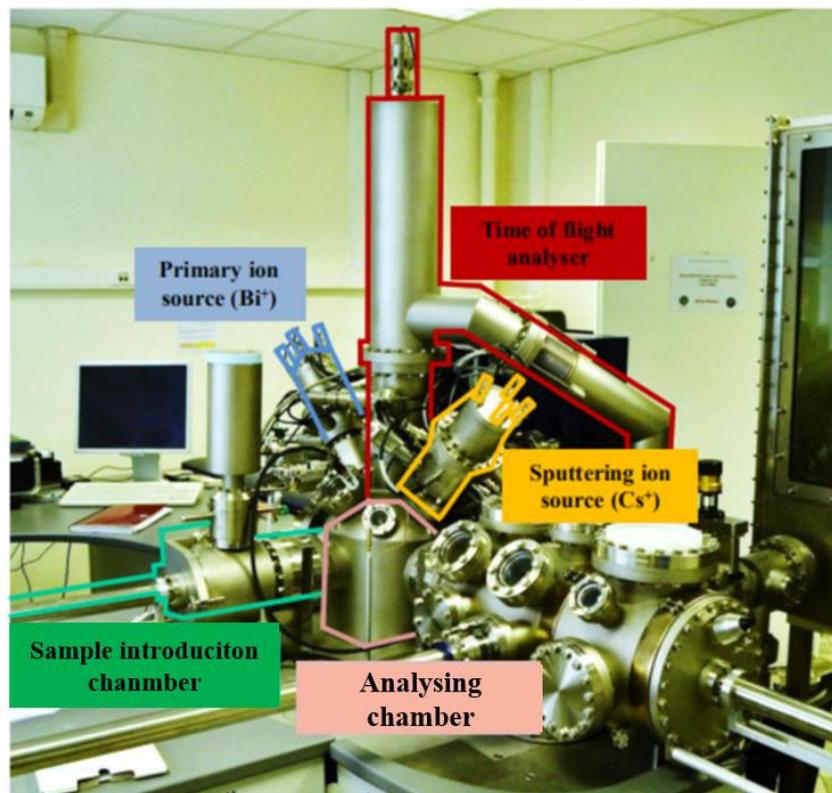


**Fig.II-2** Photo of the ToF-SIMS 5 spectrometer

**Fig.II-2** shows the photo of the ToF-SIMS instrument. The spectrometer is made up of:

- An analysis chamber, operating under UHV, which can be equipped with a sample holder on which the sample to be analyzed is fixed. A heated sample holder is also available allowing temperature analysis (up to 600 °C, depending on the size of sample). This sample holder will be used in the ToF-SIMS experiments at elevated temperatures (Chapter IV, V and VI).

- A source of primary ions, composed of the ion gun allowing the production of primary mono-atomic ion ($Bi^+$) with an energy of a few keV and an optics column allowing to finely focus the ion beam on the surface. The ion source is pulsed (as opposed to SIMS where the source is used continuously). This is mandatory for ToF-SIMS analysis since the emitted ions are not directly sorted as function of their masses but as function of the time needed to reach the detector (thus an accurate time 0 for analysis is required).

- The ToF-SIMS analyzer is composed of the ion flying tube and the secondary ion detector. The secondary ions, produced by the collision of the primary ions with the substrate, are accelerated under an electric field and enter the flying tube, where they freely travel under UHV until the secondary ion detector. The spent time in the flying tube is function of the mass of the emitted species. The details of the equation governing a ToF-SIMS analysis are given in II-3.1.

- An ion etching gun used in alternation with the primary gun. This beam allows the surface of the sample to be etched in a controlled manner, by selecting the appropriate sputtering energy and current, in order to obtain in-depth composition profiles.

## II-3.1. Principles

ToF-SIMS analysis requires maintaining a static situation. This means that the dose of primary ions ($Bi^+$) striking the surface must remain low enough for the surface to be modified locally only. Under static conditions, the primary ion dose received by the surface must remain below $10^{12}$ at.cm$^{-2}$ to ensure that an undisturbed surface is analyzed during successive primary ion pulses. Although local destruction of the surface exists, it is negligible in static mode compared to dynamic SIMS which results in rapid destruction of the surface.
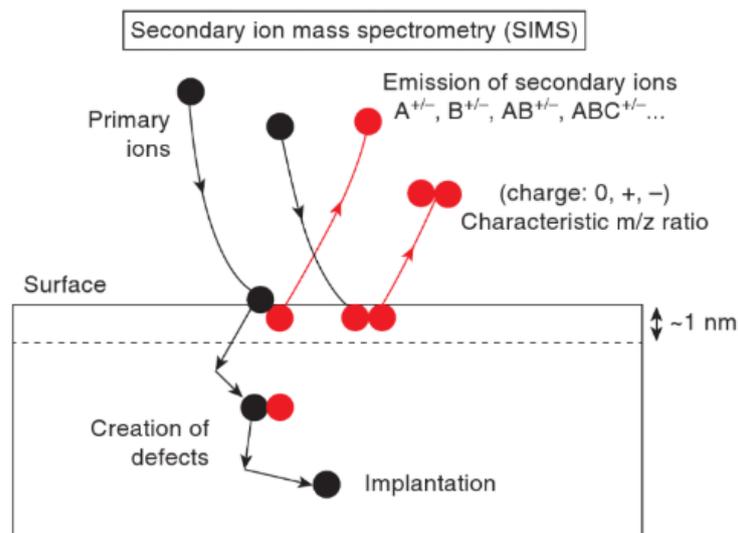


**Fig.II-3** Principle of secondary ion emission (from [1])

As showed in Fig.II-3, during a ToF-SIMS analysis, the impact of primary ions with the

substrate is responsible for cascades of collisions in the material with ejection of particles (ions, atoms, electrons), characteristic of the first monolayers (1-3 monolayers) of the surface of the material. The emitted secondary ions are then accelerated by the application of an intense electric field between the sample and the entrance of the ToF analyzer. All the secondary ions gain a kinetic energy following the equation:

$$E = qU = \frac{1}{2}mv^2 \qquad \text{(equation II-1)}$$

Where q is the charge of the secondary ions, U is the electric field used to accelerate the produced secondary ions, m is the mass of the secondary ion, v is the speed of secondary ions.

These secondary ions then enter the time-of-flight analyzer (operating under UHV) and fly to the detector with a velocity equal to:

$$v = \sqrt{\frac{2qU}{m}} \qquad \text{(equation II-2)}$$

Thus, the time (t) needed to travel through the analyser (length L) is function of the mass of the species and follows the equation:

$$t = \frac{L}{v} = L\sqrt{\frac{m}{2qU}} \qquad \text{(equation II-3)}$$

Therefore, we see that, for a given charge, the lighter ions travel faster and the heavier ions travel slower. This means that in ToF-SIMS measurement, it is not directly a mass detection but it is a time detection which is converted into mass.

Different operating modes exist, providing different data depending on whether we are going to favour mass resolution (spectroscopy, depth profile) or lateral resolution (chemical imaging). In this study, the profile mode was mainly used. A ToF-SIMS profile expresses the intensity of a signal (number of counts) as a function of sputtering time (s). It was chosen to work in negative polarity (the secondary ions collected are negative), because it is more sensitive to species originating from oxides.

The ToF-SIMS spectrometer used is a ToF-SIMS V from IONTOF company. The primary source used is a Bi[+] ion source. The ion erosion gun used to erode the surface is a Cs+ ion

gun. The successive use of each beam allows us to make a ToF-SIMS analysis at the bottom of a crater eroded during the sputtering phase of the measurement. Thus, one obtains a complete mass spectrum at each sputtering step and one can build in-depth elemental composition profiles that correspond to the intensity of each secondary ion as a function of the sputtering time.

The first step in processing ToF-SIMS data is the calibration of the mass spectra obtained. Then the profiles can be reconstructed. All data processing is carried out using the commercial software IonSpec©.

### II-3.2. Choice of ions

ToF-SIMS spectrometry is a technique used to obtain chemical information on the surface of a sample. The secondary ions emitted can be single ions or molecules which will be characteristic of the surface of the sample but which do not necessarily account for the nature and chemical composition of the surface of the substrate. In this work, the surface oxides formed on different Cr-containing alloys, including CoCrFeMnNi HEA, 316L SS and 304L SS, have been studied. The characteristic ions for oxide films on different alloys are listed in Table II-1. It should be noticed that secondary ions can have very similar masses (separated by less than 0.0001 uma). Thus, in a mass spectrometry measurement, a single peak can be associated to two overlapping ion signals. For example, it is the case in the re-oxidation experiments performed in this work on SS alloys, where the pre-formed iron oxide signal, $Fe^{16}O_2^-$ (that composes the outer oxide layer) overlaps with the chromium oxide peak, $Cr^{18}O_2^-$, formed during the $^{18}O_2$ re-oxidation. Thus, although it is less intense to the $Fe^{16}O_2^-$ signal, one prefers to use the $Fe_2^{16}O_3^-$ ion as characteristic of the pre-formed iron oxide to avoid the signal overlapping problem.

| Experiments | Samples | Species | Characteristic ion | Remark |
|---|---|---|---|---|
| Surface analysis | CoCrFeMnNi HEA | Chromium oxide | $^{52}CrO_2^-$ | Oxide film |
| | | Iron oxide | $^{56}FeO_2^-$ | |
| | | Manganese oxide | $^{55}MnO_2^-$ | |
| | | Cobalt oxide | $^{59}CoO_2^-$ | |
| | | Metallic Ni | $^{58}Ni_2^-$ | Metallic substrate |
| | | Metallic Fe | $^{56}Fe_2^-$ | |
| | | Metallic Co | $^{59}Co_2^-$ | |
| | | Metallic Mn | $^{55}Mn_2^-$ | |
| Thermal stability | 316L SS | Hydroxide | $(OH)_2^-$ | Oxide film |
| | | Oxide film | $^{18}O^-$ | |
| | | Iron oxide | $^{56}FeO_2^-$ | |
| | | Chromium oxide | $^{53}CrO_2^-$ | |
| | | Molybdenum oxide | $^{98}MoO_3^-$ | |
| | | Metallic Fe | $^{56}Fe_2^-$ | Metallic substrate |
| | | Metallic Ni | $^{58}Ni_2^-$ | |
| | | Metallic Cr | $^{52}Cr_2^-$ | |
| Ion transport mechnisms | 304L SS 316L SS | Oxide/Hydroxide | $^{16}O^-$ / $^{16}OH^-$ | Pre-formed oxide ($^{16}O$) |
| | | Iron oxide | $Fe^{16}O_2^-$ ; $Fe_2^{16}O_3^-$ | |
| | | Chromium oxide | $Cr^{16}O_2^-$ | |
| | | Molybdenum oxide | $Mo^{16}O_3^-$ | (For 316L SS) |
| | | Oxide | $^{18}O^-$ | Newly-formed oxide ($^{18}O$) |
| | | Iron oxide | $Fe^{18}O_2^-$ | |
| | | Chromium oxide | $Cr^{18}O_3^-$ | |
| | | Molybdenum oxide | $Mo^{18}O_3^-$ | (For 316L SS) |
| | | Metallic Fe | $Fe_2^-$ | Metallic substrate |
| | | Metallic Ni | $Ni_2^-$ | |
| | | Metallic Cr | $Cr_2^-$ | |

**Table II-1** Summary of the choice of ions for the analysis of the oxide films formed on Cr-containing alloys by ToF-SIMS

## II-4. X-ray Photoelectron Spectroscopy (XPS)

X-ray photoelectron spectroscopy (XPS) is a technique for determining the surface chemistry of a material. XPS can measure the elemental composition, chemical state and electronic state of the elements at the surface of a material. XPS spectra are obtained by irradiating the solid

surface with a beam of X-rays while simultaneously measuring the kinetic energy and the number of electrons that are emitted from the extreme surface of the material being analyzed. The majority (99.7 %) of photoelectrons will come from a depth of $3\lambda$ ($\lambda$ being the inelastic mean free path) and for most core electrons excited by Al K$\alpha$ X-rays this depth is on the order of a few nm. A photoelectron spectrum is recorded by counting ejected electrons over a range of electron kinetic energies. Peaks appear in the spectrum from atoms emitting electrons of a particular characteristic energy. The energies and intensities of the photoelectron peaks enable identification and quantification of all surface elements (except hydrogen) [2].

### II-4.1. Principles

The phenomenon of XPS is based on the photoelectric effect: the ejection of electrons from a surface due to the impinging of photons as outlined by Einstein in 1905, which was first observed by Hertz in 1887. In the 1950s Kai Siegbahn developed methods for achieving highly accurate measurements of energy levels in atoms by irradiating them with photons and measuring the energy of the electrons emitted using the photoelectric effect. Siegbahn obtained the Nobel Prize for developing the method of X-ray photoelectron spectroscopy (XPS) in 1981.

A typical XPS spectrum is a plot of the number of electrons of electrons detected versus the binding energy of the electrons detected. Each element produces a characteristic set of XPS peaks at characteristic binding energy values that directly identify each element that exists on the surface of the material being analyzed. These characteristic peaks correspond to the electron configuration of the electrons within the atoms, e.g., 1s, 2s, 2p, 3s, etc. The number of detected electrons in each of the characteristic peaks is directly related to the concentration of element within the area emitting the photoelectrons.

To be detected, the electrons have to escape into the vacuum, meaning that they originate from a limited depth of the sample (1-10nm) corresponding to $\sim 3\lambda$, $\lambda$ being the inelastic mean free path the photoelectrons mentioned above ($\lambda$ depends on the kinetic energy of the electrons and the nature of the materials). All of the photoelectrons emitted by deeper regions of the sample cannot escape as they are either recaptured or trapped in various excited states

within the material.

Since the energy of the primary X-ray beam with particular wavelength is known, the electron binding energy of each electrons can be determined (as showed in Fig.II-4) from the measured kinetic energy of the emitted electrons by using the equation:

$$hv = E_{kinetic} + E_{binding} + \emptyset_{sp}$$ (equation II-4)

where hv is the energy of the X-ray photons, $E_{kinetic}$ is the kinetic energy of the electron as measured by the instrument, $E_{binding}$ is the binding energy of the electron and $\emptyset_{sp}$ is the work function of the spectrometer (calibrated for a given spectrometer). A major property of XPS is that the binding energy shift observed by XPS can be related to the chemical state of surface species. The chemical shift is the modification of the energy of the photoelectrons due to the charge on the atom associated to the chemical bond.
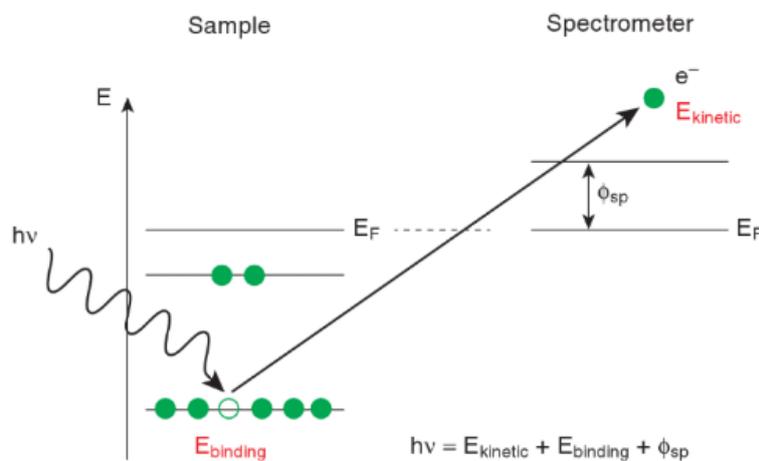


**Fig.II-4** Principle of XPS: the photoelectron energy [1]

Two different types of X-ray sources are used: Mg $K_\alpha$ (*hv* = 1253. 6 eV) and Al $K_\alpha$ (*hv* = 1486:6 eV) which is only used for monochromatic source.

The Auger effect is a physical phenomenon in which the filling of an inner-shell vacancy of an atom is accompanied by the emission of an electron from the same atom. When a core electron is removed, leaving a vacancy, an electron from a higher energy level may fall into the vacancy, resulting in a release of energy. Although most often this energy is released in the form of an emitted photon, the energy can also be transferred to another electron, which is

ejected from the atom; this second ejected electron is called an Auger electron. The energy of this Auger electron is independent of the energy of the incident radiation and has its own kinetic energy. It is therefore possible to qualitatively identify the Auger lines on a general spectrum by changing the energy of the incident photons. These Auger lines can be problematic in our case for the high entropy alloy (see Chapter III, discussion part), as they can be overlap with the core level signals of other species.
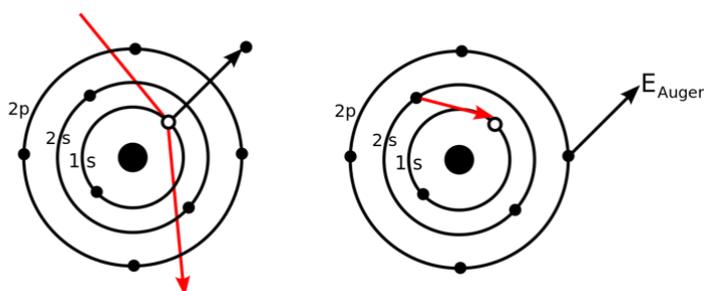


**Fig.II-5** The scheme for Auger process

The chemical composition and oxide thickness calculation will be fully elucidated in the Chapter III.

# Reference

[1] A. Seyeux, S. Zanna, P. Marcus, Surface analysis techniques for investigating biocorrosion, Understanding Biocorrosion: Fundamentals and Applications, (2014) 197.

[2] S. Hofmann, Auger-and X-ray photoelectron spectroscopy in materials science: a user-oriented guide, Springer Science & Business Media, 2012.

# Chapter III

# Study of the surface oxides and corrosion behaviour of an equiatomic CoCrFeMnNi high entropy alloy by XPS and ToF-SIMS

**Abstract**

XPS and ToF-SIMS analysis have been combined with electrochemical measurements to determine the corrosion behavior of the equiatomic CoCrFeMnNi high entropy alloy. An XPS methodology based on analysis of the 3p core level spectra was developed to determine the composition and thickness of oxide films. Both native oxide (~1.4nm) and passive films (~ 1.6nm) formed in acidic medium are duplex, comprising Cr and Mn inner layer and Cr/Fe/Co mixture outer layer. No nickel is observed in the oxide layer. The effects of exposure of the native film to sulfuric acid and passivation under anodic polarization have been investigated.

## III-1. Introduction

Equiatomic high entropy alloys (HEAs), compared to the traditional alloys usually comprising a base metal and alloy elements, are a new class of alloys in which the distinction between major and minor elements is not relevant anymore. Indeed, they are composed of four, five or more metallic elements, in near equimolar concentration [1, 2]. For some compositions, depending mainly on the balance between the entropy of configuration of the solid solution and the enthalpy of mixing of the intermetallic [3, 4], HEAs form a single phase solid solution (without any intermetallic or other secondary phases), such as face-centered cubic (FCC) alloys elaborated from transition metals [5-8] and body-centered cubic (BCC) alloys elaborated from refractory metals [9-12]. The FCC CoCrFeMnNi HEA, which was first discovered by Brian Cantor et al. [13], has received a great deal of research interest due to its

excellent mechanical properties [14-16]. Although this type of HEA has been developed since 2004, very little research focused on the corrosion behaviour of CoCrFeMnNi HEA [17-20].

The CoCrFeNi alloy was reported to have good anti-corrosion properties due to the formation of a protective oxide film rich in Cr species [18]. Generally, for conventional alloys containing chromium, such as stainless steel and Ni-base alloys, a high corrosion resistance is provided by the Cr-rich oxide layer playing the role of a barrier against the attack of aggressive ions from the environment [21-25]. The impact of other elements at high contents (Co and Mn) in the bulk alloys has been rarely studied. Normally, for alloys with high contents of Mn (range from 21 to 28 wt%), the corrosion resistance will decrease caused by the instability of the Mn oxide in the film [26]. The high Co concentration (15%) will also decrease the corrosion resistance of the alloys [27]. The corrosion behavior of CoCrFeNi-based HEAs, including Al, Cu, W, Mo and Ru [28-33], has been studied. Lee et al. [28] investigated the corrosion performance of $Al_xCrFe1.5MnNi0.5(x=0,0.3,0.5)$ HEAs in 1M NaCl solution, and the results demonstrated that the addition of Al to the alloys reduces the resistance to pitting corrosion. The addition of Al in the $Al_xCoCrFeNi(x=0,0.25,0.5,1)$ HEAs had a similar effect in chloride-containing solution, with Al leading to the formation of a porous passive film [29]. The corrosion behaviour of $FeCoNiCrCu_x(x=0,0.5,1)$ HEA was studied in sulfuric acid, and it was suggested that the corrosion resistance of the alloys was deteriorated by the segregation of Cu resulting in galvanic corrosion [31]. The $CoCrFeNiMo_x(x=0.1-0.5at\%)$ HEAs demonstrated good corrosion resistance in Cl-containing solution due to the beneficial effect of Mo [32]. Scully et al. [33] reported excellent passivity for 38Ni-21Cr-20Fe-13Ru-6Mo-2W HEA with the enrichment of Cr (48 at%) and small amount of Mo (8 at%) in the oxide film. Some recent work was focused on the corrosion behavior of CoCrFeMnNi HEA. For example, a comparison between a CoCrFeMnNi HEA and a commercial alloy (Hastelloy® C276) in 3.5wt% NaCl solution has demonstrated an improvement of the corrosion resistance properties for the HEA [34]. A similar comparison with a 304 stainless steel in sulfuric acid solution, showing relatively low anti-corrosion performance of the HEA, could be explained by a lower content of Cr oxide and large quantity of hydroxide in the passive film. Characterization of oxidized CoCrFeMnNi HEA in air from 500 to 900°C showed the dependence of the oxide film composition on oxidation temperature. The oxide film is mainly composed of $Mn_2O_3$ with a thin inner Cr oxide at temperatures lower than 800°C, while at 900°C, the oxide film was composed of $Mn_3O_4$ [35]. However, up to now, there is a limited number of investigations of the corrosion behavior of

CoCrFeMnNi HEA related to modification of composition and structure of the surface oxide films.

In this paper, we investigate the corrosion behavior of an equimolar CoCrFeMnNi high entropy alloy using electrochemical measurements coupled with advanced surface characterization techniques, including Time-of-Flight Secondary Ions Mass Spectrometry (ToF-SIMS) and X-ray Photoelectron Spectroscopy (XPS). Particularly, the composition of the surface oxide layers (native oxide and passive films) was determined using a new XPS approach based on the peak fitting of the 3p photopeaks.

## III-2. Experimental

### III-2.1 Sample preparation

Pure Fe, Co, Cr, Ni and Mn ingots (purity exceeding 99.9 wt%) were used to prepare the HEA by high frequency electromagnetic induction melting in a water-cooled copper crucible under He atmosphere. Before melting, samples were prepared by mechanical polishing of raw materials. Afterwards, the ingot was shaped into a rod with a diameter of 13 mm and a length of around 8 cm by gravity casting. The cooling rate was estimated to be about $10^3$ $K.s^{-1}$. Finally, the samples were wrapped into a tantalum sheet, and were annealed at 1373 K during 13h under a He atmosphere to limit oxidation. At the end of the annealing, the samples were air quenched. The objective of this homogenization annealing is to eliminate the dendritic microstructure formed during casting process. To refine the grain size, HEA samples were rolled and then annealed at a temperature of 900°C for 30min under a He atmosphere, followed by air quenching. The average grain size of the HEA is ~ 30µm. Table III-1 presents the measured chemical composition of the HEA in atomic percentage (measured by scanning electron microscopy coupled with Energy-dispersive X-ray spectroscopy (EDX)). As shown in previous papers [6, 36], the obtained CoCrFeMnNi is a face centered cubic solid solution, which is representative of the high temperature (i.e.: 1373 K) stable state.

| Elements | Fe | Co | Ni | Cr | Mn |
|----------|------|-----|------|------|-----|
| at.% | 19.8 | 20 | 19.9 | 20.3 | 20 |

**Table III-1** Chemical composition of the CoCrFeMnNi alloy obtained by EDX

The samples were ground with SiC paper from 320 up to 2400 grit, and then polished with 6µm, 3µm, 1µm and 0.25µm diamond suspension until a mirror like finish is obtained. They were then cleaned in ultrasonic baths of acetone, ethanol and ultra-pure water for 10 mins, and

dried in compressed air. The sample surfaces were mechanically polished before each electrochemical experiment.

### III-2.2. Electrochemical measurements

A three-electrode cell comprising a saturated calomel reference electrode (SCE, +0.245V/NHE), a Pt wire as the counter electrode and a HEA sample as a working electrode (area 1.3 cm$^2$ delimited by a Viton O ring) was used. The electrochemical measurements were carried out at room temperature in 0.05 M $H_2SO_4$ (aq) prepared with ultra-pure water (Millipore, resistivity 18.5Mohm.cm) pre-deaerated by Ar bubbling for 30 min. An EC_Lab SP200 potentiostat from Bio-Logic was used. Before the potentiodynamic and potentiostatic tests, the open circuit potential (OCP) was monitored for 30 min, corresponding to the stabilization time of the potential. The potentiodynamic polarization tests were performed at a potential scan rate of 1 mV.s$^{-1}$, and the potential range was from -800mV/SCE to 1200mV/SCE. The potentiostatic tests were carried out at 200mV/SCE, 400mV/SCE and 600mV/SCE.

### III-2.3. Surface characterization

Surface analysis was performed by a combination of X-Ray Photoelectron Spectroscopy (XPS), and Time-of-Flight Secondary Ions Mass Spectrometry (ToF-SIMS).

X-ray Photoelectron Spectroscopy (XPS) analysis was performed using a Thermo Electron Escalab 250 spectrometer, with a monochromatic Al Kα X-ray source (hv=1486.6eV) operating at a pressure around 10$^{-9}$ mbar. The analyzer pass energy was 50eV for survey spectra and 20 eV for high resolution spectra. Beforehand the spectrometer was calibrated using Au4f7/2 at 84.1eV. Spectra were recorded and analyzed using Thermo Avantage software (Version 5.956).

Elemental depth profiles were obtained using a ToF-SIMS 5 spectrometer (IONTOF GmbH). The spectrometer was run at an operating pressure of 10$^{-9}$ mbar. A pulsed 25 keV Bi$^+$ primary ion source was employed for analysis, delivering a current of 1.2 pA over a 100 × 100 μm$^2$ area. Depth profiling was carried out by interlacing static analysis with sputtering using a 0.5 keV Cs$^+$ sputter beam giving a 17 nA target current over a 300×300 μm$^2$ area.

# III-3. Results

## III-3.1. The native oxide film

(a)



(b)



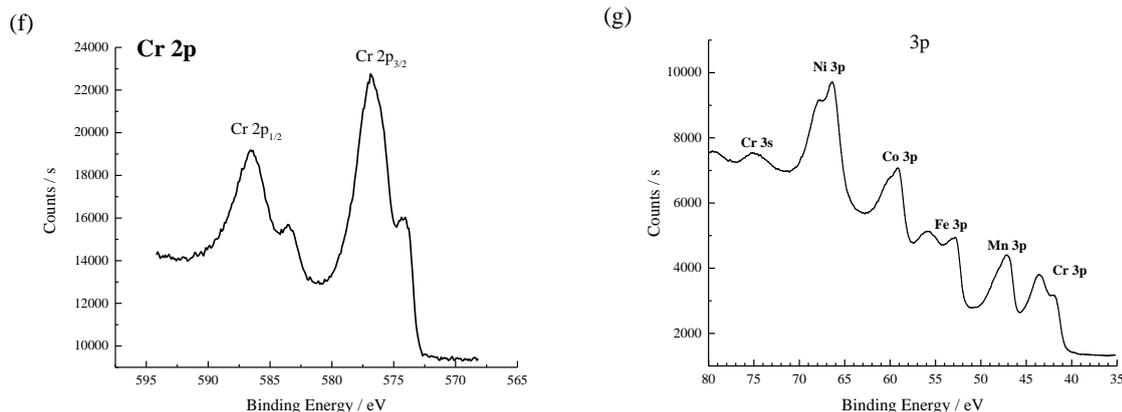(c)



(d)



(e)
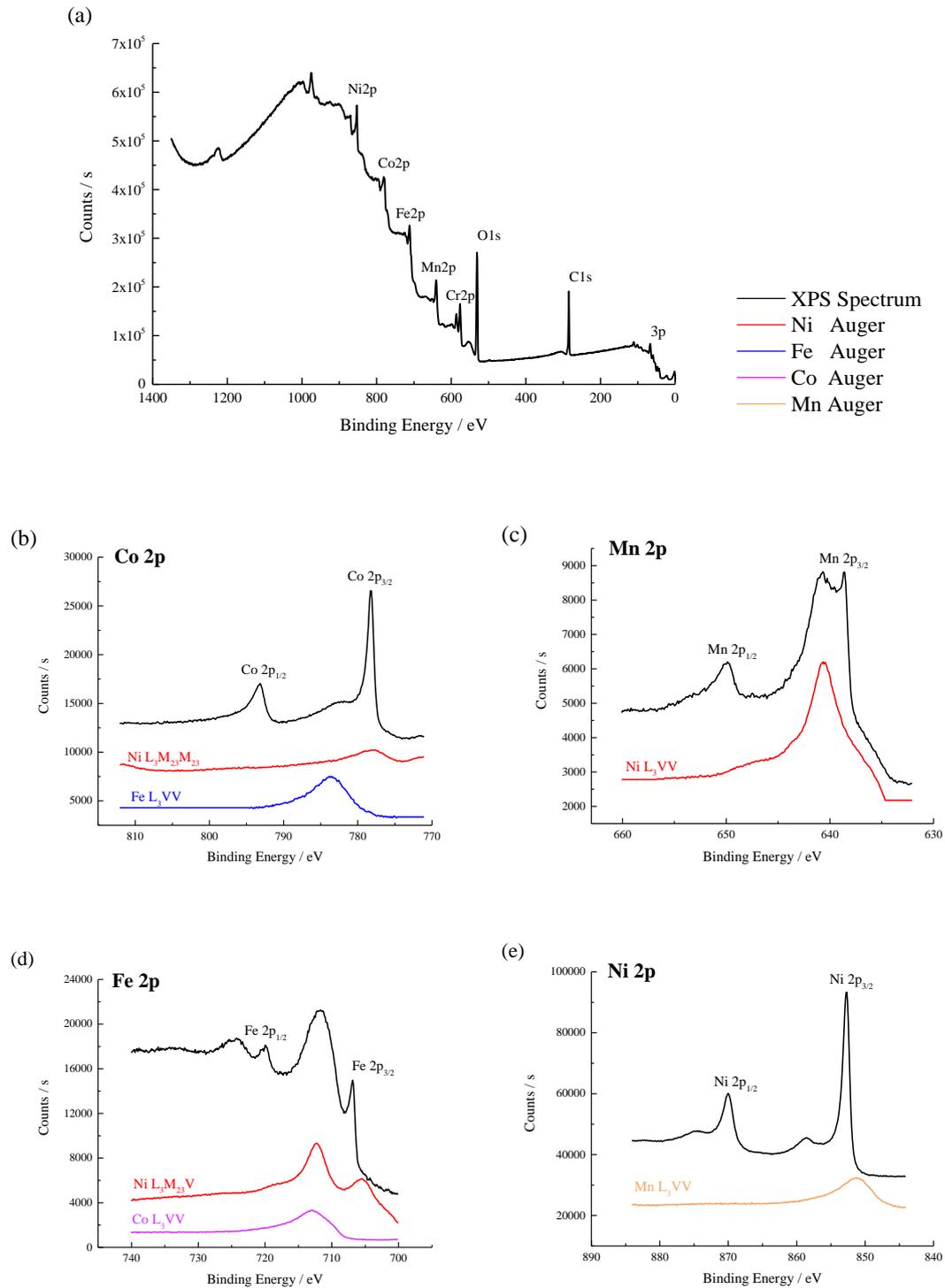
**Fig.III-1** High resolution XPS **(a)** survey spectrum, **(b)-(f)** 2p core level spectra and **(g)** 3p core level spectrum recorded for the native oxide film formed on the HEA and Auger transitions of pure elements constituting the CoCrFeMnNi alloy

X-Ray Photoelectron Spectroscopy (XPS) is an appropriate method to investigate the composition of nanometer-thick surface oxide films [21, 22, 37-40]. Generally, for alloys containing Fe, Cr, Ni, Co and Mn, the 2p core level peaks are recorded with high resolution and many references are available to study the chemical states of the analyzed elements [41-46]. However, for the CoCrFeMnNi HEA with five elements in equiatomic ratios, new challenges appear to analyse the XPS data due to the interference of the Auger transitions which overlap with 2p peaks of the main elements in the alloy.

The characteristic high resolution XPS 2p core level spectra obtained for a native oxide film formed on the equiatomic CoCrFeMnNi HEA are presented on Fig.III-1(b)-(f). For each spectrum, the Auger transitions of constituting elements of the HEA have been added. It is observed that using the Al Kα X-ray source all photopeaks overlap with Auger transitions except the Cr $2p_{3/2}$ peak (Co$2p_{3/2}$ / NiL$_3$M$_{23}$M$_{23}$ and FeL$_3$VV, Mn$2p_{3/2}$ / NiL$_3$VV, Fe$2p_{3/2}$ / NiL$_3$M$_{23}$V and CoL$_3$VV, Ni$2p_{3/2}$ / MnL$_3$VV). An Mg Kα X ray source could be used, but overlap with Auger transitions (Fe$2p_{3/2}$ / Mn L$_3$M$_{23}$M$_{23}$) still exist making quantification difficult.

Thus, another approach based on the 3p core level peaks (Fig.III-1(g)) was developed to characterize the HEA surfaces. Although the sensitivity of 3p peaks is lower than for 2p peaks, the 3p spectra do not present overlapping with Auger peaks and the narrow energy range for the analyzed elements allows probing the same thickness for all elements.

To develop this new approach, a new database for 3p core level spectra must be established.

|  |  | BE (eV) | FWHM (eV) | L/G Mix (%) | Tail Mix (%) | Tail Height (%) | Tail Exponent |
| --- | --- | --- | --- | --- | --- | --- | --- |
| Metal | Cr3p$_{(met)}$ | 41.62 | 1.21 | 30.26 | 0.01 | 0.15 | 0.0929 |
|  | Mn3p$_{(met)}$ | 46.78 | 1.09 | 37.8 | 0 | 0.02 | 0.0926 |
|  | Fe3p$_{(met)}$ | 52.65 | 0.96 | 10.9 | 0.33 | 99.97 | 0.0545 |
|  | Co3p$_{(met)}$ | 58.94 | 1.26 | 85.89 | 8.63 | 0 | 0.0431 |
|  | Ni3p$_{3/2(met)}$ | 66.25 | 2.06 | 86.31 | 79.96 | 0.13 | 6.1493 |
|  | Ni3p$_{1/2(met)}$ | 68.1 | 2.06 | 86.31 | 79.96 | 0.13 | 6.1493 |
| Oxide | Cr3p$_{(ox)}$ | 43.72 | 2.4 | 30 | 100 | 0 | 0 |
|  | Cr3p$_{(hyd)}$ | 44.45 | 2.4 | 30 | 100 | 0 | 0 |
|  | Mn3p$_{(ox)}$ | 48.09 | 2.4 | 30 | 100 | 0 | 0 |
|  | Fe3p$_{(ox)}$ | 54.73 | 2.9 | 30 | 100 | 0 | 0 |
|  | Co3p$_{(ox)}$ | 59.74 | 2.2 | 30 | 100 | 0 | 0 |

**Table III-2** The parameters for fitting the XPS 3p spectra of the pure metals and oxides

Firstly, the standard 3p core level peaks for the pure metals were recorded using pure metals from batches used to manufacture the CoCrFeMnNi HEA. These pure metal samples were polished with 2400 grit SiC paper, and then introduced into the XPS analysis chamber. Samples were sputtered using an Ar$^+$ ion beam to remove surface oxides and contaminants

and obtain metallic surfaces. High resolution XPS 3p core level spectra were recorded and curve fitted using the Thermo Electron software Avantage with an iterative Shirley-type background subtraction. All the parameters, including binding energy (BE), full width at half maximum (FWHM), Gaussian-Lorentzian (GL) ratio and asymmetry factor, were automatically adjusted by the software to best fit the peaks of pure metals. An asymmetric function was necessary for the peak fitting of metal peaks, as expected for transition metals (owing to the conduction electron scattering amplitude for inter-band absorption or emission in metals, at the Fermi level[47, 48]). The detailed parameters for fitting the 3p peaks of pure metals are shown in Table III-2. For Ni 3p, a splitting of the metallic component is observed (spin orbit coupling is due to the coupling between the electron spin momentum and its orbital angular momentum). Generally, this effect is visible for p, d and f core levels but spectral resolution can limit this splitting. It is the case here for the 3p orbitals of Cr, Mn, Fe and Co.

A similar approach based on the decomposition of the native oxide covering the pure metals has also been used. For components characteristic of the oxide layer, a Lorentzian/Gaussian peak shape with a fixed ratio of 30/70 was used. The detailed parameters for fitting the 3p peaks of oxides are shown in Table III-2.

The spectrum (35-75eV) characteristic of the 3p peaks of Cr, Mn, Fe, Co and Ni, and the peak fitting for a native oxide film formed on CoCrFeMnNi HEA surface are presented in Fig.III-2(a). This decomposition has been carried out by introducing the fit parameters determined previously for each element (metal state and oxide state) (Table III-2).

The Cr 3p core level spectrum is fitted with three peaks, corresponding to metallic $Cr_{met}$ (BE=41.6±0.1eV), oxide $Cr_{ox}$ (BE=43.7±0.1eV) and hydroxide $Cr_{hyd}$ (BE=44.4±0.1eV) chemical states. As previously indicated, the absence of overlap between the Cr $2p_{3/2}$ core level spectrum and Auger transitions of other metals makes it possible to decompose the Cr $2p_{3/2}$ photopeak and compare the decomposition of the Cr 3p core level. Fig.III-Fi2(b) shows the fitting of Cr $2p_{3/2}$ core level spectrum. The Cr $2p_{3/2}$ spectrum is fitted by three components characteristic of metallic $Cr_{met}$ (BE=573.9±0.1eV, FWHM=1.25eV), hydroxide $Cr_{hyd}$ (BE=577.1±0.1eV, FWHM=2.55eV) and oxide, which is represented by five peaks, based on the peak fitting method proposed by Biesinger [41], $Cr_{ox}$ (BE=575.7±0.1eV, 576.6±0.1eV, 577.4±0.1eV, 578.4±0.1eV and 579±0.1eV, FWHM=1.05eV). In our work, the area ratio between the 5 components of decomposed Cr $2p_{3/2ox}$ (chromium oxide) has been determined and considered as fixed for all analysed surfaces.
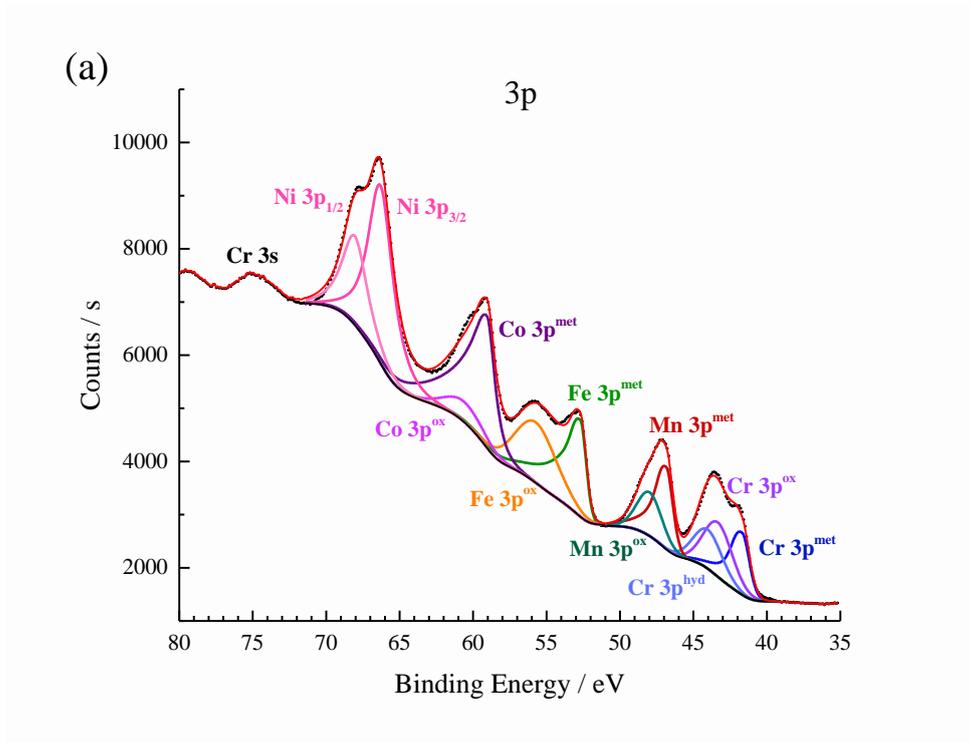
**Fig.III-2** XPS core level spectra for the native oxide film formed on the HEA:**(a)** Cr 3p, Mn 3p, Fe 3p, Co 3p, Ni 3p and **(b)** Cr $2p_{3/2}$. The black dots represent the experimental spectra and the colored lines show the peak fitting.

The Co 3p, Fe 3p and Mn 3p spectra show two components representing the metallic states $Co_{met}$ (BE=58.9±0.1eV), $Fe_{met}$ (BE=52.7±0.1eV) and $Mn_{met}$ (BE=46.8±0.1eV), and the oxide states $Co_{ox}$ (BE=59.7±0.1eV), $Fe_{ox}$ (BE=54.7±0.1eV) and $Mn_{ox}$ (BE=48.1±0.1eV). The decomposition of Ni 3p into two components, Ni $3p_{3/2}$ at 66.3eV and Ni $3p_{1/2}$ at 68.1eV only

shows the presence of metallic nickel underneath the oxide layer. No oxidized nickel is observed in the surface oxide layer.

To calculate the thickness of the oxide film and the chemical composition of the film and the modified alloy layer under the oxide, a model consisting in a homogeneous and continuous oxide layer on the sample surface, comprising $Fe_{ox}$, $Cr_{ox/hyd}$, $Mn_{ox}$ and $Co_{ox}$, and a modified alloy layer with $Fe_{met}$, $Cr_{met}$, $Mn_{met}$, $Co_{met}$ and $Ni_{met}$ was assumed. Based on this model, the following 11 equations with 11 unknowns ($k$, $d_{oxide}$, $D_{Cr}^{Met}$, $D_{Mn}^{Met}$, $D_{Fe}^{Met}$, $D_{Co}^{Met}$, $D_{Ni}^{Met}$, $D_{Cr}^{Ox}$, $D_{Mn}^{Ox}$, $D_{Fe}^{Ox}$, $D_{Co}^{Ox}$) was used :

$$I_X^{Met} = k\sigma_X \lambda_X^{Met} D_X^{Met} T_X \exp(-\frac{d_{oxide}}{\lambda_X^{Ox}}), \text{ with X=Cr, Mn, Fe, Co and Ni} \qquad \text{(equation III-1)}$$

$$I_Z^{Ox} = k\sigma_Z \lambda_Z^{Ox} D_Z^{Ox} T_Z \left[1 - \exp(-\frac{d_{oxide}}{\lambda_Z^{Ox}})\right], \text{ with Z=Cr, Mn, Fe and Co} \qquad \text{(equation III-1)}$$

$$D_{Cr}^{Met} + D_{Mn}^{Met} + D_{Fe}^{Met} + D_{Co}^{Met} + D_{Ni}^{Met} = D^{Met} \qquad \text{(equation III-3)}$$

$$D_{Cr}^{Ox} + D_{Mn}^{Ox} + D_{Fe}^{Ox} + D_{Co}^{Ox} = D^{Ox} \qquad \text{(equation III-4)}$$

with $I_X^Y$ the intensity of photoelectrons (cps eV) emitted by the considered core level X in the matrix Y, $k$ a constant characteristic of the spectrometer, $\sigma_X$ the photoionization cross-section of the considered core level X, $\lambda_X^Y$ the inelastic mean free path of photoelectrons emitted by the considered core level X in the matrix Y(in nm), $T_X$ the transmission function of the analyse for the considered core level X, $d_{oxide}$ the thickness of the oxide layer (nm) and $D_X^Y$ the density of the element X in the matrix Y (mol.cm$^{-3}$) defined by $D_X^Y = \frac{\rho_Y}{M_Y} \times x_X^Y$ with $\rho_Y$ the density of the matrix Y (g.cm$^{-3}$), $M_Y$ the molar mass of the matrix Y (g.mol$^{-1}$) and $x_X^Y$ the atomic percentage of the element X in the matrix Y. The $\rho_{Met}$ value is 8 g.cm$^{-3}$ [49, 50]. The $\rho_{Ox}$ value is taken as 5.22 g.cm$^{-3}$, which is the density of chromium oxide, as it is shown later that the surface oxide layer is enriched in Cr(III). The density of $Fe_2O_3$ would be similar (5.24 g.cm$^{-3}$). The values of the photoionization cross-sections ($\sigma_X$) at 1486.6 eV are taken from Scofield [51] and the inelastic mean free paths ($\lambda_X^Y$) calculated by the TPP2 formula [52] are compiled in the Table III-3.

| Core level | Cr 3p | Mn 3p | Fe 3p | Co 3p | Ni 3p |
|---|---|---|---|---|---|
| $\sigma_X$ | 1.173 | 1.423 | 1.669 | 1.93 | 2.217 |
| $\lambda_X^{oxide}$ (nm) | 2.6 | 2.6 | 2.59 | 2.58 | 2.57 |
| $\lambda_X^{metal}$ (nm) | 2.14 | 2.14 | 2.14 | 2.14 | 2.14 |

**Table III-3** Values of the photoionization cross-section ($\sigma_X$) and inelastic mean free paths ($\lambda_X^Y$) used for XPS quantification

Using the intensities of the 3p peaks obtained after peak fitting and equations (1) to (4), the thickness of the oxide layer as well as the elemental compositions of the oxide layer and of the modified layer under the oxide (alloy/oxide interface) are determined. The results are reported in Table III-4.

The thickness for the native oxide film is estimated at 1.4 nm. The native oxide film presents a strong enrichment of chromium (46.3 at%, including 26.5 at% of oxide and 19.8 at% of hydroxide) and iron (30.3 at%) while a depletion of Co (8.2 at%) is clearly observed. No nickel oxide is detected by XPS in the oxide layer.

In the modified metallic alloy layer under the native oxide, a depletion of metallic Cr (11.7 at%), Mn (12.5 at%) and Fe (17.1 at%) is observed, while the concentration of metallic Ni (33.8 at%) and Co (24.9 at%) are significantly higher than in the bulk. The chromium depletion zone in the modified alloy layer is correlated to the enrichment of chromium oxide in the oxide film. The chromium enrichment in the oxide is due to the higher oxygen affinity to Cr [53] (standard free energy of formation for chromium oxide ($\Delta G_{298.15k}°$) is -1058.067 kJ/mol [54], i.e more negative than for the other alloy elements). A Cr depleted-zone in the alloy beneath the oxide film appears due to slow diffusion in the alloy matrix at room temperature [55, 56].

| | Thickness(nm) | Oxide composition(Atomic%) | | | | | Modified alloy composition(Atomic%) | | | | |
|---|---|---|---|---|---|---|---|---|---|---|---|
| | | $Cr_{(ox)}$ | $Cr_{(hyd)}$ | $Mn_{(ox)}$ | $Fe_{(ox)}$ | $Co_{(ox)}$ | $Cr_{(met)}$ | $Mn_{(met)}$ | $Fe_{(met)}$ | $Co_{(met)}$ | $Ni_{(met)}$ |
| Native oxide | 1.4 | 26.5 | 19.8 | 15.2 | 30.3 | 8.2 | 11.7 | 12.5 | 17.1 | 24.9 | 33.8 |
| OCP 1min | 1.4 | 30.4 | 26.0 | 18.5 | 13.9 | 11.2 | 15.6 | 12.4 | 17.8 | 19.5 | 34.7 |
| OCP 30min | 1.8 | 36.5 | 31.4 | 19.0 | 8.7 | 4.5 | 16.6 | 15.0 | 16.9 | 21.3 | 30.2 |
| OCP 60min | 2 | 36.2 | 32.9 | 16.7 | 8.0 | 6.2 | 16.8 | 16.3 | 17.9 | 17.6 | 31.5 |
| Passivation 200mV | 1.6 | 48.8 | 13.8 | 18.1 | 14.2 | 5.2 | 16.2 | 15.3 | 18.2 | 21.3 | 29.1 |
| Passivation 400mV | 1.7 | 53.4 | 11.8 | 13.1 | 16.4 | 5.4 | 16.8 | 15.4 | 18.0 | 20.6 | 29.1 |
| Passivation 600mV | 1.6 | 49.2 | 19.7 | 14.4 | 12.2 | 4.6 | 16.3 | 14.9 | 18.4 | 20.7 | 29.8 |
| Passivation(400mV) 10μA | 1.6 | 35.5 | 32.2 | 11.0 | 16.4 | 5.0 | 16.8 | 16.6 | 17.3 | 21.0 | 28.4 |
| Passivation(400mV) 1μA | 1.6 | 48.7 | 19.2 | 12.9 | 14.0 | 5.2 | 16.5 | 15.7 | 18.1 | 21.0 | 28.7 |
| Passivation(400mV) 0.1μA | 1.7 | 53.4 | 11.8 | 13.1 | 16.4 | 5.4 | 16.8 | 15.4 | 18.0 | 20.6 | 29.1 |

**Table III-4** Thickness and chemical composition of the native oxide, the oxide after exposure to acidic solution at the open circuit potential (OCP) and passive films formed in 0.05M $H_2SO_4$ on equiatomic CoCrFeMnNi HEA surface

Fig.III-3 shows the ToF-SIMS negative ion depth profiles for the native oxide film formed on the surface of the HEA sample. The intensity is plotted in logarithmic scale versus sputtering time. The $^{84}CrO_2^-$ ion profile is used to define the oxide film region (ending at 84% of the maximum intensity in the depth profile) since the chromium oxide is located throughout the oxide film region, and the $^{112}Fe_2^-$ ion profile is used to define the metallic region (starting at beginning of the intensity plateau). Thus, an intermediate region is determined from 35s to 70s of sputtering. The colour dashed lines mark the limits between the oxide film, modified alloy layer and metallic substrate.
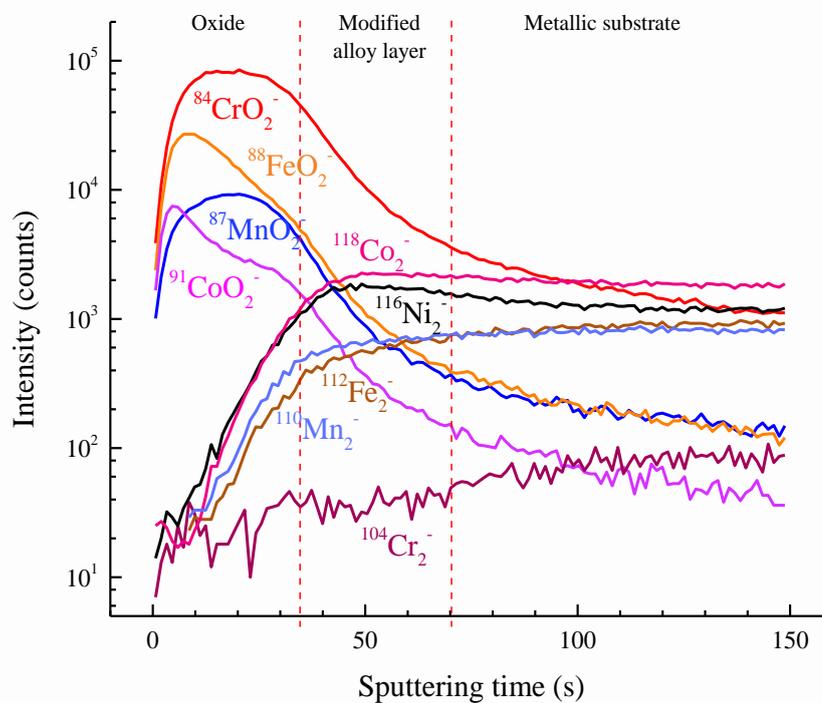


**Fig.III-3** ToF-SIMS depth profiles for the native oxide film formed on the HEA

In the oxide region, one observes that the $^{88}FeO_2^-$ profile peaks in the outer part of the oxide film region and decreases slowly through the oxide. Oxidized iron is therefore mainly located in the outer part of the film, although its presence in small amount in the inner oxide cannot be excluded. The $^{91}CoO_2^-$ profile also has its maximum in the outer region of the oxide film, indicating that the cobalt oxide is mainly located in the outer oxide. Furthermore, $^{91}CoO_2^-$ appears to peak before the maximum intensity of the $^{88}FeO_2^-$ signals, indicating that Co oxide is the main species at the surface. The $^{84}CrO_2^-$ profile exhibits a wide peak throughout the whole region of the film. Oxidized chromium is thus distributed in the whole film. Finally, the

$^{87}MnO_2^-$ profile has its maximum in the inner region of the oxide film (around 20s of sputtering time), indicating that manganese oxide is preferentially located in the inner oxide film region. The $^{90}NiO_2^-$ ion is not plotted in Fig.III-3, since its intensity is extremely low compared to those of $^{84}CrO_2^-$, $^{88}FeO_2^-$, $^{91}CoO_2^-$ and $^{87}MnO_2^-$ ions. It means that Ni oxide is present only at trace level in the oxide film.

Focussing on the intermediate region, one can see that it is characterised by increasing intensities of the signals of the metallic compounds ($^{112}Fe_2^-$, $^{110}Mn_2^-$, $^{116}Ni_2^-$ and $^{118}Co_2^-$) and a fast decrease of the intensity of the signals characteristic of the oxides, i.e. $MO_2^-$ (with M=Cr, Fe, Mn, Co), making the passage of the oxide/alloy interface. The alloy region under the oxide is enriched in Ni and Co, as indicated by the hump in the $Ni_2^-$ and $Co_2^-$ signals. The $^{104}Cr_2^-$ profile shows very low intensity due to low secondary emission yield.

From ToF-SIMS observations, it is thus possible to establish the presence of a duplex oxide structure composed of chromium, iron and cobalt oxides in the outer layer and chromium and manganese oxides in the inner layer. Under this duplex oxide film, near the metal/oxide interface, there is a modified alloy layer, enriched in Ni and Co. The alloy substrate can be located for sputtering times over 70s.

### III-3.2. Surface oxide film after exposure to acidic aqueous solution at the open circuit potential
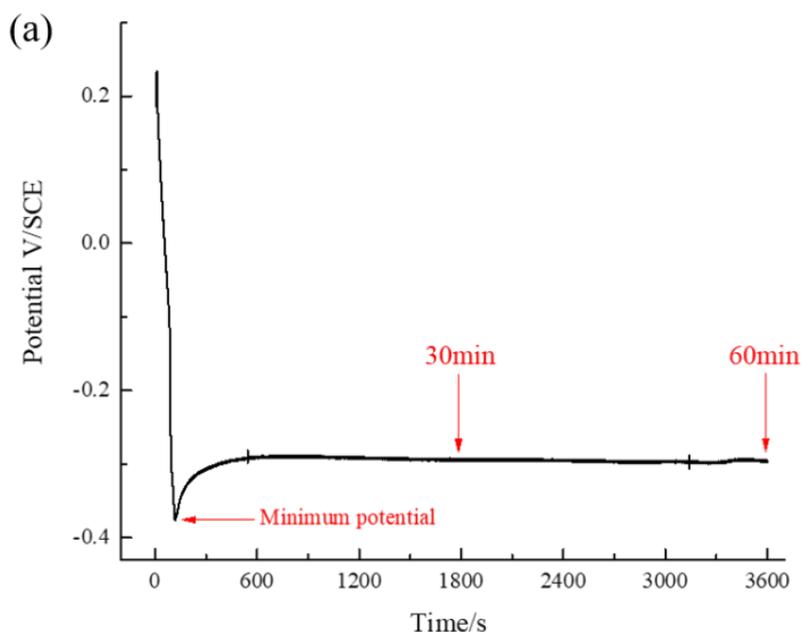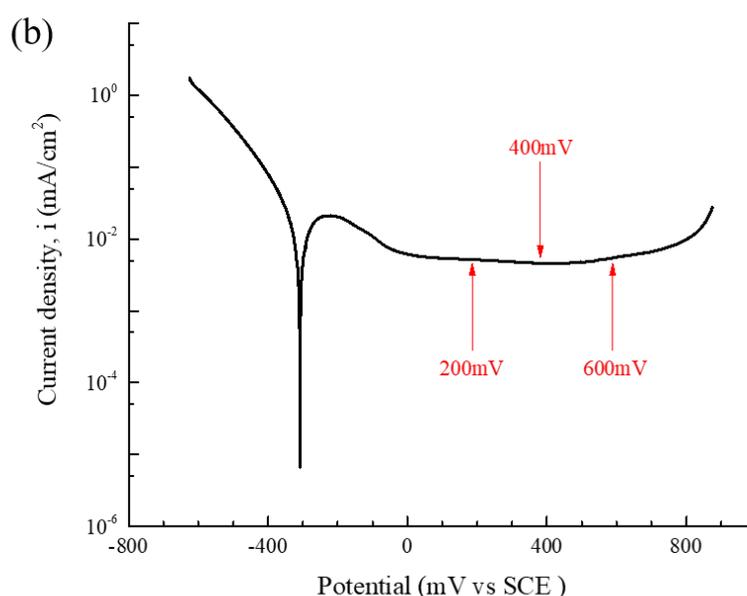
**Fig.III-4 (a)** Open circuit potential evolution for the CoCrFeMnNi HEA with a native oxide film in 0.05M $H_2SO_4$ and **(b)** Potentiodynamic polarization curve of the CoCrFeMnNi HEA in 0.05M $H_2SO_4$ (scan rate of 1mV/s)

The evolution of the open circuit potential (OCP) for the CoCrFeMnNi HEA with a native oxide film in 0.05M $H_2SO_4$ electrolyte is presented in Fig.III-4(a). The potential exhibits a sharp decrease and reaches its minimum value after ~1min of immersion, suggesting some dissolution of the native film. Then the potential increases slightly to reach a stabilisation plateau after 600s. In order to determine the chemical changes at the surface during immersion at OCP, surfaces immersed for 1min (minimum potential), 30 and 60 min were analysed by XPS and ToF-SIMS. The XPS data are compiled in Table III-4 and ToF-SIMS profiles are presented on Fig.III-5.

Fig.III-5 shows ToF-SIMS depth profiles obtained on HEA samples after exposure to acidic aqueous solution at the OCP. The general behaviour is similar to the one observed on the native oxide. Fe and Co oxides are located in the outer layer while Mn oxide is in the inner layer. Cr oxide is distributed in the whole film. The maximum intensity of $^{88}FeO_2^-$ strongly decreases with increasing immersion time (compared to the native oxide) indicating a decrease of the iron content in the outer oxide.

The sputtering time associated to the thickness of the oxide layer is increasing from 60s to 90s for 1min and 60min immersion in acidic aqueous solution at OCP, meaning that the thickness of the oxide film is increasing with prolonged immersion time, which is in agreement with
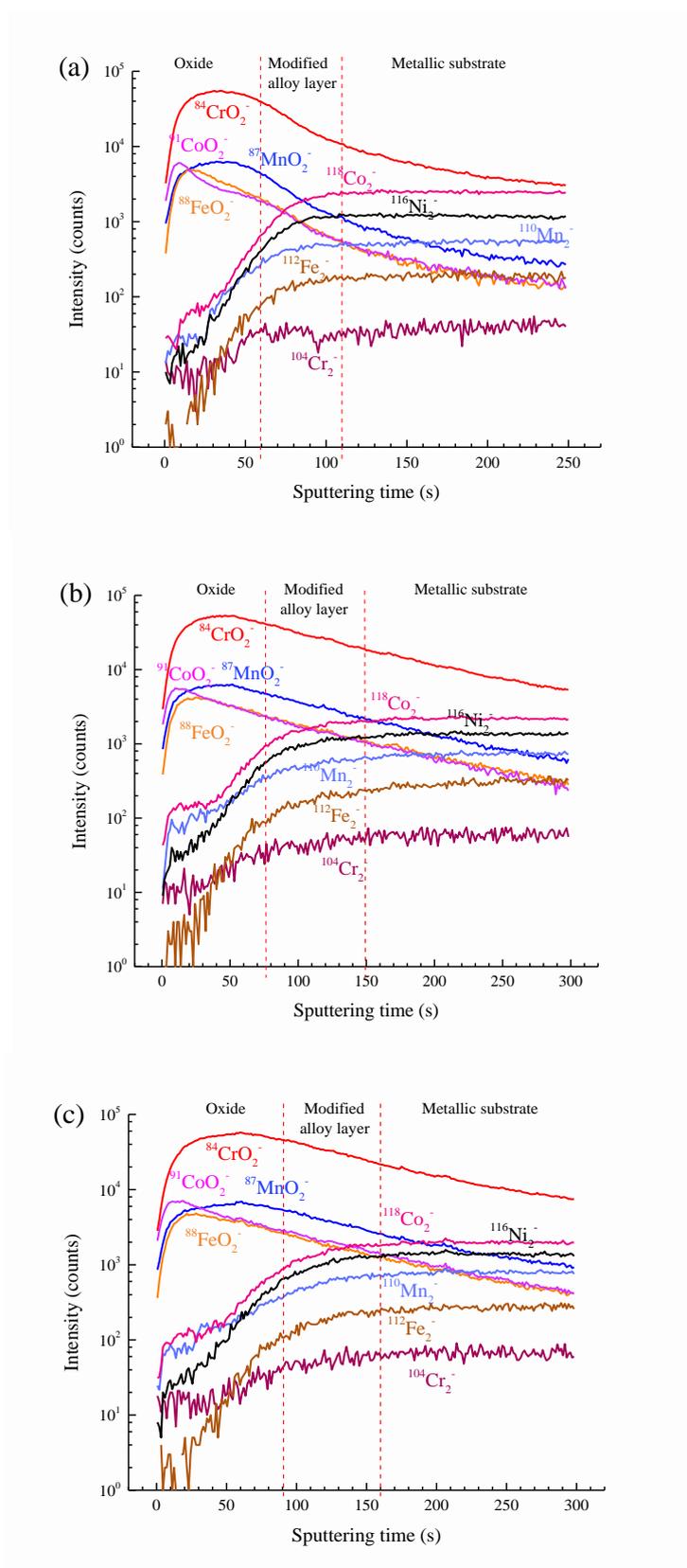
XPS data (1.4 and 2 nm, respectively).



**Fig.III-5** ToF-SIMS depth profiles for the HEA with a native oxide film after exposure to 0.05M $H_2SO_4$ at OCP for **(a)** 1min, **(b)** 30min and **(c)** 60min

The immersion time in sulfuric acid has also an effect on the shape of the oxide depth profiles. For all characteristic ions of the oxides, a slow decrease of the signal is observed in the metallic substrate region. This indicates a roughening of the metal/oxide interface.

The chemical composition and thickness of the film and modified alloy layer for different immersion times in 0.05M $H_2SO_4$ are reported in Table III-4. Although the thickness of the film after 1 minute of immersion is similar to the one of the native oxide layer, the chemical composition is strongly modified. A sharp decrease of iron content is observed (13.9 at% compared to 30.3 at% for the native oxide), which can be explained by the dissolution of iron oxide during the immersion in acidic solution. The content of chromium compounds, and particularly the chromium hydroxide, increases strongly (26.0 at% as compared to 19.8 at% for the native oxide). For increasing immersion time at the open circuit potential, the amount of iron in the oxide layer continues to decrease until it becomes stationary (8.7 at% after 30min and 8.0 at% after 1h), and the amount of chromium in the oxide film continues to increase until it becomes stationary (Cr oxide: 36.5 at% for 30min and 36.2 at% after 1h; Cr hydroxide: 31.4 at% for 30min and 32.9 at% after 1h). During the immersion, the amounts of cobalt and manganese oxides remain nearly constant. Nickel oxide is not detected. A thickening of the oxide layer is observed during the immersion.

### III-3.3. Passivity of the HEA alloy

To further understand the reactivity of the CoCrFeMnNi HEA surfaces, different passive layers have been elaborated by chronoamperometry in 0.05M $H_2SO_4$. The experimental parameters for the formation of passive layers have been determined from potentiodynamic polarization curves in 0.05M $H_2SO_4$ solution, presented in Fig.III-4(b) for a scan rate of 1 mV.s$^{-1}$. In the anodic region, the HEA shows an anodic current peak at -250mV/SCE caused by active dissolution, then a wide passive range from 0mV/SCE to 800mV/SCE. The lowest current density is observed at 400 mV/SCE. To investigate the passive state of the HEA, it was maintained in 0.05M $H_2SO_4$(aq) at a passive potential until current went down to 0.1µA/cm² for three different passive potentials (200 mV, 400 mV and 600 mV). The passive film and the alloy underneath the film were subsequently analysed by XPS, and the XPS 3p core level spectra for the passive films formed on the HEA for three different passive potentials are shown in Fig.III-6.
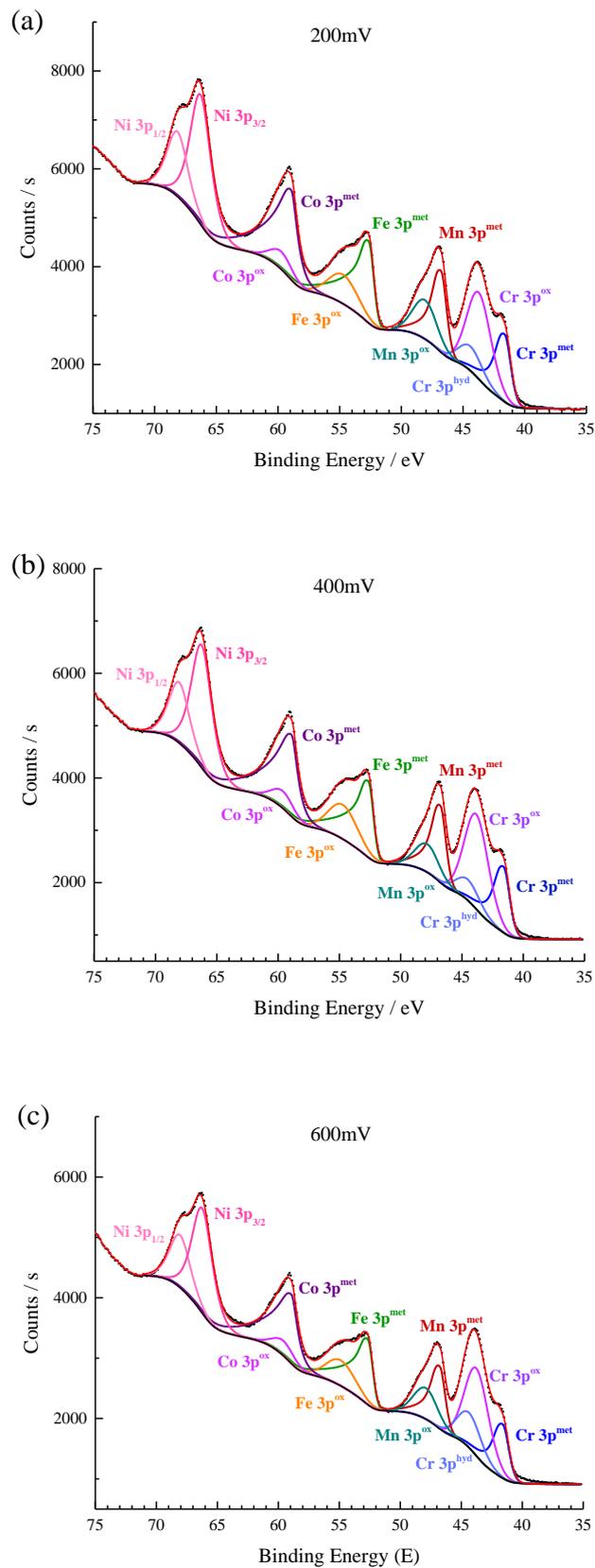
**Fig.III-6** XPS 3p core level spectra for the passive films formed on the HEA at three different passive potentials:**(a)** 200 mV, **(b)** 400 mV and **(c)** 600 mV

The results of composition and thickness of the passive films, obtained from the XPS 3p core level spectra, are reported in Table III-4. The thickness of the passive films is found to be 1.6 nm after passivation at 200 mV and 600 mV, and 1.7 nm at 400 mV. Thus, the passivation potential has no significant effect on the thickness of the film. In the passive film a chromium enrichment is always observed compared to the native oxide. This enrichment is mainly reflected in a strong increase of the chromium oxide (48.8 at% at 200 mV, 53.4 at% at 400 mV and 49.2 at% at 600 mV compared to 26.5 at% for the native oxide) while chromium hydroxide is in average slightly lower (13.8 at% at 200 mV, 11.8 at% at 400 mV and 19.7 at% at 600 mV) than in the native oxide (19.8 at%). The amounts of Mn and Co measured in the passive film are similar to those measured in the native oxide. The iron content shows a strong decrease, which was also observed at the OCP, assigned to a selective dissolution of iron oxide.

The Cr, Mn and Fe contents in the modified alloy layer under the passive film are found to be around 16 at%, 15 at% and 18 at%, respectively. This shows a slight depletion of Cr, Mn and Fe in the modified alloy layer compared to the contents in the bulk. The concentrations of Co in the modified alloy region are found to be around 20 at%, i.e. similar to the Co bulk content. The Ni contents in the modified alloy layer reach 29 at%, revealing a strong Ni enrichment under the oxide compared to the bulk (20 at%). The composition of the modified alloy layer under the passive film is similar to the one of the native oxide. It is to be noted that despite the stronger enrichment of chromium oxide in the passive film compared to the native oxide, the content of Cr (16 at%) in the modified alloy layer is slightly higher than that for the native oxide (12 at%). This is related to the passivation process in which there is no dissolution of Cr, whereas Fe is dissolved.

Table III-4 also shows the composition and thickness obtained for the passive film formed at 400mV at different passive currents. Increasing the passivation time at 400mV causes a decrease of the passive current. The passive film was analysed at three different stages (10µA/cm² (45s), 1µA/cm² (530s) and 0.1µA/cm² (4600s)). The thickness of the films remains unchanged (1.6 nm) with increasing passivation time (decreasing passive current). As for the concentration of the oxides in the film, the contents of Mn oxide (11 to 13 at%), Fe oxide (14 to 16 at%), Co oxide (5 at%) do not change significantly during prolonged passivation. The marked modification occurring in the film during the passivation is the increase of the Cr oxide (from 35.5 at% to 53.4 at%) combined with the decrease of the Cr hydroxide (from 32.2 at% to 11.8 at%), indicating dehydroxylation during the passivation

process. In the modified alloy layer, the fractions of metallic Cr (16 at%), Mn (16 at%), Fe (18 at%), Co (21 at%) and Ni (29 at%) are stable.
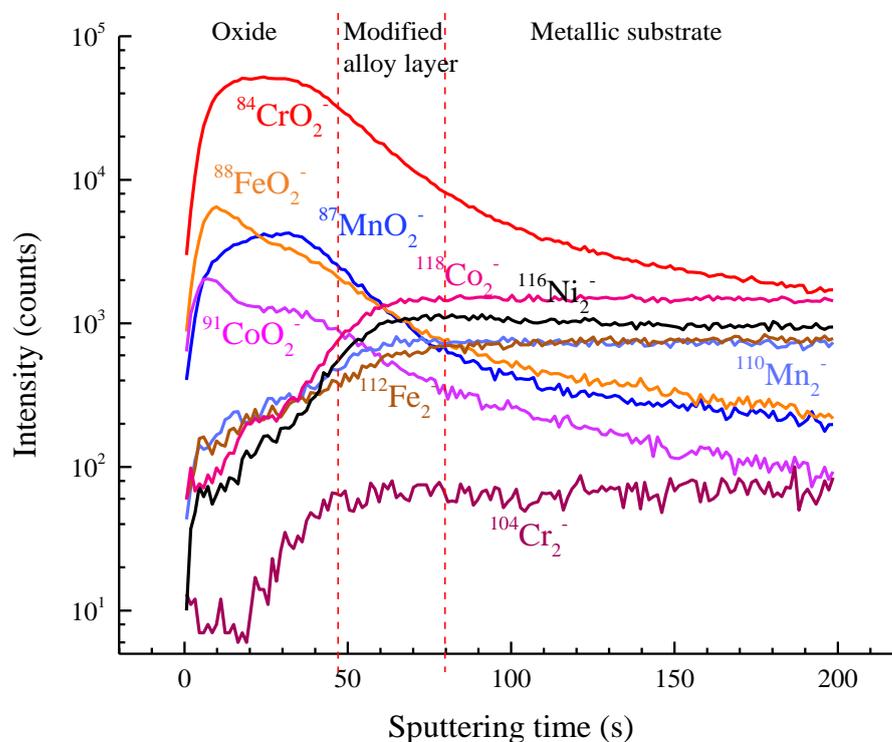


**Fig.III-7** ToF-SIMS depth profiles for the passive film formed on the HEA at 400 mV/SCE in 0.05M $H_2SO_4$ (Passivation time:4600s; passive current:0.1µA/cm²)

Fig.III-7 shows the ToF-SIMS depth profile for the passive film formed on the CoCrFeMnNi HEA sample after passivation for 4600s in 0.05M $H_2SO_4$(aq) at 400 mV/SCE.

As previously, the depth profiles can be splitted into 3 regions corresponding to the passive film, the modified alloy and the metallic substrate. After passivation, the structure of the oxide film is not modified. The $^{91}CoO_2^-$ and $^{88}FeO_2^-$ signals in the outer oxide show a lower intensity, indicating a lower Co and Fe concentration; the oxides of the other elements remain unchanged. As for the modified alloy layer, a slight Ni enrichment is observed.

## III-4. Discussion

In this work, XPS and ToF-SIMS have been used to determine the nature (chemical composition) and thickness of different oxides (native oxide, passive layers) formed on the surface of a CoCrFeMnNi HEA. The native oxide presents an enrichment of $Cr^{3+}$ (46.3 at %) and $Fe^{3+}$ (30.3 at%) while passive films comprise mainly $Cr^{3+}$ (>60%). In all cases, Ni oxide

is not detected by XPS. The chromium enrichment in the oxide layer is in agreement with the Gibbs standard free energy of formation ($\Delta G_{298.15k}°$) for $Cr_2O_3$, which is -1058.067kJ/mol, i.e. much more negative than for $Fe_2O_3$ (-742.294 kJ/mol), $MnO_2$ (-465.138 kJ/mol) and CoO (-214.198 kJ/mol) [54].

A duplex layer covers the substrate. Fe and Co are located preferentially in the outer layer, Mn in the inner layer. Cr is distributed in the whole film. A modified alloy layer, enriched in Ni, is observed under the oxide film.

After exposure of the alloy covered by the native oxide to acidic aqueous solution at OCP, the CoCrFeMnNi HEA shows a marked dissolution of Fe oxide from the film, in agreement with others [57]. The amounts of Cr oxide and hydroxide in the film are increased after immersion for 60 min. This is explained by the slow dissolution rate of Cr compared to Fe oxide in the acid media [22, 38]. Despite the dissolution of species in sulfuric acid, the thickness of the film is increased after immersion. There is a balance between dissolution of the species and growth of the oxide which seems to bring a stationary thickness after ~30 min of immersion. The thickening of the oxide film is observed by both XPS and ToF-SIMS measurements.

The passivity of the HEA at different passive potentials (200mV, 400mV and 600mV) has been studied. The XPS characterization has shown that the passivation potential has a weak effect on the composition and thickness of the oxide layer and modified alloy layer. The studied passive films are found to be enriched in Cr species, particularly Cr oxide, compared to the native oxide film. The contents of Mn and Co oxides in the passive films are similar to that in the native oxide film. Much less Fe oxide is observed in the passive film after passivation, which is consistent with the high dissolution of Fe oxide in the acidic solution. The total thickness for the passive films is found to be 1.6-1.7 nm, which is of the same order of magnitude as the thickness of the passive film (1.5-2 nm) on stainless steel after passivation in sulfuric acid [22, 58]. During passivation at 400 mV in sulfuric acid, the main modification of the composition observed in the passive film is the increase of Cr oxide and decrease of Cr hydroxide. Considering that the total content of Cr species (Cr oxide and hydroxide) in the film is stationary, the passivation process is correlated to the transformation of Cr hydroxide into Cr oxide. This transformation process is also responsible for the decrease of passive current. This passivation mechanism has been already proposed by Marcus et al. [38] for the passivation of stainless steel. The thickness of the film is maintained at 1.6-1.7 nm, hence the passivation time has no significant effect on the thickness of the passive film,

which has already been verified by Maurice et al. [22] for Fe-17Cr-14.5Ni-2.3Mo stainless steel.

## III-5. Conclusions

XPS, ToF-SIMS and electrochemical measurements were combined in order to study the corrosion behavior of the equiatomic CoCrFeMnNi high entropy alloy, with emphasis on characterization of the native oxide and passive films. A new XPS approach based on the analysis of 3p core level spectra has been developed. The parameters for fitting the 3p core level peaks of pure metals were used as reference for fitting the XPS 3p spectra for the oxide covered high entropy alloy. The decomposition of Cr 3p core level peaks into oxide and hydroxide have been verified by fitting also the Cr 2p spectra.

For all studied oxide films (native oxide and passive films), a duplex structure is observed. $Cr^{3+}$ is distributed in the whole film, while Fe and Co oxides are located preferentially in the outer layer and Mn oxide in the inner layer. Ni is not observed in the oxide layer. A modified metallic layer is observed under the oxide, with a significant enrichment of nickel.

During immersion in sulfuric acid at OCP, a selective dissolution of iron oxide combined with an increase of the chromium hydroxide is clearly demonstrated. Mn and Co oxide contents and locations in the film are not significantly modified.

After passivation of the HEA, an increase of chromium content is observed in the passive film. The transformation from Cr hydroxide to Cr oxide (by dehydroxylation) is observed for increasing passivation time.

### References

[1] D.B. Miracle, O.N. Senkov, A critical review of high entropy alloys and related concepts, Acta Materialia, 122 (2017) 448-511.

[2] Y. Zhang, T.T. Zuo, Z. Tang, M.C. Gao, K.A. Dahmen, P.K. Liaw, Z.P. Lu, Microstructures and properties of high-entropy alloys, Progress in Materials Science, 61 (2014) 1-93.

[3] O. Senkov, J. Miller, D. Miracle, C. Woodward, Accelerated exploration of multi-principal element alloys with solid solution phases, Nature Communication, 6 (2015) 6529.

[4] Y. Zhang, High-Entropy Materials: A Brief Introduction, Springer 2019.

[5] T. Nagase, P.D. Rack, J.H. Noh, T. Egami, In-situ TEM observation of structural changes in nano-crystalline CoCrCuFeNi multicomponent high-entropy alloy (HEA) under fast electron irradiation by high voltage electron microscopy (HVEM), Intermetallics, 59 (2015) 32-42.

[6] G. Bracq, M. Laurent-Brocq, L. Perrière, R. Pirès, J.-M. Joubert, I. Guillot, The fcc solid solution stability in the Co-Cr-Fe-Mn-Ni multi-component system, Acta Materialia, 128 (2017) 327-336.

[7] Z. Wu, H. Bei, F. Otto, G.M. Pharr, E.P. George, Recovery, recrystallization, grain growth and phase stability of a family of FCC-structured multi-component equiatomic solid solution alloys, Intermetallics, 46 (2014) 131-140.

[8] G. Bracq, M. Laurent-Brocq, C. Varvenne, L. Perrière, W. Curtin, J.-M. Joubert, I. Guillot, Combining experiments and modeling to explore the solid solution strengthening of high and medium entropy alloys, Acta Materialia, 177 (2019) 266-279.

[9] M. Feuerbacher, T. Lienig, C. Thomas, A single-phase bcc high-entropy alloy in the refractory Zr-Nb-Ti-V-Hf system, Scripta Materialia, 152 (2018) 40-43.

[10] J. Couzinié, G. Dirras, L. Perrière, T. Chauveau, E. Leroy, Y. Champion, I. Guillot, Microstructure of a near-equimolar refractory high-entropy alloy, Materials Letters, 126 (2014) 285-287.

[11] L. Lilensten, J.-P. Couzinie, L. Perriere, A. Hocini, C. Keller, G. Dirras, I. Guillot, Study of a bcc multi-principal element alloy: Tensile and simple shear properties and underlying deformation mechanisms, Acta Materialia, 142 (2018) 131-141.

[12] O.N. Senkov, G. Wilks, J. Scott, D.B. Miracle, Mechanical properties of Nb25Mo25Ta25W25 and V20Nb20Mo20Ta20W20 refractory high entropy alloys, Intermetallics 19 (2011) 698-706.

[13] B. Cantor, I.T.H. Chang, P. Knight, A.J.B. Vincent, Microstructural development in equiatomic multicomponent alloys, Materials Science and Engineering: A, 375-377 (2004) 213-218.

[14] B. Gludovatz, A. Hohenwarter, D. Catoor, E.H. Chang, E.P. George, R.O. Ritchie, A fracture-resistant high-entropy alloy for cryogenic applications, Science, 345 (2014) 1153-1158.

[15] B. Schuh, F. Mendez-Martin, B. Völker, E.P. George, H. Clemens, R. Pippan, A. Hohenwarter, Mechanical properties, microstructure and thermal stability of a nanocrystalline CoCrFeMnNi high-entropy alloy after severe plastic deformation, Acta Materialia, 96 (2015) 258-268.

[16] Y. Zhao, D.-H. Lee, M.-Y. Seok, J.-A. Lee, M. Phaniraj, J.-Y. Suh, H.-Y. Ha, J.-Y. Kim, U. Ramamurty, J.-i. Jang, Resistance of CoCrFeMnNi high-entropy alloy to gaseous hydrogen embrittlement, Scripta Materialia, 135 (2017) 54-58.

[17] Y. Shi, B. Yang, P. Liaw, Corrosion-resistant high-entropy alloys: A review, Metals 7 (2017) 43.

[18] Y. Qiu, S. Thomas, M.A. Gibson, H.L. Fraser, N. Birbilis, Corrosion of high entropy alloys, NPJ Materials degradation, 1 (2017) 15.

[19] Z. Tang, L. Huang, W. He, P.K. Liaw, Alloying and processing effects on the aqueous corrosion behavior of high-entropy alloys, Entropy, 16 (2014) 895-911.

[20] M.-H. Tsai, J.-W. Yeh, High-entropy alloys: a critical review, Materials Research Letters, 2 (2014) 107-123.

[21] E. Gardin, S. Zanna, A. Seyeux, A. Allion-Maurer, P. Marcus, Comparative study of the surface oxide films on lean duplex and corresponding single phase stainless steels by XPS and ToF-SIMS, Corrosion Science, 143 (2018) 403-413.

[22] V. Maurice, H. Peng, L.H. Klein, A. Seyeux, S. Zanna, P. Marcus, Effects of molybdenum on the composition and nanoscale morphology of passivated austenitic stainless steel surfaces, Faraday Discussions, 180 (2015) 151-170.

[23] V. Maurice, P. Marcus, Progress in corrosion science at atomic and nanometric scales, Progress in Materials Science, 95 (2018) 132-171.

[24] V. Maurice, W. Yang, P. Marcus, XPS and STM Study of Passive Films Formed on Fe-22Cr (110) Single-Crystal Surfaces, Journal of the Electrochemical Society, 143 (1996) 1182-1200.

[25] Y. Dou, S. Han, L. Wang, X. Wang, Z. Cui, Characterization of the passive properties of 254SMO stainless steel in simulated desulfurized flue gas condensates by electrochemical analysis, XPS and ToF-SIMS, Corrosion Science, (2019) 108405.

[26] S. Fajardo, I. Llorente, J.A. Jiménez, J. Bastidas, D.M. Bastidas, Effect of Mn additions on the corrosion behaviour of TWIP Fe-Mn-Al-Si austenitic steel in chloride solution, Corrosion Science, 154 (2019) 246-253.

[27] S. Peissl, G. Mori, H. Leitner, R. Ebner, S. Eglsäer, Influence of chromium, molybdenum and cobalt on the corrosion behaviour of high carbon steels in dependence of heat treatment, Materials and Corrosion, 57 (2006) 759-765.

[28] C.P. Lee, C.C. Chang, Y.Y. Chen, J.W. Yeh, H.C. Shih, Effect of the aluminium content of AlxCrFe1.5MnNi0.5 high-entropy alloys on the corrosion behaviour in aqueous environments, Corrosion Science, 50 (2008) 2053-2060.

[29] Y.F. Kao, T.D. Lee, S.K. Chen, Y.S. Chang, Electrochemical passive properties of AlxCoCrFeNi (x= 0, 0.25, 0.50, 1.00) alloys in sulfuric acids, Corrosion Science, 52 (2010) 1026-1034.

[30] C.M. Lin, H.L. Tsai, Evolution of microstructure, hardness, and corrosion properties of high-entropy Al0.5CoCrFeNi alloy, Intermetallics, 19 (2011) 288-294.

[31] Y.J. Hsu, W.C. Chiang, J.K. Wu, Corrosion behavior of FeCoNiCrCux high-entropy alloys in 3.5% sodium chloride solution, Materials Chemistry and Physics, 92 (2005) 112-117.

[32] X.L. Shang, Z.J. Wang, Q.F. Wu, J.C. Wang, J.J. Li, J.K. Yu, Effect of Mo Addition on Corrosion Behavior of High-Entropy Alloys CoCrFeNiMo x in Aqueous Environments, Acta Metallurgica Sinica (English Letters), 32 (2019) 41-51.

[33] K.F. Quiambao, S.J. McDonnell, D.K. Schreiber, A.Y. Gerard, K.M. Freedy, P. Lu, J.E. Saal, G.S. Frankel, J.R. Scully, Passivation of a corrosion resistant high entropy alloy in non-oxidizing sulfate solutions, Acta Materialia, 164 (2019) 362-376.

[34] A. Rodriguez, J.H. Tylczak, M. Ziomek-Moroz, Corrosion Behavior of CoCrFeMnNi High-Entropy Alloys (HEAs) Under Aqueous Acidic Conditions, ECS Transaction, 77 (2017) 741-752.

[35] G. Laplanche, U. Volkert, G. Eggeler, E. George, Oxidation behavior of the CrMnFeCoNi high-entropy alloy, Oxidation of Metals, 85 (2016) 629-645.

[36] M. Laurent-Brocq, A. Akhatova, L. Perrière, S. Chebini, X. Sauvage, E. Leroy, Y. Champion, Insights into the phase diagram of the CrMnFeCoNi high entropy alloy, Acta Materialia, 88 (2015) 355-365.

[37] F. Di Franco, A. Seyeux, S. Zanna, V. Maurice, P. Marcus, Effect of High Temperature Oxidation Process on Corrosion Resistance of Bright Annealed Ferritic Stainless Steel, Journal of the Electrochemical Society, 164 (2017) C869-C880.

[38] V. Maurice, W. Yang, P. Marcus, X-Ray photoelectron spectroscopy and scanning tunneling microscopy study of passive films formed on (100) Fe-18Cr-13Ni single-crystal surfaces, Journal of the Electrochemical Society, 145 (1998) 909-920.

[39] A. Machet, A. Galtayries, P. Marcus, P. Combrade, P. Jolivet, P. Scott, XPS study of oxides formed on nickel-base alloys in high-temperature and high-pressure water, Surface and Interface Analysis, 34 (2002) 197-200.

[40] P. Marcus, M.E. Bussell, XPS study of the passive films formed on nitrogen-implanted austenitic stainless steels, Applied Surface Science, 59 (1992) 7-21.

[41] M.C. Biesinger, B.P. Payne, A.P. Grosvenor, L.W.M. Lau, A.R. Gerson, R.S.C. Smart, Resolving surface chemical states in XPS analysis of first row transition metals, oxides and hydroxides: Cr, Mn, Fe, Co and Ni, Applied Surface Science, 257 (2011) 2717-2730.

[42] M. Aronniemi, J. Sainio, J. Lahtinen, Chemical state quantification of iron and chromium oxides using XPS: the effect of the background subtraction method, Surface Science, 578 (2005) 108-123.

[43] T. Yamashita, P. Hayes, Analysis of XPS spectra of Fe2+ and Fe3+ ions in oxide materials, Applied Surface Science, 254 (2008) 2441-2449.

[44] B. Payne, M. Biesinger, N. McIntyre, X-ray photoelectron spectroscopy studies of reactions on chromium metal and chromium oxide surfaces, Journal of Electron Spectroscopy and Related Phenomena, 184 (2011) 29-37.

[45] A.M. Salvi, J.E. Castle, J.F. Watts, E. Desimoni, Peak fitting of the chromium 2p XPS spectrum, Applied Surface Science, 90 (1995) 333-341.

[46] E. Ünveren, E. Kemnitz, S. Hutton, A. Lippitz, W. Unger, Analysis of highly resolved x-ray photoelectron Cr 2p spectra obtained with a Cr2O3 powder sample prepared with adhesive tape, Surface Interface Analysis, 36 (2004) 92-95.

[47] S. Doniach, M. Sunjic, Many-electron singularity in X-ray photoemission and X-ray line spectra from metals, Journal of Physics C: Solid State Physics, 3 (1970) 285.

[48] J.W. Gadzuk, M. Šunjić, Excitation energy dependence of core-level x-ray-photoemission-spectra line shapes in metals, Physical Review B, 12 (1975) 524.

[49] N.D. Stepanov, D.G. Shaysultanov, G.A. Salishchev, M.A. Tikhonovsky, E.E. Oleynik, A.S. Tortika, O.N. Senkov, Effect of V content on microstructure and mechanical properties of the CoCrFeMnNiVx high entropy alloys, Journal of Alloys and Compounds, 628 (2015) 170-185.

[50] J. He, W. Liu, H. Wang, Y. Wu, X. Liu, T. Nieh, Z. Lu, Effects of Al addition on structural evolution and tensile properties of the FeCoNiCrMn high-entropy alloy system, Acta Materialia, 62 (2014) 105-113.

[51] J.H. Scofield, Hartree-Slater subshell photoionization cross-sections at 1254 and 1487 eV, Journal of Electron Spectroscopy and Related Phenomena, 8 (1976) 129-137.

[52] S. Tanuma, C.J. Powell, D.R. Penn, Calculations of electorn inelastic mean free paths. II. Data for 27 elements over the 50–2000 eV range, Surface Interface Analysis, 17 (1991) 911-926.

[53] L. Wang, A. Seyeux, P. Marcus, Thermal stability of the passive film formed on 316L stainless steel surface studied by ToF-SIMS, Corrosion Science, (2019) 108395.

[54] I. Barin, Thermochemical data of pure substances, VCH, (1989).

[55] H.E. Evans, D.A. Hilton, R.A. Holm, Chromium-depleted zones and the oxidation process in stainless steels, Oxidation of Metals, 10 (1976) 149-161.

[56] C. Leygraf, G. Hultquist, Initial oxidation stages on Fe-Cr(100) and Fe-Cr(110) surfaces, Surface Science, 61 (1976) 69-84.

[57] H. Luo, Z. Li, A.M. Mingers, D. Raabe, Corrosion behavior of an equiatomic CoCrFeMnNi high-entropy alloy compared with 304 stainless steel in sulfuric acid solution, Corrosion Science, 134 (2018) 131-139.

[58] Z. Wang, F. Di-Franco, A. Seyeux, S. Zanna, V. Maurice, P. Marcus, Passivation-induced physicochemical alterations of the native surface oxide film on 316L austenitic stainless steel, Journal of the Electrochemical Society, 166 (2019) C3376-C3388.

# Chapter IV

# Thermal stability of the passive film formed on 316L stainless steel surface studied by ToF-SIMS

## Abstract

The modifications of the passive film formed on 316L stainless steel surface during stepwise heating in ultra-high vacuum up to 300°C have been studied in situ by ToF-SIMS. The pre-formed passive film (in 0.05M $H_2SO_4$) has a bilayer structure, comprising Fe-rich, Mo-rich (outer) and Cr-rich (inner) layers. Below 100°C, the passive film is stable. At 100°C - 250°C, dehydroxylation and dehydration is observed. Above 250°C, the main modification in the film is formation of chromium oxide at the expense of oxidized iron. At higher temperature, thicker Cr-rich inner layer with sharper inner/outer oxide interface is formed.

## IV-1. Introduction

Stainless steels are employed in a wide range of technical applications due to the formation of a protective surface oxide layer, that can provide high corrosion resistance of the material in aggressive environments [1, 2]. The passive films formed on stainless steel surfaces, typically a few nanometres thick at room temperature, are known to be duplex with an outer layer rich in iron oxide while the inner layer is enriched in chromium oxide [3, 4]. The corrosion resistance of the surface depends mainly on the chromium rich inner oxide, which serves as a barrier against the attack of aggressive ions from the environment [5, 6].

The formation of oxide film on the stainless steel surface at different temperatures has been widely studied. The oxidation temperature and the oxygen pressure are the two key factors influencing the oxidation rate and the composition of the oxide film on SS alloys. Oxidation of SS surface in air at most temperatures (temperatures lower than 800°C), leads to the formation of a duplex oxide layer, consisting of an outer iron oxide and an inner chromium rich layer [7, 8]. Under reduced oxygen partial pressures (lower than $10^{-3}$ mbar), at oxidation

temperatures above 800°C, chromium oxide is the predominant layer on the stainless steel surface [9, 10], while for the oxide films formed at temperatures lower than 400°C, both the iron and chromium oxide were reported to grow on the SS surfaces [11-14].

Heating the SS at high temperatures in vacuum, may lead to modifications of chemical composition and structure in the alloy at the metal/oxide interface, such as phase transformation as already shown in the literature [15, 16]. Many phenomena, including diffusion, selective oxidation and evaporation of elements, are ongoing in the process of vacuum annealing of SS [17, 18]. It is well known that the vacuum annealing for stainless steel at high temperatures (above 1000°C) will produce a marked chromium depletion zone in the alloy surface under the oxide film because the selective evaporation rate is much faster than the bulk diffusion rate of chromium [18, 19]. For vacuum annealing of SS at intermediate temperatures [17, 20], about 400°C to 800°C, the evaporation rate of chromium oxidized at the surface is strongly reduced, and a strong chromium enrichment could be observed in the alloy surface under the oxide film. Studies of vacuum annealing of stainless steel, especially under ultra-high vacuum (pressure lower than $10^{-9}$ mbar), at relatively low temperature (lower than 300°C) are still under discussion.

Native oxide films, formed in air on stainless steel surfaces, have been studied in the past, especially thanks to UHV techniques like XPS and ToF-SIMS [2, 21-24]. Among these studies, very few have focused on the thermal stability of native oxide films during annealing under UHV [25-27]. Asami et al. [25] have used XPS spectroscopy to study the modifications of the native oxide film for a series of Fe-Cr alloys by UHV annealing up to 380°C. When the temperature is higher than 300°C, the authors showed the iron oxide reduction and the modification of the chromium oxidation state in the oxide film. Castle et al. [26] used the energy loss features within XPS spectra to study the oxidation and subsequent vacuum annealing of an Fe/Cr alloy at 200-300°C. An iron oxide reduction and chromium oxide formation were observed. Recent in situ measurements, performed by Bouheida et al. [27] on Fe-12Cr alloy, show that annealing in UHV with a thermal ramp rate of 2°C/min up to 550°C, leads to iron oxide reduction due to chromium oxidation. Although XPS can provide information on composition changes after heat treatment, the evolution of the oxide film structure is not obtained with XPS after set temperature. ToF-SIMS is a promising way to study the thermal stability of the oxide structure during the stepwise heating.

The aim of the present work was to investigate the thermal stability and the modification of pre-formed passive films on 316L stainless steel up to 300°C in ultra-high vacuum (UHV). To

this end, 316L SS were electrochemically passivated in $H_2SO_4$ and then annealed in UHV by increasing step by step the temperature, from room temperature up to 300°C. The stability of the passive oxide film has been monitored in situ during heating, and modifications of the composition and structure of the oxide films have been analyzed by ToF-SIMS.

## IV-2. Experimental

### IV-2.1. Sample preparation

A Fe-19Cr-13Ni-2.7Mo (wt%) polycrystalline sample was used. The samples were mechanically polished down to 0.25μm with diamond paste and then washed with acetone, ethanol and water in ultrasonic bath for 10 mins. The samples were then dried in compressed air.

A Gamry electrochemical workstation was used for electrochemical experiments. The electrochemical passivation was performed with a standard three-electrode configuration with an Au counter electrode and a saturated calomel electrode as the reference electrode. The electrolyte was 0.05M $H_2SO_4$ prepared with ultrapure chemicals (VWR®) and Millipore® water. Before measurement, the solution was deaerated by Ar bubbling for 30 minutes.

### IV-2.2. ToF-SIMS investigation

ToF-SIMS depth profiles were obtained using a ToF-SIMS 5 spectrometer (IONTOF GmbH - Germany). The spectrometer was run at an operating pressure of $10^{-9}$ mbar. The total primary ion flux was less than $10^{12}$ ions.cm$^{-2}$ ensuring static conditions. A pulsed 25 keV Bi$^+$ primary ion source was employed for analysis, delivering 1.2 pA current over a $100 \times 100$ μm$^2$ area. High current bunched mode was used in order to get high mass resolution ($\Delta M/M$ ~10 000). Depth profiling was carried out by interlacing secondary ion analysis with sputtering using a 0.5 keV Cs$^+$ sputter beam giving a 17 nA target current over a $300 \times 300$ μm$^2$ area. Both Bi$^+$ and Cs$^+$ ion beams were impinging the sample surface at an angle of 45° and were aligned in such a way that the analyzed ions were taken from the center of the sputtered crater.

Data acquisition and post-processing were performed using the Ion-Spec software. The exact mass values of at least 5 known species were used to calibrate the data acquired in the negative ion mode.

| Species | Characteristic ion |
|---|---|
| Hydroxide | $(OH)_2^-$ |
| Metallic Fe | $^{56}Fe_2^-$ |
| Metallic Ni | $^{58}Ni_2^-$ |
| Iron oxide | $^{56}FeO_2^-$ |
| Chromium oxide | $^{53}CrO_2^-$ |
| Molybdenum oxide | $^{98}MoO_3^-$ |

**Table IV-1** ToF-SIMS characteristic ions used to characterize the composition and structure of the oxide film formed on 316L SS

ToF-SIMS depth profiles were used to determine the composition and structure of the passive film, and to study its thermal stability. The characteristic ions were selected as shown in Table IV-1. It should be noted that the selected ions do not reflect the real stoichiometry of the species constituting the sample, but are the appropriate markers of the studied species. Since ToF-SIMS is a non-quantitative technique (due to strong matrix effect on ion emission), the intensity of the plotted ions in the depth profiles cannot be compared directly and do not reflect the concentrations of the associated species in the substrate. However, variations of a single signal reflect in depth variations of the concentration. The depth profiles are plotted versus the sputtering time, and the sputtering time directly translates into oxide thickness. The oxide sputtering rate was determined by measuring, with a mechanical profilometer (Dektak 150, Veeco, Veeco-Instrument Europe, Dourdan, France), the depth of various craters after depth profiling. Assuming a similar oxide composition and density, a 0.04 nm/s sputtering rate was measured.

## IV-3. Results and discussion

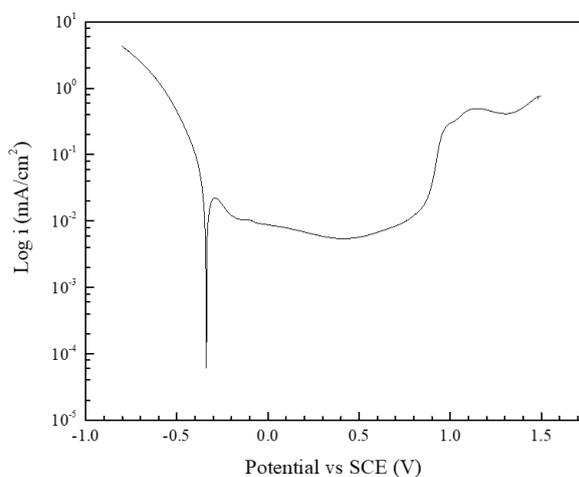### IV-3.1. Passive film formation and analysis



**Fig.IV-1** Polarization curve of the 316L SS in 0.05M $H_2SO_4$ with a scan rate of 1mV/s

Fig.IV-1 shows the polarization curve obtained on 316L stainless steel in 0.05M $H_2SO_4$ aqueous solution with a scan rate of 1mV/s. Within the passive range (-0.1 ~ 0.8V/SCE), the lowest current is obtained at 0.4V/SCE, corresponding to the lowest dissolution rate of metallic ions in the solution. The oxide film formed at this potential shows the highest corrosion resistance. Maurice et al. have already demonstrated that the strong enrichment in chromium in the passive film formed in sulphuric acid, compared to the native oxide, is the result of the extremely low dissolution rate of Cr(III) oxide compared to the one of Fe(II)/Fe(III) oxides [21]. In this study, a static polarization potential (0.4V/SCE) was applied on the 316L SS for 1h in 0.05M $H_2SO_4$ aqueous solution to obtain a protective passive film on the sample surface.

Fig.IV-2 shows the ToF-SIMS negative ion depth profiles for the passive film formed in 0.05M $H_2SO_4$ (aq) at 0.4V/SCE for 1h on the 316L SS. To study the thermal stability of the electrochemically pre-formed oxide film, the position of the metal/oxide interface on the ToF-SIMS depth profiles is crucial to extract the structure and composition of the oxide. The $^{53}CrO_2^-$ ion profile is used to define the oxide film region (ending at 80% of the maximum intensity of the depth profile) due to the duplex structure of the film with chromium enriched inner layer, and the $^{56}Fe_2^-$ ion profile is used to define the metallic region (starting at 80% of the intensity plateau). An intermediate region is determined in Fig.IV-2 from 60s to 100s of sputtering. This region characterized by a hump in the $^{58}Ni_2^-$ signal, is assigned to a modified

93

alloy layer under the oxide film in the vicinity of the oxide-metal interface. In this intermediate region, the progressive increase of the $^{56}Fe_2^-$ signal indicates, in contrast with the $^{58}Ni_2^-$ signal, a depletion in metallic Fe gradually disappearing. Thus, the alloy is enriched in Ni and depleted in Fe close to the metal/oxide interface.
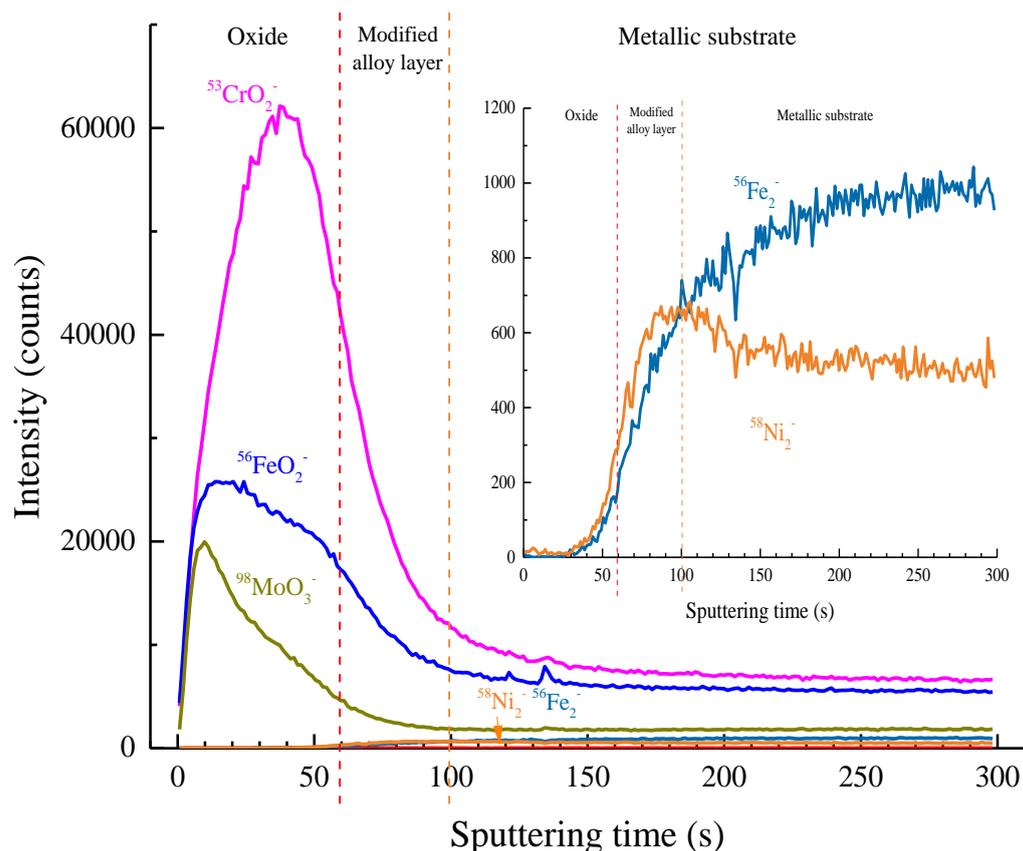


**Fig.IV-2** ToF-SIMS depth profiles of the passive film formed on 316L SS surface in 0.05M $H_2SO_4$ (aq) at 0.4V/SCE for 1h. The colour lines mark the limits between oxide film, modified alloy layer and metallic substrate region

Focusing on the $^{56}FeO_2^-$ and $^{98}MoO_3^-$ signals, the depth profile shows that their maxima are located in the outer part of the passive film and they decrease slowly through the oxide film region. Oxidized Fe and Mo are therefore mainly located in the outer part of the film, although they are also present in the inner oxide. The $^{53}CrO_2^-$ profile exhibits a maximum intensity in the inner part of the film. Oxidized chromium is thus preferentially located in the inner part, close to the metal/oxide interface. The $^{58}NiO_2^-$ ion is not plotted in Fig.IV-2, since its intensity is too low, meaning that Ni oxide is present only as traces in the oxide film.

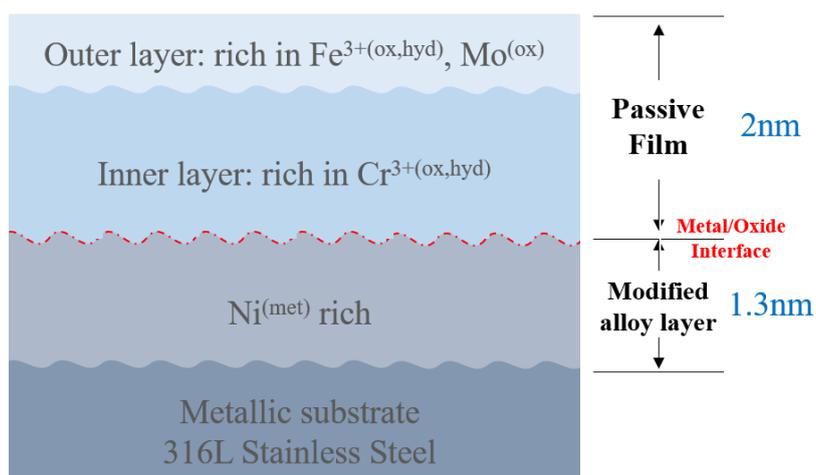## IV-3.2. The model for the composition of passive film



**Fig.IV-3** The model for the passive film formed on 316L SS surface in 0.05M $H_2SO_4$ (aq) at 0.4V/SCE for 1h

Based on the ToF-SIMS depth profiles data, a model for the passive film and the alloy underneath the oxide is presented in Fig.IV-3. In the model, it is considered that the passive film formed electrochemically is duplex with iron and chromium mainly in the outer and inner layers, respectively. Molybdenum oxide is mainly located in the outer part of the film. Nickel oxide is present only at trace amount. In a modified interfacial alloy layer, metallic nickel is enriched, compared to the metallic substrate. The model also suggests that the interfaces are not sharp.

## IV-3.3. Thermal stability of the passive film
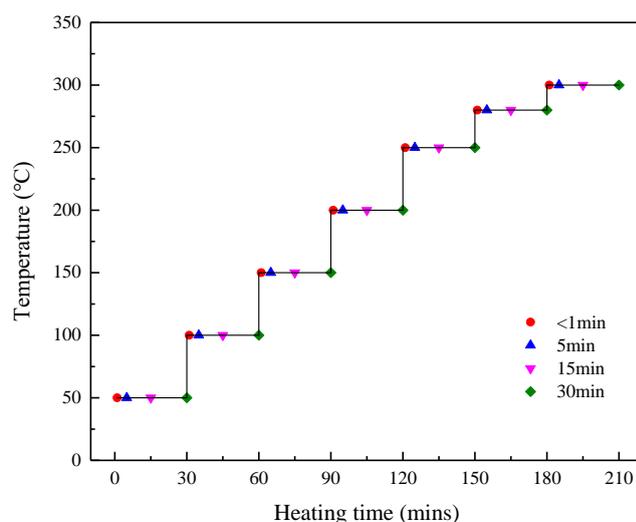


**Fig. IV-4** Scheme for studying thermal stability of the passive film in UHV as a function of temperature and heating time (The color symbols on each temperature step indicate the time at which ToF-SIMS depth profiles were acquired)

The thermal stability of the passive film in vacuum was studied in situ by ToF-SIMS. Fig.IV-4 shows the scheme used for the thermal treatment given to the passive oxide film under UHV in the ToF-SIMS analysis chamber. After passivation of the 316L SS sample (0.4V/SCE in 0.05M $H_2SO_4$ for 1h), it was introduced in the ToF-SIMS analysis chamber under a base pressure lower than $10^{-9}$ mbar. The experiments were performed through stepwise heating from 50°C to 300°C with steps of 50°C. The temperature of 280°C was added in the experiments since under relatively high temperature, even slight increase of the temperature could cause modifications of the composition and structure of the passive oxide. After each temperature step, ToF-SIMS depth profiles were acquired for heating times of 1 minute, 5 minutes, 15 minutes and 30 minutes. Each profile was obtained on a new area of the sample surface.
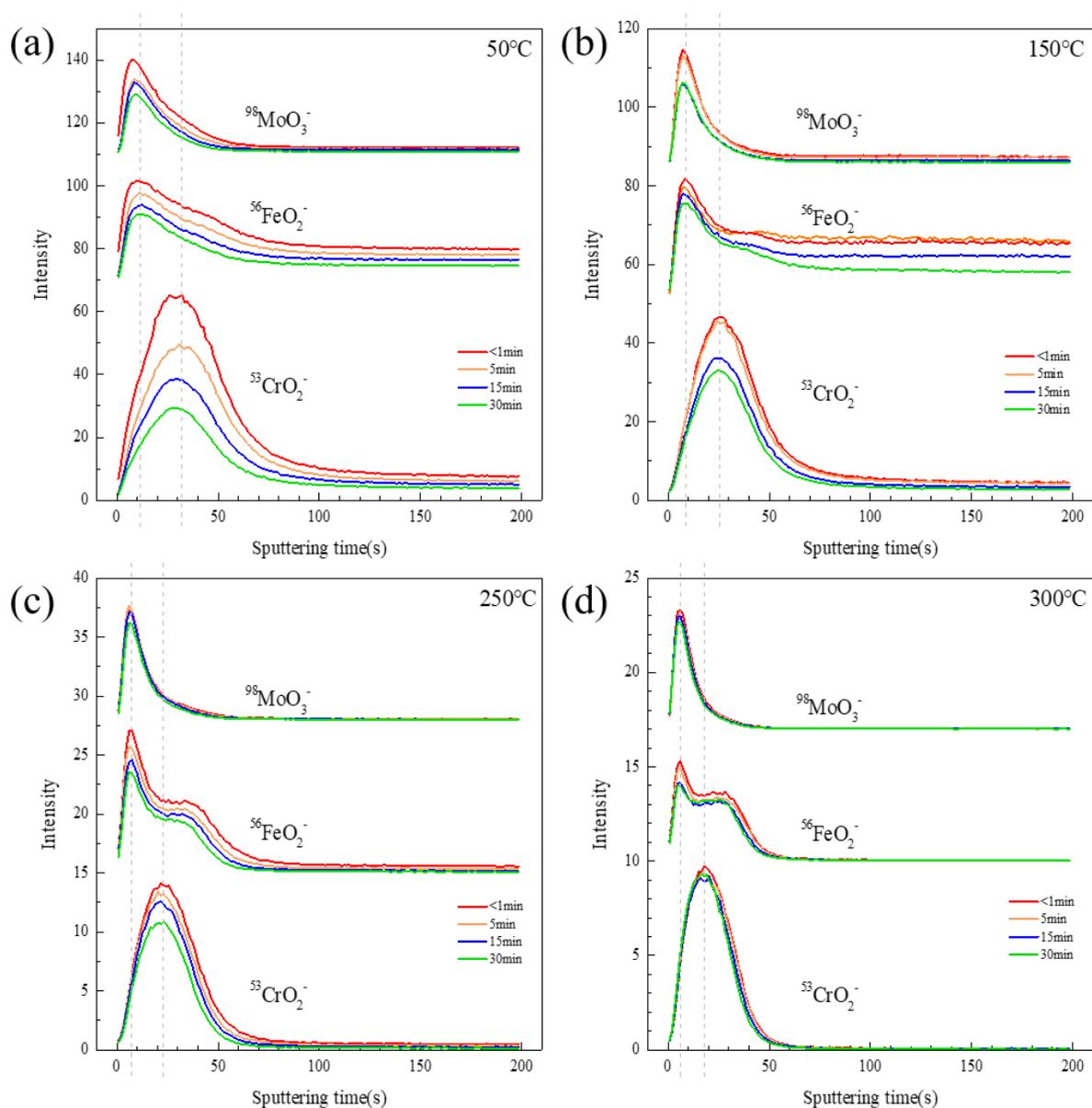
**Fig.IV-5** ToF-SIMS depth profiles of $^{53}CrO_2^-$, $^{56}FeO_2^-$ and $^{98}MoO_3^-$ at **(a)** 50°C, **(b)** 150°C, **(c)** 250°C and **(d)** 300°C for different heating times. (The intensities are normalized by the intensity of $Fe_2^-$ in the substrate)

Fig.IV-5 shows the $^{53}CrO_2^-$, $^{56}FeO_2^-$ and $^{98}MoO_3^-$ ToF-SIMS depth profiles recorded on the passive film heated up to 50°C, 150°C, 250°C and 300°C for different heating times. Although all the temperatures indicated in Fig.IV-4 have been investigated, only the data for these 4 temperatures are discussed here since no strong change occurred on the passive film at the other intermediate temperatures. The depth profiles of $Ni_2^-$ and $Fe_2^-$ ions are not included in Fig.IV-5, since they were unchanged during heat treatment.

As observed in Fig.IV-5(a), when the sample is heated up to 50°C and maintained at this temperature for 1, 5, 15 and 30 min, the shapes of $^{53}CrO_2^-$, $^{56}FeO_2^-$ and $^{98}MoO_3^-$ profiles are not significantly modified as compared with the profile obtained at room temperature. This demonstrates that the native oxide layer is stable at 50°C, with a duplex structure formed by an Fe and Mo rich outer oxide and a Cr rich inner oxide.

Upon heating at 150°C in vacuum, the separation between outer layer composed of Fe oxide ($^{56}FeO_2^-$) and Mo oxide ($^{98}MoO_3^-$) and inner layer composed of Cr oxide ($^{53}CrO_2^-$) is enhanced. The inner oxide/outer oxide interface becomes sharper as shown by the sharper decrease of both the $^{98}MoO_3^-$ and $^{56}FeO_2^-$ signals after heating at 150°C (Fig.IV-5(b)).

At temperatures higher than 200°C, as showed in Fig.IV-5(c) for 250°C and (d) for 300°C, the $^{56}FeO_2^-$ and $^{98}MoO_3^-$ depth profiles show again maxima of intensity located in the outer part of the oxide film. However, for the $^{56}FeO_2^-$ signal, a clear plateau of lower intensity is observed in the inner chromium oxide rich layer and then a sharp decrease when going through the oxide/alloy interface.

Although the $^{53}CrO_2^-$ depth profiles remain high in the inner part of the oxide film, the intensity ratio between the $^{53}CrO_2^-$ and $^{56}FeO_2^-$ in the inner oxide region (taken around 40s of sputtering on Fig.IV-6(b)), is decreasing from 2.3 at 50°C to 1.3 with increasing the temperature up to 200°C. The modification of the $^{53}CrO_2^-/^{56}FeO_2^-$ ratio demonstrates the modification of the inner oxide layer. To understand this evolution, one also has to look at the $OH_2^-$ species. Fig.IV-6(a) shows the ToF-SIMS depth profiles of the $OH_2^-$ species as function of temperature. The intensity maxima of the $OH_2^-$ signal remarkably drop from 0.8 at 50°C to 0.2 at 200°C. The composition of the passive film formed in 0.05M $H_2SO_4$ (aq) has already been studied by Maurice and Marcus [6, 21]. It was shown that the passive film formed at room temperature contains 6% of iron hydroxide, 23% of chromium hydroxide, and about

10% of water ligand. Thus, the evolution of $OH_2^-$ is assigned to the decomposition of hydroxides and dehydration. The decreasing of the $^{53}CrO_2^-/^{56}FeO_2^-$ ratio in the inner oxide with increasing temperature is assigned mainly to the decomposition of Cr hydroxide (a major constituent of the inner oxide at low temperature) yielding Cr oxide.
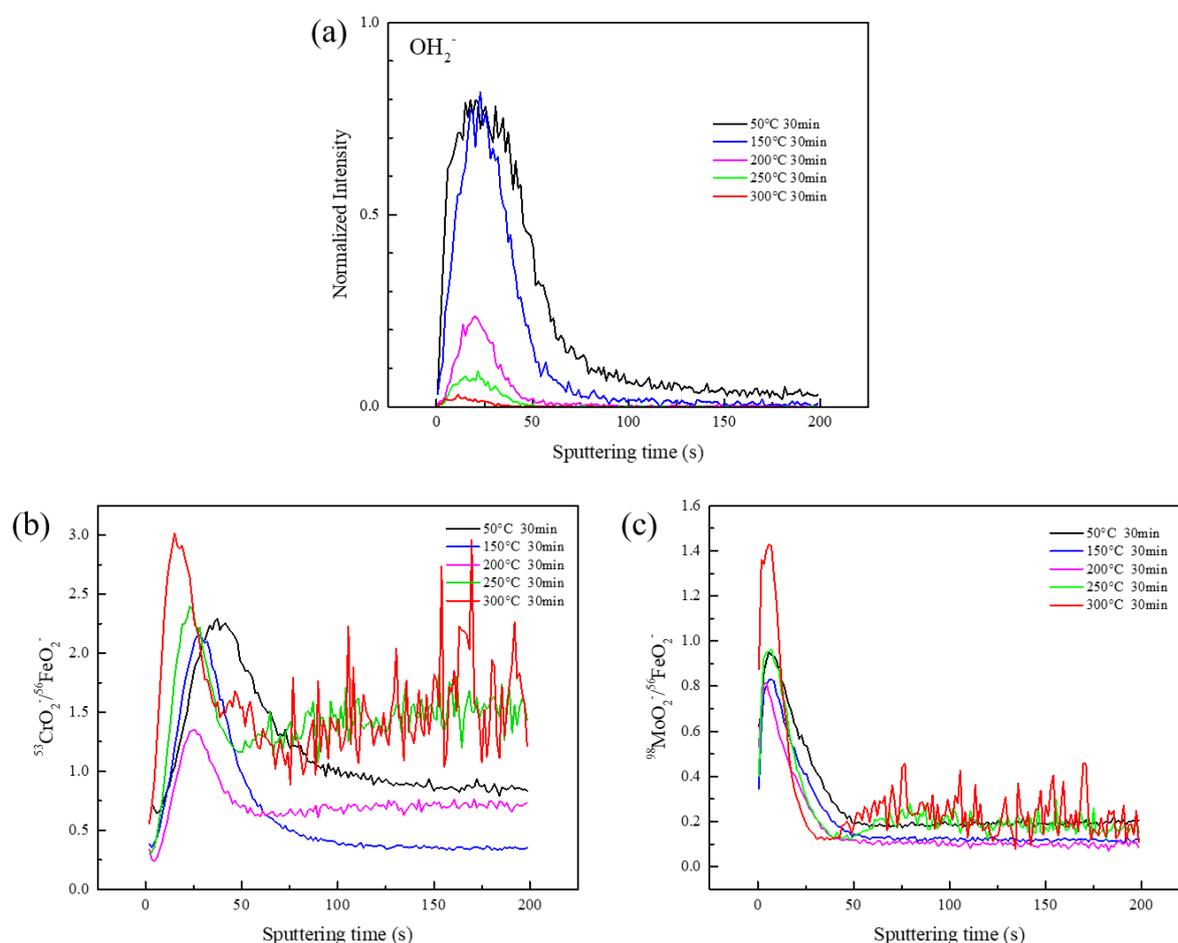


**Fig.IV-6** ToF-SIMS depth profiles as function of temperature after 30 mins at each temperature: **(a)** $OH_2^-$ secondary ion, **(b)** $^{53}CrO_2^-/^{56}FeO_2^-$ intensity ratio, and **(c)** $^{98}MoO_3^-$ /$^{56}FeO_2^-$ intensity ratio. (In (a), the intensity is normalized by the intensity of $Fe_2^-$ in the substrate)

Although dehydroxylation and dehydration have been showed this effect cannot explain the modification of the $^{56}FeO_2^-$ and $^{53}CrO_2^-$ depth profiles and the sharpness of the inner oxide/outer oxide interface. Looking more precisely at the $^{53}CrO_2^-/^{56}FeO_2^-$ ratio, one observes that it decreases with increasing temperature up to 200°C. When the temperature is increased over 250°C, the $^{53}CrO_2^-/^{56}FeO_2^-$ ratio increases from 1.3 to 2.4. This indicates that the inner oxide becomes more concentrated in Cr. This effect may be due to the increase of Cr diffusion from the metallic substrate to the passive film. Cr being more reactive towards oxygen, the higher concentration of Cr in the inner part of the oxide is related to the reduction of the Fe

oxide to form Cr oxide according to the reaction $Fe_2O_3+2Cr \rightarrow Cr_2O_3+2Fe$. This mechanism is in agreement with the standard free energy of formation ($\Delta G500k°$) of chromium oxide and iron oxide (-1004.265 kJ/mol and -687.720 kJ/mol, respectively [28]), and Ellingham oxidation-reaction plot [29-31]. The bilayer structure of the oxide film becomes more marked with an outer oxide that is almost exclusively comprised of Fe oxide and an inner oxide that is almost exclusively comprised of Cr oxide. This also correlates to the modification of the inner oxide / outer oxide interface that becomes sharper when increasing the temperature. Thus, two effects linked with the increase of the temperature have been shown, the first one, which is the main effect at temperatures lower than 250°C, is the dehydroxylation and dehydration of the oxide film, and the second one, that is the main effect at temperatures over 250°C, is the Fe oxide reduction due to bulk Cr diffusing into the inner part of the oxide.

In Fig.IV-6(c), the $^{98}MoO_3^-/^{56}FeO_2^-$ intensity ratio shows only minor changes up to 250°C. Above 250°C, there is a marked increase of the $^{98}MoO_3^-/^{56}FeO_2^-$ intensity ratio, from 0.9 at 250°C up to 1.4 at 300°C. This is also assigned to the formation of molybdenum oxide and reduction of iron oxide. This is similar to the formation of chromium oxide but at higher temperature. This effect is assigned to molybdenum diffusing from the metallic substrate and being oxidized at the expense of iron oxide.
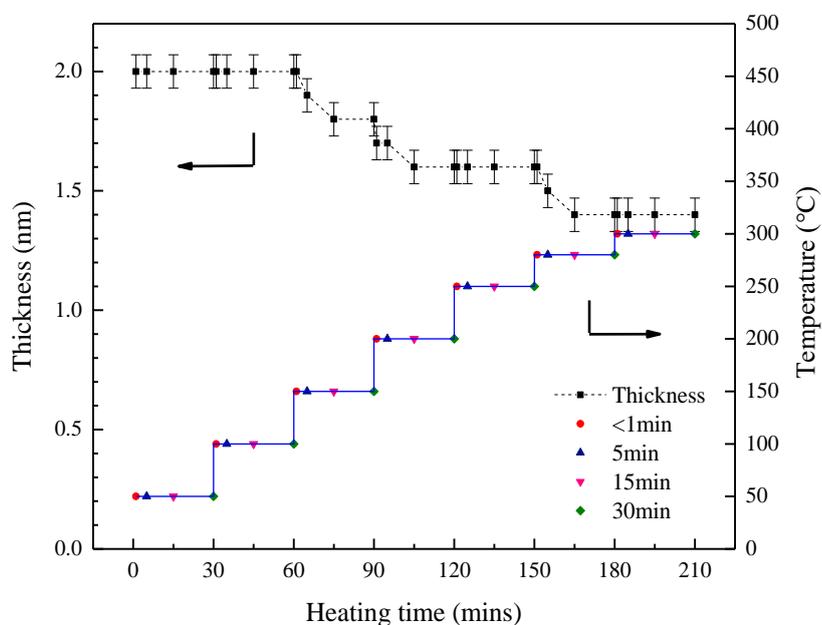


**Fig.IV-7** The thickness of the passive film as a function of heating temperature and time

Fig.IV-7 shows the changes of the passive film thickness as a function of heating temperature and time. The passive film thickness remains constant at 2 nm up to 100°C. At higher temperature (up to 250°C), the passive film thickness gradually decreases to 1.6 nm. This change is assigned to the decomposition of the hydroxide and removal of water ligands present after passivation in sulphuric acid. According to the density of chromium oxide and iron oxide (5.22 g/cm$^3$ and 5.24 g/cm$^3$), and those of chromium hydroxide and iron hydroxide (3.11 g/cm$^3$ and 3.4 g/cm$^3$), the decomposition of hydroxide to oxide will result in a denser and thinner film as observed on Fig.IV-7. Above 200°C, the passive film composition and structure seem more stable, as indicated by the very limited change in oxide film thickness in the 200°C - 300°C (from 1.6 nm to 1.4 nm). This slight film modification in this temperature range is related to the formation of chromium and molybdenum oxide, and reduction of iron oxide. According to the density of Mo(IV) oxide (6.47 g/cm$^3$), Cr oxide and Fe oxide, the formation of Mo oxide and reduction of Fe oxide will lead to a denser film. In addition, the formation of Mo oxide will consume more Fe oxide due to its higher stoichiometry.

According to the results above, a model for the evolution of the passive film formed on 316L SS during step by step heat treatment in UHV is proposed in Fig.IV-8.
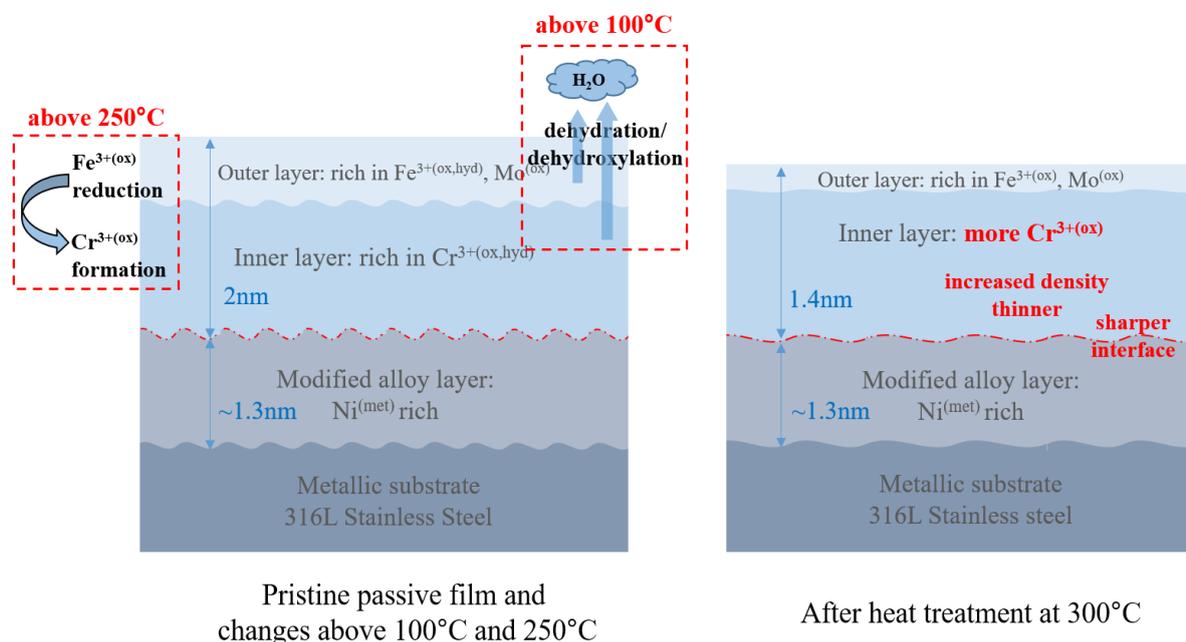


**Fig.IV-8** Model for the passive film evolution during UHV heat treatment

After heat treatment at 300°C, the outer layer of the passive film is rich in iron oxide, with a small amount of molybdenum oxide. The inner part of the passive film is mainly comprised of

chromium oxide. The interface between the outer and inner oxide layer becomes sharper compared to the film formed at room temperature.

## IV-4. Conclusions

The thermal stability of the passive film formed on 316L stainless steel surface in 0.05M $H_2SO_4$ (aq) at 0.4V/SCE has been investigated through step by step heating in UHV up to 300°C by means of ToF-SIMS. The pristine passive film on the 316L stainless steel presents a bilayer structure. The outer layer is enriched in iron oxide and molybdenum oxide while the inner layer is rich in chromium oxide. The interface between these outer and inner layers is not sharp, meaning that some iron oxide is distributed in the inner region.

At temperatures below 100°C, the passive film is stable and the composition is not modified. At heating temperatures higher than 100°C, the inner oxide/outer oxide interface of the passive film stars to become sharper. The temperature of 250°C is a critical point. In the temperatures range between 100°C and 250°C, the main change in the passive film is the decomposition of hydroxide (mainly the Cr hydroxide) and removal of the water ligands, giving a higher chromium oxide content. At temperatures above 250°C, the main change on the passive film is the reduction of Fe oxide caused by bulk Cr diffusing into the inner part of the oxide. The thickness of the passive film (2 nm) is not changed at heating temperatures up to 100°C. Then, at higher temperature (up to 250°C), the passive film thickness gradually decreases to 1.6 nm, which corresponds to the dehydroxylation and dehydration of the oxide film. Very limited change in the film thickness is observed at temperatures higher than 250°C (from 1.6 nm to 1.4 nm). This slight film modification in this temperature range is assigned to the formation of chromium and molybdenum oxide, and reduction of iron oxide.

The passive film, after stepwise heating in UHV, still exhibits a bilayer comprising Fe oxide and Mo oxide in the outer film, and Cr oxide in the inner part. The content of Cr oxide in the film becomes higher than in the pristine passive film. The interface between the outer and inner oxide layer becomes sharper compared to the film formed at room temperature.

### References

[1] V. Maurice, P. Marcus, Progress in corrosion science at atomic and nanometric scales, Progress in Materials Science, 95 (2018) 132-171.

[2] V. Maurice, P. Marcus, Current developments of nanoscale insight into corrosion protection by passive oxide films, Current Opinion in Solid State and Materials Science, 22 (2018) 156-167.

[3] V. Maurice, W. Yang, P. Marcus, X-Ray Photoelectron Spectroscopy and Scanning Tunneling Microscopy Study of Passive Films Formed on (100) Fe-18Cr-13Ni Single-Crystal Surfaces, Journal of the Electrochemical Society, 145 (1998) 909-920.

[4] V. Maurice, W. Yang, P. Marcus, XPS and STM Study of Passive Films Formed on Fe-22Cr (110) Single-Crystal Surfaces, Journal of the Electrochemical Society, 143 (1996) 1182-1200.

[5] Z. Feng, X. Cheng, C. Dong, L. Xu, X. Li, Passivity of 316L stainless steel in borate buffer solution studied by Mott–Schottky analysis, atomic absorption spectrometry and X-ray photoelectron spectroscopy, Corrosion Science, 52 (2010) 3646-3653.

[6] Z. Wang, F. Di-Franco, A. Seyeux, S. Zanna, V. Maurice, P. Marcus, Passivation-induced physicochemical alterations of the native surface oxide film on 316L austenitic stainless steel, Journal of The Electrochemical Society, 166 (2019) C3376-C3388.

[7] N.E. Hakiki, Comparative study of structural and semiconducting properties of passive films and thermally grown oxides on AISI 304 stainless steel, Corrosion Science, 53 (2011) 2688-2699.

[8] Č. Donik, A. Kocijan, J.T. Grant, M. Jenko, A. Drenik, B. Pihlar, XPS study of duplex stainless steel oxidized by oxygen atoms, Corrosion Science, 51 (2009) 827-832.

[9] R.K. Wild, High temperature oxidation of austenitic stainless steel in low oxygen pressure, Corrosion Science, 17 (1977) 87-104.

[10] I. Saeki, H. Konno, R. Furuichi, T. Nakamura, K. Mabuchi, M. Itoh, The effect of the oxidation atmosphere on the initial oxidation of type 430 stainless steel at 1273 K, Corrosion Science, 40 (1998) 191-200.

[11] N.E. Hakiki, M.F. Montemor, M.G.S. Ferreira, M. da Cunha Belo, Semiconducting properties of thermally grown oxide films on AISI 304 stainless steel, Corrosion Science, 42 (2000) 687-702.

[12] L. Ma, F. Wiame, V. Maurice, P. Marcus, New insight on early oxidation stages of austenitic stainless steel from in situ XPS analysis on single-crystalline Fe–18Cr–13Ni, Corrosion Science, 140 (2018) 205-216.

[13] S.C. Tjong, J. Eldridge, R.W. Hoffman, EAS studies of the oxides formed on iron-chromium alloys at 400°C, Applications of Surface Science, 14 (1983) 297-306.

[14] T.J. Driscoll, P.B. Needham, The oxidation of Fe-Cr surface and bulk alloys at 300°C, Oxidation of Metals, 13 (1979) 283-298.

[15] L.Q. Guo, M. Li, X.L. Shi, Y. Yan, X.Y. Li, L.J. Qiao, Effect of annealing temperature on the corrosion behavior of duplex stainless steel studied by in situ techniques, Corrosion Science, 53 (2011) 3733-3741.

[16] L. Zhang, W. Zhang, Y. Jiang, B. Deng, D. Sun, J. Li, Influence of annealing treatment on the corrosion resistance of lean duplex stainless steel 2101, Electrochimica Acta, 54 (2009) 5387-5392.

[17] G. Bombara, A. Alderisio, U. Bernabai, M. Cavallini, The effects of heating in a vacuum on the surface properties of a low chromium stainless steel, Surface Technology, 14 (1981) 17-23.

[18] R.L. Park, J. Houston, D. Schreiner, Chromium depletion of vacuum annealed stainless steel surfaces, Journal of Vacuum Science and Technology, 9 (1972) 1023-1027.

[19] R.K. Wild, Vacuum annealing of stainless steel at temperatures between 770 and 1470K, Corrosion Science, 14 (1974) 575-586.

[20] P. Konarski, K. Kaczorek, J. Senkara, Effects of vacuum heating in AISI 410 and AISI 321 stainless steels' surface layer revealed by SIMS/GDMS depth profile analysis, Surface and Interface Analysis, 43 (2011) 217-220.

[21] V. Maurice, H. Peng, L.H. Klein, A. Seyeux, S. Zanna, P. Marcus, Effects of molybdenum on the composition and nanoscale morphology of passivated austenitic stainless steel surfaces, Faraday Discussions, 180 (2015) 151-170.

[22] E. Gardin, S. Zanna, A. Seyeux, A. Allion-Maurer, P. Marcus, Comparative study of the surface oxide films on lean duplex and corresponding single phase stainless steels by XPS and ToF-SIMS, Corrosion Science, 143 (2018) 403-413.

[23] P. Marcus, V. Maurice, Investigations of Structure and Stability of Passive Films by Surface Analytical Techniques, (2018) 259-266.

[24] E. Gardin, S. Zanna, A. Seyeux, A. Allion-Maurer, P. Marcus, XPS and ToF-SIMS characterization of the surface oxides on lean duplex stainless steel – Global and local approaches, Corrosion Science, 155 (2019) 121-133.

[25] K. Asami, K. Hashimoto, S. Shimodaira, Changes in the surface compositions of FeCr alloys caused by heating in a high vacuum, Corrosion Science, 18 (1978) 125-137.

[26] J.E. Castle, R. Ke, J.F. Watts, Additional in-depth information obtainable from the energy loss features of photoelectron peaks: the oxidation and reduction of an Fe/Cr alloy in oxygen at low partial pressures and ultra high vacuum, Corrosion Science, 30 (1990) 771-798.

[27] S. Bouhieda, F. Rouillard, V. Barnier, K. Wolski, Selective Oxidation of Chromium by O2 Impurities in CO2 During Initial Stages of Oxidation, Oxidation of Metals, 80 (2013) 493-503.

[28] I. Barin, Thermochemical data of pure substances, VCH, (1989).

[29] F. Richardson, The Thermodynamics of Substances of Interest in Iron and Steel Making from 0°C to 2400°C I-Oxides, The Journal of the Iron and Steel Institute, 160 (1948) 261-270.

[30] H.J.T. Ellingham, Reducibility of oxides and sulfides in metallurgical processes, Journal of the Society of Chemical Industry, 63 (1944) 125-133.

[31] T. Ohmi, Y. Nakagawa, M. Nakamura, A. Ohki, T. Koyama, Formation of chromium oxide on 316L austenitic stainless steel, Journal of Vacuum Science & Technology A: Vacuum, Surfaces, and Films, 14 (1996) 2505-2510.

# Chapter V

# Ion transport mechanisms in the passive film formed on 304L stainless steel studied by ToF-SIMS with $^{18}$O isotopic tracer

## Abstract

The ion transport in the pre-formed passive film on 304L stainless steel surface has been investigated by in situ ToF-SIMS with isotopic tracer. The passive film, formed electrochemically in sulfuric acid, has a bilayer structure with outer iron oxide and inner chromium oxide layers. Further exposure of the passive film to $^{18}$O$_2$ gas (isotopic tracer) at 300°C reveals that outward cation diffusion is the governing ion transport mechanism for the oxide growth. The parabolic rate constant for the oxide growth was determined. The cation diffusion coefficient is found to be markedly higher than the oxygen diffusion coefficient.

## V-1. Introduction

Stainless steels (SS) are widely used in many industries, including energy (from nuclear to solar power plants), spacecraft, pulp and paper industry, due to their high corrosion resistance, which is assigned to the nanometer thick oxide film naturally formed on the surface [1-6]. The composition and structure of the oxide film formed on SS surface has been extensively studied [7-14]. The results revealed that oxide film exhibits a bilayer structure with an iron rich outer layer and a chromium rich inner layer. The surface oxide film is known to play a key role in the corrosion resistance of metals and alloys. Thus, the understanding of their nature, structure, composition and growth kinetics is important and requires a detailed knowledge of the ion-transport mechanisms [15-17]. Until now, there is still a lack of data on the ion transport process in the oxide film formed on stainless steel surfaces.

Oxidation kinetics of metals or alloys are controlled either by the diffusion of cation species (outward diffusion of metallic ions through the oxides) [18] or anion species (inward oxygen

diffusion) [19]. Mechanisms including both cation and anion diffusion have also been reported [20, 21]. Using Time of Flight Secondary Ions Spectrometry (ToF-SIMS), an isotopic tracer, such as 18O, can be used to identify the predominant ion transport during surface oxidation, by exposing the sample to a 'labelled' $^{18}O_2$ atmosphere. Determination of the $^{18}O_2$ tracer specific distribution in the grown oxide layer can disclose the mobile species in the oxidation process [22]. Graham et al. [19] and Poulain et al. [23] have investigated the ion transport in $Cr_2O_3$ oxide film. Both works used the "two oxidation step procedure" consisting in the successive use of the two oxygen isotopes ($^{16}O$ and $^{18}O$), the position of each oxide being determined by SIMS. In Graham's work, the oxidation of clean polycrystalline and monocrystalline (100) Cr metallic surfaces at temperatures above 800°C was studied. The first oxidation in dry and low $^{18}O_2$ gas followed by re-oxidation in low pressure $^{16}O_2$ gas, allowed the authors to conclude that under the temperature and pressure conditions used, the oxide film grows by outward cation diffusion. In Poulain's work, the Cr metal oxidation was performed in situ at 300°C in the ToF-SIMS main chamber (the native oxide being reduced by successive sputtering annealing prior to the oxidation). A first low $^{16}O_2$ pressure oxidation was followed by a low pressure re-oxidation with pure $^{18}O_2$ gas. The use of isotopic tracer revealed that the new 18-oxide was formed at the inner metal/oxide interface indicating that the oxidation process is governed by anion diffusion under the conditions used. The different ion transport mechanisms in the growing chromium oxide may be assigned to the oxidation temperature and pressure ranges which may affect the crystal structure, the defect type in the oxide [24, 25] and the intra or transgranular nature of ion transport. The two-stage oxidation method using oxygen isotopes has also been applied to study the ion transport mechanisms in the oxide film of pure Zr at 450K, and oxygen transport was found to be the governing oxidation process [26]. More recently, the high temperature oxidation mechanisms for Ni-based alloys, including Alloy 600 [27] and Hastelloy BC-1[18], have been investigated in situ by ToF-SIMS with oxygen isotopic tracer. Anion diffusion was found to be the dominant ion transport mechanism for Alloy 600, whereas cation diffusion is the governing oxidation mechanism for Hastelloy BC-1 alloy.

Measurements of ion transport mechanisms in the oxide film formed on Fe-Cr based alloys are limited, and mainly focused on the ion diffusivities in the oxide scales at high temperatures (above 700°C) [28-33]. These data were performed by depositing the isotopic markers ($^{54}Cr$ and $^{57}Fe$) on the oxidized surface of the alloy followed by diffusion annealing. Lobnig et al. [28] determined cation diffusivities in the oxide film on Fe-20Cr and Fe-20Cr-

12Ni at 900°C. Sabioni et al. [31-33] studied the ion diffusion in the oxide films grown on different alloys (AISI 304 austenitic stainless steel, AISI 439 ferritic stainless steel and a ferritic Fe-15Cr alloy), between 750°C and 900°C, in air, and the ion diffusivities in the oxide scales of these steels were calculated. Although these works provide values of ion diffusivity in the oxide film, they do not elucidate the ion transport processes during oxide growth.

The aim of the present work was to investigate the ion transport process in a pre-formed passive film on 304L SS. The 18O isotopic tracer was used for in situ ToF-SIMS re-oxidation experiments to investigate the ion transport process in the passive film.

## V-2. Experimental

### V-2.1. Sample preparation

Polycrystalline austenitic 304L stainless steel, purchased from Goodfellow company, with annealed state, was used. The alloy composition is Fe-18%Cr-10%Ni (wt%). The sample surface was mechanically polished down to 0.25 μm with diamond paste and then successively washed with acetone, ethanol and water in ultrasonic bath for 10 mins. The sample was then dried in compressed air, and finally a controlled passive film was formed electrochemically on the surface.

A Gamry electrochemical workstation was used for electrochemical experiments. The electrochemical passivation was performed with a standard three-electrode configuration with an Au counter electrode and a saturated calomel electrode as the reference electrode. The electrochemical passivation was done in 0.05M $H_2SO_4$ prepared with ultrapure chemicals (VWR®) and Millipore® water. Before measurement, the solution was deaerated by Ar bubbling for 30 minutes.

### V-2.2. ToF-SIMS investigation

ToF-SIMS depth profiles were obtained using a ToF-SIMS 5 spectrometer (IONTOF GmbH – Münster, Germany). A pulsed 25 keV $Bi^+$ primary ion source was employed for analysis, delivering 1.2 pA and 0.1 pA currents over a $100 \times 100$ μm$^2$ area. The pulsed primary ion beam was used in the bunched mode, with pulse width of 1.2 ns, providing a resolution M/dM=7500. The $Bi^+$ primary ion source with 0.1 pA current was used to get the depth profiles of oxygen signals ($^{16}O^-$ and $^{18}O^-$), since higher current will result in the saturation of oxygen signals on the detector. In this paper, all the oxygen depth profiles ($^{16}O^-$ and $^{18}O^-$)

were obtained with low $Bi^+$ current (0.1pA), whereas the depth profiles of all the other ion signals were obtained with higher $Bi^+$ current (1.2 pA) to get higher signals. Depth profiling was carried out by interlacing primary beam with sputtering using a 0.5 keV $Cs^+$ sputter beam giving a 17 nA target current over a $300 \times 300$ $\mu m^2$ area. $Cs^+$ beam was used for sputtering due to its contribution to the secondary ionization yield. Both $Bi^+$ and $Cs^+$ ion beams were impinging the sample surface at an angle of 45° and were aligned in such a way that the analyzed ions were taken from the centre of the sputtered crater.

| | Species | Characteristic ion |
|---|---|---|
| Metallic substrate | Metallic Fe | $Fe_2^-$ |
| | Metallic Ni | $Ni_2^-$ |
| | Metallic Cr | $Cr_2^-$ |
| Pre-formed oxide ($^{16}O$) | Oxide/Hydroxide | $^{16}O^-$ / $^{16}OH^-$ |
| | Iron oxide | $Fe^{16}O_2^-$ ; $Fe_2{}^{16}O_3^-$ |
| | Chromium oxide | $Cr^{16}O_2^-$ |
| Newly-formed oxide ($^{18}O$) | Oxide | $^{18}O^-$ |
| | Iron oxide | $Fe^{18}O_2^-$ |
| | Chromium oxide | $Cr^{18}O_3^-$ |

**Table V-1** ToF-SIMS characteristic ions used to characterize the composition and structure of the oxide film formed on 304L SS

ToF-SIMS depth profiles were recorded to determine the composition and layer structure of the passive film. The characteristic ions were selected as shown in Table V-1. The pre-formed iron oxide is associated to two different characteristic ions ($Fe^{16}O_2^-$ with high intensity and $Fe_2{}^{16}O_3^-$ with low intensity). Despite the high mass resolution that allows us to locate the maximum intensity of each single peak, the characteristic ion of newly formed chromium oxide ($Cr^{18}O_2^-$) slightly overlaps with the tail of characteristic ion of the pre-formed iron oxide ($Fe^{16}O_2^-$). To avoid this problem, $Cr^{18}O_3^-$ and $Fe_2{}^{16}O_3^-$ ions (that do not suffer for overlapping) are used to characterize the oxide composition during re-oxidation in $^{18}O_2$ of the oxide pre-formed in $H_2SO_4$. It should be noted that the selected ions do not reflect the real stoichiometry of the species constituting the sample, but are the appropriate markers of the studied species. Since ToF-SIMS is a non-quantitative technique (due to strong matrix effect on secondary ion emission), the intensities of the plotted ions in the depth profiles cannot be compared directly and do not reflect the concentrations of the associated species in the substrate. However, variations of a single signal reflect mainly in-depth variations of the

concentration. The depth profiles are plotted versus sputtering time. The sputtering rate has been calculated knowing for passivated 304L SS (in $H_2SO_4$ at 0.4V/SCE) (i) the total oxide layer thickness measured from XPS (results not shown here), and (ii) the position of the metal/oxide interface on the ToF-SIMS depth profile. Assuming a constant sputtering rate (0.015 nm/s) in the oxide, independent of the oxide layer composition, the sputtering time directly translates into oxide thickness.
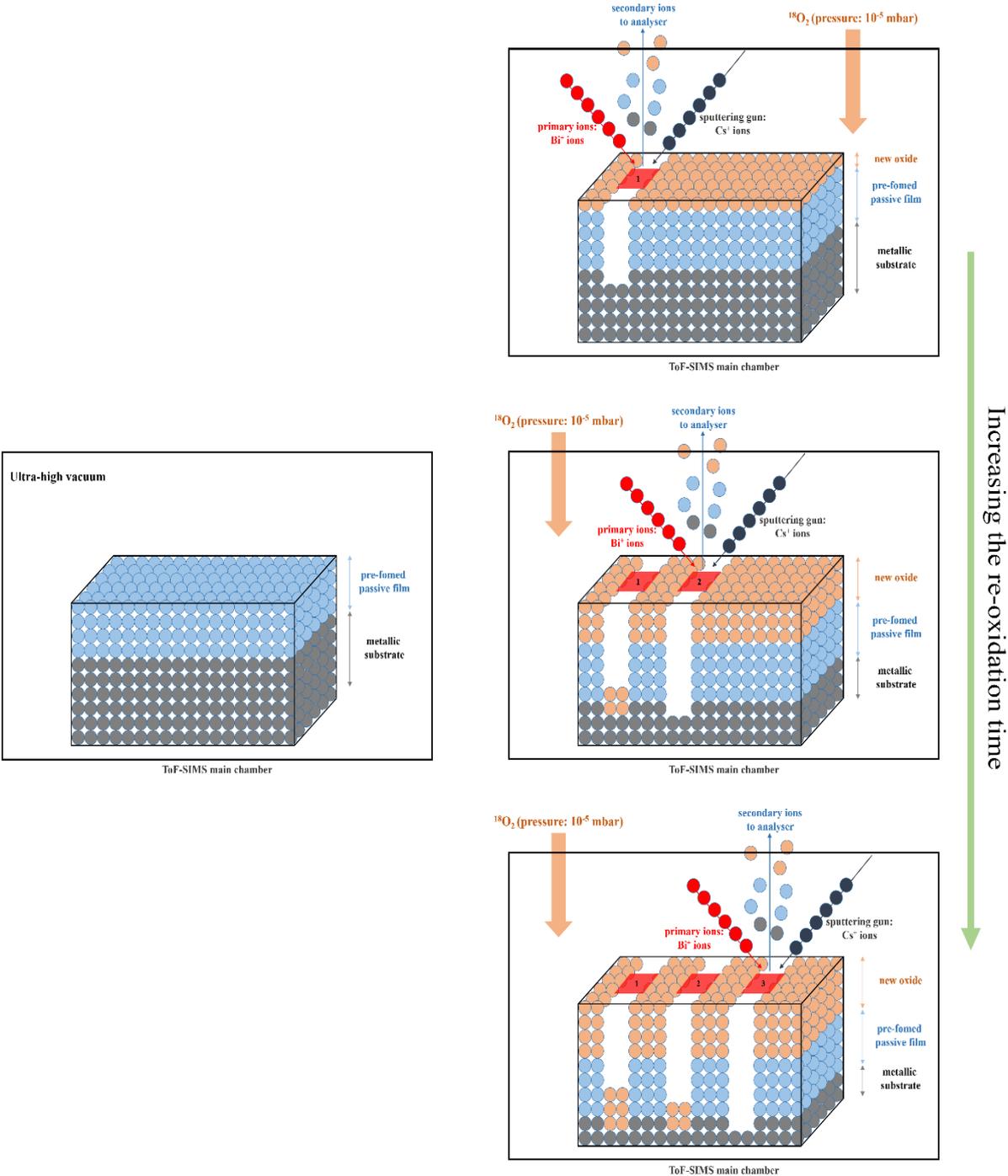


**Fig.V-1** Scheme of the *in situ* experiment in the ToF-SIMS spectrometer

Immediately after the specimen was introduced into the ToF-SIMS analysis chamber, and prior to the application of heat treatment, the passive film was analysed at both primary beam currents. Due to the destructive nature of sputtering, each depth profile was collected at a different, unperturbed area of the sample surface. The specimen was then heated up to a temperature of $300 \pm 1\ °C$ (an IONTOF heating stage was used). Modifications of the passive oxide film due to the increase of temperature were studied [34]. A precision leak valve was then used to introduce a constant and low $^{18}O_2$ pressure into the analysis chamber, such that the partial pressure $P(^{18}O_2)$ was constant at $1\times10^{-5}$ mbar. After the designated oxidation time had elapsed, the leak valve was closed while the sample temperature was maintained at $300 \pm 1\ °C$, and the chamber immediately pumped down to the base pressure ($10^{-9}$ mbar), in order to record the ToF-SIMS depth profiles. A scheme of the *in situ* re-oxidation experiment is shown in Fig.V-1.

## V-3. Results and discussion

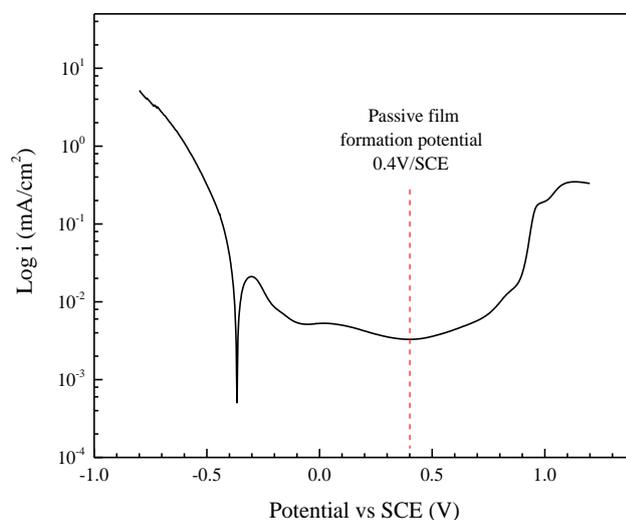### V-3.1. Passive film formation and analysis



**Fig.V-2** Polarization curve of the 304L SS in 0.05M $H_2SO_4$ with a scan rate of 1mV/s

Fig.V-2 shows the polarization curve obtained on 304L SS in 0.05M $H_2SO_4$ aqueous solution with a scan rate of 1mV/s. Within the passive range (-0.1~0.8V/SCE), the lowest current is obtained at 0.4V/SCE. Anodic polarization at this potential in sulfuric acid causes the Cr oxide enrichment and Fe oxide dissolution, which leads to the formation of passive film with high corrosion resistance [7, 8]. In this study, a static potential polarization at 0.4V/SCE was

applied to the 304L SS for 1h to form a protective passive film on the stainless steel surface.
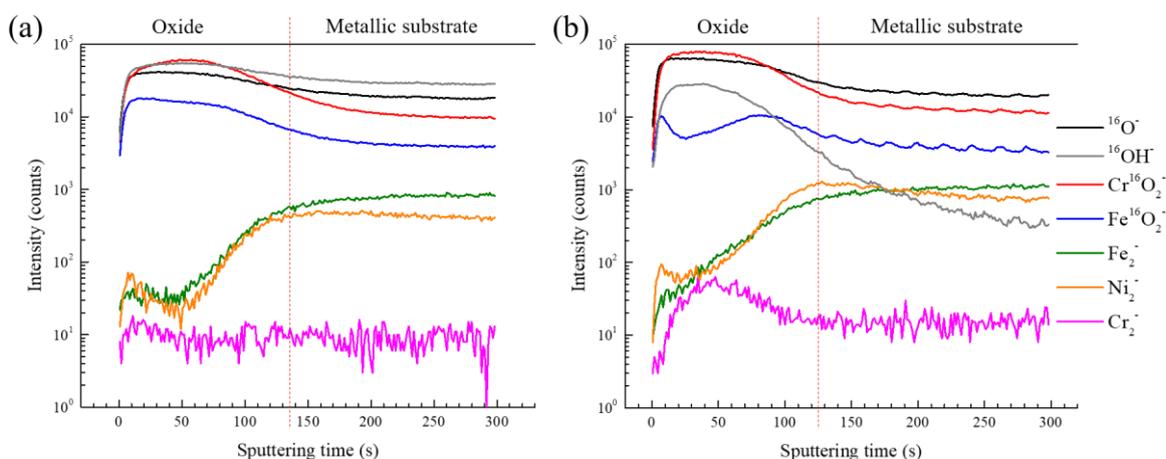


**Fig.V-3** ToF-SIMS depth profiles for passive film formed on 304L SS surface in 0.05M $H_2SO_4$(aq) at 0.4V/SCE for 1h at **(a)** room temperature, and **(b)** after heat treatment in vacuum (UHV) at 300°C (the position of the oxide/metal interface is determined by the maximum intensity of $Ni_2^-$ in the depth profile)

Fig.V-3(a) shows the ToF-SIMS negative ion depth profiles for the passive film formed on 304L SS at room temperature. The position of the metal/oxide interface on the ToF-SIMS depth profiles is crucial to extract the total thickness of the oxide layer. As previously reported, the $Ni_2^-$ species is a good marker of the metal/oxide interface (maximum intensity of $Ni_2^-$ signal) [27, 35]. Thus, the passive film thickness is estimated to be 2 nm when the 304L SS sample is passivated 1h at room temperature in 0.05M $H_2SO_4$ at 0.4V/SCE.

Focusing on the layered structure of the passive film formed at room temperature (Fig.V-3(a)), it appears that the $Fe^{16}O_2^-$ signal peaks in the outer part of the passive film and decreases slowly through the oxide film region, indicating that oxidized iron is mainly located in the outer part of the film with low content in the inner part of the film. On the contrary, the $Cr^{16}O_2^-$ depth profile shows its maximum in the inner part of the film. Thus, chromium oxide is mainly located in the inner oxide layer. This duplex structure for the passive oxide film on 304L SS surface at room temperature is consistent with previous studies [7, 8].

In order to investigate at higher temperature, the transport of species in the passive film formed on 304L SS, we first studied the thermal stability of this electrochemically formed passive film when heated up to 300°C, so that the re-oxidation experiments could be carried out under $^{18}O_2$ at this temperature. At lower temperatures, the ion-transport process would be very slow, and it would take a long time to observe the transport of species in the passive

film. At temperatures higher than 300°C, the composition and structure of the pre-formed passive film would be changed too rapidly. Based on the previous study of the thermal stability of the passive film in ultra-high vacuum by ToF-SIMS, it is known that 300°C is a suitable temperature, ensuring sufficiently fast kinetics of the ion transport and stability of pre-formed passive film [34].

Fig.V-3(b) shows the characteristic ToF-SIMS depth profile for the electrochemically formed passive film in $H_2SO_4$ after increasing the temperature to 300°C under UHV. The passive film thickness is estimated to be 1.9 nm. The structure of the passive film remains duplex as indicated by the $Fe^{16}O_2^-$ signal that reaches its maximum intensity in the outer part of the oxide scale whereas the $Cr^{16}O_2^-$ signal has its maximum in the inner part of the oxide. However some changes are observed when increasing the temperature from room temperature to 300°C: (i) the lower intensity of the $Fe^{16}O_2^-$ in the outer oxide, which is correlated with (ii) the slightly higher intensity of the $Cr^{16}O_2^-$ signal, as well as its distribution throughout the oxide film (signal spreading in the oxide). These observations have already been done and explained in a previous work on 316 SS when studying the thermal stability of the native oxide film [34]. This is assigned to (i) the reduction of the Fe hydroxide species that happens above 100°C and (ii) the formation of chromium oxide at the expense of iron oxide when the temperature is above 250°C. The decrease of the passive oxide film thickness is assigned to the dehydroxylation and dehydration. Nevertheless, the structure of the oxide is still a bilayer and the main species in the film are still iron and chromium oxides.

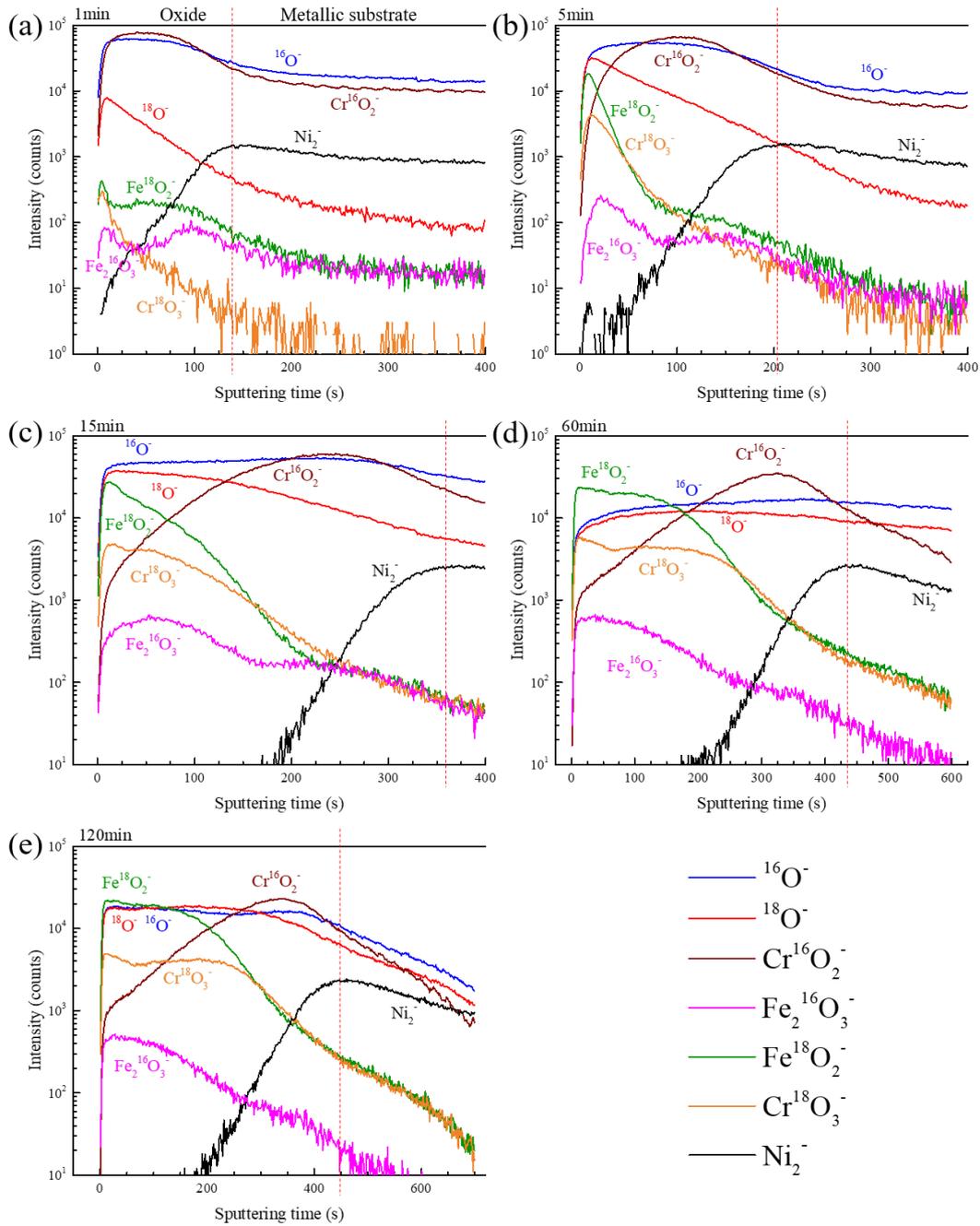## V-3.2. Investigation of ion transport process in oxide layers



**Fig.V-4** ToF-SIMS profiles obtained on pre-passivated 304L SS after re-oxidation at 300°C for **(a)** 1 min, **(b)** 5 min, **(c)** 15min, **(d)** 1h and **(e)** 2 h (the position of the oxide/metal interface is determined by the maximum intensity of $Ni_2^-$ in the depth profile)

Fig.V-4 shows the ToF-SIMS depth profiles obtained on the pre-passivated 304L SS after exposure to low pressure isotopic $^{18}O_2$ gas ($10^{-5}$ mbar) at 300°C for different times. After 1 min of re-oxidation (Fig.V-4(a)), the metal/oxide interface, still defined by the maximum

intensity of the $Ni_2^-$ signal, is located at 137.5s of sputtering time, which corresponds to 2.1 nm. By looking at both the $^{16}O^-$ and $^{18}O^-$ signals on the depth profile, one observes that the new $^{18}O^-$ signal is located at the prior oxide surface. A closer examination of $Cr^{16}O_2^-$, $Fe_2^{16}O_3^-$, $Cr^{18}O_3^-$ and $Fe^{18}O_2^-$, characteristic signals of the Cr oxide and Fe oxide formed with $^{16}O$ and $^{18}O$, respectively, confirms the location of the newly formed oxides (during re-oxidation in $^{18}O$ gas) at the surface of the prior oxide film, the pre-formed $^{16}O$ species remaining deeper into the oxide scale.

With further exposure to $^{18}O_2$ for 5 min, the oxide film becomes thicker, from 2.1 nm to 3.1 nm (oxide/metal interface recorded for 205s of sputtering). The intensities of $Cr^{18}O_3^-$ and $Fe^{18}O_2^-$ profiles are found to significantly increase, and their location at the external surface indicates that the oxide film thickens at the oxide/gas interface due to the formation of both chromium and iron oxides. The re-oxidation process clearly reveals that, for short re-oxidation time, the oxide growth is mainly governed by the transport of Cr and Fe cation species through the pre-formed oxide.

For a re-oxidation time of 15 min, the $Ni_2^-$ signal indicates that the metal/oxide interface is reached after 360s of sputtering, corresponding to a total oxide layer thickness of 5.4 nm. The oxide film is clearly growing. Looking at the depth profile of $^{18}O^-$ signal, its maximum intensity remains located at the outer surface, and its intensity slowly decreases through the pre-formed passive oxide layer. This shows that the newly oxides ($^{18}O$) is still formed at the oxide/gas interface due to cation diffusion through the oxide, but that $^{18}O$ species also diffuse towards the metal/oxide interface following an inward isotopic exchange. Although the main growth mechanism is still by outward cation diffusion, there is clearly an $^{18}O^-$ concentration gradient in the inner oxide, assigned to $O^{2-}$ inward diffusion and isotopic exchange. Isotopic exchange in such experiments has already been described by Poulain et al. [23] for oxidation of pure Cr sample and Voyshnis et al. [27] for oxidation of nickel base alloy.

For 1h of re-oxidation, the oxide film thickness is 6.5 nm (corresponding to 435s of sputtering), while for a 2h re-oxidation time, the thickness of the oxide film remains nearly constant (6.8 nm, ~ 450s of sputtering time). By looking at the depth profiles of the $^{16}O^-$ and $^{18}O^-$ signals, one observes that the $^{18}O^-$ signal still has a wide peak in the external surface and the $^{16}O^-$ signal peak in the inner region for 1h re-oxidation, whereas for 2h re-oxidation, the $^{16}O^-$ and $^{18}O^-$ depth profiles overlap in the oxide film region, which is assigned to the $^{16}O/^{18}O$ isotopic exchange. Thus, after 1h of re-oxidation, the oxide film reaches a quasi-stationary

state, and the main mechanism dominating the depth profile is the $^{16}O/^{18}O$ isotopic exchange.



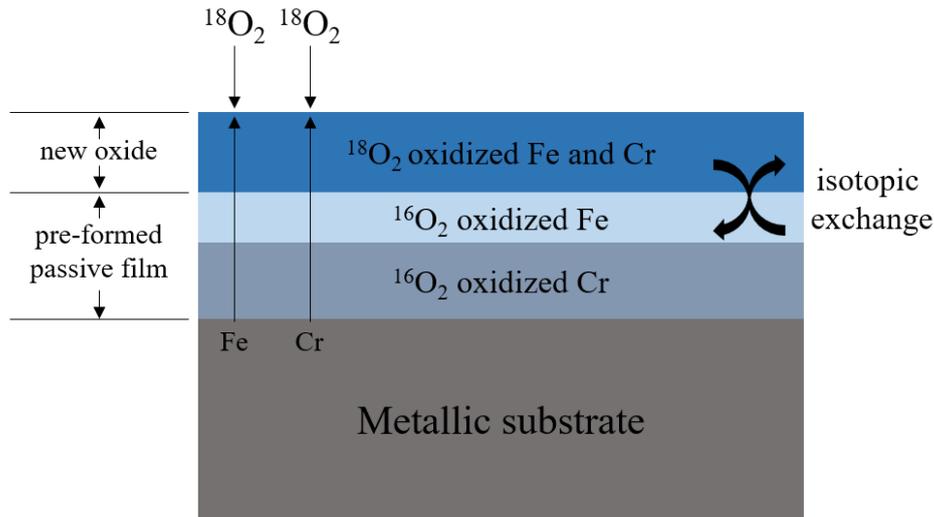**Fig.V-5** Scheme of the evolution of the passive oxide layer exposed to $^{18}O_2$ at 300°C

A scheme of the evolution of the oxide layer exposed to $^{18}O_2$ at 300°C based on the ToF-SIMS depth profiling data is shown in Fig.V-5. As demonstrated before, the main mechanism governing the growth of the oxide for short re-oxidation of the pre-passivated surface is the outward cation transport, meaning that iron and chromium cations diffuse from the metallic substrate to the oxide/gas interface where they react with oxygen ($^{18}O_2$). Thus, the newly formed chromium and iron oxides are located at the outer oxide/gas interface. The higher $^{18}O$ concentration at the external surface leads to an oxygen isotopic exchange with $^{16}O$. After 15 min of re-oxidation with low $^{18}O_2$ pressure, cation diffusion is still governing the growth of the oxide. Isotopic exchange is also evidenced as shown by the $^{18}O^-$ profile into the pre-formed $^{16}O$ oxide. At longer re-oxidation time (more than 1h), the oxide film reaches a quasi-stationary thickness (the growth rate becomes very low) and the isotopic exchange becomes the main mechanism leading to increased amount of $^{18}O$ in the inner part of the oxide layer. Some volatilization of chromium oxide evidenced by Poulain et al. [23] for oxidation of pure Cr at the same temperature cannot be excluded.

The thickness of the oxide layer, measured by ToF-SIMS at different oxidation times on pre-passivated 304L SS during re-oxidation at 300°C is reported in Fig.V-6. The kinetics of re-oxidation is well fitted by a logarithmic-type law, which, according to previous work [23, 35], can be explained by the competition between parabolic growth and oxide layer volatilization. From Fig.V-6, two regions can be observed: a first region from 0 min to 30 min of fast oxide layer growth (with chromium and iron oxides appearing at the outer surface), as previously.

Then, for longer re-oxidation, the oxide film growth becomes slower and a quasi-stationary thickness is observed (which is explained by a growth rate equal to the volatilization rate).
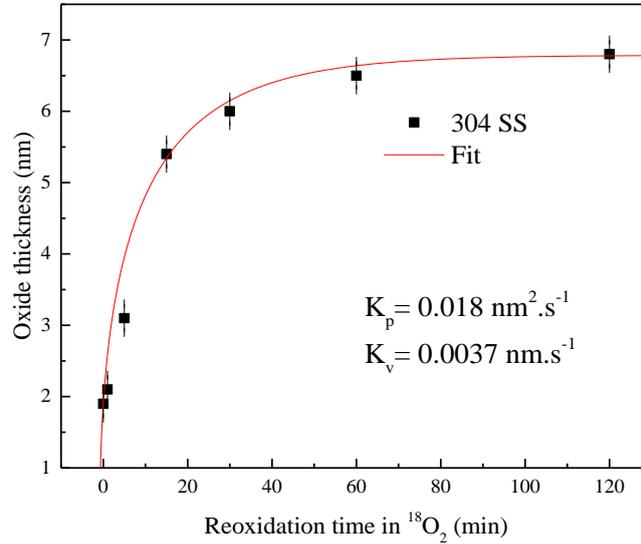


$K_p = 0.018 \ nm^2.s^{-1}$

$K_v = 0.0037 \ nm.s^{-1}$

**Fig.V-6** Oxidation kinetics of 304L SS at 300°C. Fit of kinetics by Eq.1 (solid line)

The oxidation kinetics can then be fitted by Eq. (1), as shown in a previous paper [23]:

$$t = \frac{k_p}{k_v^2}[-\frac{k_v}{k_p}(x - x_0) - \ln\left(1 - \frac{k_v}{k_p}(x - x_0)\right)]$$
(equation V-1)

where $k_p$ is the parabolic constant, $k_v$ is the constant of volatilization, and $x_0$ is the thickness of pre-passivated oxide film.

Both the fitting curve and the results calculated for the parabolic and volatilization constants are shown in Fig.V-6. The values of $k_p$ derived from the fit is $1.8 \times 10^{-2}$ $nm^2.s^{-1}$ and $k_v$ is $3.7 \times 10^{-3}$ $nm.s^{-1}$. These values are close to that calculated for pure Cr at 300°C ($k_p = 1.9 \times 10^{-2}$ $nm^2.s^{-1}$ and $k_v = 1.8 \times 10^{-3}$ $nm.s^{-1}$) [23], but $k_p$ is higher than the value obtained on polycrystalline Ni alloy ($k_p = 5.9 \times 10^{-3}$ $nm^2.s^{-1}$) [35]. This difference is assigned to the different structures of the oxide film.

On the basis of a simplified relationship between diffusion coefficient and parabolic rate constant $k_p = 2D_c$ [36], one would conclude that the diffusion coefficient for outward cation diffusion ($D_c$) in the oxide film is $9 \times 10^{-17}$ $cm^2.s^{-1}$.

Although, as discussed above, the main ion transport mechanism during the re-oxidation

process of passive film formed on 304L SS is outward cation diffusion, a mixed mechanism including both cation and anion diffusion cannot be excluded, according to the depth profile of $^{18}O^-$ in the oxide layer. Thus, it is interesting to assess the oxygen diffusion coefficient through the oxide film and compare it to the cation diffusion coefficient. The semi-infinite integration of Fick's second diffusion law for one-dimensional diffusion, modified to include isotopic exchange can be tested on the $^{18}O^-$ depth profiles, as already done by Voyshnis et al. [27]. Possible chemical reactivation of Cs implanted during the acquisition of the depth profile and chemical activity of the diffusing species are not considered in the model. With this model, the oxygen diffusion coefficient [$D_o$, in cm$^2$.s$^{-1}$] and isotopic exchange coefficient [k, in at.cm$^{-2}$.s$^{-1}$] can be obtained. The differential equation to be solved is the following:

$$\frac{\partial C}{\partial t} = -D\frac{\partial^2 C}{\partial x^2} + k_c C \qquad \text{(equation V-2)}$$

where the first term is for the diffusion and the second one for isotopic exchange, C is the concentration of $^{18}O$ in the oxide film at depth x and after oxidation time t.

This differential equation can be analytically solved:

$$\frac{C(x,t) - C_{max}}{C_0 - C_{max}} = \frac{1}{2}\left\{ exp-\left(\sqrt{\frac{k}{D}}x\right)erfc\left(\frac{x}{2\sqrt{Dt}} - \sqrt{kt}\right) + exp\left(\sqrt{\frac{k}{D}}x\right)erfc\left(\frac{x}{2\sqrt{Dt}} + \sqrt{kt}\right) \right\}$$

$$\text{(equation V-3)}$$

using the following boundary conditions:

$$\begin{cases} C(x,0) = 0, x > 0 \\ C(0,t) = C_0, t > 0 \\ C(x = M/O\,, t) = C_{max}, t > 0 \end{cases} \qquad \text{(equation V-4)}$$

where $C_{max}$ is the initial $^{18}O$ concentration at the metal/oxide interface, $C_0$ the initial $^{18}O$ concentration at the outer interface (x = 0).

More details on this model are provided in ref [23, 27].

Eq.V-3 takes into account both the solid state diffusion and the isotopic exchange, and is used to fit the experimental data and determine the oxygen diffusion coefficient ($D_o$) and the isotopic exchange coefficient of the O species. The results shown in Fig.V-7 are the best fits of the experimental data of normalized depth profile of the $^{18}O^-$ signals (black points) with the theoretical model (red curve) for the 304L SS re-oxidation in $^{18}O_2$ for 1 min (Fig.V-6(a)) and

5 min (Fig.V-6(b)). It is observed that the model fits well the experimental data. The oxygen diffusion coefficients ($D_o$) determined in this way are $2 \times 10^{-17}$ cm$^2$.s$^{-1}$ (Fig.V-7(a)) and $1.6 \times 10^{-17}$ cm$^2$.s$^{-1}$ (Fig.V-7(b)), and the isotopic exchange coefficients (k) are $3.7 \times 10^{-10}$ at.cm$^{-2}$.s$^{-1}$ (Fig.V-7(a)) and $1 \times 10^{-11}$ at.cm$^{-2}$.s$^{-1}$ (Fig.V-7(b)). For longer re-oxidation times, the experimental data cannot be fitted by this model, because of the significant modifications of the structure and composition of the oxide after 15 min of re-oxidation, as shown in Fig.V-4(c).
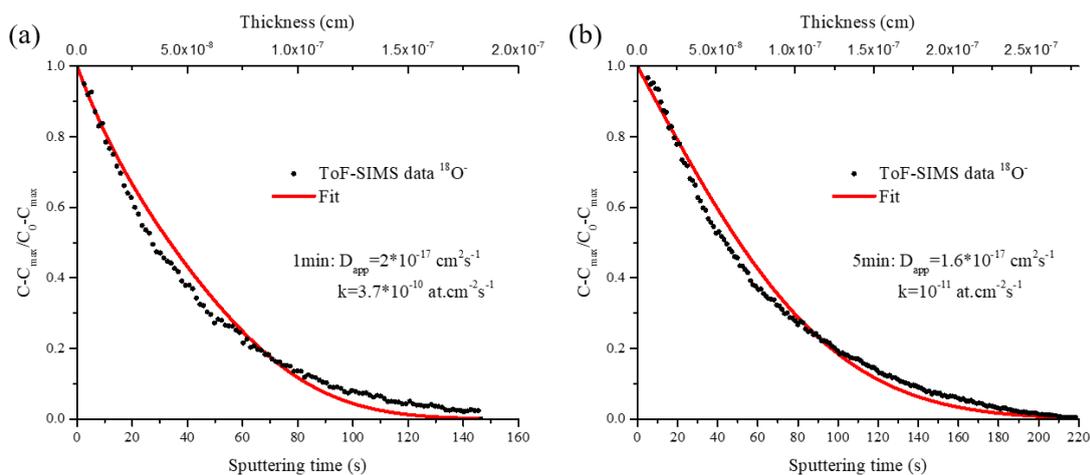


**Fig.V-7** Normalized $^{18}$O$^-$ ion ToF-SIMS depth profiles (black points) and fit of the experimental data with the theoretical model (red solid line), for the 304L SS re-oxidized in $^{18}$O$_2$ *in situ* in the ToF-SIMS chamber at 300 °C during (a)1 min and (b) 5 min.

It appears that the cation diffusion coefficient ($9\times10^{-17}$ cm$^2$.s$^{-1}$) deduced from the thickness measurement is about 5 times higher than the oxygen diffusion coefficient ($1.6 \sim 2\times 10^{-17}$ cm$^2$.s$^{-1}$). Thus, outward cation diffusion plays the main role in the oxide growth on 304L SS. This is in agreement with observations done during the oxidation of Fe-15%Cr alloy [32], at 750°C, where $D_{Fe}$ ($3.6\times10^{-16}$ cm$^2$.s$^{-1}$) and $D_{Cr}$ ($2\times10^{-16}$ cm$^2$.s$^{-1}$) are one order of magnitude higher than $D_O$ ($3.4\times10^{-17}$ cm$^2$.s$^{-1}$).

## V-4. Conclusions

The nature, composition and structure of the passive film formed on 304L SS in acid solution and after heating in vacuum at 300°C has been investigated by ToF-SIMS. The passive oxide film formed electrochemically in 0.05 M H$_2$SO$_4$ solution at 0.4V/SCE for 1h has a duplex structure, comprising an iron rich outer layer and a chromium rich inner layer. The duplex structure of the passive film is thermally stable at 300°C in vacuum, with however partial dehydroxylation and iron oxide reduction.

Insight into the ion transport process in the pre-formed passive film on 304L SS has been obtained by ToF-SIMS. The pre-formed passive film was exposed to $^{18}O_2$ at 300°C. The enrichment of $^{18}O$ species at the oxide/gas interface, provided direct evidence of outward cation diffusion. After 1h re-oxidation, the oxide film reaches a quasi-stationary thickness, assigned to the limiting transport of cation from the substrate and the chromium oxide evaporation. Then the $^{16}O$ /$^{18}O$ isotopic exchange becomes the main mechanism governing the O depth profile. Based on a model built up to describe the re-oxidation kinetics obtained from the measurements, the parabolic and volatilization constants for the oxide growth are determined. They are 0.018 $nm^2.s^{-1}$ and 0.0037 $nm.s^{-1}$, respectively. According to the parabolic constant, the diffusion coefficient of cations is found to be $D_c=9\times10^{-17}$ $cm^2.s^{-1}$, which is several times higher than the oxygen diffusion coefficient ($D_o=1.6 \sim 2\times 10^{-17}$ $cm^2.s^{-1}$) determined from the $^{18}O$ depth profile. This work evidences that the growth of the passive oxide film is governed by outward cation diffusion.

### References

[1] V. Maurice, P. Marcus, Current developments of nanoscale insight into corrosion protection by passive oxide films, Current Opinion in Solid State and Materials Science, 22 (2018) 156-167.

[2] T. Massoud, V. Maurice, L.H. Klein, P. Marcus, Nanoscale morphology and atomic structure of passive films on stainless steel, Journal of the Electrochemical Society, 160 (2013) C232-C238.

[3] V. Maurice, P. Marcus, Passive films at the nanoscale, Electrochimca Acta 84 (2012) 129-138.

[4] J.R. Davis, Stainless steels, ASM international, 1994.

[5] S.E. Ziemniak, M. Hanson, Corrosion behavior of 304 stainless steel in high temperature, hydrogenated water, Corrosion Science, 44 (2002) 2209-2230.

[6] B. Stellwag, The mechanism of oxide film formation on austenitic stainless steels in high temperature water, Corrosion Science, 40 (1998) 337-370.

[7] V. Maurice, H. Peng, L.H. Klein, A. Seyeux, S. Zanna, P. Marcus, Effects of molybdenum on the composition and nanoscale morphology of passivated austenitic stainless steel surfaces, Faraday Discussions, 180 (2015) 151-170.

[8] Z. Wang, F. Di-Franco, A. Seyeux, S. Zanna, V. Maurice, P. Marcus, Passivation-induced physicochemical alterations of the native surface oxide film on 316L austenitic stainless steel, Journal of the Electrochemical Society, 166 (2019) C3376-C3388.

[9] E. Gardin, S. Zanna, A. Seyeux, A. Allion-Maurer, P. Marcus, XPS and ToF-SIMS characterization of the surface oxides on lean duplex stainless steel – Global and local approaches, Corrosion Science, 155 (2019) 121-133.

[10] E. Gardin, S. Zanna, A. Seyeux, A. Allion-Maurer, P. Marcus, Comparative study of the surface oxide films on lean duplex and corresponding single phase stainless steels by XPS and ToF-SIMS, Corrosion Science, 143 (2018) 403-413.

[11] Z. Wang, E.-M. Paschalidou, A. Seyeux, S. Zanna, V. Maurice, P. Marcus, Mechanisms of Cr and Mo Enrichments in the Passive Oxide Film on 316L Austenitic Stainless Steel, Frontiers in Materials, 6 (2019) 232.

[12] S. Tardio, M.-L. Abel, R.H. Carr, J.E. Castle, J.F. Watts, Comparative study of the native oxide on 316L stainless steel by XPS and ToF-SIMS, Journal of Vacuum Science & Technology A, 33 (2015) 05E122.

[13] P. Stefanov, D. Stoychev, M. Stoycheva, T. Marinova, XPS and SEM studies of chromium oxide films chemically formed on stainless steel 316 L, Materials Chemistry and Physics, 65 (2000) 212-215.

[14] X. Cheng, Z. Feng, C. Li, C. Dong, X. Li, Investigation of oxide film formation on 316L stainless steel in high-temperature aqueous environments, Electrochimical Acta 56 (2011) 5860-5865.

[15] A. Seyeux, V. Maurice, P. Marcus, Oxide film growth kinetics on metals and alloys I. Physical model, Journal of the Electrochemical Society, 160 (2013) C189-C196.

[16] D. Barnes, J. Calvert, K. Hay, D. Lees, The role of oxygen transport in oxidation of Fe-Cr alloys, Philosophical Magazine, 28 (1973) 1303-1318.

[17] K. Leistner, C. Toulemonde, B. Diawara, A. Seyeux, P. Marcus, Oxide film growth kinetics on metals and alloys II. Numerical simulation of transient behavior, Journal of the Electrochemical Society, 160 (2013) C197-C205.

[18] J.D. Henderson, A. Seyeux, S. Zanna, M.C. Biesinger, D.W. Shoesmith, J.J. Noël, P. Marcus, Investigating the transport mechanisms governing the oxidation of Hastelloy BC-1 by in situ ToF-SIMS, Corrosion Science, (2019) 108138.

[19] M.J. Graham, J. Eldrige, D. Mitchell, R. Hussey, Anion transport in growing Cr2O3 scales, Materials Science Forum, (1989) 207-242.

[20] C. Wagner, Theoretical analysis of the diffusion processes determining the oxidation rate of alloys, Journal of the Electrochemical Society, 99 (1952) 369-380.

[21] S. Brenner, Oxidation of Iron-Molybdenum and Nickel-Molybdenum Alloys, Journal of the Electrochemical Society, 102 (1955) 7-15.

[22] J.A. Bardwell, B. MacDougall, M. Graham, Use of 18O/SIMS and electrochemical techniques to study the reduction and breakdown of passive oxide films on iron, Journal of the Electrochemical Society, 135 (1988) 413-418.

[23] C. Poulain, A. Seyeux, S. Voyshnis, P. Marcus, Volatilization and transport Mechanisms

during Cr oxidation at 300 °C studied in situ by ToF-SIMS, Oxidation of Metals, 88 (2017) 423-433.

[24] P. Kofstad, K. Lillerud, On high temperature oxidation of chromium II. Properties of and the oxidation mechanism of chromium, Journal of the Electrochemical Society, 127 (1980) 2410-2419.

[25] P. Kofstad, Nonstoichiometry, diffusion, and electrical conductivity in binary metal oxides, Wiley (1972).

[26] G. Bakradze, L. Jeurgens, T. Acartürk, U. Starke, E. Mittemeijer, Atomic transport mechanisms in thin oxide films grown on zirconium by thermal oxidation, as-derived from 18O-tracer experiments, Acta materialia, 59 (2011) 7498-7507.

[27] S. Voyshnis, A. Seyeux, S. Zanna, B. Martin-Cabanas, T. Couvant, P. Marcus, Oxide layer growth on nickel-base alloy surfaces in high temperature water and in O2 studied by ToF-SIMS with isotopic tracers, Corrosion Science, 145 (2018) 212-219.

[28] R. Lobnig, H. Schmidt, K. Hennesen, H. Grabke, Diffusion of cations in chromia layers grown on iron-base alloys, Oxidation of Metals, 37 (1992) 81-93.

[29] A.C.S. Sabioni, A.M. Huntz, J. Philibert, B. Lesage, C. Monty, Relation between the oxidation growth rate of chromia scales and self-diffusion in Cr2O3, Journal of Materials Science, 27 (1992) 4782-4790.

[30] T. Horita, K. Yamaji, Y. Xiong, H. Kishimoto, N. Sakai, H. Yokokawa, Oxide scale formation of Fe–Cr alloys and oxygen diffusion in the scale, Solid State Ionics, 175 (2004) 157-163.

[31] A.C.S. Sabioni, E.A. Malheiros, V. Ji, F. Jomard, W.A. de Almeida Macedo, P.L. Gastelois, Ion Diffusion Study in the Oxide Layers Due to Oxidation of AISI 439 Ferritic Stainless Steel, Oxidation of Metals, 81 (2014) 407-419.

[32] A.C.S. Sabioni, J.N.V. Souza, V. Ji, F. Jomard, V.B. Trindade, J.F. Carneiro, Study of ion diffusion in oxidation films grown on a model Fe–15%Cr alloy, Solid State Ionics, 276 (2015) 1-8.

[33] A.C.S. Sabioni, R.P.B. Ramos, V. Ji, F. Jomard, W.A.d.A. Macedo, P.L. Gastelois, V.B. Trindade, About the Role of Chromium and Oxygen Ion Diffusion on the Growth Mechanism of Oxidation Films of the AISI 304 Austenitic Stainless Steel, Oxidation of Metals, 78 (2012) 211-220.

[34] L. Wang, A. Seyeux, P. Marcus, Thermal stability of the passive film formed on 316L stainless steel surface studied by ToF-SIMS, Corrosion Science, (2019) 108395.

[35] X. Wu, S. Voyshnis, A. Seyeux, Y. Chumlyakov, P. Marcus, ToF-SIMS study of oxide films thermally grown on nickel-base alloys, Corrosion Science, 141 (2018) 175-181.

[36] National Research Council. Committee on Coatings, High-temperature oxidation-resistant coatings: coatings for protection from oxidation of superalloys, refractory metals, and graphite, National Academies, 1970.

# Chapter VI

# Ion transport mechanisms in the oxide film formed on 316L stainless steel surfaces studied by ToF-SIMS with $^{18}O_2$ isotopic tracer

### Abstract

The composition and structure of the native and passive oxide films formed on 316L stainless steel have been studied in situ by ToF-SIMS. High temperature re-oxidation experiments in isotopic $^{18}O_2$ gas have also been done to assess the ion transport mechanisms in the native and passive oxide films. Duplex oxides with an inner Cr rich layer and an outer layer rich in Fe and Mo oxide have been observed on native and passive oxide films. Exposure of the oxide films to isotopic $^{18}O_2$ tracer at 300°C reveals that the outward cationic diffusion governs the inner oxide growth. The outer Mo-rich layer prevents the continued transport of Cr to the outermost surface. The passive film, due to its composition and structure, exhibits a markedly lower oxidation rate compared to native oxide films.

## VI-1. Introduction

In many industrial sectors, stainless steels (SS) have a wide range of applications due to their high corrosion resistance in severe environments [1]. It is well known that this corrosion resistance originates from the surface oxide film covering the metallic substrate. Many studies have been carried out to characterize the composition and structure of the oxide film formed on SS surface in order to better understand the good corrosion resistance properties of the stainless steel [2-4]. The performance of the oxide films (including the native and passive films) has been tested in various conditions, such as aqueous, gaseous and high temperature environments [5-7].Surface analysis, including X-ray Photoelectron Spectroscopy (XPS) and Time-of-Flight Secondary Ion Mass Spectrometry (ToF-SIMS), have demonstrated that the native oxide film formed on Fe-Cr based stainless steels generally shows a duplex structure, with an iron rich outer layer and a chromium rich inner layer [2-6]. The chromium rich oxide

plays a key role in the corrosion resistance [7, 8]. The passive film, formed electrochemically within the passive range in sulfuric acid, shows strong chromium enrichment compared to the native oxide film. This is attributed to the lower dissolution rate of chromium oxide compared to iron oxide in acidic media.[8, 11]

The knowledge of ion transport processes in the nanometer thick oxide layer is of major interest in order to better understand the nature, composition and thickness of the oxide film, and a prerequisite to control and optimize the functional properties of the stainless steels under varying operating conditions, such as electrolysers, or gas sensors [15, 16]. A $Cr_2O_3$ scale is frequently used as a barrier to protect metallic alloys at high temperatures [17]. As a consequence, the transport properties in $Cr_2O_3$ are of considerable interest [9-12]. Poulain et al. [13] investigated the oxide growth kinetics of $Cr_2O_3$ on a pure Cr substrate at 300°C and under low oxygen pressure. Following a two-step oxidation procedure starting with oxidation in $^{16}O_2$ gas and followed with a re-oxidation in $^{18}O_2$ isotopic tracer, they identified that the growth was controlled by anion transport via oxygen vacancies through the $Cr_2O_3$ layer. Following the same re-oxidation procedure, Voyshnis et al. [23] studied the oxidation behaviour of nickel-base alloy in high temperature water and in low $O_2$ gas pressure. They also showed that the process governing the oxide film growth is the inward (from the surface towards the metal/oxide interface) diffusion of oxygen species. Moreover, they showed an evolution of the inner oxide composition from $Cr_2O_3$ towards $NiCr_2O_4$ with increasing oxidation time. Recently, the two step oxidation procedure has also been used with success to study the ion transport process governing the growth in a pre-formed passive film formed on 304L SS in $H_2SO_4$ solution [24]. It was shown that during the low $O_2$ pressure re-oxidation step (exposure of the pre-formed film to the $^{18}O_2$ isotopic tracer), the outward diffusion of metallic cations governs the oxide growth.

Usually alloys containing small amounts of molybdenum, like 316L SS, exhibit an improved resistance to the localized corrosion (pitting) in Cl-containing solutions. However, up to now, the effect of molybdenum addition on the ion-transport processes taking place during the growth of the oxide film is not well documented. Yu et al. [25] investigated the early stage oxidation of Ni-Cr and Ni-Cr-Mo alloys by using in situ transmission electron microscopy, and the effect of Mo was discussed. Based on their results, Mo doping in the alloy can both stabilize the cation vacancies and inhibit the voids formation in the oxide. Recently, Henderson et al. [26] studied by in situ ToF-SIMS the ion transport processes in Hastelloy BC-1 (Ni-Cr-Mo alloy) during re-oxidation under low $O_2$ pressure. The governing transport

species were metallic cations, and the Mo rich outer layer seemed to be a barrier preventing the continued transport of Cr to the outermost layer.

The aim of the present work was to investigate by ToF-SIMS the ion transport processes in the native oxide and the passive film on 316L SS during a re-oxidation step performed at 300°C in low oxygen atmosphere. The passive film on 316L SS was electrochemically formed at 0.4V/SCE in 0.05M $H_2SO_4$ solution for 1h. The re-oxidation experiments were performed *in situ* by ToF-SIMS with $^{18}O$ isotopic marker to characterise the difference of ion transport processes in native and passive oxide films, and the effect of Mo on the ion transport.

## VI-2. Experimental

### VI-2.1. Sample preparation

The 316L SS was a Fe-19Cr-13Ni-2.7Mo (wt%) polycrystalline alloy. The sample surface was mechanically polished down to 0.25 μm with diamond paste and then successively washed with acetone, ethanol and water in ultrasonic bath for 10 mins. The sample was then dried in compressed air. The native oxide film was formed by leaving the sample in air during 12 hours. The passive film was formed electrochemically in 0.05M $H_2SO_4$ at 0.4V/SCE for 1h [27]. After electrochemical passivation, the sample with passive film was taken out from the cell, rinsed with water, and then dried in compressed air.

A Gamry electrochemical workstation was used for electrochemical experiments. The electrochemical passivation was performed with a standard three-electrode cell with an Au counter electrode and a saturated calomel electrode as the reference electrode. The electrolyte was prepared with ultrapure chemicals (VWR®) and Millipore® water. Before measurement, the solution was deaerated by Ar bubbling for 30 minutes.

### VI-2.2. ToF-SIMS investigation

ToF-SIMS depth profiles were obtained using a ToF-SIMS 5 spectrometer (IONTOF GmbH - Germany). A pulsed 25 keV $Bi^+$ primary ion source was employed for analysis, delivering 1.2 pA current over a $100 \times 100$ μm$^2$ area. Depth profiling was carried out by interlacing secondary ion analysis with sputtering using a 0.5 keV $Cs^+$ sputter beam giving a 17 nA target current over a $300 \times 300$ μm$^2$ area. Both $Bi^+$ and $Cs^+$ ion beams impinged the sample surface at an angle of 45° and were aligned in such a way that the analyzed ions were taken from the

center of the sputtered crater.

ToF-SIMS depth profiles were used to determine the composition, structure and thickness of the oxide films (air-formed native oxide and passive oxide). The characteristic ions were selected as shown in Table VI-1. The iron oxide in the native or passive films is associated with two different characteristic ions ($^{56}Fe^{16}O_2^-$ with high intensity and $^{56}Fe_2^{16}O_3^-$ with a lower intensity). Since, in mass spectrometry, the characteristic ion of newly formed chromium oxide ($^{52}Cr^{18}O_2^-$) will overlap with the characteristic ion of pre-formed iron oxide ($^{56}Fe^{16}O_2^-$), $^{52}Cr^{18}O_3^-$ and $^{56}Fe_2^{16}O_3^-$ ions were used to characterize the oxide composition during re-oxidation in $^{18}O_2$ of the oxide pre-formed in $H_2SO_4$. It should be noted that the selected ions do not reveal the real stoichiometry of the species constituting the sample, but are the appropriate markers of the studied species. Since ToF-SIMS is a non-quantitative technique (due to a strong matrix effect on ion emission), the intensity of the plotted ions in the depth profiles cannot be compared directly and do not reflect the concentrations of the associated species in the substrate. However, ToF-SIMS depth profiles can be used to evaluate the intensity evolution for a given ion at different oxidation stages if the matrix remains similar. Thus, when a comparison between two samples is done for a similar matrix, it is considered that the ionization yield is similar for the two samples. In this study, we assume that despite the different passivation and/or heat treatments given to the 316L SS substrates, the ionization yields of the oxidized species remain similar, making the comparison of the intensities of same ions between recorded ToF-SIMS depth profiles possible to evaluate the composition variation as function of the received treatment. The depth profiles are plotted versus the sputtering time. The sputtering rate has been calculated knowing for passivated 316L SS (in $H_2SO_4$ at 0.4V/SCE) (i) the total oxide layer thickness measured from XPS (results not shown here), and (ii) the position of the metal/oxide interface on the ToF-SIMS depth profile. Assuming a constant sputtering rate (0.02 nm/s) in the oxide, independent of the oxide layer composition, the sputtering time directly translates into oxide thickness.

Immediately after introduction of the specimen into the chamber, and prior to the application of heat, the air formed oxide was depth profiled using ToF-SIMS. Due to the destructive nature of sputtering, each depth profile was collected at a different, unperturbed area of the sample surface. The specimen was then heated up to a temperature of 300 ±1 °C using the heating stage integrated in the system. Modifications to the air-formed oxide due to temperature increase were analysed on both native and passive oxide films. After reaching 300°C, a precision leak valve was then used to introduce $^{18}O_2$ into the analysis chamber, and

the partial pressure $P(^{18}O_2)$ was maintained constant at $1\times10^{-5}$ mPa. After a designated oxidation time, the gas inlet valve was closed while the sample temperature was maintained at $300 \pm 1$ °C, and the chamber immediately pumped down to the base pressure ($10^{-9}$ mPa). A ToF-SIMS depth profile was then acquired in order to assess the oxide film growth mechanism.

| | Species | Characteristic ion |
|---|---|---|
| Metallic substrate | Metallic Fe | $^{56}Fe_2^-$ |
| | Metallic Ni | $^{58}Ni_2^-$ |
| Pre-formed oxide ($^{16}O$) | Iron oxide | $^{56}Fe^{16}O_2^-$ ; $^{56}Fe_2^{16}O_3^-$ |
| | Chromium oxide | $^{52}Cr^{16}O_2^-$ |
| | Molybdenum oxide | $^{98}Mo^{16}O_3^-$ |
| Newly-formed oxide ($^{18}O$) | Iron oxide | $^{56}Fe^{18}O_2^-$ |
| | Chromium oxide | $^{52}Cr^{18}O_3^-$ |
| | Molybdenum oxide | $^{98}Mo^{18}O_3^-$ |

**Table VI-1** ToF-SIMS characteristic ions used to investigate the composition and structure of the oxide films formed on 316L SS
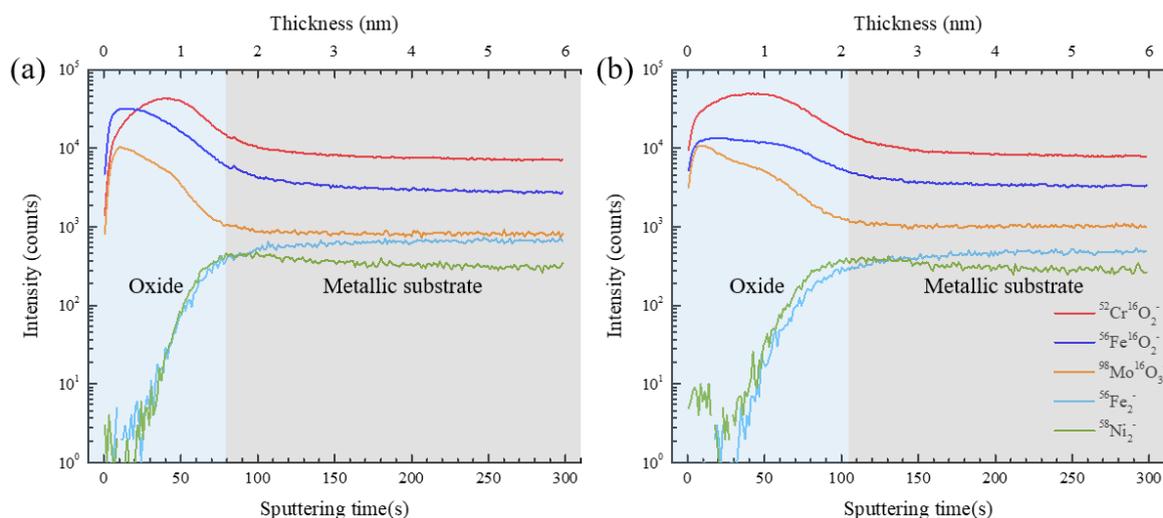
## VI-3. Results and discussion



**Fig.VI-1** ToF-SIMS depth profiles of **(a)** the air-formed native oxide film and **(b)** the passive oxide film formed on 316L SS at room temperature (The passive film was formed electrochemically on 316L SS surface in 0.05M $H_2SO_4$(aq) at 0.4V/SCE for 1h)

Fig.VI-1 shows the ToF-SIMS negative ion depth profiles for the (a) air-formed native oxide

film and (b) the passive film formed at 0.4V/SCE in 0.05M sulfuric acid for 1h, on 316L SS surfaces. The secondary ions, selected for the interpretation of depth profiles, include $^{52}Cr^{16}O_2^-$, $^{56}Fe^{16}O_2^-$, $^{98}Mo^{16}O_3^-$, $^{56}Fe_2^-$ and $Ni_2^-$. The ions ($^{52}Cr^{16}O_2^-$, $^{56}Fe^{16}O_2^-$, $^{98}Mo^{16}O_2^-$) are used to characterize the corresponding oxides, while the ions ($^{56}Fe_2^-$ and $^{58}Ni_2^-$) represent the underlying metallic substrate [24, 26]. The intensities of $^{52}Cr_2^-$ and $Mo_2^-$ ions are extremely low (in negative ion polarity) and are not shown in the figure. As in previous papers, the maximum intensity of $^{58}Ni_2^-$ ion signal is used to define the oxide/metal interface [23, 24, 28]. The thicknesses of the native and passive oxide films, corresponding to around ~80 s and 104 s of sputtering time, are 1.6±0.2 nm and 2±0.2 nm, respectively.

For the native oxide film, as shown in Fig.VI-1(a), both the $^{56}Fe^{16}O_2^-$ and $^{98}Mo^{16}O_3^-$ depth profiles have their maximum in the outer part of the oxide film region, showing that oxidized iron and molybdenum are preferentially located in the outer region of the film. The $^{52}Cr^{16}O_2^-$ depth profile shows its peak in the inner part of the oxide film, indicating that chromium oxide is concentrated in the inner oxide layer. For the passive film (Fig.VI-1(b)), while the $^{98}Mo^{16}O_3^-$ depth profile exhibits a similar trend (maximum intensity in the outer oxide) as the one observed for the native oxide, indicating that oxidized molybdenum is located in the outer film, the $^{56}Fe^{16}O_2^-$ depth profile is slightly different. $^{56}Fe^{16}O_2^-$ maximum intensity is still located in the outer oxide (with a lower intensity compared to that measured on the native oxide), but decreases slowly though the inner oxide film. This indicates that iron oxide is still mainly located in the outer film, but is also present in the inner oxide film. Finally, the $^{52}Cr^{16}O_2^-$ depth profile has its maximum in the inner oxide region but displays a wider peak width compared to that of the native oxide layer. This indicates a thicker, Cr rich, inner oxide film, which contributes to a thickening of the passive film.

Both the native and passive films have duplex structures, with a Mo and Fe rich outer layer and a Cr rich inner layer (possibly including more Fe oxide in the inner layer of the passive film). Passivation by anodic polarization increased the oxide film thickness, which corresponds to the thickening of the Cr rich inner layer. The concentration of iron oxide in the outer film is reduced after passivation, which is due to the enhanced dissolution of iron oxide in sulfuric acid [8].
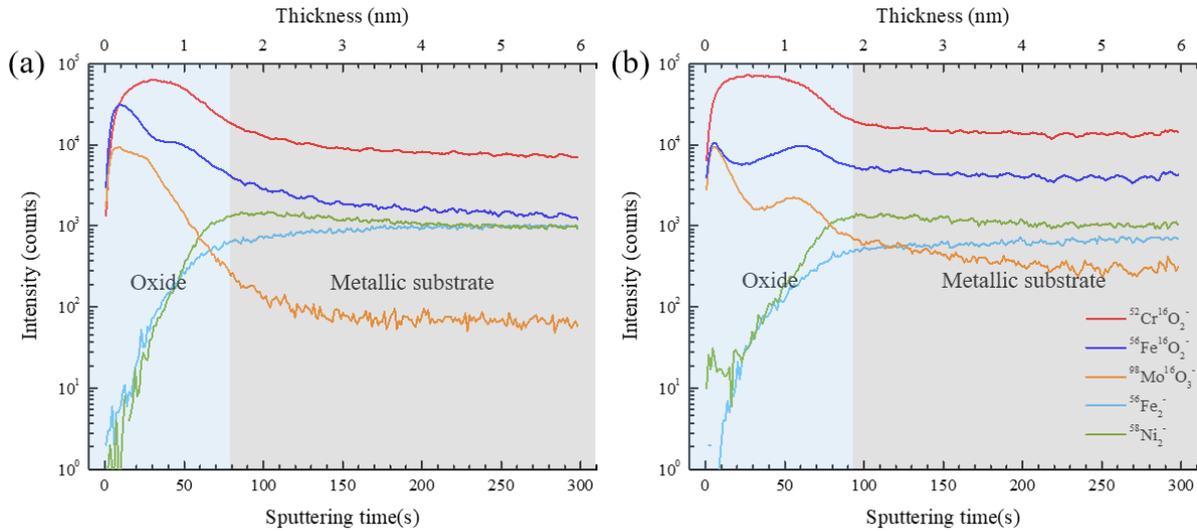
**Fig.VI-2** ToF-SIMS depth profiles of **(a)** the native oxide and **(b)** the passive film on 316L S at 300°C

The *in situ* re-oxidation experiments in the ToF SIMS were carried out at 300°C. Such experiments have been already described in a previous study [24, 27]. The thermal stability of both the native and passive films have been studied. Fig.VI-2 shows the depth profiles of the native and passive films recorded immediately after heating up to 300°C under high vacuum conditions in the ToF-SIMS chamber. Based on the maximum intensities of $Ni_2^-$ depth profiles, the oxide/metal interface for native and passive films are located at 80 s and 92 s of sputtering time, corresponding to oxide thicknesses of 1.6±0.2 nm and 1.8±0.2 nm, respectively. The native oxide film thickness remains unchanged at 300°C, while the passive film thickness decreases.

For the native oxide film (Fig.VI-2(a)), the $^{98}Mo^{16}O_3^-$ and $^{56}Fe^{16}O_2^-$ depth profiles still peak in the outer oxide film, and the $^{52}Cr^{16}O_2^-$ depth profile has its maximum in the inner film. Thus, Mo and Fe oxides are preferentially located in the outer layer, and Cr oxide is rich in the inner layer. It is noticed that the width of $^{56}Fe^{16}O_2^-$ depth profile is now narrower, while the width of $^{52}Cr^{16}O_2^-$ depth profile is wider compared to the native film at room temperature, showing the thickening of the chromium rich inner layer at the expense of the iron rich outer layer [24]. Looking at the $^{98}Mo^{16}O_3^-$ signal, it also shows a narrower width in the outer oxide layer, meaning that molybdenum is more concentrated in this outer oxide layer.

After heating the passive film at 300°C in vacuum the Mo content in the outer oxide layer is higher (Fig.VI-2(b)). Whereas the $^{98}Mo^{16}O_3^-$ signal was almost distributed through the total layer thickness at room temperature (with a higher content in the outer oxide), it is, at 300°C,

mainly localized in the outer oxide. Moreover, heating the sample up to 300°C also has an effect on the $^{52}Cr^{16}O_2^-$ signal profile that becomes wider and on the $^{56}Fe^{16}O_2^-$ signal profile that becomes narrower and exhibits a lower intensity in the outer oxide layer (up to 50s of sputtering approximately). Those modifications are attributed to formation of Cr oxide at the expense of the Fe oxide partial decomposition of hydroxide and removal of water ligands as already observed on passivated 304L SS when exposed to high temperature [24, 27]. Thus, the decrease of the passive oxide film thickness is attributed to the dehydroxylation and dehydration. For the native oxide film, reduction of iron oxide and formation of chromium oxide are mainly observed. The enhanced dehydroxylation and dehydration of the passive film is not surprising, since after passivation the hydroxide and the water ligand contents in the film are high.

Fig.VI-3 shows the ToF-SIMS negative ion depth profiles obtained on the native oxide film on 316L SS surface after exposure to isotopic $^{18}O_2$ gas (10-5 mbar) at 300°C for different times. After 1 min of re-oxidation (Fig.VI-3(a)), the metal/oxide interface, always defined by the maximum intensity of the $Ni_2^-$ signal, is located at 100 s of sputtering time, corresponding to a thickness of 2 nm. Looking at the characteristic ions ($^{52}Cr^{18}O_3^-$, $^{56}Fe^{18}O_2^-$ and $^{98}Mo^{18}O_3^-$) of the newly formed oxide (18O) species, the maximum intensity locations of these depth profiles are in the outermost region of the film, demonstrating that the newly formed oxides are concentrated at the outer surface of the native film. Thus, the governing ion transport mechanism in the native oxide film on 316L SS is cation diffusion.

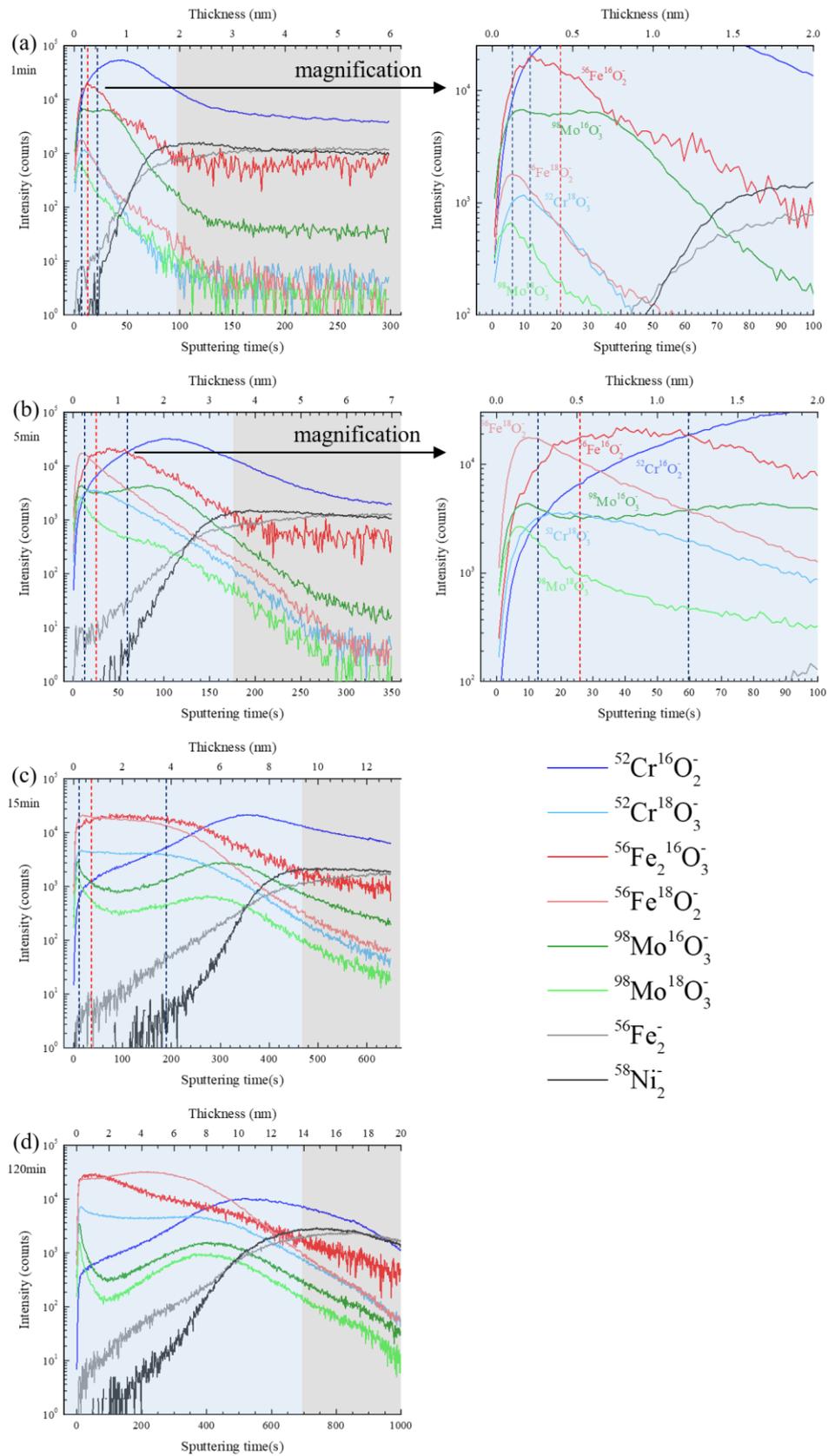**Fig.VI-3** ToF-SIMS profiles obtained on the native oxide film formed on 316L SS surface after re-oxidation at 300°C for **(a)** 1 min, **(b)** 5 min, **(c)** 15min and **(d)** 2 h. (The intensity of $^{56}Fe_2^{16}O_3^-$ signal is multiplied by 50)

After exposure to $^{18}O_2$ for 5 min (Fig.VI-3b), the oxide film thickens from 2±0.2 nm to 3.6±0.2 nm (corresponding to 178 s of sputtering). The locations of maximum intensities of the new oxide ($^{18}O$) species are again found in the outer layer (ranging from 0 s to 60 s of sputtering), while the inner layer (ranging from 60 s to 178 s of sputtering) remains the previously formed Cr oxide ($^{16}O$). A closer look at the distributions of each species ($^{52}Cr^{18}O_3^-$, $^{56}Fe^{18}O_2^-$, $^{98}Mo^{18}O_3^-$, $^{98}Mo^{16}O_3^-$ and $^{56}Fe_2^{16}O_3^-$) in the outer oxide layer, corresponding to the region from 0 s to 60 s of sputtering time, shows that this region can be divided into three parts. The first part, representing the outermost layer (0 s to 13 s of sputtering time), is comprised of the newly formed Mo, Fe oxides ($^{18}O$), and the original Mo oxide ($^{16}O$). The middle region (13 s to 26 s of sputtering time) is rich in the newly formed Cr oxide ($^{18}O$). The third part (26 s to 60 s of sputtering time) is the original Fe rich oxide ($^{16}O$) layer. Thus, the Mo-rich outermost oxides ($^{16}O$ and $^{18}O$) layer appears to play the role of a barrier layer for the continued diffusion of chromium cations toward the oxygen gas/oxide interface, while this Mo-rich layer does not prevent the diffusion of Fe cations to the oxide surface. Thus, the formation of the new chromium oxide ($^{18}O$) needs the $^{18}O$ ions penetration through the Mo-rich outer oxide ($^{16}O$ and $^{18}O$) layer to react with Cr cations diffusing from the substrate. This interpretation is supported by the clear evidence that the Mo-free oxides have Cr oxide ($^{18}O$) in the outer oxide [24].

When the re-oxidation time reaches 15 min (Fig.VI-3c), the oxide film thickness is 9.4±0.2 nm (470 s of sputtering time). The intensities from $^{18}O$-containing ions markedly increased, especially the intensity of $^{56}Fe^{18}O_2^-$ ion, which is approximately equal to that of $^{56}Fe_2^{16}O_3^-$ ion, the characteristic ion of the pre-formed Fe oxide ($^{16}O$). The fast increasing of Fe 18-oxide signal ($^{56}Fe^{18}O_2^-$) in the oxide compared to that of Cr oxide ($^{18}O$) ($^{52}Cr^{18}O_3^-$), is a consequence of the blocking effect of the Mo rich oxide layer on diffusion of Cr ions. The effect of isotopic exchange between $^{18}O$ and $^{16}O$, which was already reported and discussed in previous studies[13-15], cannot be ignored. It causes peak broadening for all oxidized species with increasing re-oxidation time.

After a re-oxidation time of 120 min (Fig.VI-3d), the oxide film thickness is around 14 nm (700 s of sputtering time). The $^{56}Fe^{18}O_2^-$ signal has shifted its maximum intensity from the external surface before 15 min of re-oxidation to the internal oxide, which is assigned mainly to isotopic exchange between $^{18}O$ with $^{16}O$ species.

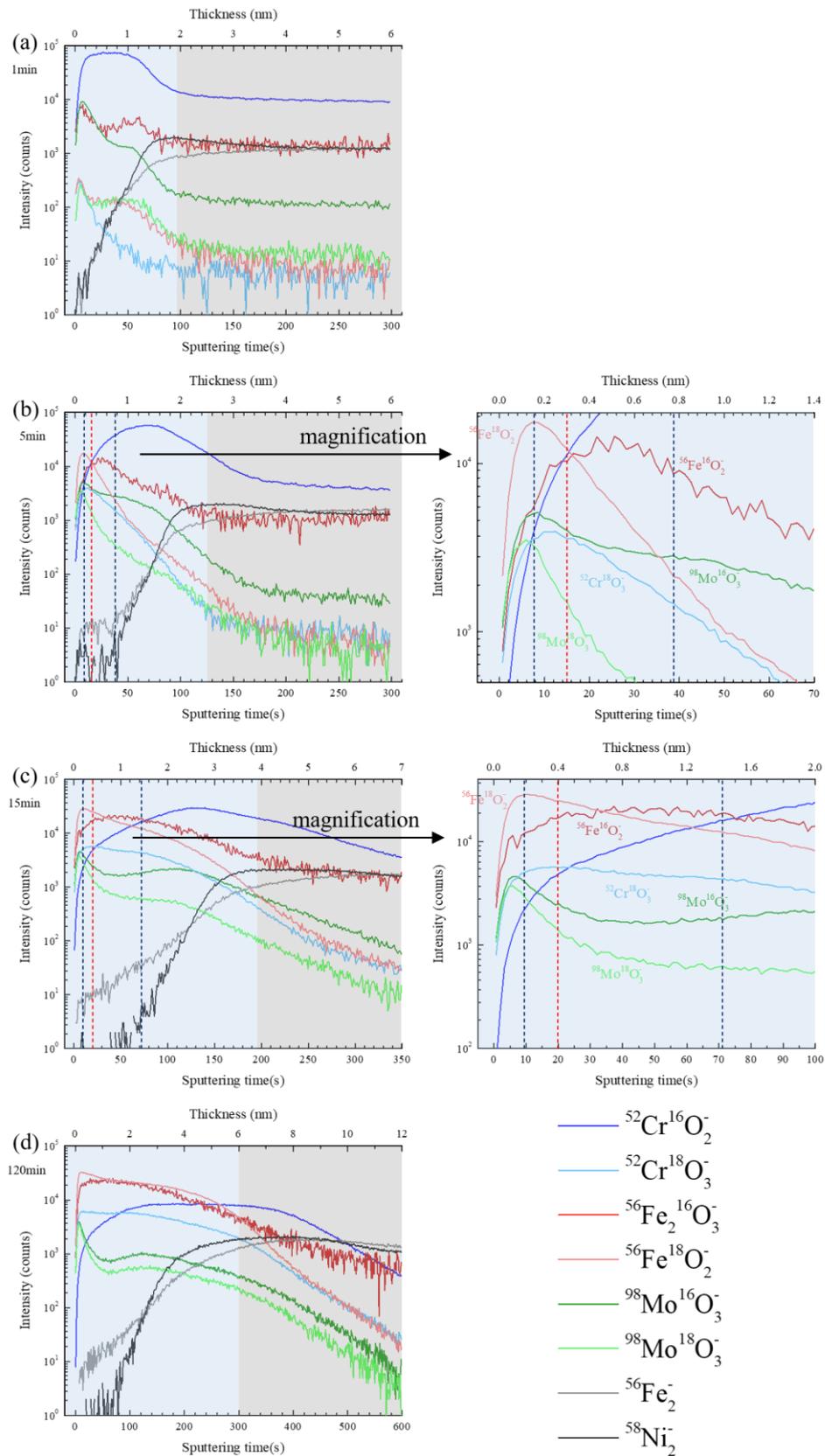**Fig.VI-4** ToF-SIMS profiles obtained on the passive film formed on 316L SS surface after re-oxidation at 300°C for **(a)** 1 min, **(b)** 5 min, **(c)** 15min and **(d)** 2 h. (The intensity of $^{56}Fe_2{}^{16}O_3{}^-$ signal is multiplied by 70)

The re-oxidation study was also performed for the passive film on 316L SS, and the results are shown in Fig.VI-4. Using the same data analysis method, we can conclude that the ion-transport mechanisms in the passive film on 316L SS are the same as in the native oxide film. Cation diffusion is the governing process for oxide film growth. The molybdenum rich outer oxide layer is a barrier for the diffusion of Cr towards the outermost oxide surface. During oxidation, isotopic exchange between the $^{18}O$ and $^{16}O$ species is observed.
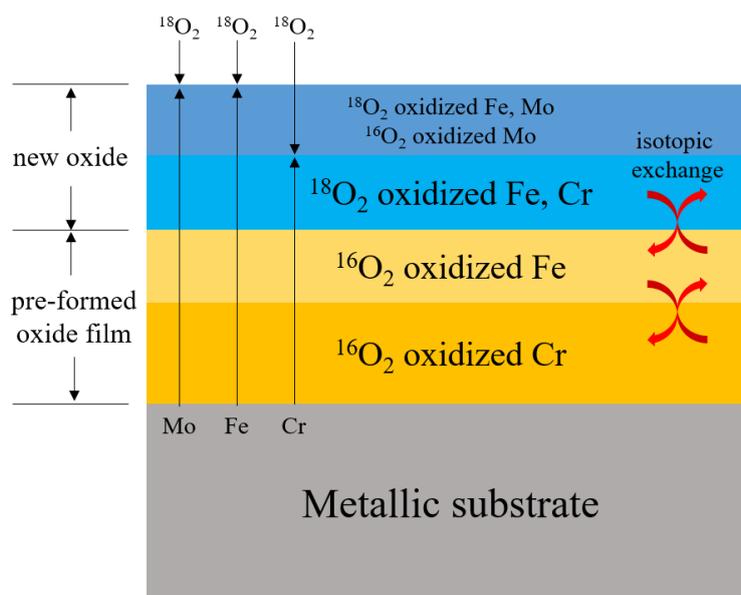


**Fig.VI-5** Scheme of the ion transport mechanisms for oxide films (native oxide and passive film) formed on 316L stainless steel

A schematic depiction of the ion transport process for the oxide films (native and passive) formed on 316L SS is shown in Fig.VI-5. At the early re-oxidation stage, the governing ion transport mechanism in oxide film is the outward cations diffusion, meaning the metallic ions (Mo, Fe and Cr) diffuse from the metallic substrate towards the outer surface. Meanwhile, the Mo rich outermost layer acts as a barrier that blocks the further diffusion of Cr to the oxygen gas/oxide interface. Thus, the governing step also includes the penetration of oxygen through the Mo rich oxide layer. The newly formed Mo and Fe oxides are located in the outer layer, while the newly formed Cr oxide is under this outermost layer. For long exposure to oxygen, isotopic exchange between the $^{18}O$ and $^{16}O$ species dominates. Some volatilization of chromium oxide, evidenced by Poulain et al. [22] for oxidation of pure Cr at the same temperature, cannot be excluded.

Since the thickness of the oxide layer can be measured based on the ToF-SIMS profiles obtained for different oxidation times, we can determine the growth rate of the oxide at

300°C. The data are shown in Fig.VI-6, and the data previously reported for the passive film on 304L SS are shown for comparison [24].
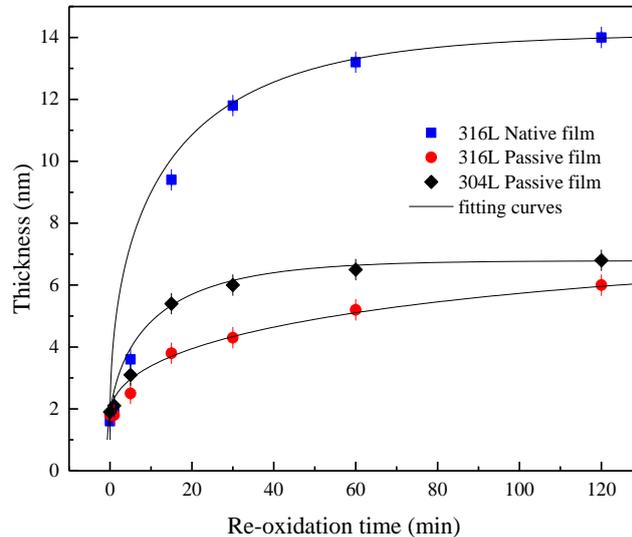


**Fig.VI-6** Re-oxidation kinetics (experimental data and fit) for the native and passive films on 316L SS, and passive film on 304L SS (from ref [15]) at 300°C ($^{18}O_2$ pressure = $10^{-5}$ mbar)

The kinetics of oxidation seems to follow a logarithmic-type law, which, according to previous work, can be explained by the competition between parabolic growth and oxide layer volatilization [22, 24]. Although volatilization is a well-known phenomenon at very high temperature, it has been shown by Poulain et al. [22] that volatilization of oxide and particularly Cr oxide also happens at lower temperature. Thus, oxide volatilization must be taken into account to explain the kinetics of oxide film growth on stainless alloys even at medium temperature. From Fig.VI-6, two parts can be observed on each curve. In the first part (before about 1h of re-oxidation) the oxide layer grows rapidly (newly formed outer oxide layer). Then, after 1h of re-oxidation, the growth of the oxide layer is slow, and a quasi-stationary film thickness is observed (growth rate about equal to volatilization rate).

We can notice that the oxide growth on the passive film of 316L SS at 300°C is significantly slower than on the native oxide film (Fig.VI-6). The passive film thickness after 120 min re-oxidation in $^{18}O_2$ is 6 nm, which is much lower than that of the native oxide film (14 nm). The different oxidation rates between native and passive oxide films can be attributed to the different composition and structure of the films. Firstly, the passive film has higher Cr content and less Fe compared to the native oxide film, as already evidenced by previous XPS results

obtained on 316L SS [8, 11]. The ion diffusion coefficient in chromium oxide is known to be much lower than that in iron oxide, due to a lower concentration of ionic defects in chromium oxide [29-33]. Moreover, passive films are known to have less grain boundaries, which are fast diffusion paths for the diffusing species, than air-formed native oxide, due to the coalescence of the oxide grains induced by electrochemical passivation, as shown previously [11, 34, 35]. This was shown to result in larger lateral grain dimensions for passive film than air-formed native oxide on 316L SS surface ($11.5\pm2.6$ nm and $5.3\pm0.9$ nm, respectively). Thus, passive films with larger grain size have less grain boundary than native oxide films, making the oxidation rate of passive oxide films lower than that of native oxide films.

When we look at the oxidation kinetics on passive films on 304L SS and 316L SS, we observe a lower oxidation rate for the 316 stainless steel, which can be assigned to the Mo-rich outer oxide layer, which acts as a barrier preventing Cr diffusion to the outer surface. The growth of the chromium-rich oxide film requires both the diffusion of Cr from the substrate and the penetration of oxygen through the Mo-rich outer oxide layer.

The oxidation kinetics can then be fitted by Eq.VI-1, as shown in the previous papers [22-24].

$$t = \frac{k_p}{k_v^2}[-\frac{k_v}{k_p}(x - x_0) - \ln\left(1 - \frac{k_v}{k_p}(x - x_0)\right)$$

(equation VI-1)

where $k_p$ is the parabolic constant, $k_v$ is the constant of volatilization, and $x_0$ is the thickness of pre-formed oxide film.

The fittings of the curves are also shown in Fig.Vi-6, and the results calculated for the parabolic and volatilization constants are given in Table VI-2.

| | $k_p$ (nm$^2$.s$^{-1}$) | $k_v$ (nm.s$^{-1}$) |
|---|---|---|
| 316L SS Native film | 0.0079 | 0.0063 |
| 316L SS Passive film | 0.0026 | 0.00043 |
| 304L SS Passive film | 0.018 | 0.0037 |

**Table VI-2** Oxidation kinetics of the native and passive films on 316L SS, and passive film on 304L SS at 300°C

From Table VI-2 we can see that, for the native film on 316L SS, the value of $k_p$ derived from the fit is $7.9\times10^{-2}$ nm$^2$.s$^{-1}$ and $k_v$ is $6\times10^{-3}$ nm.s$^{-1}$. These values are markedly higher than that

calculated for passive films on 316L SS ($k_p = 3 \times 10^{-3}$ nm$^2$.s$^{-1}$ and $k_v = 4 \times 10^{-4}$ nm.s$^{-1}$) and 304L SS ($k_p = 1.8 \times 10^{-2}$ nm$^2$.s$^{-1}$ and $k_v = 4 \times 10^{-3}$ nm.s$^{-1}$). This is mainly due to the fact that the native oxide film has: (i) a higher grain boundary density that react as fast diffusion path for the diffusing species, and (ii) a lower Cr oxide content compared to the electrochemically formed passive film. When we compared the $k_p$ and $k_v$ values for the passive films on 316L SS and 304L SS, the values for 316L SS are almost one magnitude lower than that for 304L SS. This is attributed to the Mo outer most layer, which inhibits the diffusion of Cr and also prevents the exposure of Cr oxide in the outer surface.

Assuming that only the outward cation diffusion is the governing ion transport for oxide growth (an oversimplified view as oxygen diffusion through the outer Mo layer has been shown to be required), and using a simplified relationship between diffusion coefficient and parabolic rate constant $k_p = 2D_c$, the outward cation diffusion coefficient (D$_c$) in the oxide film is $1.5 \times 10^{-17}$ cm$^2$.s$^{-1}$ and $4 \times 10^{-16}$ cm$^2$.s$^{-1}$ for passive film and native film, respectively. The chromium content and possibly the grain size in the passive film have significantly decreased the cation diffusion coefficient in the film.

## VI-4. Conclusions

The transport of ions in oxide films (both the native and passive films) on 316L SS surfaces has been investigated by ToF-SIMS with [18]O isotopic tracer. The native oxide film was formed in air, whereas the passive oxide film was formed electrochemically in 0.05M sulfuric acid at 0.4V/SCE for 1h. Both the native film and passive film have duplex structures with a Mo and Fe rich outer layer and a Cr rich inner layer. Passivation in sulfuric acid causes oxide enrichment in Cr due to the preferential dissolution of the Fe oxide. The native oxide film is quasi stable in vacuum up to 300°C, while the passive film becomes thinner at this temperature, due to dehydroxylation and dehydration of the oxide.

The results of *in situ* re-oxidation of the oxide films (native and passive films) on 316L SS surface at 300°C with [18]O isotopic tracer reveal that the governing ion transport is the outward diffusion of metallic cations (Cr, Fe and Mo) to the oxide surface. The outer Mo-rich oxide layer acts as a barrier preventing the further diffusion of Cr to the oxygen gas/oxide interface, while it has no barrier effect on the diffusion of Fe and Mo. Based on a model taking into account oxidation and possible volatilization, the measured oxide growth kinetics was fitted. The parabolic oxidation constant for the native oxide is $7.9 \times 10^{-2}$ nm$^2$.s$^{-1}$, while it is only $3 \times 10^{-3}$ nm$^2$.s$^{-1}$ for the passive film. The higher Cr content, and a lower density of grain boundary in

the passive oxide, significantly reduce the re-oxidation rate of passive oxide film. A very significant role of the Mo rich outer oxide layer, acting as a barrier to Cr outward diffusion, is evidenced by the use of $^{18}O$ isotopic label.

## References

[1] A.J. Sedriks, Corrosion of stainless steel, 2. edition, John Wiley and Sons, Inc., 1996.

[2] V. Maurice, P. Marcus, Progress in corrosion science at atomic and nanometric scales, Progress in Materials Science, 95 (2018) 132-171.

[3] H.-H. Strehblow, Passivity of Metals Studied by Surface Analytical Methods, a Review, Electrochimica Acta, 212 (2016) 630-648.

[4] Z. Feng, X. Cheng, C. Dong, L. Xu, X. Li, Passivity of 316L stainless steel in borate buffer solution studied by Mott–Schottky analysis, atomic absorption spectrometry and X-ray photoelectron spectroscopy, Corrosion Science, 52 (2010) 3646-3653.

[5] V. Maurice, P. Marcus, Passive films at the nanoscale, Electrochimica Acta, 84 (2012) 129-138.

[6] C.O. Olsson, D. Landolt, Passive films on stainless steels—chemistry, structure and growth, Electrochimica acta, 48 (2003) 1093-1104.

[7] S.R.J. Saunders, M. Monteiro, F. Rizzo, The oxidation behaviour of metals and alloys at high temperatures in atmospheres containing water vapour: A review, Progress in Materials Science, 53 (2008) 775-837.

[8] Z. Wang, F. Di-Franco, A. Seyeux, S. Zanna, V. Maurice, P. Marcus, Passivation-induced physicochemical alterations of the native surface oxide film on 316L austenitic stainless steel, Journal of The Electrochemical Society, 166 (2019) C3376-C3388.

[9] E. Gardin, S. Zanna, A. Seyeux, A. Allion-Maurer, P. Marcus, XPS and ToF-SIMS characterization of the surface oxides on lean duplex stainless steel – Global and local approaches, Corrosion Science, 155 (2019) 121-133.

[10] E. Gardin, S. Zanna, A. Seyeux, A. Allion-Maurer, P. Marcus, Comparative study of the surface oxide films on lean duplex and corresponding single phase stainless steels by XPS and ToF-SIMS, Corrosion Science, 143 (2018) 403-413.

[11] V. Maurice, H. Peng, L.H. Klein, A. Seyeux, S. Zanna, P. Marcus, Effects of molybdenum on the composition and nanoscale morphology of passivated austenitic stainless steel surfaces, Faraday discussions, 180 (2015) 151-170.

[12] L. Ma, F. Wiame, V. Maurice, P. Marcus, New insight on early oxidation stages of austenitic stainless steel from in situ XPS analysis on single-crystalline Fe–18Cr–13Ni, Corrosion Science, 140 (2018) 205-216.

[13] Z. Wang, E.-M. Paschalidou, A. Seyeux, S. Zanna, V. Maurice, P. Marcus, Mechanisms of Cr and Mo enrichments in the passive oxide film on 316L austenitic stainless steel, Frontiers in Materials, 6 (2019) 232.

[14] V. Maurice, W. Yang, P. Marcus, XPS and STM investigation of the passive film formed on Cr (110) single-crystal surfaces, Journal of The Electrochemical Society, 141 (1994) 3016-3027.

[15] A. Tuthill, Stainless steels and specialty alloys for modern pulp and paper mills, Nickel Development Institute (NiDI): Toronto, ON, Canada, (2002) 47-50.

[16] M. Palcut, L. Mikkelsen, K. Neufeld, M. Chen, R. Knibbe, P.V. Hendriksen, Corrosion stability of ferritic stainless steels for solid oxide electrolyser cell interconnects, Corrosion Science, 52 (2010) 3309-3320.

[17] A.M. Huntz, S.C. Tsai, Diffusion in oxide scales: application to Cr2O3 scales, Journal of Materials Science Letters, 13 (1994) 821-825.

[18] S. Tsai, A. Huntz, C. Dolin, C. Monty, Diffusion of 18O in Cr2O3: Bulk and scales and relation with oxidation kinetics, Radiation Effects and Defects in Solids, 137 (1995) 285-290.

[19] S.C. Tsai, A.M. Huntz, C. Dolin, Diffusion of18O in massive Cr2O3 and in Cr2O3 scales at 900°C and its relation to the oxidation kinetics of chromia forming alloys, Oxidation of Metals, 43 (1995) 581-596.

[20] S.C. Tsai, A.M. Huntz, C. Dolin, Growth mechanism of Cr2O3 scales: oxygen and chromium diffusion, oxidation kinetics and effect of yttrium, Materials Science and Engineering: A, 212 (1996) 6-13.

[21] A. Sabioni, A. Huntz, L. Borges, F. Jomard, First study of manganese diffusion in Cr2O3 polycrystals and thin films by SIMS, Philosophical Magazine, 87 (2007) 1921-1937.

[22] C. Poulain, A. Seyeux, S. Voyshnis, P. Marcus, Volatilization and transport mechanisms during Cr oxidation at 300 °C studied in situ by ToF-SIMS, Oxidation of Metals, 88 (2017) 423-433.

[23] S. Voyshnis, A. Seyeux, S. Zanna, B. Martin-Cabanas, T. Couvant, P. Marcus, Oxide layer growth on nickel-base alloy surfaces in high temperature water and in O2 studied by ToF-SIMS with isotopic tracers, Corrosion Science, 145 (2018) 212-219.

[24] L. Wang, S. Voyshnis, A. Seyeux, P. Marcus, Ion transport mechanisms in the passive film formed on 304L stainless steel studied by ToF-SIMS with 18O2 isotopic marker, Submitted, (2020).

[25] X.X. Yu, A. Gulec, C.M. Andolina, E.J. Zeitchick, K. Gusieva, J.C. Yang, J.R. Scully, J.H. Perepezko, L.D. Marks, In Situ Observations of Early Stage Oxidation of Ni-Cr and Ni-Cr-Mo Alloys, Corrosion, 74 (2018) 939-946.

[26] J.D. Henderson, A. Seyeux, S. Zanna, M.C. Biesinger, D.W. Shoesmith, J.J. Noël, P. Marcus, Investigating the transport mechanisms governing the oxidation of Hastelloy BC-1 by in situ ToF-SIMS, Corrosion Science, (2019) 108138.

[27] L. Wang, A. Seyeux, P. Marcus, Thermal stability of the passive film formed on 316L stainless steel surface studied by ToF-SIMS, Corrosion Science, (2019) 108395.

[28] X. Wu, S. Voyshnis, A. Seyeux, Y. Chumlyakov, P. Marcus, ToF-SIMS study of oxide films thermally grown on nickel-base alloys, Corrosion Science, 141 (2018) 175-181.

[29] G. Wallwork, The oxidation of alloys, Reports on Progress in Physics, 39 (1976) 401.

[30] K. Hoshino, N. Peterson, Cation Self-Diffusion in Cr2O3, Journal of the American Ceramic Society, 66 (1983) c202-c203.

[31] M.J. Graham, J. Eldrige, D. Mitchell, R. Hussey, Anion transport in growing Cr2O3 scales, in:  Materials Science Forum, Trans Tech Publications, 1989, pp. 207-242.

[32] A.C.S. Sabioni, A.M. Huntz, J. Philibert, B. Lesage, C. Monty, Relation between the oxidation growth rate of chromia scales and self-diffusion in Cr2O3, Journal of Materials Science, 27 (1992) 4782-4790.

[33] A.C.S. Sabioni, A.M.J. Daniel, W. Macedo, M. Martins, A.M. Huntz, F. Jomard, A. Persiano, First study of iron self-diffusion in Fe2O3 single crystals by SIMS, in:  Defect and Diffusion Forum, Trans Tech Publ, 2005, pp. 277-281.

[34] V. Maurice, W. Yang, P. Marcus, X-Ray photoelectron spectroscopy and scanning tunneling microscopy study of passive films formed on (100) Fe-18Cr-13Ni single-crystal surfaces, Journal of the Electrochemical Society, 145 (1998) 909-920.

[35] V. Maurice, W. Yang, P. Marcus, XPS and STM Study of Passive Films Formed on Fe-22Cr (110) Single-Crystal Surfaces, Journal of the Electrochemical Society, 143 (1996) 1182-1200.

# Conclusions and perspectives

The aim of the first part of this thesis was to understand the corrosion behaviour of CoCrFeMnNi high entropy alloy with emphasis on the characterization of the surface oxide layers (native oxide and passive film) by XPS and ToF-SIMS.

A new XPS approach based on the analysis of 3p core level spectra has been developed. The parameters for fitting the 3p core level peaks of pure metals were used as reference for fitting the XPS 3p spectra for the oxide-covered high entropy alloy. The decomposition of Cr 3p core level peaks into oxide and hydroxide have been verified by fitting also the Cr 2p spectra.

The native oxide film formed on a mechanically polished CoCrFeMnNi high entropy alloys surface has a bilayer structure with a total thickness of ~1.4 nm. Fe oxide (30.3at%) and Co oxide (8.2at%) are located preferentially in the outer layer, Mn oxide (15.2at%) in the inner layer. Cr (46.3at%) is distributed in the whole film. Ni oxide is not detected by XPS. A modified alloy layer, enriched in Ni, is observed under the oxide film.

After exposure of the alloy covered by the native oxide to acidic aqueous solution (0.05M $H_2SO_4$) at OCP, the CoCrFeMnNi HEA shows a marked dissolution of Fe oxide from the film. The amounts of Cr oxide and hydroxide in the film are increased after immersion for 60 min. Despite the dissolution of species in sulfuric acid, the thickness of the film is increased after immersion. There is a balance between dissolution of the species and growth of the oxide which seems to bring a stationary thickness after ~30 min of immersion.

The passivity of the HEA at different passive potentials (200mV, 400mV and 600mV) in 0.05M $H_2SO_4$ has been studied. The passivation potential has a weak effect on the composition and thickness of the oxide layer and modified alloy layer. The studied passive films still have bilayer structures, Fe/Co/Cr mixed outer layer and Cr and Mn inner layer, with total thicknesses of 1.6-1.7 nm. The passive films are found to be enriched in Cr species (57.6at% at 200mV, 65.2at% at 400mV and 68.9at% at 600mV), particularly Cr oxide, compared to the native oxide film. The contents of Mn and Co oxides in the passive films are similar to that in the native oxide film. Much less Fe oxide is observed in the passive film after passivation, which is consistent with the high dissolution of Fe oxide in the acidic

solution. During passivation at 400mV in sulfuric acid, the transformation from Cr hydroxide to Cr oxide (by dehydroxylation) is observed for increasing passivation time.

The aim of the second part of this thesis was to determine the ion transport mechanisms in surface oxides on Cr-containing alloys (304L and 316L stainless steels).

First, we investigated the thermal stability of the passive films on stainless steel. The modifications of the passive film formed on 316L stainless steel surface during stepwise heating in vacuum from room temperature to 300°C has been studied. The pristine passive film, electrochemically formed in 0.05M $H_2SO_4$ solution at 0.4V/SCE for 1h, on the 316 L stainless steel, has a bilayer structure. The outer layer is enriched in iron oxide and molybdenum oxide while the inner layer is rich in chromium oxide. The interface between these outer and inner layers is not sharp, meaning that some iron oxide is distributed in the inner region. Up to 100°C, the passive film is stable. In the range 100°C - 250°C, dehydroxylation and removal of water ligands is observed. Above 250°C, the main modification in the passive film is the formation of chromium oxide at the expense of oxidized iron content. A thicker Cr rich inner layer with sharper inner / outer oxide interface is formed in the passive film after step-wise heating up to 300°C.

The ion transport mechanism in the pre-formed passive film on 304L SS surface has been investigated by in situ ToF-SIMS with isotopic tracer. The passive film, formed electrochemically in sulfuric acid solution at 0.4V/SCE, has a bilayer structure with outer iron oxide and inner chromium oxide layers. Further exposure of the passive film to isotopic $^{18}O_2$ gas at 300°C reveals that the newly formed oxide is located at the external oxide surface, demonstrating that cation diffusion is the governing ion transport mechanism for the oxide growth. After 1h re-oxidation, the oxide film reaches a quasi-stationary thickness, assigned to the limiting transport of cation from the substrate and the chromium oxide evaporation. Then the 16O /18O isotopic exchange becomes the main mechanism governing the O depth profile. A model is proposed to describe the re-oxidation kinetics obtained from the measurements. The parabolic constant (0.018 $nm^2.s^{-1}$) and volatilization constant (0.0037 $nm.s^{-1}$) for the oxide growth are determined, and the diffusion coefficient of cations is found to be $D_c=9\times10^{-17}$ $cm^2.s^{-1}$, which is markedly higher than the oxygen diffusion coefficient ($D_o=1.6 \sim 2\times 10^{-17}$ $cm^2.s^{-1}$). The growth of the passive oxide film is governed by outward cation diffusion.

The transport of ions in oxide films (both the native and passive films) on 316L SS surfaces has been investigated. Both the air-formed native film and passive film (formed in sulfuric

acid solution at 0.4V/SCE) have bilayer structures with a Mo and Fe rich outer layer and a Cr rich inner layer. The results of in situ re-oxidation of the oxide films reveal that outward cations diffusion (Cr, Fe and Mo) through the inner oxide layer is the governing ion transport. The outer Mo-rich oxide layer acts as a barrier preventing the further diffusion of Cr to the oxygen gas/oxide interface, while it has no barrier effect on the diffusion of Fe and Mo. Based on a model similar to the model of re-oxidation for 304L SS, the measured oxide growth kinetics was fitted. The parabolic oxidation constant for the native oxide is $7.9 \times 10^{-2}$ $cm^2.s^{-1}$, while it is only $3 \times 10^{-3}$ $cm^2.s^{-1}$ for the passive film. The higher Cr content, and a lower density of grain boundary in the passive oxide, significantly reduce the re-oxidation rate of passive oxide film.

Several perspectives for further work can be proposed based on the present research work. It would be interesting to use the same methodology and investigate the thermal stability and ion transport in CoCrFeMnNi HEA. This could help us have further understanding on the corrosion behaviour of HEA and give instructions on the improving and modifying the design and properties of HEA.

# Annexe :

# Résumé étendu en français des travaux présentés dans la thèse

Cette thèse contient 6 chapitres. Après une synthèse bibliographique des principaux travaux réalisés sur les alliages inoxydables contenant du Cr, en particulier i) l'étude de la nature, structure, composition et cinétique de croissance des couches d'oxyde formées, ii) l'analyse des principaux modèles de croissance des oxydes et iii) les mécanismes de transport ionique à travers la couche d'oxyde, le chapitre 1 présente les objectifs de ce travail. Le Chapitre II présente les différentes techniques électrochimiques et d'analyse de surface utilisées pour réaliser le travail de recherche expérimentale. Le chapitre III traite de l'étude du comportement à la corrosion des alliages à haute entropie CoCrFeMnNi en mettant l'accent sur la caractérisation de la nature, la structure et la composition des couches d'oxyde de surface. Dans ce chapitre, le film d'oxyde natif formé à l'air et le film passif formé à 0,4 V (SCE) en milieu acide sulfurique (0,05 M) ont été finement étudiés afin d'identifier et discuter les modifications de composition et structure du film d'oxyde liées à la passivation sous potentiel imposé. Dans le chapitre IV, la stabilité thermique d'une surface d'acier inoxydable 316L passivée ($H_2SO_4$ 0,05M ; 0,4V (SCE)) a été testée sous ultra haut vide depuis la température ambiante et jusqu'à 300 °C. Les chapitres V et VI se sont concentrés sur l'étude des processus de transport des espèces ioniques dans les films d'oxyde natif (formé à l'air) et passif (formé électrochimiquement dans l'acide sulfurique) sur des surfaces d'acier inoxydable 304L et 316L.

### Chapitre I

Ce chapitre bibliographique présente les principaux alliages inoxydables, contenant du Cr, en se focalisant sur les aciers inoxydables 304 et 316 et l'alliage à haute entropie CoCrFeMnNi. Les aciers inoxydables sont des alliages à base de fer qui présentent une teneur massique minimale en chrome de 12% et une teneur massique maximale en carbone de 1,2 %. Quatre familles d'acier inoxydable ont pu être définies : martensitique, ferritique, austénitique et duplex. Elles sont fonction de leur structure cristallographique. Les aciers inoxydables martensitiques contiennent la phase martensite qui est une structure cristallographique tétragonale centrée métastable due à la présence d'atomes de carbone dans les sites

interstitiels de la maille. Les aciers inoxydables ferritiques ont une structure cristallographique cubique centrée (α) et sont ferromagnétiques. Les aciers inoxydables austénitiques ont une structure cristallographique cubique à faces centrées (γ) et sont paramagnétiques. Enfin, les aciers duplex sont des aciers inoxydables ayant une structure biphasée composée de ferrite complétée de 40 à 60 % d'austénite.

Le premier alliage a haute entropie, CoCrFeMnNi équimolaire, a été fabriqués par Cantor en 2004 par filage à chaud. Du fait d'une très grande intersolubilité des éléments (métaux de transition) composant ces alliages à haute entropie, ils forment une solution solide monophasique cubique centrée. Ces alliages, aux propriétés spécifiques, font l'objet de recherches depuis plusieurs années. Leur meilleure compréhension a permis de progressivement lever certaines limites (structure monophasées et équimolaires) permettant la mise au point d'une seconde génération d'alliages à haute entropie, dite à solution solide multiphasique non équimolaire ou alliages concentrés complexes. Les quatres principales caractéristiques des alliages à haute entropie ont été résumées par Yeh, à savoir : (1) Thermodynamique: effets à haute entropie, qui facilite la formation de phases en solution solide et à températures élevées; (2) Cinétique: diffusion lente; (3) Structures: distorsion importante du réseau; et (4) Propriétés: effets de cocktail (interaction des différents éléments d'alliage), conférant des caractéristiques spécifiques au matériau.

Pour ces alliages contenant du Cr (aciers inoxydables et alliages à haute entropie), la passivité est basée sur la formation spontanée d'une fine couche d'oxyde de chrome (le film passif). Ce film, continu, adhérent et stable dans le milieu, joue un rôle barrière ralentissant les réactions de corrosion (dissolution) de plusieurs ordres de grandeur. Les films passifs ont des épaisseurs le plus souvent limitées à quelques nanomètres.

Généralement, les propriétés du film passif et donc la résistance à la corrosion des métaux et alliages sont régies par leur composition et leur structure. Pour les alliages Fe-Cr, la structure de la couche d'oxyde est duplex avec une couche externe d'oxyde/hydroxyde de Fer et une couche interne d'oxyde de Cr. La résistance à la corrosion est liée à la formation de la couche d'oxyde de Cr. L'analyse de surface nous montre que l'épaisseur totale du film passif formé en milieu acide est comprise entre 1 et 3 nm. L'addition de nouveaux éléments d'alliage, comme le Ni et/ou le Mo, confèrent des effets bénéfiques aux alliages Fe-Cr. Par exemple, l'addition de nickel améliore les propriétés mécaniques telles que la ductilité et la ténacité. L'ajout de molybdène aura, par contre, limitera la dissolution active conférant ainsi une résistance accrue

à la corrosion localisée des alliages. Le Mn est également un élément d'alliage très utilisé. Il permet, à faible cout, de stabiliser la phase austénitique et augmente significativement la solubilité de l'azote dans les alliages à base de Fe. Cependant, l'addition de Mn est connu pour réduire la résistance à la corrosion des aciers inoxydables.

Compte tenu du rôle clé joué par le film d'oxyde sur la résistance à la corrosion des métaux et alliages, la caractérisation détaillée de leur nature, structure, composition et cinétique de croissance est importante. Ainsi, l'étude des mécanismes d'oxydation et en particulier les mécanismes de transport ionique à travers le film d'oxyde est capital et a fait et fait toujours l'objet de nombreux travaux.

Différents modèles ont été proposés pour décrire les mécanismes de croissance des couches d'oxyde sur les métaux et alliages. Le premier modèle a été proposé par Carl Wagner en 1933. Il permettait de décrire les processus de transport des espèces à travers le film d'oxyde lors de l'oxydation à haute température de métaux purs. Dans ce modèle, l'équilibre thermodynamique est considéré établi aux interfaces métal-oxyde et oxyde-gaz. Ainsi, des gradients de concentration des différentes espèces (métalliques et non métalliques (oxygène, soufre, etc.)) sont établis à travers la couche d'oxyde, à l'origine de la migration de ces espèces.

Plus tard et en se basant sur la théorie de Wagner, le modèle des défauts ponctuels (PDM) et le modèle Marcus-Seyeux-Leistner (MSL) ont été développés. Ils permettent de décrire la formation des couches d'oxyde sur les métaux et alliages. L'évolution majeure de ces modèles concernent la prise en compte du champ électrique à travers le film d'oxyde. En effet, du fait de la migration d'espèces chargées, un champ électrique s'établit dans la couche d'oxyde, responsable de la migration des cations, anions et électrons. Les modèles PDM ou MSL sont généralement utilisés pour décrire la formation de couche d'oxyde par voie électrochimique.

Lors de l'oxydation gazeuse à haute température, la théorie de Wagner permet d'exprimer la cinétique de croissance de la couche d'oxyde comme : $\frac{dx}{dt} = \frac{k_p}{x}$, où $k_p$ est la constante parabolique, x est l'épaisseur de l'oxyde. La théorie de Wagner a été appliquée pour décrire l'oxydation gazeuse à haute température des alliages contenant du Cr. Néanmoins, Compte tenu de la volatilisation du $Cr_2O_3$ à haute température, une constante de volatilisation, kv, a été introduite dans le modèle de Wagner. Elle ralentit la cinétique apparente de la manière

suivante: $\frac{dx}{dt} = \frac{k_p}{x} - k_v$ , ce qui donne après intégration: $t = \frac{k_p}{k_v^2}[-\frac{k_v}{k_p}x - \ln\left(1 - \frac{k_v}{k_p}x\right)]$ (**équation annexe-1**).

La cinétique d'oxydation des métaux et alliages est contrôlée par la diffusion des espèces cationiques (diffusion vers l'extérieur des ions métalliques à travers la couche d'oxyde), par la diffusion des espèces anioniques (diffusion vers l'intérieur des ions oxygènes) ou une diffusion mixte cationique/anionique. Pour déterminer les mécanismes de transport des ions sur les films d'oxyde, une technique d'oxydation en deux étapes a été mise au point au laboratoire (doi: j.corsci.2018.10.009). Elle permet, dans l'enceinte même du spectromètre ToF-SIMS, de réaliser une première oxydation dans l'oxygène isotopique $^{16}O_2$ suivi d'une seconde oxydation sous oxygène isotopique $^{18}O_2$. La distribution de l'oxygène isotopique dans la couche d'oxyde révélant des informations directes sur les mécanismes de transport pendant l'oxydation. La spectroscopie de masse des ions secondaires est une technique appropriée pour localiser le traceur isotopique dans la couche d'oxyde et ainsi conclure sur les mécanismes de transport mis en jeu. La diffusion anionique conduisant à la formation du nouvel oxyde $^{18}O$ à l'interface substrat métallique/oxyde, tandis que la diffusion cationique entraînera la formation du nouvel oxyde en surface, c'est-à-dire à l'interface oxyde/gaz.

Après la revue bibliographique, les objectifs de ce travail de thèse ont été posés. Le premier objectif est d'étudier en détail la nature, structure et composition du film d'oxyde natif et du film passif formé en milieu acide sulfurique sur l'alliage à haute entropie CoCrFeMnNi et les alliages inoxydable, contenant du Cr. Ensuite, le deuxième objectif de ce travail était d'étudier les processus de transport des ions régissant les cinétiques de croissance de la couche d'oxyde (couche d'oxyde native et passive) sur une surface d'alliage inoxydable.

**Chapitre II**

Le chapitre II correspond à une revue des techniques de caractérisation de surface, électrochimiques, ainsi que les méthodes de préparation des échantillons utilisées pour mener à bien les objectifs de ce travail. Tous les échantillons sont préparés par polissage avant leur caractérisation. Ainsi, les échantillons sont polis sur papier abrasif SiC jusqu'au grade 2400, puis avec des pâtes diamantées jusqu'à 0,25 μm afin d'obtenir un poli miroir. Après polissage, les échantillons sont rincés successivement dans des bains d'acétone (VWR Chemicals, pureté 99%), d'éthanol (VWR Chemicals, pureté 99,5%) et d'eau ultra-pure (résistivité supérieur à 18,2 MΩcm) sous ultra-sons.

Les techniques électrochimiques utilisées pour l'étude de la résistance à la corrosion et du processus de passivation sont la polarisation potentiodynamique et la polarisation potentiostatique. Le système électrochimique utilisé est constitué d'une cellule classique à trois électrodes. L'électrode de référence est une électrode au calomel saturé (SCE). La contre-électrode est une spirale de fil en or. L'électrode de travail est notre échantillon dont la surface est délimitée par un joint Viton. Dans cette étude, l'électrolyte est une solution aqueuse d'acide sulfurique de concentration 0,05 M, préalablement désaérée par un bullage d'argon.

Les techniques de caractérisation de surface mises en œuvre sont la spectroscopie de photoélectrons induits par rayons X (XPS) et la spectrométrie de masse d'ions secondaires à temps de vol (ToF-SIMS).

La spectrométrie de masse d'ions secondaires à temps de vol (ToF-SIMS) permet l'analyse élémentaire et moléculaire de la surface avec une très haute sensibilité. Dans une analyse ToF-SIMS, la surface de l'échantillon est bombardée par un faisceau pulsé d'ions primaires $Bi^+$ ayant une énergie de 25 keV. La dissipation de l'énergie des ions primaires entraine en une cascade de collisions, avec rupture des liaisons chimiques et émission de particules secondaires issues des 2 ou 3 premières monocouches atomiques. Les ions secondaires sont ensuite post-accélérés pour être analysés en temps de vol et ainsi triés en fonction du temps nécessaire pour atteindre le détecteur, un lien existant entre le temps et la masse. Plusieurs types d'analyse peuvent être réalisées : Spectres de masse de surface, des profils de composition en profondeur et des imageries chimiques de la surface. Dans notre étude, nous avons réalisé des profils de concentration permettant de déterminer la distribution en profondeur des différents éléments présents dans les films passifs et à l'interface avec le substrat. La spectrométrie ToF-SIMS étant une technique « statique », un second canon, d'abrasion est utilisé pour éroder la surface. Il s'agit d'un canon d'ion $Cs^+$. La succession de phases d'analyse et de décapage permet d'obtenir les profils de composition en profondeur.

L'analyse XPS permet d'obtenir un spectre représentant le nombre de photoélectrons détectés (en coups par seconde) en fonction de l'énergie de liaison (en eV) des niveaux de cœur des éléments présents en surface. Le principe de l'XPS repose sur l'émission de photoélectrons suite à l'interaction rayonnement-matière. Cette technique permet l'identification qualitative des principaux éléments présents à la surface de l'échantillon et de leur environnement chimique. La décomposition des spectres XPS permet d'obtenir des informations

quantitatives, composition de la surface, épaisseur de la couche d'oxyde, à partir des intensités spectrales mesurées. Dans notre cas le logiciel utilisé pour la décomposition spectrale est Avantage. La ligne de base est fixée et soustraite sous forme Shirley.

**Chapitre III**

Dans ce chapitre, le comportement à la corrosion de l'alliage CoCrFeMnNi à haute entropie (HEA) a été étudié en mettant l'accent sur la caractérisation des couches d'oxyde de surface (oxyde natif et film passif).

XPS est une méthode appropriée pour étudier la composition de films d'oxyde de surface d'épaisseur nanométrique. Généralement, pour les alliages contenant Fe, Cr, Ni, Co et Mn, les pics de niveau de cœur 2p sont enregistrés avec une haute résolution et de nombreuses références sont disponibles pour étudier les états chimiques des éléments analysés. Cependant, pour le CoCrFeMnNi HEA avec cinq éléments dans des rapports équiatomiques, de nouveaux défis apparaissent dans l'analyse des données XPS en raison de l'interférence des transitions Auger avec les photopics 2p des principaux éléments de l'alliage. Ainsi, une approche nouvelle basée sur l'étude des pics des niveaux de cœur 3p a été développée pour caractériser les surfaces HEA. Pour développer cette nouvelle approche, une nouvelle base de données pour les spectres de niveau de cœur 3p doit être établie. Premièrement, les pics de niveau de cœur standard 3p pour les métaux purs ont été enregistrés en utilisant des métaux purs provenant de lots utilisés pour fabriquer le CoCrFeMnNi HEA. Ces échantillons de métal pur ont été polis avec du papier SiC à grain 2400, puis introduits dans la chambre d'analyse XPS. Les échantillons ont été pulvérisés à l'aide d'un faisceau d'ions Ar + pour éliminer les oxydes de surface et les contaminants et obtenir des surfaces métalliques. Les spectres de haute résolution XPS 3p ont été enregistrés et la courbe ajustée à l'aide du logiciel Thermo Electron Avantage et tous les paramètres ont été automatiquement ajustés par le logiciel pour s'adapter au mieux aux pics de métaux purs. Cette approche a été testée avec succès pour étudier par XPS les oxydes natif et passif sur l'alliage HEA.

Le spectre caractéristique des pics 3p de Cr, Mn, Fe, Co et Ni, et l'ajustement de pic pour un film d'oxyde natif formé sur la surface de CoCrFeMnNi HEA sont présentés sur la figure annexe-1. Cette décomposition a été réalisée en introduisant les paramètres d'ajustement déterminés précédemment pour chaque élément (état métallique et état oxyde). L'épaisseur du film d'oxyde natif est estimée à 1,4 nm. Le film d'oxyde natif présente un fort enrichissement en chrome (46,3 at%, dont 26,5 at% d'oxyde et 19,8 at% d'hydroxyde) et en fer (30,3 at%)

tandis qu'un appauvrissement en Co (8,2 at%) est clairement observé. Aucun oxyde de nickel n'est détecté par XPS dans la couche d'oxyde. Dans la couche d'alliage métallique modifiée sous l'oxyde natif, un appauvrissement en Cr métallique (11,7 at%), Mn (12,5 at%) et Fe (17,1 at%) est observé, tandis que la concentration en Ni métallique (33,8 at%) et Co (24,9 at%) sont nettement plus élevés que dans la masse. La zone d'appauvrissement en chrome dans la couche d'alliage modifiée est corrélée à l'enrichissement en oxyde de chrome dans le film d'oxyde.
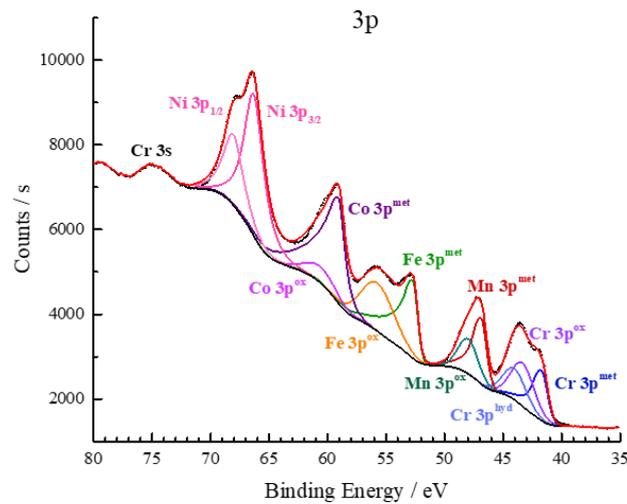


**Fig.Annexe-1** Spectres de niveau de noyau XPS pour le film d'oxyde natif formé sur le HEA: Cr 3p, Mn 3p, Fe 3p, Co 3p, Ni 3p. Les points noirs représentent les spectres expérimentaux et les lignes colorées montrent l'ajustement du pic

Le profil ToF-SIMS (figure annexe-1) obtenu sur une couche d'oxyde native formée sur un alliage HEA montre une structure d'oxyde duplex composée d'oxydes de chrome, de fer et de cobalt dans la couche externe et d'oxydes de chrome et de manganèse dans la couche interne. A l'interface métal / oxyde, l'alliage métallique est modifié. Il est enrichie en Ni et Co.
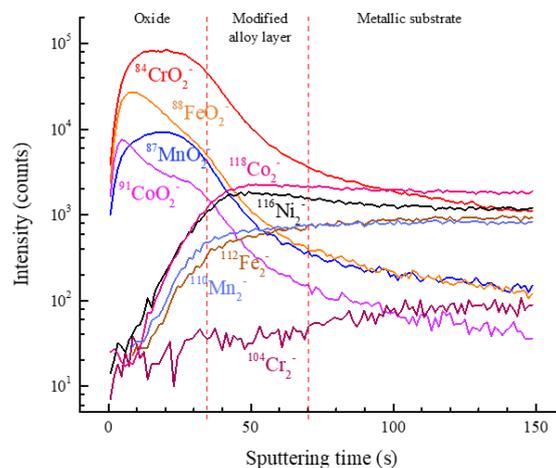


**Fig.Annexe-2** Profils de profondeur ToF-SIMS pour le film d'oxyde natif formé sur le HEA

Après exposition de l'oxyde natif à une solution aqueuse d'acide sulfurique (0,05 M $H_2SO_4$) au potentiel de circuit ouvert, on observe une modification de la composition du film d'oxyde recouvrant le CoCrFeMnNi HEA. En effet, on observe une dissolution marquée de l'oxyde de Fe, une augmentation significative de la concentration en oxyde/hydroxyde de Cr, et une augmentation de l'épaisseur totale de la couche d'oxyde. Cela s'explique par la vitesse de dissolution élevée de l'oxyde de Fe dans les milieux acides. Malgré la dissolution des espèces dans l'acide sulfurique, l'épaisseur du film augmente après immersion du fait de la formation d'une couche plus épaisse d'oxyde de chrome. Il existe un équilibre entre la dissolution de l'oxyde de fer et la croissance de l'oxyde de chrome qui semble apporter une épaisseur stationnaire après ~ 30 min d'immersion. L'épaississement du film d'oxyde est observé à la fois par les mesures XPS et ToF-SIMS.

La passivité du HEA à différents potentiels (200 mV, 400 mV et 600 mV) a été étudiée. Les observations ToF-SIMS montrent que la structure des films passifs formés à différents potentiels sont des bicouches, avec une couche externe de Fe/Co/Cr riche et une couche interne de Cr/Mn. La caractérisation XPS a montré que les films passifs formés à trois potentiels différents ont presque la même composition et épaisseur de la couche d'oxyde et la composition de l'alliage métallique sous la couche. Les films passifs étudiés se sont révélés être enrichis en oxyde de Cr par rapport au film d'oxyde natif. Les teneurs en oxydes de Mn et de Co dans les films passifs sont similaires à celles du film d'oxyde natif. Par contre, On observe une diminution importante de la concentration en oxyde de Fe dans le film passif, ce qui correspond à la forte dissolution de l'oxyde de Fe dans la solution acide. L'épaisseur totale des films passifs se situe entre 1,6 et 1,7 nm. En étudiant davantage l'effet du temps de passivation sur la composition de l'oxyde à 400 mV, la principale modification de la composition observée dans le film passif est l'augmentation de la concentration en oxyde de Cr au détriment de la concentration en hydroxyde de Cr. La teneur totale en espèces Cr (oxyde et hydroxyde de Cr) restant constante. Ce processus de transformation de l'hydroxyde en oxyde est responsable de la diminution du courant passif. L'épaisseur du film est maintenue à 1,6-1,7 nm, donc le temps de passivation n'a pas d'effet significatif sur l'épaisseur du film passif.

**Chapitre IV**

Le chapitre IV a étudié la stabilité thermique du film passif formé sur la surface d'un acier inoxydable 316L lors du chauffage de la température ambiante jusqu'à 300°C sous ultra haut

vide.

Avant exposition à haute température, le film passif formé sur l'acier inoxydable 316L présente une structure bicouche. Les profils ToF-SIMS obtenus montrent la formation d'une couche externe enrichie en oxyde de fer et en oxyde de molybdène tandis que la couche interne est riche en oxyde de chrome. Le profil ToF-SIMS caractéristique de l'oxyde de Fer montre une interface diffuse entre les couches externe et interne indiquant que l'oxyde de fer est distribué dans la couche interne.

A partir des profils ToF-SIMS obtenu, un scénario décrivant l'évolution du film passif formé sur 316L SS durant le traitement thermique sous UHV a été établi et est présenté sur la figure annexe-3. A des températures inférieures à 100 °C, le film passif est stable et la composition n'est pas modifiée. À des températures supérieures à 100 °C, l'interface oxyde interne / oxyde externe du film passif devient plus nette sur les profils de composition ToF-SIMS, indiquant une structure bicouche plus marquée avec un oxyde externe qui est presque exclusivement composé d'oxyde de Fe et un oxyde interne composé majoritairement d'oxyde de Cr. La température de 250°C est un point critique. Pour des températures comprises entre 100 °C et 250°C, la principale modification observée dans la couche d'oxyde est la décomposition de l'hydroxyde de Cr et l'élimination des ligands aqueux, entrainant un enrichissement de la couche en oxyde de chrome. À des températures supérieures à 250 °C, on observe la réduction de l'oxyde de Fe causée par la diffusion massive de Cr dans la partie intérieure de l'oxyde. En effet, la plus grande stabilité de l'oxyde de Cr entraine sa formation au dépend de l'oxyde de Fer à l'interface oxyde interne/ oxyde externe.
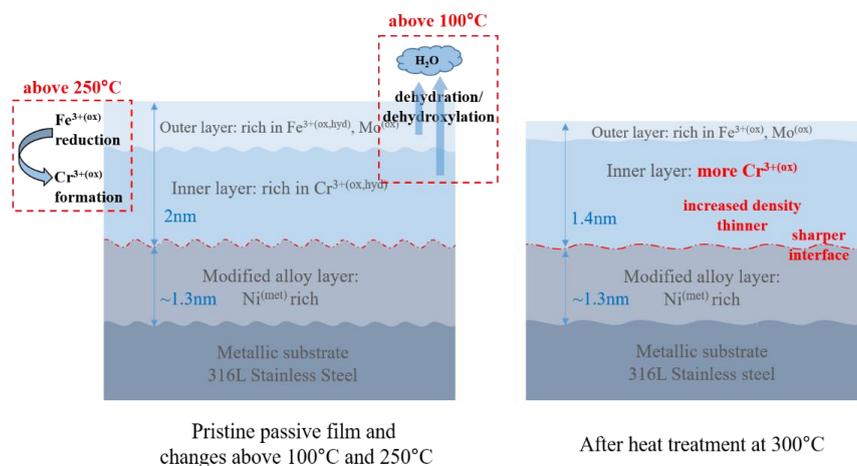


**Fig.Annexe-3** Model for the passive film evolution during UHV heat treatment

L'épaisseur du film passif (2 nm) n'est pas modifiée à des températures de chauffage jusqu'à 100 °C. Ensuite, à température plus élevée (jusqu'à 250°C), l'épaisseur du film passif diminue progressivement jusqu'à 1,6 nm, ce qui correspond à la déshydroxylation et à la déshydratation du film d'oxyde. Un changement très limité de l'épaisseur du film est observé à des températures supérieures à 250°C (de 1,6 nm à 1,4 nm). Cette légère modification de l'épaisseur du film dans cette plage de température est attribuée à la formation d'oxyde de chrome (5,22 g/cm$^3$) et d'oxyde de molybdène (6,47 g/cm$^3$) au détriment de l'oxyde de fer (5,24 g/cm$^3$), les variations de densité étant responsable de la modification en épaisseur. De plus, la formation d'oxyde de Mo consommera encore plus d'oxyde de Fe en raison de sa stœchiométrie plus élevée.
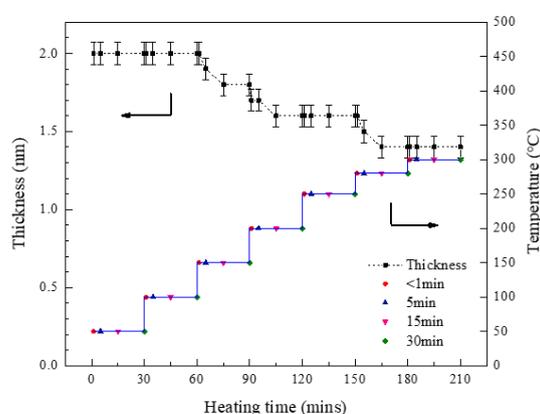


**Fig.Annexe-4** The thickness of the passive film as a function of heating temperature and time

Le film passif, après chauffage sous UHV, présente toujours une structure bicouche avec une couche externe d'oxyde de Fe et de Mo et une couche interne très enrichie en oxyde de Cr. La concentration en oxyde de Cr dans le film passif exposé à haute température est supérieure à la concentration dans le film passif initialement formé. Cela est, à nouveau, le résultat de la formation d'oxyde de Cr aux dépens de l'oxyde de Fe, du fait de l'enrichissement de l'interface métal/oxyde en Cr à haute température (diffusion plus grande dans le substrat).

### Chapitre V

Dans ce chapitre, le transport ionique dans le film passif préformé sur une surface en acier inoxydable 304L a été étudié par ToF-SIMS au moyen de traceur isotopique.

Le film d'oxyde passif formé électrochimiquement dans une solution de 0,05 M H$_2$SO$_4$ à 0,4 V/SCE pendant 1 h a une structure duplex, comprenant une couche externe riche en fer et une couche interne riche en chrome. L'épaisseur du film passif est d'environ 2 nm. Après avoir chauffé l'échantillon jusqu'à 300 °C dans la chambre principale du ToF-SIMS. L'épaisseur du

film passif est estimée à 1,9 nm. La structure et la nature du film passif reste inchangée. Cependant, des changements de composition et d'épaisseur sont observés lors de l'augmentation de la température jusqu' à 300 °C. Comme discuté précédemment, ceci est attribué à (i) la déshydroxylation et à la déshydratation du film d'oxyde dès 100°C. (ii) la formation d'oxyde de chrome au détriment de l'oxyde de fer lorsque la température est supérieure à 250 °C.

Ensuite, une nouvelle exposition du film passif au gaz $^{18}O_2$ (traceur isotopique) à 300 °C révèle que la diffusion des cations vers l'extérieur est le mécanisme de transport des ions qui régit la croissance des oxydes. Un schéma de l'évolution de la couche d'oxyde exposée à $^{18}O_2$ à 300 °C sur la base des données de profilage en profondeur ToF-SIMS est présenté sur la figure annexe-4. Bien que dans ces manipulations, l'échange isotopique $^{16}O/^{18}O$ ne puisse pas être négligé, le principal mécanisme régissant la croissance de l'oxyde pour une réoxydation courte de la surface pré-passivée a pu être déterminé. Il s'agit du transport des cations métalliques à travers le film d'oxyde, ce qui signifie que les cations de fer et de chrome diffusent du substrat métallique vers l'interface oxyde/gaz où ils réagissent avec l'oxygène isotopique ($^{18}O_2$). Ainsi, les oxydes de chrome et de fer nouvellement formés sont situés à l'interface externe oxyde/gaz. Après 15 min de ré-oxydation sous une faible pression de $^{18}O_2$, la diffusion cationique régit toujours la croissance de l'oxyde. L'échange isotopique est également mis en évidence comme le montre le profil $^{18}O$ dans l'oxyde $^{16}O$ préformé. À un temps de réoxydation plus long (plus de 1 h), le film d'oxyde atteint une épaisseur quasi stationnaire (le taux de croissance devient très faible) et l'échange isotopique devient le principal mécanisme conduisant à une augmentation de la quantité de $^{18}O$ dans la partie intérieure de l'oxyde couche. La volatilisation de l'oxyde de chrome à haute température et sous UHV comme observé sur un échantillon de Cr pur oxydé sous UHV à haute température ne peut pas être exclue.
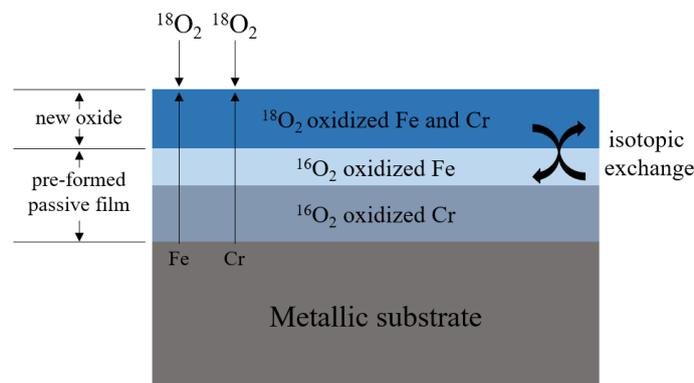


**Fig.Annexe-5** Scheme of the evolution of the passive oxide layer exposed to $^{18}O_2$ at 300°C

La cinétique de réoxydation est bien ajustée par une loi de type « logarithmique », qui peut s'expliquer par la compétition entre la croissance parabolique et la volatilisation de la couche d'oxyde (expliquée dans le chapitre I partie). La cinétique d'oxydation peut alors être ajustée par **l'équation annexe-1** qui prend en considération la croissance et la volatilization de la couche d'oxyde de Cr. Les valeurs de $k_p$ et $k_v$ dérivées de l'ajustement sont $1,8\times10^{-2}$ $nm^2.s^{-1}$ et $3,7\times10^{-3}$ $nm.s^{-1}$, respectivement. Sur la base d'une relation simplifiée entre le coefficient de diffusion et la constante de vitesse parabolique $k_p = 2D_c$, nous concluons que le coefficient de diffusion pour la diffusion cationique vers l'extérieur ($D_c$) dans le film d'oxyde est de $9\times10^{-17}$ $cm^2.s^{-1}$.

Bien que, comme discuté ci-dessus, le principal mécanisme de transport d'espèces ioniques pendant le processus de ré-oxydation du film passif formé sur 304L SS soit la diffusion vers l'extérieur des cations, un mécanisme mixte comprenant à la fois la diffusion des cations et des anions ne peut être complètement exclu. Ainsi, il est intéressant d'évaluer le coefficient de diffusion d'oxygène à travers le film d'oxyde et de le comparer au coefficient de diffusion cationique. L'intégration semi-infinie de la deuxième loi de diffusion de Fick pour la diffusion unidimensionnelle, modifiée pour inclure l'échange isotopique, peut être testée sur les profils de profondeur ToF-SIMS du signal 18O. Avec ce modèle, le coefficient de diffusion de l'oxygène ($D_o = 1,6 \sim 2 \times 10^{-17}$ $cm^2.s^{-1}$) et le coefficient d'échange isotopique ($k = 3,7 \times 10^{-10}$ $at.cm^{-2}.s^{-1}$ et $1 \times 10^{-11}$ $at.cm^{-2}.s^{-1}$) sont obtenus.

Il apparaît que le coefficient de diffusion cationique ($9 \times 10^{-17}$ $cm^2.s^{-1}$) issu de la cinétique de croissance de la couche d'oxyde est environ 5 fois plus élevé que le coefficient de diffusion de l'oxygène ($1,6 \sim 2 \times 10^{-17}$ $cm^2.s^{-1}$). Ainsi, la diffusion cationique est bien le principal mécanisme de diffusion permettant la croissance de la couche d'oxyde sur l'alliage inoxydable 304L.

### Chapitre VI

Dans ce chapitre, le processus de transport des ions dans les films d'oxyde (à la fois natifs et passifs) sur les surfaces en acier inoxydable 316L a été étudié.

Comme précédemment sur l'alliage 304, les films d'oxyde natif et passif formés sur l'alliage 316 ont des structures duplex, avec une couche externe riche en Mo et Fe et une couche interne riche en Cr. Après polarisation anodique, le film passif est plus épais que le film d'oxyde natif, résultat de la croissance de la couche interne riche en Cr. De même, après

passivation, la concentration en oxyde de fer dans la couche externe est réduite, dû fait de la dissolution accrue de l'oxyde de fer dans l'acide sulfurique.

Après avoir chauffé les films d'oxyde à 300 °C, le film natif et le film passif possèdent toujours des structures duplex avec une couche externe riche en Fe et Mo et une couche interne riche en Cr. La réduction de l'oxyde de fer et la formation d'oxyde de chrome sont observées comme précédemment sur les couches native et passive formées sur l'acier inoxydable 304L. L'épaisseur du film natif formé sur l'acier inoxydable 316 n'est pas modifié à haute température, contrairement à celle du film passif, qui est réduite du fait de la déshydroxylation et de la déshydratation. Ces phénomènes de déshydroxylation et déshydratation observés sur les couches passives ne sont pas surprenantes, compte tenu de la plus grande concentration en hydroxyde et en molécule d'eau de la couche d'oxyde après passivation.

Lors des expériences de réoxydation à 300 °C au moyen de traceur isotopique $^{18}O_2$, les résultats révèlent qu'au temps courts de réoxydation, la croissance du film d'oxyde est le résultat de la diffusion des cations métalliques (Mo, Fe et Cr) vers l'extérieur. Néanmoins, alors que les cations Mo et Fe diffuse librement à travers la couche d'oxyde initialement formée dans $^{16}O_2$, la diffusion des cations Cr est bloquée par la couche externe riche en oxyde de Fe et Mo. Ainsi, durant la phase de réoxydation dans l'oxygène isotopique, les oxydes de Mo et Fe nouvellement formés sont situés dans la couche externe. Au contraire, l'oxyde de Cr nouvellement formé est localisé à l'interface couche interne / couche externe du fait de la diffusion lente de $^{18}O$ dans la couche externe. Pour des temps longs de réoxydation, la couche d'oxyde atteint une épaisseur stationnaire indiquant un équilibre entre la vitesse de croissance de la couche d'oxyde et sa volatilization. Dans ces conditions, l'échange isotopique entre les espèces $^{18}O$ et $^{16}O$ est le mécanisme dominant les modifications observées dans la couche d'oxyde. La figure Annexe 6 est une représentation schématique des mécanismes de diffusion dans la couche d'oxyde formée sur l'alliage inoxydable 316 issue des analyses ToF-SIMS.
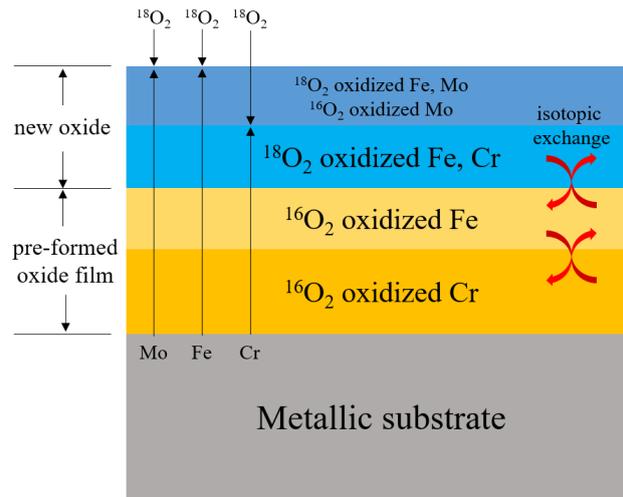
**Fig.Annexe-6** Scheme of the ion transport mechanisms for oxide films (native oxide and passive film) formed on 316L stainless steel

La cinétique d'oxydation a été ajustée par l'équation annexe-1, et la constante parabolique kp et la constante de volatilisation kv peuvent être obtenues. Pour le film natif sur acier inoxydable 316L, les valeurs de kp et kv dérivées de l'ajustement sont de $7,9 \times 10^{-2}$ nm$^2$.s$^{-1}$ et $6 \times 10^{-3}$ nm.s$^{-1}$, respectivement. Ces valeurs sont nettement supérieures à celles calculées pour les films passifs formés sur 316L ($k_p = 3 \times 10^{-3}$ nm$^2$.s$^{-1}$ et $k_v = 4 \times 10^{-4}$ nm.s$^{-1}$) et 304L ($k_p = 1,8 \times 10^{-2}$ nm$^2$.s$^{-1}$ et $k_v = 4 \times 10^{-3}$ nm.s$^{-1}$). Cela est principalement dû au fait que le film d'oxyde natif a: (i) une densité de limite de grain plus élevée qui réagit comme un chemin de diffusion rapide pour les espèces diffusantes, et (ii) une teneur en oxyde de Cr inférieure par rapport au film passif formé électrochimiquement. Lorsque nous avons comparé les valeurs $k_p$ et $k_v$ pour les films passifs sur 316L et 304L, les valeurs pour 316L sont presque une grandeur inférieures à celles pour 304L. Cela est attribué à la couche la plus externe de Mo, qui inhibe la diffusion du Cr et empêche également l'exposition à l'oxyde de Cr dans la surface externe.

# RÉSUMÉ

Le comportement à la corrosion et les mécanismes de transport des ions ont été étudiés par des techniques d'analyse de surface (spectrométrie d'ions secondaires à temps de vol et spectroscopie de photoélectrons) combinées à des mesures électrochimiques sur des alliages métalliques contenant du Cr, comme l'alliage à haute entropie CoCrFeMnNi, et les aciers inoxydables 304L et 316L. Pour l'alliage à haute entropie, à la fois l'oxyde natif formé à l'air et les films passifs (formés dans l'acide sulfurique) ont une structure bicouche, comprenant une couche interne riche en oxyde de Cr et Mn et une couche externe d'oxydes de Cr/Fe/Co. La couche d'oxyde ne contient pas de Ni. Les effets de l'exposition du film natif à l'acide sulfurique et de la passivation sous polarisation anodique ont été étudiés.

Pour les aciers inoxydables 304L et 316L, des films d'oxyde à structure bicouche ont également été mis en évidence sur les films natif et passif, avec une couche externe riche en Fe et Mo (pour 316L) et une couche interne riche en Cr. La stabilité thermique du film passif formé sur une surface en acier inoxydable 316L a été testée lors de l'exposition progressive, sous Ultra Haut Vide, du film d'oxyde depuis la température ambiante jusqu'à 300°C. Pour des températures inférieures à 250°C, les profils ToF-SIMS ont mis en évidence la déshydroxylation et la déshydratation des films d'oxyde de surface. Au-dessus de 250°C, la principale modification du film est liée à la diffusion de cations Cr3+ dans la couche d'oxyde avec pour conséquence la formation d'oxyde de chrome aux dépens de l'oxyde de fer (thermodynamiquement moins stable) à l'interface oxyde interne/ oxyde externe. Les mécanismes de transport des espèces ioniques à travers la couche d'oxyde formée sur les aciers inoxydables 304L et 316L ont ensuite été élucidés grâce à la mise au point d'un processus d'oxydation en 2 étapes, où la première étape (croissance d'un oxyde natif ou passif) est suivie d'une oxydation en milieu gazeux à haute température (300°C) sous faible pression d'oxygène isotopique $^{18}O_2$. Les résultats révèlent que la diffusion des cations vers l'extérieur régit la croissance des oxydes. Sur l'alliage inoxydable 316L, la couche externe d'oxyde de Mo empêche le transport continu des ions Cr vers la surface. Les films passifs, en raison de leur composition et de leur structure, présentent une vitesse d'oxydation nettement inférieure à celle des films d'oxyde natifs.

# MOTS CLÉS

**alliage à haute entropie, acier inoxydable, corrosion, analyse de surface, film d'oxyde, transport ionique, stabilité thermique**

# ABSTRACT

The corrosion behaviour and ion transport mechanisms were investigated by surface analytical techniques (Time-of-Flight Secondary Ion Mass Spectrometry and X-ray Photoelectron Spectroscopy) combined with electrochemical measurements on Cr-containing alloys, including CoCrFeMnNi high entropy alloy (HEA), 304L and 316L stainless steels (SS). For HEA, both air-formed native oxide and passive films (formed in sulfuric acid) have a bilayer structure, comprising Cr and Mn inner layer and Cr/Fe/Co mixture outer layer. No nickel is observed in the oxide layer. The effects of exposure of the native film to sulfuric acid and passivation under anodic polarization have been investigated.

For SS, both the native and passive films formed on 304L and 316L SS exhibit a bilayer structure, with Fe-rich and Mo-rich (for 316L SS) outer layer and Cr-rich inner layer. The thermal stability of the passive film formed on 316L stainless steel surface was tested during the gradual exposure, under Ultra High Vacuum, of the oxide from room temperature to 300°C. Below 250 °C, the dehydroxylation and dehydration of the surface oxide films were observed by ToF-SIMS in-depth profiling. Above 250 °C, the main modification in the film is linked to the diffusion of $Cr^{3+}$ cations in the oxide, resulting in the formation of chromium oxide at the expense of iron oxide (thermodynamically less stable) at the internal oxide / external oxide interface. The ion transport mechanism on SS was then elucidated thanks to the development of a 2-step process, where the first step (native or passive oxide growth) is followed by oxidation in oxygen gas at high temperature (300°C) under low pressure of isotopic $^{18}O_2$. The results reveal that the outward diffusion of cations governs the growth of the oxides. On the 316L stainless steel, the outer layer of Mo oxide prevents the continuous transport of Cr ions to the surface. Passive films, due to their composition and structure, have an oxidation rate significantly lower than that of native oxide films.

# KEYWORDS

**HEA, stainless steel, corrosion, surface analysis, oxide film, ion transport, thermal stability**